



HAL
open science

Development of a lattice Boltzmann-based numerical method for the simulation of reacting flows

Seyed Ali Hosseini

► **To cite this version:**

Seyed Ali Hosseini. Development of a lattice Boltzmann-based numerical method for the simulation of reacting flows. Chemical and Process Engineering. Université Paris-Saclay; Otto-von-Guericke-Universität Magdeburg, 2020. English. NNT : 2020UPASC012 . tel-02893963v2

HAL Id: tel-02893963

<https://theses.hal.science/tel-02893963v2>

Submitted on 9 Jul 2020

HAL is a multi-disciplinary open access archive for the deposit and dissemination of scientific research documents, whether they are published or not. The documents may come from teaching and research institutions in France or abroad, or from public or private research centers.

L'archive ouverte pluridisciplinaire **HAL**, est destinée au dépôt et à la diffusion de documents scientifiques de niveau recherche, publiés ou non, émanant des établissements d'enseignement et de recherche français ou étrangers, des laboratoires publics ou privés.

Development of a lattice Boltzmann-based numerical method for the simulation of reacting flows

Thèse de doctorat de l'Université Paris-Saclay

École doctorale n° 579, Sciences Mécaniques et
Énergétiques, Matériaux et Géosciences (SMEMAG)
Spécialité de doctorat: Énergétique
Unité de recherche: Université Paris-Saclay, CNRS, CentraleSupélec,
Laboratoire EM2C, 91190, Gif-sur-Yvette, France.
Réfèrent: : CentraleSupélec

**Thèse présentée et soutenue à Magdebourg, le 22 Avril 2020,
par**

Seyed Ali HOSSEINI

Composition du jury:

Mr. Berend Van Wachem Professeure, Université Otto von Guericke (Institut de génie des procédés)	Président
Vincent Giovangigli Professeure, École Polytechnique (Centre de Mathématiques Appliquées)	Rapporteur
Ilya Karlin Professeure, École polytechnique fédérale de Zürich (Laboratoire d'aerothermochimie et de systèmes de combustion)	Rapporteur
Benedetta Franzelli Docteure, Université Paris-Saclay (CentraleSupélec, EM2C)	Examinatrice
Nasser Darabiha Professeure, Université Paris-Saclay (CentraleSupélec, EM2C)	Directeur
Dominique Thévenin Professeure, Université Otto von Guericke (Laboratoire de dynamique des fluides et d'écoulements techniques)	Directeur

Title: Development of a lattice Boltzmann-based numerical method for the simulation of reacting flows

Keywords: Lattice Boltzmann, Multi-species flows, detailed chemistry, combustion, reacting flows

Abstract: The lattice Boltzmann (LB) method has emerged as an efficient alternative to classical methods for fluid flow simulation. It can also potentially be used for such complex flows as those involved in low Mach number combustion involving large numbers of field variables, temperature variations, variable properties and spanning multiple scales. Given the variations in diffusion parameters and existing stability issues in the LB, the choice of the collision operator is of the utmost importance. Furthermore, dilatation effects must be introduced as the original LB scheme was developed for isothermal flows. The flow solver has to be supplemented with components modeling balance equations for the energy and species mass fields. In the present work, first the LB solver (with plethora of collision operators) is analyzed using approaches like the von Neumann method. A variety of collision models including multiple relaxation, regularized, and equilibrium distribution functions, like different orders of

the Hermite expansion, and the entropic equilibrium are considered. Then, two different approaches for introducing dilatation into the flow solver are proposed and validated. These approaches include one relying on a decomposition of pressure into a uniform thermodynamic and fluctuating hydrodynamic components, and a fully compressible formulation relying on a thermal Hermite expansion of the equilibrium. Appropriate collision operators, resulting on the widest stability domain for the latter are also proposed. In addition, minimalist LB solvers appropriate for the targeted flows are derived to model energy and species mass transport. Contrary to the classical passive scalar lattice Boltzmann models, the proposed formulations are not limited to constant specific heat capacity and/or density and include higher-order effects such as viscous dissipation heating. A variety of cases, covering premixed and diffusion flames, 1-, 2- and 3-D flows are then considered for validation of the overall solvers.

Titre: Développement d'une méthode basée sur les réseaux de Boltzmann pour la simulation d'écoulements réactifs

Mots clés: Méthode des réseaux de Boltzmann, Écoulements multi-espèces, Chimie détaillée, Combustion, Écoulements réactifs

Abstract: La méthode des réseaux de Boltzmann est une alternative efficace aux approches classiques de simulation des écoulements. Cette méthode peut potentiellement être étendue à des écoulements complexes, comme la combustion à nombre de Mach faible avec un grand nombre de variables, variation de température, propriétés variables et couvrant différentes échelles. Étant donné les variations importantes des paramètres de diffusion et les problèmes de stabilité de la méthode des réseaux de Boltzmann, le choix de l'opérateur de collision est de la plus haute importance. De plus, la méthode des réseaux de Boltzmann dans sa forme originelle étant formulée pour des écoulements isothermes, les effets de dilatation doivent être introduits dans le solveur. Des composantes additionnelles pour modéliser le transport de variables telles que l'énergie et les espèces doivent être ajoutées au solveur fluide. Dans un premier temps, les propriétés numériques du solveur (en prenant en compte une multitude de modèles de collision) sont étudiées via des méthodes telles que l'analyse de von Neumann. L'étude couvre des modèles de collision comme l'opérateur de collision avec plusieurs temps de relaxation (MRT),

le modèle régularisé, et l'effet du choix de la fonction d'équilibre notamment les différents ordres du développement d'Hermite ou l'équilibre entropique. Ensuite, deux différentes approches sont proposées pour l'introduction de la dilatation dans le solveur fluide : Une basée sur une décomposition d'échelle de la pression en pression thermo- et hydrodynamique et une basée sur un développement non-isotherme d'Hermite de la fonction d'équilibre. Un opérateur de collision approprié est aussi proposé pour cette dernière, afin de maximiser le domaine de stabilité linéaire. De plus, des modèles minimalistes adaptés aux équations de transport d'énergie et d'espèces basés sur la formulation des réseaux de Boltzmann sont proposés et validés. Contrairement aux solveurs dits de scalaires passifs, ces derniers ne sont pas limités à des densités et/ou capacités calorifiques constantes et prennent en compte des termes de couplage telles que la production de chaleur par dissipation visqueuse. Enfin, afin de valider le solveur dans son intégralité une multitude de cas, couvrant les flammes pré-mélangées et de diffusion, et des configurations en 1-, 2- et 3-D sont étudiés.



To my parents

Acknowledgements

First of all, I have to express my gratitude to the committee members who agreed to take part in my defense (especially given the rather unusual circumstances under which we have all been living for the past couple of months), took the time to read the manuscript and with whom I had very insightful discussions.

Though hard to resume in a couple of sentences or even write down on a piece of paper, I have to thank my supervisors, Dominique Thévenin and Nasser Darabiha who have, without an ounce of a doubt, played the most important role in the accomplishment of this thesis. None of what is presented in this manuscript would have been possible without their support. The present work is also the product of collaborations with colleagues from around the world. First and foremost, I have to acknowledge a very instructive (on a professional level) and delightful (on a personal level) stay at the CCE laboratory at Tsinghua university. This stay would not have been possible without the support of my host, Kai Luo, with whom I had very interesting discussions on the lattice Boltzmann method. I also got the opportunity to get to know colleagues, and now friends, such as Linlin and Chuandong who also spend their days working kinetic models for computational fluid dynamics. I also have to thank Christophe Coreixas, a very knowledgeable colleague and friend, with whom I had, and still regularly have, interesting discussions on the lattice Boltzmann method.

I also have to thank office-mates and colleagues both in France and Germany. A number of them, like Gabor Janiga to cite just one, were detrimental to the progress of this work.

Last but not least, I would like to thank my family to whom I owe everything and finish with this verse by Ibn Malik:

بَابِ اَقْدَى عَدَى فِى الْكُرْمِ وَمِنْ يَشَابِهِ اَبَ فَمَا ظَلَمَ

Magdeburg,
May 2020

Seyed Ali Hosseini

Declaration

I hereby declare that I prepared the submitted work without inadmissible assistance and without the use of any aids other than those indicated. Facts or ideas taken from other sources, either directly or indirectly have been marked as such.

In particular, I did not use the services of a commercial graduation consultation. Furthermore, I have not made payments to third parties either directly or indirectly for any work connected with the content of the submitted dissertation.

This work has so far not been submitted either in France, Germany or abroad in same or similar form as a dissertation and has also not yet been published as a whole.

Magdeburg,

May 04, 2020

Seyed Ali Hosseini

Résumé substantiel

Apparu au début des années 90, la méthode des réseaux de Boltzmann est rapidement devenue une alternative efficace et populaire aux approches classiques de simulation des écoulements incompressibles. La localité des effets hors-équilibres avec des termes non-linéaires et la linéarité de la convection non-locale des fonctions de distribution de probabilité font de cette approche une méthode simple à implémenter et adaptée aux nouvelles architectures de processeurs parallèles. Bien qu'étendu à d'autres domaines d'application tels que les écoulements multiphasiques (solide-liquide et/ou gaz-liquide) ou les écoulements en milieux poreux, les études sur le développement de schémas numériques pour des écoulements complexes comme la combustion à nombre de Mach faible, avec un grand nombre de variables, variation de température, propriétés variables et couvrant différentes échelles, restent limitées. Etant donné les variations importantes des paramètres de diffusion dans ce type d'écoulement, liées aux variations de température, composition et densité, et les problèmes de stabilité de la méthode des réseaux de Boltzmann dans la limite de nombre de Fourier (coefficient de diffusion adimensionnée par les valeurs caractéristiques de la discrétisation en temps et en espace) faible, le choix de l'opérateur de collision est de la plus haute importance. De plus, la méthode des réseaux de Boltzmann dans sa forme originelle étant formulée pour des écoulements isothermes, les effets de dilatation doivent être introduits dans le solveur. Etant donné le nombre limité de degrés de liberté dans la quadrature d'ordre trois utilisée pour la discrétisation de l'équation de Boltzmann en espace-phase, celle-ci ne peut pas résoudre l'équation de Fourier pour le transfert d'énergie. De ce fait, des composantes additionnelles pour modéliser le transport de variables telles que l'énergie et les espèces doivent être ajoutés au solveur fluide. Dans un premier temps, les propriétés numériques du solveur isotherme (en prenant en compte une multitude de modèles de collision) sont étudiées via des méthodes telles que l'analyse de von Neumann. L'étude couvre des modèles de collision comme l'opérateur de collision avec plusieurs temps de relaxation (MRT), le modèle régularisé, et l'effet du choix de la fonction d'équilibre notamment les différents ordres du développement d'Hermite ou l'équilibre entropique. Celle-ci permet d'établir des domaines de stabilité linéaire et l'effet des opérateurs de collision avancé sur les propriétés spectrales du schéma numérique. Il est observé que l'opérateur de collision régularisé par récursion a le domaine de stabilité le plus large aux côtés de l'opérateur à temps de relaxation multiple dans l'espace des moments centrés. Cela étant, ce dernier est plus efficace en termes de coût de calculs et simplicité et a plus de degrés de liberté permettant de contrôler la dissipation numérique et étendre, encore plus, le domaine de stabilité. Ensuite, deux différentes approches sont proposées pour l'introduction de la dilatation dans le solveur fluide : Une basée sur une décomposition d'échelle de la pression en pression thermo- et hydrodynamique et une basée sur un développement non-isotherme d'Hermite de la fonction d'équilibre. La première suit la philosophie générale des solveurs Navier-Stokes à nombre de Mach faible en faisant abstraction des effets acoustiques. La deuxième approche, moyennant des termes de correction pour les moments d'ordre trois, permet de résoudre les équations de Navier-Stokes compressibles. Un opérateur de collision approprié est aussi proposé pour cette dernière, afin de maximiser le domaine de stabilité linéaire. De plus, des modèles minimalistes adaptés

aux équations de transport d'énergie et des espèces basés sur la formulation des réseaux de Boltzmann sont proposés et validés. Contrairement aux solveurs dit de scalaires passifs, ces derniers ne sont pas limités à des densités et/ou capacités calorifiques constantes et prennent en compte des termes de couplage tels que la production de chaleur par dissipation visqueuse. Des solveurs en différences finies pour les équations de transport d'énergie et des espèces sont aussi couplés au solveur fluide comme alternative aux schémas numériques Boltzmann sur réseaux développé a cet effet. Enfin, afin de valider le solveur dans son intégralité une multitude de cas, couvrant les flammes pré-mélangées et de diffusion, et des configurations en 1-, 2- et 3-D sont étudiés.

Contents

Contents	x
List of Figures	xi
Nomenclature	xix
1 Introductory remarks	1
1.1 Context, motivations and objectives	2
1.2 Thesis outline	3
1.3 Miscellaneous activities	4
2 Discrete kinetic theory of gases for the hydrodynamic regime	6
2.1 Introduction to the kinetic theory of gases and the Boltzmann equation	8
2.1.1 The Boltzmann equation	8
2.1.2 Macroscopic variables and equilibrium balance equations	10
2.1.3 Thermodynamic equilibrium: the Maxwell-Boltzmann distribution	12
2.1.4 Approximations to the collision term	13
2.1.4.1 Linear approximation: Bhatnagar-Gross-Krook	13
2.1.4.2 Extension to variable Prandtl numbers	13
2.2 Brief overview of reduced kinetic models	14
2.2.1 Grad’s moments method	14
2.2.2 Chapman-Enskog approach	16
2.3 Phase-space discretization and construction of discrete thermodynamic attractors	17
2.3.1 Direct moment-matching methods	17
2.3.2 Quadrature-based methods: projection onto Hermite polynomials basis	18
2.3.3 Entropic discrete equilibrium distribution functions	21
2.4 Space and time-discretization	22
2.4.1 Eulerian approaches	22
2.4.2 Lagrangian method with on-lattice propagation	23
2.5 Enhanced collision operators for the LBM	25
2.5.1 Collision operator in momentum space	25
2.5.1.1 Raw moments-based decomposition	25
2.5.1.2 Central moments-based decomposition	27
2.5.2 Pre-collision population reconstruction via regularization	28
2.5.3 Entropic lattice Boltzmann method	29
2.6 Summary	31

3	The isothermal lattice Boltzmann method: detailed study of properties	33
3.1	Bulk flow solver analysis : Asymptotic behavior	35
3.1.1	Asymptotic analysis : the Chapman–Enskog development	35
3.1.2	Asymptotic error analysis	37
3.2	Bulk flow solver analysis: non-vanishing wave-numbers	42
3.2.1	Methodology : The von Neumann formalism	43
3.2.2	Stability domain: Effect of equilibrium state	44
3.2.3	Equilibration strategy I: Filtering out higher-order contributions with regularization	47
3.2.4	Equilibration strategy II: Independent relaxation of ghost moments, the minimalist example of the LKS	49
3.2.5	Equilibration strategy III: Choice of basis moments, LKS vs TRT . . .	51
3.2.6	Equilibration strategy IV: central moments	52
3.3	Numerical applications	53
3.3.1	2-D periodic shear layer: Stability for under-resolved simulations . . .	54
3.3.2	3-D Taylor-Green vortex: Effect of ghost modes relaxation on under and moderately resolved features	56
3.4	Summary and closing remarks	59
4	Species and Energy balance	62
4.1	Introduction to macroscopic equations	65
4.1.1	Species mass balance equations	65
4.1.1.1	Production rate	65
4.1.1.2	Diffusion velocity	66
4.1.2	Energy balance equation	68
4.1.3	Parameter evaluation	70
4.2	Modified advection-diffusion LB solver for energy balance equation	71
4.2.1	Theoretical background	71
4.2.1.1	Brief overview of different LB formulations for energy balance	71
4.2.1.2	CE analysis: shortcomings of the advection-diffusion LB model	73
4.2.1.3	Advection-diffusion model for the mixture-averaged energy balance equation	74
4.2.2	Numerical application and validation	78
4.2.2.1	Heat diffusion with variable thermal conductivity	78
4.2.2.2	Transient diffusion with variable specific heat capacity . . .	78
4.2.2.3	Validation of viscous heating term: 2-D thermal Couette flow	79
4.2.2.4	2-D channel flow with heated obstacles	80
4.2.2.5	Heated lid-driven cavity with variable thermo-physical prop- erties	82
4.2.2.6	Turbulent flow over a multi-layered wall-mounted cube . . .	85
4.3	Species mass balance equations	88
4.3.1	Background and theory	88
4.3.1.1	Brief overview of the literature with a focus on low-order models	88

4.3.1.2	Overcoming issues in the advection-diffusion model: advanced diffusion models and variable density	91
4.3.2	Validation of the proposed model	93
4.3.3	Hirschfelder-Curtiss diffusion: pseudo 1-D diffusion	93
4.3.4	Validation of mass corrector: 2-D counterflow Propane/air flame	95
4.3.5	Validation of mass corrector: 3-D counterflow non-premixed Ozone/air reacting flow	99
4.4	Final remarks	100
5	Thermo-compressibility on standard stencils	102
5.1	Beyond Boussinesq: Low Mach number approximation	105
5.1.1	Model formalism	105
5.1.1.1	Decoupling of density: introducing hydrodynamic pressure	106
5.1.1.2	Introducing thermo-compressibility: Evaluation of velocity divergence	107
5.1.1.3	Space and time-discretized equations	108
5.1.2	Validation and numerical application	109
5.1.2.1	Natural convection in a 2-D heated cavity with large temperature ratios	109
5.1.2.2	Three-dimensional thermo-compressible Taylor-Green vortex with species	111
5.2	Implicit approach: Thermal discrete equilibrium	114
5.2.1	Equilibrium distribution function: Thermal Hermite expansion	115
5.2.2	Chapman-Enskog analysis	115
5.2.3	Further extension of stability domain: temperature-scaled central moments	117
5.2.4	Validation and numerical application	118
5.2.5	Galilean invariance: sound speed, acoustic and shear wave dissipation rate	119
5.2.5.1	Low Mach number viscous 1-D Sod shock tube	121
5.3	Spectral analysis of the implicit scheme	123
5.3.1	Effect of EDF order	123
5.3.2	Advanced collision model: effect of regularization	124
5.3.3	Central moments MRT versus temperature-scaled central moments	124
5.3.4	Effect of correction term	126
5.4	Concluding remarks	127
6	Numerical application: Combustion simulation	129
6.1	Employed code and models	131
6.2	Numerical applications and validation	133
6.2.1	1-D flame simulations	134
6.2.1.1	First validation case: 1-D premixed Propane/air flame with simple thermo-chemistry	134

6.2.1.2	Order of accuracy: Methane/Air 1-D freely-propagating flame with BFER scheme	136
6.2.2	Complex configurations	138
6.2.2.1	Premixed Propane/air 2-D counterflow flame with simple chemistry	139
6.2.2.2	Premixed Propane/air counterflow flame with simple chemistry in 3-D	140
6.2.2.3	Methane/air 2-D coflow diffusion flame with two-step chemistry	141
6.2.2.4	Flame/vortex interaction	143
6.3	Concluding remarks	148
7	Shifted stencils: A promising approach to extend the stability domain of the lattice Boltzmann method	151
7.1	Adaptive phase-space discretization of distribution function: brief overview	153
7.2	Galilean invariance of Gauss-Hermite quadratures	154
7.3	Shifted stencils with on-lattice streaming	155
7.4	Final remarks	162
8	Conclusions and perspectives	163
8.1	Conclusions	164
8.2	Perspectives	165
A	Journal publications of the candidate	185
B	Hermite expansion	187
B.1	Single variable Hermite polynomials	188
B.2	Multivariate Hermite polynomials	190
C	First-neighbor stencils	193
C.1	2-Dimensional stencils	194
C.2	3-Dimensional stencils	195
D	Raw moments-based MRT solvers	197
D.1	Transformation matrices	198
D.1.1	D2Q5 stencil	198
D.1.2	D2Q9 stencil	198
D.1.3	D3Q7 stencil	199
E	Jacobians of different collision operators	200
E.1	SRT collision model	201
E.1.1	Hermite-expansion based EDF	201
E.1.2	Exact entropic EDF	201
E.2	RLBM collision model	202

F	Detailed chemical schemes	203
F.1	Detailed kinetic scheme for an Ozone/air reacting flow (from [1])	203
F.2	Two-step BFER scheme for Methane/air flame [2])	204

List of Figures

2.1	Schematic representation of the relaxation process in the ELBM. Dashed lines represent entropy levels while the triangle illustrates the positivity polytope.	30
3.1	(left) $\Pi_{x^2}^{(eq)}$ moment and (right) relative deviations δ for (in red) first- and (in blue) second-order Hermite polynomial expansion and (in green) entropic EDF. The continuous moment is shown with black plain line. The third-order error line in the left plot is not visible as it is equal to zero.	38
3.2	(left) $\Pi_{x^3}^{(eq)}$ moment and (right) relative deviations δ for (in red) second- and (in blue) third-order Hermite polynomial expansion and (in green) entropic EDF. The continuous moment is shown with black plain line. The red and blue lines are not visible as the green lines fall exactly on top of them.	39
3.3	(left) $\Pi_{x^2y}^{(eq)}$ moment and (right) relative deviations δ for (in red) second- and (in blue) third-order Hermite polynomial expansion and (in green) entropic EDF. The continuous moment is shown with black plain line. The blue lines in the left plot fall exactly on the black plain lines. They are also not visible in the right plot as they are equal to zero.	39
3.4	(left) $\Pi_{x^4}^{(eq)}$ moment and (right) relative deviations δ for (in red) second- and (in blue) third-order Hermite polynomial expansion and (in green) entropic EDF. The continuous moment is shown with black plain line. The red lines are not visible as they coincide with the blue ones.	40
3.5	(left) $\Pi_{x^2y^2}^{(eq)}$ moment and (right) relative deviations δ for (in red) second- and (in blue) third-order Hermite polynomial expansion and (in green) entropic EDF. The continuous moment is shown with black plain line.	41
3.6	(left) $\Pi_{x^3y}^{(eq)}$ moment and (right) relative deviations δ for (in red) second- and (in blue) third-order-Hermite polynomial expansion and (in green) entropic EDF. The continuous moment is shown with black plain line. The red and blue lines are not visible as they coincide with the green lines.	41
3.7	Hierarchy of moments on the D2Q9 stencil. Moments correctly recovered with (Green boxes) entropic, (Green+Red boxes) second, (Green+Red+Blue boxes) third and (Green+Red+Blue+Yellow boxes) fourth-order EDFs. Boxes in gray are moments that cannot be recovered on this stencil. Aliasing effects between moments induced by the quadrature are shown with red arrows. . .	42
3.8	Linear stability domains of SRT collision operator with EDFs of orders (from left to right) two, three and four	45

3.9	Illustration of anisotropy of linear stability domains for EDFs of orders (from left to right) two, three and four, and for seven different non-dimensional kinematic viscosities, i.e. (—) 5×10^{-4} , (—) 1×10^{-3} , (—) 5×10^{-3} , (—) 0.01, (—) 0.05, (—) 0.1, (—) 0.5.	46
3.10	Shear mode dissipation rate (normalized by its physical counterpart) for (left) third- and (right) second-order EDF for three different Mach numbers, i.e. (in red) 0.1, (in blue) 0.2 and (in green) 0.3. The continuum reference is shown with a plain black line.	46
3.11	Linear stability domains of (from left to right) second-order projection, third and fourth-order recursive regularized collision operators. Stability domains of corresponding SRT operators are shown with grey dashed lines.	47
3.12	Orientation-dependence of stability domains for (from left to right) second-order projection, third and fourth-order recursive regularized collision operators. Considered non-dimensional viscosities are: (—) 5×10^{-4} , (—) 1×10^{-3} , (—) 5×10^{-3} , (—) 0.01, (—) 0.05, (—) 0.1, (—) 0.5.	48
3.13	Spectral dissipation of physical modes for (left) second-order project and (right) third-order recursive regularized models with $\nu\delta_t/\delta_x^2 = 10^{-5}$ for three Mach numbers: (in red) 0.05, (in blue) 0.1 and (in green) 0.2.	48
3.14	Linear stability domain iso-contours of the LKS with EDFs of orders (from left to right) two, three and four. The color bar shows the maximum achievable Mach number.	49
3.15	Effects of the second relaxation coefficient for $\nu\delta_t/\delta_x^2 = 5 \times 10^{-4}$ and Ma=0.1 on (from left to right) dissipation of acoustic and shear modes, and dissipation of hydrodynamic and kinetic modes. The dissipation curves of shear and acoustic modes for all values of $\eta\delta_t/\delta_x^2$ can not be clearly distinguished as they exactly fall onto each other.	50
3.16	Dissipation rate of acoustic modes using the LKS with different values of the second relaxation coefficient versus SRT, obtained using the decaying acoustic wave test-case.	50
3.17	Linear stability domain of the TRT collision operator for EDF of orders (from left to right) two, three and four. The color bar shows the maximum achievable Mach number.	51
3.18	Effects of the second relaxation coefficient for $\nu\delta_t/\delta_x^2 = 5 \times 10^{-4}$ and Ma=0.1 on different modes using the (in blue) TRT and (in red) LKS models. The second relaxation coefficient is set to 5×10^{-5} for both models.	52
3.19	Stability domain of a two relaxation time collision operator (similar to the LKS) based on central moments instead of raw moments.	53
3.20	Stability limits of (left) raw and (right) central multiple relaxation time collision operator (Hermite coefficients are the chosen moments basis) for different orders of the EDF (N). All relaxation coefficients except those tied to the shear and bulk viscosity are set to one.	54

3.21	Vorticity fields for the periodic shear layer case at $t = t_c$ using (from left to right) second-order projection regularized, third-order recursive regularized, LKS with fourth-order EDF and MRT with central Hermite polynomials at three different resolutions (from top to bottom): 32×32 , 64×64 and 128×128	55
3.22	Normalized (left axes and plain lines) kinetic energy and (right axes and dashed lines) kinetic energy dissipation rates at three different resolutions: (from left to right) 32×32 , 64×64 and 128×128 using four different collision models: (in black) second-order projection regularized, (in red) third-order recursive regularized, (in blue) fourth-order LKS and (in green) central Hermite MRT.	56
3.23	Effect of resolution on stability: maximum amplification $\max[\mathfrak{S}(\omega) \delta_x^2 / \delta_t]$ in the $k_x - k_y$ space obtained using SRT collision operator with second-order EDF for three different resolutions, (from left to right) 16×16 , 64×64 and 128×128 points. Unstable wave-numbers are shown with red contour lines, only visible as a very small dot in the right-most figure.	57
3.24	Energy spectra at $t = 10t_c$ as obtained with different resolutions. The reference result at 512^3 using the SRT collision operator is shown with a black plain line.	58
3.25	Energy spectra at $t = 10t_c$ as obtained with (from left to right) 32^3 , 64^3 and 128^3 using the LKS collision model. The reference result at 512^3 using the SRT collision operator is shown with a black plain line.	58
3.26	Iso-surfaces of the z -component of vorticity $\omega_z = 0$ (bottom view in the z -direction, only the upper left quadrant –of the full domain as shown in Fig. 3.27– is shown) at $t = 10t_c$ obtained using the LKS at three different resolutions (from top to bottom): 32^3 , 64^3 , 128^3 with five different values for the free parameter (from left to right): $\lambda = 0.515, 0.53, 0.59, 0.65, 1$.	59
3.27	Iso-surfaces of the z -component of vorticity $\omega_z = 0$ (bottom view in the z -direction) at $t = 10t_c$ obtained using the SRT at resolutions 512^3 as the reference solution.	60
3.28	Spectral dispersion of the shear mode using the SRT with fourth-order EDF, for $Ma = 0.172$ and viscosities corresponding to TGV simulation with (in red) 32^3 and (in blue) 128^3 grid points. Reference is shown with black plain line.	60
4.1	Steady-state (red plain line) analytical and (black symbols) numerical solutions, obtained using the proposed model, for the (left) two-block and (right) temperature-dependent thermal conductivity test-cases.	79
4.2	Unsteady (red plain line) spectral and (black symbols) numerical solutions, obtained using the proposed model, at different times for the three-block media configuration.	80
4.3	Steady-state (red plain line) analytical and (black symbols) numerical solutions, obtained using the proposed model, for the thermal 2-D Couette flow.	81
4.4	Configuration for 2-D channel flow with heated obstacles mounted on upper and lower walls	81

4.5	Steady-state streamlines for the 2-D channel flow with heated obstacles at $Re=400$	82
4.6	Non-dimensional temperature distribution on the surfaces of the three heated obstacles. Red plain lines represent reference data from [3] while black symbols designate results from the present work.	83
4.7	Heated lid-driven cavity configuration.	83
4.8	Steady-state velocity profiles along the (left) horizontal and (right) vertical centerlines, obtained using (red plain lines) Fluent and (black symbols) the LB solver.	84
4.9	Steady-state temperature profiles along the (left) horizontal and (right) vertical centerlines, obtained using (red plain lines) Fluent and (black symbols) the LB solver.	84
4.10	Steady-state (left) velocity and (right) temperature profiles along the horizontal centerlines at different resolutions: (in black) 200×200 , (in red) 100×100 and (in blue) 50×50	85
4.11	Geometrical configuration of channel flow with heated multi-layered wall-mounted obstacle.	86
4.12	Iso-surface of the average vorticity magnitude. The iso-surface value is fixed at 3% of the maximum value	87
4.13	Instantaneous (left) velocity and (right) temperature fields for the turbulent channel flow with a heated obstacles.	88
4.14	Normalized time-averaged turbulent velocity profiles along three vertical lines on the vertical plane located at $y/h=2$. From left to right: $x/h=1.2$, 1.8 and $x/h=2.8$. From top to bottom: average stream-wise velocity, stream-wise diagonal component of Reynolds stress tensor and span-wise diagonal component of Reynolds stress tensor respectively. Symbols: Black solid line: present study, red solid line: LES [4] and black symbols: experimental [5]	89
4.15	Surface temperature distribution along the 0–1–2–3 path-line on a vertical plane at $y/h=2$. Black solid line: present study, red solid line: LES [4], blue solid line: KBC [6] and black symbols: experimental [5]	90
4.16	Surface temperature distribution along the 0–1–2–3–0 path-line on a horizontal plane at $z/h=0.5$. Black solid line: present study, red solid line: LES [4], blue solid line: KBC [6] and black symbols: experimental [5]	90
4.17	Species profiles for the $C_6H_{14}/N_2/H_2$ pure diffusion test-case at $t=1s$. Red plain lines have been obtained using a FD solver while black symbols represent results from the proposed LB solver.	95
4.18	Geometrical configuration 2-D counterflow Propane/air flame.	96
4.19	Velocity distribution along (left) vertical and (right) horizontal centerlines from (plain red line) [7] and (black symbols) current study.	97
4.20	Comparison of (left) temperature and (right) species profiles along vertical centerlines from (plain red line) [7] and (black symbols) current study.	98
4.21	Overall mass fraction along vertical centerline obtained using (red) classical advection-diffusion formulation, (blue) classical model with mass corrector and (black) proposed model with mass corrector.	98

4.22	Geometrical configuration of 3-D counterflow non-premixed Ozone/air reacting flow.	99
4.23	Velocity profile along vertical (z-direction) centerline from (plain red line) REGATH and (black symbols) current study.	100
4.24	Species profiles along vertical (z-direction) centerline from (plain red line) REGATH and (black symbols) current study.	101
4.25	Overall mass fraction along vertical (z-direction) centerline with (red) classical AD-LB and (black) the proposed model.	101
5.1	Steady-state velocity profiles along the (red) horizontal and (blue) vertical centerlines for (left) $Ra=10^4$ and (right) $Ra=10^6$ obtained from (red and blue plain lines) [8] and (black symbols) the LB solver.	110
5.2	Steady-state temperature profiles along three horizontal lines for (left) $Ra=10^4$ and (right) $Ra=10^6$ obtained from (red plain lines) [8] and (black symbols) the LB solver.	111
5.3	Temperature field and iso-contours for (left) $Ra=10^4$ and (right) $Ra=10^6$. Iso-contours go from $T = 240K$ to $960K$ with $\delta T = 30K$	112
5.4	Flow state at different times for the thermal Taylor-Green vortex. From left to right: vorticity magnitude, temperature, H_2 and O_2 mass fractions. From top to bottom: $t = 0, 0.5, 1, 1.5$ ms.	113
5.5	(left) Velocity profiles along the x -direction at $y = N_y/2$ and $z = N_z/2$ and (right) along the y -direction at $x = N_x/2$ and $z = N_z/2$. Results obtained through the proposed model are shown with black symbols while reference solutions from DINO are plotted with plain red lines.	114
5.6	(left) Species mass fraction profiles along the x -direction at $y = N_y/2$ and $z = N_z/2$ and (right) variations of maximum temperature in the domain with time. Results obtained through the proposed model are shown with black symbols while reference solutions from DINO are plotted with plain red lines.	114
5.7	Error in (left) the deviatoric component of the third-order moments tensor for a second-order EDF and (right) in the diagonal components for a third-order EDF, both shown as a function of local temperature.	117
5.8	Isentropic sound speeds obtained using the compressible model for different non-dimensional temperatures and specific heat ratios. Reference sound speed are shown with plain lines while simulations results are represented with symbols.	119
5.9	Effective dissipation rate of the shear mode for the (in black) third- and second-order EDF (in blue) with and (in red) without the correction term obtained for the decaying shear wave test-case. The reference viscosity is shown with a plain line.	120
5.10	Effective dissipation rate of the acoustic modes for the third-order EDF (in blue) with and (in red) without the correction term obtained for the decaying acoustic wave test-case. The reference viscosity is shown with a plain line. Black symbols are not visible as they fall exactly on top of the blue ones.	121

5.11	Sod shock tube simulation results at $t = 1273\delta_t$. Black symbols represents results obtained through the LB simulation while the red lines are the reference profiles from [9].	122
5.12	Stability domain (in the $\theta - \nu\delta_t/\delta_x^2$ space) of the SRT collision operator with (from left to right) second, third and fourth-order EDFs. The colorbar shows the maximum achievable velocity, i.e. $\frac{u}{\delta_x/\delta_t}$	123
5.13	Stability domain (in the $\theta - \nu\delta_t/\delta_x^2$ space) of the regularized collision operator of different order, (from left to right) second-, third- and fourth-order. The color bar shows the maximum achievable velocity, i.e. $\frac{u}{\delta_x/\delta_t}$	124
5.14	Stability domain (in the $\theta - \nu\delta_t/\delta_x^2$ space) of (left) central moments and (right) temperature-scaled central moments MRT collision operators. The color bar shows the maximum achievable velocity, i.e. $\frac{u}{\delta_x/\delta_t}$	125
5.15	(left) Dispersion and (right) dissipation of the acoustic and shear modes for a third-order EDF (in blue) with and (in red) without the correction term at $u_x = 0.05$ and $\theta = 0.5$ for $\nu\delta_t/\delta_x^2 = 1 \times 10^{-4}$. Plain black lines are the reference spectral dispersion and dissipation curves.	126
5.16	Spectral dissipation of the acoustic modes using a third-order EDF and the correction term evaluated using (in black) second-, (in red) fourth-, and (in blue) sixth-order central-differences for (left) $\theta = 0.05$ and (right) $\theta = 1.4$. Plain black lines are the reference spectral dispersion and dissipation curves.	127
6.1	Overall algorithm structure and communication scheme for the low Mach formulation coupled to a finite-difference solver (Approach I).	132
6.2	Overall algorithm structure and communication scheme for the compressible LBM coupled to a FD solver (Approach II).	133
6.3	Overall algorithm structure and communication scheme for the compressible LBM coupled to LB advection-diffusion solvers for the energy and species mass balance (Approach III).	134
6.4	Propane/air laminar flame speed and adiabatic temperature obtained using the different approaches.	136
6.5	Convergence of the different approaches for the Methane/air free flame.	138
6.6	(left) species mass fraction and (right) density and velocity profiles at the flame front for the Methane/air 1-D freely propagating flame. Results from the LB simulation (with approach III) with the highest resolution are shown with black symbols while reference profiles from Cantera are shown with plain lines.	138
6.7	Geometrical configuration of the 2-D counterflow premixed Propane/air flame.	139
6.8	Density and Propane consumption rate fields at steady-state as obtained from LBM and Fluent.	140
6.9	Profiles of y -component of velocity on the vertical centerline as obtained from (red plain line) Fluent and (black symbol) lattice Boltzmann simulations.	141
6.10	Geometrical configuration of the 3-D counter flow premixed Propane/Air flame.	141

6.11	Flow field obtained at steady-state for the 3-D counterflow test-case. Shown in this figure: Iso-surface of Propane consumption rate $\dot{\omega}_{C_3H_8}$ in light gray; streamlines colored with normalized velocity magnitude (see color scale); cut showing the z -component of the velocity vector in the central plane (see color scale).	142
6.12	Profiles of (left) species mass fractions and (right) temperature along the centerline in the z -direction as obtained from (red plain lines) REGATH and (black symbols) LB simulation.	142
6.13	Geometrical configuration of the 2-D coflow Methane/air flame.	143
6.14	Steady-state species, velocity and temperature fields for the Methane/air coflow diffusion flame.	144
6.15	(left) velocity and (right) species mass fraction profiles along the vertical centerline as obtained from (red plain line) Fluent and (black symbols) the LB solver.	144
6.16	Regime diagram for premixed turbulent combustion [10].	145
6.17	Overall configuration of the 2-D premixed flame/vortex interaction case. . .	146
6.18	Snapshots of iso-temperature contours (from 1000 to 2000K with $\delta T = 200K$) at three stages of the pocket formation process as obtained (bottom halves) from LB simulations and (top halves) from [2] using AVBP.	147
6.19	Fuel mass fraction fields at three different times, i.e. (from left to right): 0, 0.08, 0.16, 0.24 and 0.32ms for case 1.	148
6.20	Instantaneous snapshots of temperature field as obtained for different sets of parameters: (from left to right) vortex core radii 3.43×10^{-4} , 1.715×10^{-4} and $8.575 \times 10^{-5}m$; and (from top to bottom) vortex strengths 6.71×10^{-2} , 3.355×10^{-2} , 1.6775×10^{-2} and $8.3875 \times 10^{-3}m^2/s$	149
6.21	Performances of (left) the different collision models for the compressible formulation and (right) comparison of compressible solver to low Mach formulation. EQN designates the order of the EDF, CM-MRT refers to the MRT collision operator in temperature-scaled central moment space, RR to the recursive regularized collision operator and low Mach to the low Mach dilatable solver with a second-order EDF, in terms of MLUPS, short for Million Lattice Updates Per Second.	150
7.1	The concept of adaptive stencils as proposed in [11, 12, 13].	154
7.2	Shifted stencils as obtained through introducing unit shift velocities in the x - and y -directions.	156
7.3	Normalized error of moments (left) Π_{x^3} and (right) Π_{x^2y} with (in red) $\mathcal{N}_x = 0$, (in blue) $\mathcal{N}_x = \frac{\delta x}{\delta t}$ and (in green) $\mathcal{N}_x = 2\frac{\delta x}{\delta t}$. The span-wise Mach number is set to 0.2 and a second-order expansion is used for the EDF.	157

7.4	Linear stability domains of the shifted stencil ($U_x = \delta_x/\delta_t$) for (top row) different EDFs: (from left to right) entropic, second- and fourth-order, and (bottom row) different collision models (with the fourth-order EDF), i.e. (from left to right) LKS and recursive regularized, for different values of the non-dimensional viscosity: (—)0.5, (—)0.1, (—)0.05, (—)0.01, (—) 5×10^{-3} , (—) 1×10^{-3} , (—) 5×10^{-4} . The angles designate the orientation of the velocity (Mach number) vector. The Ma number axis scale is different for the entropic EDF as the domain is considerably larger.	158
7.5	Linear stability domains of the non-shifted stencil for (left) second- and fourth-order SRT, LKS and recursive regularized (shown as RR) with fourth-order EDFs and (right) the entropic EDF, for different values of the non-dimensional viscosity: (—)0.5, (—)0.1, (—)0.05, (—)0.01, (—) 5×10^{-3} , (—) 1×10^{-3} , (—) 5×10^{-4} . While stability limits for each model are shown only in one quadrant, it should be noted that they are the same in the other quadrants. The Ma number axis scale used for the entropic EDF is different from the other schemes as the corresponding linear stability region is considerably larger.	159
7.6	Comparison of pressure contours for an inviscid vortex at (dotted red lines) $t/t_c = 0$ and (plain black lines) $t/t_c = 20$ with $t_c = L/u_0$ being the convective characteristic time and L the simulation domain size. Vortices are convected at (from left to right) $u_0 = \delta_x/\delta_t$, $u_0 = 2\delta_x/\delta_t$ and $u_0 = 3\delta_x/\delta_t$ using SRT collision operator with the second-order polynomial EDF. The lattice shifts are set to the background velocity.	160
7.7	Stability domains of different EDFs and collision models as obtained from the isothermal vortex test-case on a shifted stencil with a shift of $U_x = \delta_x/\delta_t$. As shown in the plot, the SRT collision operator along with two different EDFs, i.e. second- (SRT-EQ2) and fourth-order (SRT-EQ4), are considered. Furthermore, the LKS and recursive regularized (RR) collision operators with fourth-order EDFs are also studied. Upper and lower lines represent the upper and lower stability limits.	160
7.8	Comparison of pressure contours for an inviscid vortex at (red dashed lines) $t/t_c = 0$ and (black plain lines) $t/t_c = 1$ with $t_c = L/u_0$ being the convective characteristic time. Vortices are convected at (left) $u_0 = 0.8\delta_x/\delta_t$ and (right) $u_0 = 1.2\delta_x/\delta_t$, using the entropic EDF. The lattice shifts are set to $U_x = \delta_x/\delta_t$.	161
7.9	L_2 norm of error for the entropic and fourth-order EDFs at $t/t_c = 1$ on a shifted stencil with a shift of $U_x = \delta_x/\delta_t$	161
C.1	2-D stencils used in this manuscript: (left) D2Q5 and (right) D2Q9.	194
C.2	3-D stencils used in this manuscript: (top left) D3Q7, (top right) D3Q15, (bottom left) D3Q19 and (bottom right) D3Q27.	195

Nomenclature

Abbreviations

BBGKY	Bogoliubov-Born-Green-Kirkwood-Yvon
BC	Boundary Condition
BGK	Bhatnagar-Gross-Krook
CE	Chapman-Enskog
CFD	Computational Fluid Dynamics
CFL	Courant Friedrichs Lewy
DNS	Direct Numerical Simulation
EDF	Equilibrium Distribution Function
ELBM	Entropic LBM
ENO	Essentially Non-Oscillatory
EoS	Equation of State
ES-BGK	Ellipsoidal BGK
FD	Finite Differences
KBC	Karlin-Bösch-Chiktamarla collision model, also known as entropic MRT
LB	Lattice Boltzmann
LBM	Lattice Boltzmann Method
LGA	Lattice Gas Automata
LHS	Left-Hand Side
LKS	Lattice Kinetic Scheme
MLUPS	Million Lattice Updates per Seconds

MRT	Multiple Relaxation Time
PDE	Partial Differential Equation
PonD	Particles on Demand
PR	Projection Regularization
RHS	Right-Hand Side
RKN	Runge Kutta of order N
RLBM	Regularized LBM
RR	Recursive Regularization
SRT	Single Relaxation Time
STL	STereoLithography
TGV	Taylor-Green Vortex
TRT	Two Relaxation Time
VN	von Neumann
WENO	Weighted Essentially Non-Oscillatory

Physical constants

\mathcal{R}	Ideal gas constant	8.314J/mol.K
k_B	Boltzmann constant	$1.38064852 \times 10^{-23}$ J.K $^{-1}$

Fluid properties

μ	Fluid dynamic viscosity	kg/m.s
$c_{v,k}$	Constant volume specific heat capacity of species k	J/kg.K
\bar{c}_v	Mixture-averaged constant volume specific heat capacity	J/kg.K
M_k	Molar mass of species k	kg
\bar{M}	Mixture-averaged molar mass	kg
$\mathcal{D}_{kk'}$	Binary diffusion coefficient of species k and k'	m 2 /s
D_k	Effective diffusion coefficient of species k	m 2 /s
$\dot{\omega}_k$	Net mass production rate of species k per unit volume	kg/m 3

ν	Fluid kinematic viscosity	m^2/s
λ	Thermal conductivity	$\text{W}/\text{m}\cdot\text{K}$
λ_k	Thermal conductivity of species k	$\text{W}/\text{m}\cdot\text{K}$
$\bar{\lambda}$	Mixture-averaged thermal conductivity	$\text{W}/\text{m}\cdot\text{K}$
c_p	Constant pressure specific heat capacity	$\text{J}/\text{kg}\cdot\text{K}$
$c_{p,k}$	Constant pressure specific heat capacity of species k	$\text{J}/\text{kg}\cdot\text{K}$
\bar{c}_p	Mixture-averaged constant pressure specific heat capacity	$\text{J}/\text{kg}\cdot\text{K}$
c_v	Constant volume specific heat capacity	$\text{J}/\text{kg}\cdot\text{K}$

Macroscopic variables

\mathcal{T}	Fluid viscous stress tensor	$\text{kg}/\text{m}\cdot\text{s}^2$
\mathbf{u}	Fluid velocity	m/s
\mathbf{V}^c	Mass corrector for diffusion velocity	m/s
\mathbf{V}_k	Diffusion velocity of species k	m/s
ϵ	Fluid energy per unit mass	J/kg
ϵ_k	Energy of species k per unit mass	J/kg
ϵ_s	Fluid sensible energy per unit mass	J/kg
ϵ_t	Fluid total energy per unit mass	J/kg
$\epsilon_{t,s}$	Fluid total sensible energy per unit mass	J/kg
ρ	Fluid density	kg/m^3
ρ_k	Density of species k	kg/m^3
h	Fluid enthalpy per unit mass	J/kg
h_k	Enthalpy of species k per unit mass	J/kg
h_s	Fluid sensible enthalpy per unit mass	J/kg
h_t	Fluid total enthalpy per unit mass	J/kg
$h_{t,s}$	Fluid total sensible enthalpy per unit mass	J/kg
T	Fluid temperature	K

X_k	Mole fraction of species k	—
Y_k	Mass fraction of species k	—
Mesoscopic variables		
$\boldsymbol{\xi}$	Particle velocity vector	m/s
\mathbf{c}_α	Discrete particle velocity vector	—
\mathbf{M}	Discrete populations to raw moments transform matrix	—
\mathbf{N}	Raw moments to central moments transform matrix	—
\mathbf{S}	Relaxation coefficients matrix in MRT collision model	—
$\mathcal{H}_{\alpha, x^i y^k z^k}$	Discrete Hermite polynomial of order i, j and k in the x -, y - and z -directions	—
$\mathcal{H}_{x^i y^k z^k}(\boldsymbol{\xi})$	Phase-space-continuous Hermite polynomial of order i, j and k in the x -, y - and z -directions	—
$\Omega(\boldsymbol{\xi})$	Phase-space-continuous collision operator	—
Ω_α	Discrete collision operator	—
$\Pi_{x^i y^k z^k}$	Raw moment of order i, j and k in the x -, y - and z -directions of the distribution function	—
τ	Flow field solver relaxation time	s
τ_k	Species field solver relaxation time	s
τ_T	Energy field solver relaxation time	s
$\tilde{\Pi}_{\theta, x^i y^k z^k}$	Central moment of order i, j and k in the x -, y - and z -directions of the distribution function	—
$\tilde{\Pi}_{x^i y^k z^k}$	Central moment of order i, j and k in the x -, y - and z -directions of the distribution function	—
$a_{x^i y^k z^k}$	Phase-space-continuous Hermite coefficient of order i, j and k in the x -, y - and z -directions	—
$f(\boldsymbol{\xi})$	Phase-space-continuous probability distribution function	—
$f^{(eq)}(\boldsymbol{\xi})$	Phase-space-continuous equilibrium distribution function	—
$f_\alpha^{(eq, N)}$	Discrete equilibrium distribution function of order N	—
f_α	Discrete probability distribution function for flow field solver	—

g'_α	Discrete probability distribution function for low Mach flow field solver	—
g_α	Discrete probability distribution function for energy field solver	—
$g_{\alpha,k}$	Discrete probability distribution function for species field solver	—
w_α	Discrete velocity weights	—

Miscellaneous parameters

δ_t	Time-step size	s
δ_x	Grid size	m
$\delta_{\alpha\beta}$	Kronecker delta function	—
ε	Expansion parameter in Chapman-Enskog analysis	—

Non-dimensional numbers

Br	Brinkman number
Ec	Eckert number
Kn	Knudsen number
Le	Lewis number
Ma	Mach number
Pr	Prandtl number
Ra	Rayleigh number
Re	Reynolds number
Sc	Schmidt number

Chapter 1

Introductory remarks

Contents

1.1	Context, motivations and objectives	2
1.2	Thesis outline	3
1.3	Miscellaneous activities	4

1.1 Context, motivations and objectives

The LBM in its current form made its first appearance in the literature in 1988 [14, 15] as an alternative to the lattice Gas Automata [16, 17, 18, 19]. As put forward by the authors, this formulation (the use of Boltzmann's equation and a probability function instead of discrete particles on the lattice) allowed to eliminate *the statistical noise that plagued the LGA* [14]. Since this first article, and its first numerical realization in [20], it has become a numerical method of choice for fluid dynamics simulations and a serious competitor for classical solvers (different discretization approaches for the Navier-Stokes equations are what we refer to as classical methods). According to S. Succi this success and popularity relies on *four magic ingredients* [21, 22, 23], namely : (a) Exact free streaming, (b) local lattice equilibria, (c) tunable relaxation matrix and (d) flexible external source. These ingredients also form the basis for the definition of the *Lattice Boltzmann Method*: Within the context of the present manuscript only solvers for the phase-space discretized Boltzmann equation relying on Lagrangian discretization of space and time are considered to fall in this category. The strict locality of the collision operator (involving non-linear terms) and strict linearity and exactness of the streaming operator allow for enhanced numerical properties and inexpensive operators. Furthermore, the locality of the operators and their explicit nature are well-adapted to parallel processing as they come with limited communication overhead. The subsequent growth of this numerical method and its extension to plethora of flows are clearly supporting the previously enumerated points.

While rather well-developed in many areas such as multi-phase flows (using either pseudo-potentials [24], free energy [25, 26, 27] or phase-field [28, 29] formulations) as pointed out by the number of citation of X. Shan and H. Chen's seminal article (around 3000 at the time of the writing of this manuscript) [24] or flow in porous media [30, 31] efforts at developing an efficient LB-based numerical solver for multi-species (especially reacting thermal multi-species) flows were stagnating till the end of 2016 when this project started. Although a number of models had been published in the literature, such as [32, 33, 34, 35, 36], simulation were (and still are) limited to very basic configurations. At that time only a handful of articles were published on combustion simulation (partly or entirely) with LBM, i.e. [7, 37, 38, 39, 40, 41, 42, 43, 44]. Of these articles and models most were limited to the *cold flow* assumption [7, 39, 40, 41, 42]. Three of these articles, while incorporating density change in the flow solver relied on improper solvers (the classical advection-diffusion LB solver) for the species and energy balance equations as they are only valid for constant density and specific heat capacities [37, 38, 44]. Finally, all of these articles presented simulations with simple correlations for transport properties (constant-valued), constant thermodynamic parameters (specific heat capacity and enthalpy), simple one-step global chemistry, simple species diffusion based on the Fick generalized approximation and were limited at best to 2-D simulations.

Given the previously mentioned advantages of the LBM, the aim of this project was to extend it to *Direct Numerical Simulation* of low Mach number combustion: An application involving large numbers of species and highly coupled PDEs and spanning multiple scales, making the simulations both *process* and *memory* hungry. While it was clear that the LBM

could help reduce processing load in such simulations it was unclear how it would affect the simulations memory-wise, as performances of LBM-based codes are *memory-bound*. This is of course to be expected as the LBM involves more variables per grid-points (discrete populations). The previous property of LBM-based solvers (larger number of variables per conserved macroscopic moment), along with the large number of species usually encountered in DNS with detailed chemistry and the desire to develop a numerically efficient model prompted us not to consider fully kinetic models, i.e. real multi-component kinetic models and higher-order stencils for fully compressible flows, from the early stage of this work. The approach was instead to develop a solver with only first-neighbor stencils, with, wherever necessary, top-down closures for the model. As such for the energy and species balance equations only advection-diffusion LB solvers and classical finite differences have been considered. Given the state of the literature when this work started the following challenges had to be dealt with: (a) Development of a solver incorporating thermo-compressibility effects able to deal with large deviations from the stencil reference state, (b) extension of existing advection-diffusion LB solvers to solve the energy balance equation with variable density and specific heat capacity, (c) integration of more complex species diffusion models into the advection-diffusion solver and (d) coupling of LB (or FD) species and energy balance solvers to flow solver.

1.2 Thesis outline

This thesis presents solutions for the previously-defined challenges to develop a LBM-based DNS solver for combustion. All models and simulations presented in the manuscript have been implemented and performed using the in-house solver ALBORZ. These features are detailed in section 1.3. The thesis is organised in eight chapters covering all major challenges associated to the simulation of multi-species reacting flows with the LBM:

Chapter 2 (Discrete kinetic theory of gases for the hydrodynamic regime): This chapter provides the basic principles of the kinetic theory of gases, different approaches to reduce the kinetic description for the hydrodynamic regime, a detailed derivation of the LBM along with different collision models.

Chapter 3 (The isothermal lattice Boltzmann method: detailed study of properties): This chapter illustrates the limitations of the isothermal LBM with different EDFs (Hermite-based and entropic) and collision operators. The restrictions are illustrated and studied via the Chapman-Enskog analysis and evaluation of higher-order moments error at the continuum level and then using the linearized von Neumann analysis for the spectral properties and stability domains.

Chapter 4 (Species and energy balance equations): This chapter introduces advection-diffusion LB models developed for flows with variable densities and specific heat capacities, and more advanced diffusion models for the species (i.e. Fick and Hirschfelder-Curtiss with mass corrector). The abilities of the former are illustrated through multiple cases such as conjugate heat transfer.

Chapter 5 (Thermo-compressibility on standard stencils): Two different approaches to extend the isothermal LB flow solver to thermo-compressible flows are presented: (a) A low

Mach number-type thermo-compressible solver based on decoupling thermodynamic and hydrodynamic pressure and (b) one based on a thermal Hermite expansion of the distribution function. To illustrate the ability of the latter to take into account deviations from the reference temperature, and the effects of these deviations on numerical properties, an approach similar to the one used in the previous chapter is taken, i.e. VN analysis of spectral properties.

Chapter 6 (Numerical application: Combustion simulation): All models developed and presented in previous chapters are used to perform fully coupled combustion simulations. These simulations include both diffusion and pre-mixed flames and 1-, 2- and 3-D simulations. Both numerical performances and efficiency of the models are analyzed in this chapter through these test-cases.

Chapter 7 (Shifted stencils: A promising approach to extend the stability domain of the lattice Boltzmann method): This chapter includes detailed perspectives on local state-adaptive LB stencils (based on the shifted stencils concept) to extend the stability domain of the LBM.

Chapter 8 (Conclusions and perspectives): The present manuscript ends with concluding remarks and detailed perspectives for the presented work.

A list of publications based on results and studies reported in the present manuscript is given in appendix A. Furthermore, at the beginning of each chapter corresponding publications from the author are listed.

1.3 Miscellaneous activities

Apart from results presented here, a number of side projects were also conducted during the course of this Ph.D., including multi-phase flow simulations, e.g. gas-liquid flows and solid-liquid systems for crystallization simulations. These projects are best illustrated by looking at the features of the code developed during this Ph.D. The code ALBORZ, initially developed in [45] as a single-file C++ code for particulate flow simulations, including the classical isothermal LBM with a second-order EDF using single and/or multiple relaxation time collision operators was completely re-written and re-organized as a collection of libraries taking advantage of object-oriented programming features in C++. All libraries and features (except the Immersed Boundaries module developed in [45]) available in ALBORZ as of 2020 were developed and implemented by the author and within the context of the present doctoral work. These modules and corresponding features are listed in Table 1.1.

Module	content
Flow solver.cpp	<ul style="list-style-type: none"> - Isothermal solver based on Hermite expansion (up to sixth-order expansion). - Entropic isothermal EDF [46]. - Compressible solver with Hermite expansions (up to sixth-order). - Low Mach number thermo-compressible solver [47, 48]. - Forcing schemes: Shan-Chen [24], Guo [49] and Kupershtokh [50]. - Collision models: SRT, TRT [51], LKS [52, 53, 54], MRT [55], CM-MRT [56], projection regularized [57], recursive regularized [58] and entropic [46]. - Boundary conditions: Bounce-back (velocity and pressure) [59], equilibrium, non-equilibrium extrapolation (velocity and pressure) [60]. - Stencils: D1Q3, D2Q9, D3Q15, D3Q19 and D3Q27.
Thermal solver.cpp	<ul style="list-style-type: none"> - LB-based enthalpy balance solver for compressible flow with variable specific heat capacity [61]. - Finite-difference solver, time-stepping: Euler, RK2. Convection term: central second- and fourth-order, upwind first- and third-order, WENO-3 and WENO-5. Diffusion term: second-order and fourth-order based on [62]. - Collision models: SRT, TRT, LKS and MRT. - Stencils: D1Q3, D2Q4, D2Q5, D2Q9, D3Q7, D3Q15, D3Q19 and D3Q27.
Species solver.cpp	<ul style="list-style-type: none"> - LB-based species balance solver for compressible flow with Fick, Hirschfelder-Curtiss approximation and mass corrector [63]. - Finite Differences solver, time-stepping: Euler, RK2. Convection term: central second- and fourth-order, upwind first- and third-order, WENO-3 and WENO-5. Diffusion term: second-order and fourth-order based on [62]. - Collision models: SRT, TRT, LKS and MRT. - Stencils: D1Q3, D2Q4, D2Q5, D2Q9, D3Q7, D3Q15, D3Q19 and D3Q27.
Phase Field.cpp	<ul style="list-style-type: none"> - LB-based phase-field solver for Allen-Cahn dynamics [63].
Pseudopotential.cpp	<ul style="list-style-type: none"> - Pseudo-potential model with single- and dual-range potentials. - EoS: Shan-Chen, Carnahan-Starling, Redlich-Kwong, Peng-Robinson and Van der Waals.
Geometry.cpp	<ul style="list-style-type: none"> - Parallel (MPI) STL reader based on ray-tracing method, with ability to read multiple STL files.
Parallel.cpp	<ul style="list-style-type: none"> - Parallel (MPI-based) processing with 3-D domain decomposition.

Table 1.1: List of features implemented in ALBORZ.

Chapter 2

Discrete kinetic theory of gases for the hydrodynamic regime

Contents

2.1	Introduction to the kinetic theory of gases and the Boltzmann equation	8
2.1.1	The Boltzmann equation	8
2.1.2	Macroscopic variables and equilibrium balance equations	10
2.1.3	Thermodynamic equilibrium: the Maxwell-Boltzmann distribution	12
2.1.4	Approximations to the collision term	13
2.1.4.1	Linear approximation: Bhatnagar-Gross-Krook	13
2.1.4.2	Extension to variable Prandtl numbers	13
2.2	Brief overview of reduced kinetic models	14
2.2.1	Grad's moments method	14
2.2.2	Chapman-Enskog approach	16
2.3	Phase-space discretization and construction of discrete thermodynamic attractors	17
2.3.1	Direct moment-matching methods	17
2.3.2	Quadrature-based methods: projection onto Hermite polynomials basis	18
2.3.3	Entropic discrete equilibrium distribution functions	21
2.4	Space and time-discretization	22
2.4.1	Eulerian approaches	22
2.4.2	Lagrangian method with on-lattice propagation	23
2.5	Enhanced collision operators for the LBM	25
2.5.1	Collision operator in momentum space	25
2.5.1.1	Raw moments-based decomposition	25

2.5.1.2	Central moments-based decomposition	27
2.5.2	Pre-collision population reconstruction via regularization	28
2.5.3	Entropic lattice Boltzmann method	29
2.6	Summary	31

2.1 Introduction to the kinetic theory of gases and the Boltzmann equation

The aim of this section is to introduce the most essential components of the kinetic theory of gases, starting from the single-particle distribution function and the Boltzmann equation. More general statistical formulation such as Liouville's equation [64] and the BBGKY (Bogoliubov-Born-Green-Kirkwood-Yvon) hierarchy [65, 66, 67, 68], falling outside the scope of the present manuscript, will not be reviewed. A class of approximations to the collision operator (referred to as linear models) will also be introduced, as they are one of the main ingredients of the LBM. The section will then go on to introduce some approaches to obtain reduced models from the Boltzmann equation and derive the classical LBM along with different collision models developed to enhance the numerical properties of the solver.

2.1.1 The Boltzmann equation

Let us consider a control volume, of volume \mathcal{V} filled with \mathcal{N} molecules of mass m . Ignoring the additional rovibrational degrees of freedom, the state of each component in the control volume can be fully determined via space coordinates $i \in \{x, y, z\}$ and the phase-space vector $\xi_i \in \{\xi_x, \xi_y, \xi_z\}$ giving respectively its position in space and velocity. As such each molecule represents a point in physical space $\mathbf{r} \in \mathbb{R}^3$, and in phase-space $\boldsymbol{\xi} \in \mathbb{R}^3$. The state of a gas made up of these single points can then be characterized using a probability distribution function $f(\mathbf{r}, \boldsymbol{\xi}, t)$ such that $f(\mathbf{r}, \boldsymbol{\xi}, t) \prod_{i,r=x,y,z} d\xi_i dr$ represents the number of molecules moving with velocities within the range (ξ_x, ξ_y, ξ_z) and $(\xi_x + d\xi_x, \xi_y + d\xi_y, \xi_z + d\xi_z)$ and within a box of size $dx \times dy \times dz$ located at (x, y, z) at time t . Going back to the control volume considered at the beginning of this section one can compute the total number of molecules as:

$$\mathcal{N} = \int_{\mathcal{V}} \int_{\mathbb{R}^3} f(\mathbf{r}, \boldsymbol{\xi}, t) \prod_{i,r=x,y,z} dr d\xi_i. \quad (2.1)$$

Following this same approach one can easily compute other thermo-hydrodynamic properties. For example the fluid velocity is computed as the first moment of the distribution function:

$$u_i = \frac{\int_{\mathcal{V}} \int_{\mathbb{R}^3} \xi_i f(\mathbf{r}, \boldsymbol{\xi}, t) \prod_{j,r=x,y,z} dr d\xi_j}{\int_{\mathcal{V}} \int_{\mathbb{R}^3} f(\mathbf{r}, \boldsymbol{\xi}, t) \prod_{j,r=x,y,z} dr d\xi_j}, \quad (2.2)$$

while for the internal energy (assuming only translational motion degrees of freedom) one has:

$$\rho \epsilon = \int_{\mathcal{V}} \int_{\mathbb{R}^3} \frac{1}{2} \left(\sum_{i=x,y,z} (\xi_i - u_i)^2 \right) f(\mathbf{r}, \boldsymbol{\xi}, t) \prod_{j,r=x,y,z} dr d\xi_j. \quad (2.3)$$

Other variables can also be computed using the same approach. Details are given in subsection 2.1.2.

To derive a balance equation, similar to those used in classical fluid dynamics for the macroscopic hydrodynamic variables, let us consider the infinitesimal control volume $\prod_{i,r=x,y,z} dr d\xi_i$

in physical and phase-space and the number of components in this volume:

$$d\mathcal{N}(t) = f(\mathbf{r}, \boldsymbol{\xi}, t) \prod_{i=r=x,y,z} dr d\xi_i. \quad (2.4)$$

To get the number of particles at time $t + \delta t$ one must determine the processes affecting their balance:

1. Molecular flux in physical space due to convection with velocity $\boldsymbol{\xi}$,
2. Molecular flux in phase-space via convection caused by external body forces,
3. Molecular collision.

First considering components moving at speed $\boldsymbol{\xi}$, the net flux of molecules into the control volume $\prod_{r=x,y,z} dr$ can be written as:

$$- \int_{S_r} f(\mathbf{r}, \boldsymbol{\xi}, t) \boldsymbol{\xi} \cdot \mathbf{e}_{S_r} dS_r \prod_{i=x,y,z} d\xi_i = -\boldsymbol{\xi} \cdot \nabla f(\mathbf{r}, \boldsymbol{\xi}, t) \prod_{i=r=x,y,z} dr d\xi_i, \quad (2.5)$$

where S_r is the surface surrounding the control volume in physical space, \mathbf{e}_{S_r} is the unit vector perpendicular to the aforesaid surface. The RHS is derived using Gauss's theorem. Using the same approach the net flux in phase-space can be computed as:

$$- \int_{S_\xi} f(\mathbf{r}, \boldsymbol{\xi}, t) \mathbf{F} \cdot \mathbf{e}_{S_\xi} dS_\xi \prod_{r=x,y,z} dr = -\mathbf{F} \cdot \nabla_\xi f(\mathbf{r}, \boldsymbol{\xi}, t) \prod_{i=r=x,y,z} dr d\xi_i, \quad (2.6)$$

where as for the previous equation S_ξ is the surface surrounding the control volume in phase-space and \mathbf{e}_{S_ξ} is the unit vector perpendicular to the aforesaid surface.

To compute the flux due to molecular collision let us consider a molecule moving at speed $\boldsymbol{\xi}$, colliding with another class of molecules moving at velocity $\boldsymbol{\xi}_1$ resulting in post-collision velocities $\boldsymbol{\xi}^*$ and $\boldsymbol{\xi}_1^*$. To facilitate the process we will study the collision on a frame moving at velocity $\boldsymbol{\xi}_1$. In this frame the first class of molecules are moving at velocity $\boldsymbol{\xi}' = \boldsymbol{\xi} - \boldsymbol{\xi}_1$ while the second class are stagnant. The volume swept by a molecule of the first class is $\boldsymbol{\xi}' b db d\sigma$, where b is the impact parameter and $d\sigma$ the differential cross-section, while the number of molecules of the second class per unit volume is $f(\mathbf{r}, \boldsymbol{\xi}_1, t) \prod_{i=x,y,z} d\xi_{1,i}$. As such the number of collisions is:

$$f(\mathbf{r}, \boldsymbol{\xi}_1, t) \boldsymbol{\xi}' b db d\sigma \prod_{i=x,y,z} d\xi_{1,i}.$$

Given that the number of molecules of class $\boldsymbol{\xi}$ in the infinitesimal physical and phase-space control volume is $f(\mathbf{r}, \boldsymbol{\xi}, t) \prod_{i,r=x,y,z} dr d\xi_i$ the total collision rate taking molecules outside the considered control volume is:

$$\Omega_{out} \prod_{i,r=x,y,z} dr d\xi_i = \int_{b,\sigma} \int_{\boldsymbol{\xi}_1} f(\mathbf{r}, \boldsymbol{\xi}_1, t) f(\mathbf{r}, \boldsymbol{\xi}, t) \boldsymbol{\xi}' b db d\sigma \prod_{i,r=x,y,z} dr d\xi_i d\xi_{1,i}. \quad (2.7)$$

Following the same procedure in the reverse direction, i.e. collision of particles outside the considered control volume resulting in flux of components into the volume one gets:

$$\Omega_{in} \prod_{i,r=x,y,z} dr d\xi_i = \int_{b,\sigma} \int_{\xi_1} f(\mathbf{r}, \xi_1^*, t) f(\mathbf{r}, \xi^*, t) \xi'^* b db d\sigma \prod_{i,r=x,y,z} dr d\xi_i^* d\xi_{1,i}^*, \quad (2.8)$$

which in turn, using the summational invariants of the elastic collision process can be rewritten as:

$$\Omega_{in} \prod_{i,r=x,y,z} dr d\xi_i = \int_{b,\sigma} \int_{\xi_1} f(\mathbf{r}, \xi_1^*, t) f(\mathbf{r}, \xi^*, t) \xi' b db d\sigma \prod_{i,r=x,y,z} dr d\xi_i d\xi_{1,i}. \quad (2.9)$$

Using the equations obtained for both the in- and out-flux one gets the following expression for the collision term:

$$\Omega = \int_{b,\sigma} \int_{\xi_1} (f(\mathbf{r}, \xi_1^*, t) f(\mathbf{r}, \xi^*, t) - f(\mathbf{r}, \xi_1, t) f(\mathbf{r}, \xi, t)) \xi' b db d\sigma \prod_{i=x,y,z} d\xi_{1,i}. \quad (2.10)$$

Using the expressions derived for all mechanisms the Boltzmann equation can be introduced as:

$$\boxed{\partial_t f(\mathbf{r}, \xi, t) + \xi \cdot \nabla f(\mathbf{r}, \xi, t) + \mathbf{F} \cdot \nabla_{\xi} f(\mathbf{r}, \xi, t) = \Omega.} \quad (2.11)$$

Before going into further details about the Boltzmann equation it is important to notice that a number of assumptions have been made in the here-presented derivation:

- The Boltzmann equation is only valid under the assumption that $f(\mathbf{r}, \xi, t)$ is a smooth (in space, phase-space and time) square-integrable function.
- Only two-body interactions have been taken into account in the collision operator. This only holds for a *rarefied gas* where the probability of multi-body interactions is much smaller than two-body ones.
- During collision the effect of external forces is negligible (in comparison with intermolecular effects).
- The pre- and post-collision velocities of interacting molecules are uncorrelated. In practice, this means that the collision probability can be expressed as the product of uncorrelated single component probability functions. This is known as the *molecular chaos assumption*, also referred to as *Stosszahlansatz* by Boltzmann. To lift this restriction one must consider more complex models such as the Liouville equations [64] or the BBGKY hierarchy [65, 66, 67, 68].

2.1.2 Macroscopic variables and equilibrium balance equations

As briefly discussed in the previous section, all macroscopic variables appearing in classical thermo-hydrodynamics equations can be computed as moments of the single-particle distribution function. The first three moments of the distribution function are invariants of the

collision operator (as dictated by the summational invariants of elastic microscopic collision):

$$\rho = \int_{\xi} f(\xi) d \prod_{i=x,y,z} \xi_i, \quad (2.12a)$$

$$\rho u_j = \int_{\xi} \xi_j f(\xi) d \prod_{i=x,y,z} \xi_i, \quad (2.12b)$$

$$\rho \epsilon = \int_{\xi} \frac{1}{2} \left(\sum_{j=x,y,z} (\xi_j - u_j)^2 \right) f(\xi) d \prod_{i=x,y,z} \xi_i. \quad (2.12c)$$

Other non-conserved variables can also be computed as moments of the distribution function as:

$$\mathcal{T}_{jk} = \int_{\xi} (\xi_j - u_j)(\xi_k - u_k) f(\xi) d \prod_{i=x,y,z} \xi_i, \quad (2.13a)$$

$$q_k = \int_{\xi} \frac{1}{2} \left(\sum_{j=x,y,z} (\xi_j - u_j)^2 \right) (\xi_k - u_k) f(\xi) d \prod_{i=x,y,z} \xi_i, \quad (2.13b)$$

where \mathcal{T}_{jk} and q_k are respectively the different components of the total stress tensor (including pressure) and energy flux vector.

Going back to the Boltzmann equation, the balance equations for the conserved macroscopic variables can be obtained by taking the corresponding moments. Here we will assume that the fluid is at thermodynamic equilibrium. In practice this means that the collision operator's net effect is null. At order zero one obtains the continuity equation:

$$\underbrace{\partial_t \int_{\xi} f(\xi) d \prod_{i=x,y,z} \xi_i}_{\rho} + \underbrace{\nabla \cdot \int_{\xi} \xi f(\xi) d \prod_{i=x,y,z} \xi_i}_{\rho \mathbf{u}} + \underbrace{\mathbf{F} \cdot \int_{\xi} \nabla_{\xi} f(\xi) d \prod_{i=x,y,z} \xi_i}_0 = \underbrace{\int_{\xi} \Omega d \prod_{i=x,y,z} \xi_i}_0, \quad (2.14)$$

where for the last term on LHS we have used the divergence theorem along with the fact that the distribution function vanishes at $\xi_i \rightarrow \pm\infty$. Following the same procedure at order one:

$$\begin{aligned} \partial_t \underbrace{\int_{\xi} \xi f(\xi) d \prod_{i=x,y,z} \xi_i}_{\rho \mathbf{u}} + \nabla \cdot \underbrace{\int_{\xi} \mathbf{u} \otimes \mathbf{u} f(\xi) d \prod_{i=x,y,z} \xi_i}_{\rho \mathbf{u} \otimes \mathbf{u}} + \nabla \cdot \underbrace{\int_{\xi} (\xi - \mathbf{u}) \otimes (\xi - \mathbf{u}) f(\xi) d \prod_{i=x,y,z} \xi_i}_{\mathcal{T}} \\ - \underbrace{\mathbf{F} \cdot \int_{\xi} \nabla_{\xi} \xi f(\xi) d \prod_{i=x,y,z} \xi_i}_{\rho \mathbf{F}} = \underbrace{\int_{\xi} \xi \Omega d \prod_{i=x,y,z} \xi_i}_0, \quad (2.15) \end{aligned}$$

which is Euler's equation for momentum balance (at thermodynamic equilibrium $\mathcal{T} = p\mathbf{I}$). Finally taking the second-order moment, one gets the energy balance equation (without non-equilibrium fluxes):

$$\begin{aligned} \partial_t \underbrace{\int_{\xi} \frac{\xi^2}{2} f(\xi) d \prod_{i=x,y,z} \xi_i}_{\rho(\epsilon+\mathbf{u}^2/2)} + \nabla \cdot \underbrace{\int_{\xi} \mathbf{u} \frac{\xi^2}{2} f(\xi) d \prod_{i=x,y,z} \xi_i}_{\rho\mathbf{u}(\epsilon+\mathbf{u}^2/2)} - \underbrace{\int_{\xi} \mathbf{u}(\xi - \mathbf{u})^2 f(\xi) d \prod_{i=x,y,z} \xi_i}_{\mathbf{u} \cdot \mathcal{T}} \\ - \underbrace{\mathbf{F} \cdot \nabla_{\xi} \int_{\xi} \frac{\xi^2}{2} f(\xi) d \prod_{i=x,y,z} \xi_i}_{-\rho\mathbf{u} \cdot \mathbf{F}} = \underbrace{\int_{\xi} \xi^2 \Omega d \prod_{i=x,y,z} \xi_i}_{0}. \end{aligned} \quad (2.16)$$

2.1.3 Thermodynamic equilibrium: the Maxwell-Boltzmann distribution

Going back to the Boltzmann equilibrium, it can be seen that the collision term on the RHS of the equation represents the net flux of components in/out of the considered control volume in phase-space. At equilibrium, this flux amounts to zero. As such at thermodynamic equilibrium:

$$\int_{b,\sigma} \int_{\xi_1} (f(\mathbf{r}, \xi_1^*, t) f(\mathbf{r}, \xi^*, t) - f(\mathbf{r}, \xi_1, t) f(\mathbf{r}, \xi, t)) \xi' b db d\sigma \prod_{i=x,y,z} d\xi_{1,i} = 0. \quad (2.17)$$

This equality only holds if:

$$f(\mathbf{r}, \xi_1, t) f(\mathbf{r}, \xi, t) = f(\mathbf{r}, \xi_1^*, t) f(\mathbf{r}, \xi^*, t). \quad (2.18)$$

Taking the logarithm of this expression [69]:

$$\ln f(\mathbf{r}, \xi_1, t) + \ln f(\mathbf{r}, \xi, t) = \ln f(\mathbf{r}, \xi_1^*, t) + \ln f(\mathbf{r}, \xi^*, t), \quad (2.19)$$

it can be clearly seen that $\ln f$ is a summational invariant and as such can be written as a linear combination of the conserved moments:

$$\ln f = A + \mathbf{B} \cdot \xi + C\xi^2. \quad (2.20)$$

Using this expression and the constraints on the conserved moments to determine the constants [69], one gets to the Maxwell-Boltzmann distribution:

$$\boxed{f^{(eq)}(\xi) = \rho \left(\frac{m}{2\pi k_B T} \right)^{3/2} \exp \left[-\frac{m(\xi - \mathbf{u})^2}{2k_B T} \right]}, \quad (2.21)$$

as the *equilibrium* state and extremizer of the entropy functional. More generally, the exponent can be replaced with the Hamiltonian of the considered system.

2.1.4 Approximations to the collision term

Given the complexity of the collision operator, even using simplified cross-section models, a wide number of approximations have been proposed. These simpler expressions for the collision operator are usually referred to as *kinetic models*. A number of linear kinetic models will be introduced in this section.

2.1.4.1 Linear approximation: Bhatnagar-Gross-Krook

One of the oldest, simplest and most efficient approximations to the collision term in the Boltzmann equation was proposed by Bhatnagar, Gross and Krook in [70]. In this approximation, the collision term is modeled through a linear relaxation operator towards the equilibrium state:

$$\boxed{\Omega^{(BGK)} = \frac{1}{\tau} (f^{(eq)} - f)}, \quad (2.22)$$

where τ is the relaxation time. A simple perturbation analysis shows that in order to correctly recover the Navier-Stokes equations, the relaxation coefficient must be set to:

$$\boxed{\tau = \frac{\mu}{p}}, \quad (2.23)$$

where μ is the fluid dynamic viscosity. This collision operator satisfies all the fundamental properties of the collision operator, namely invariance constraints:

$$\frac{1}{\tau} \int_{\xi} (f^{(eq)} - f) \prod_{i=x,y,z} d\xi_i = 0, \quad (2.24a)$$

$$\frac{1}{\tau} \int_{\xi} \xi_j (f^{(eq)} - f) \prod_{i=x,y,z} d\xi_i = 0, \quad (2.24b)$$

$$\frac{1}{2\tau} \int_{\xi} \left(\sum_{i=x,y,z} \xi_i^2 \right) (f^{(eq)} - f) \prod_{i=x,y,z} d\xi_i = 0. \quad (2.24c)$$

and the H-theorem. However, it is only valid in near-equilibrium regimes and leads to a restriction on the Prandtl number. The latter comes from the fact that all moments of the distribution function relax at the same rate, leading to a fixed Prandtl number. To overcome this restriction a number of solutions have been proposed [71], namely ellipsoidal BGK (ES-BGK) operators, BGK collision models with velocity-dependent relaxation coefficients or the Shakhov model. Some of these approaches will be briefly reviewed in the next section.

2.1.4.2 Extension to variable Prandtl numbers

One of the first modifications to the classical BGK collision operator, developed to overcome the fixed Prandtl number issue was the ES-BGK model. While retaining the linear relaxation

form of the original BGK, it relies on a slightly modified equilibrium function defined as:

$$f^{(eq,ES-BGK)}(\boldsymbol{\xi}) = \frac{\rho}{\sqrt{2\pi \det(\mathcal{T})}} \exp \left[-\frac{(\boldsymbol{\xi} - \mathbf{u}) \otimes (\boldsymbol{\xi} - \mathbf{u}) : \mathcal{T}^{-1}}{2} \right], \quad (2.25)$$

where \mathcal{T} is the corrected stress tensor defined as [72]:

$$\mathcal{T} = \frac{1}{\rho} (p\mathbf{I}(1-a) + a\mathcal{T}), \quad (2.26)$$

and a is the free parameter allowing the model to impose a viscosity-independent thermal diffusion coefficient ($\text{Pr} = \frac{1}{1-a}$). It is also worth nothing that in this model the relaxation coefficient is defined as:

$$\tau = (1-a) \frac{\mu}{p}. \quad (2.27)$$

To ensure that the matrix \mathcal{T}^{-1} is positive definite one must have $-\frac{1}{2} \leq a \leq 1$.

Another approach to allow for variable Prandtl numbers in the context of a linear BGK-type collision operator was proposed by Shakhov [73, 74]. Similar to the ES-BGK he proposed a modified (Maxwellian) equilibrium distribution function defined as:

$$f^{(eq,S-BGK)}(\boldsymbol{\xi}) = f^{(eq)} \left[1 + \frac{1 - \text{Pr}}{5} \frac{\mathbf{q} \cdot (\boldsymbol{\xi} - \mathbf{u})}{pk_B T/m} \left(\frac{(\boldsymbol{\xi} - \mathbf{u})^2}{k_B T/m} + \frac{5}{2} \right) \right]. \quad (2.28)$$

The relationship between the relaxation coefficient and fluid viscosity is similar to that of the BGK model. As obvious from the above definition, in this approach a correction is applied to the fourth-order moment of the EDF (controlling non-equilibrium effects in the energy balance equation at the NS level) via the corresponding Hermite polynomial and coefficients. The Hermite polynomials and their properties will be further detailed in subsection 2.3.2.

2.2 Brief overview of reduced kinetic models

To be able to model fluid flows in the rarefied regime or for large Knudsen numbers beyond the NS and Euler descriptions, from the kinetic theory of gases, a number of approaches have been proposed to *systematically* reduce the complexity of the Boltzmann equation. Two of the most popular approaches are reviewed here.

2.2.1 Grad's moments method

Grad's approach to reduce the Boltzmann equation relies on the assumption that the state of the gas can be described by a set of moments of the distribution function:

$$\boldsymbol{\Pi} = \int \boldsymbol{\Psi}(\boldsymbol{\xi}) f \prod_{i=x,y,z} d\xi_i, \quad (2.29)$$

where Ψ is a vector of polynomial functions of the phase-space variable ξ and Π the corresponding moments. For example in the case of Grad's 13-moments theory one has: $\Psi = \{1, \xi_i, \xi^2, \xi_i \xi_j, \xi^2 \xi_i\}$. In general, the number and choice of moments depends on the studied configuration described by non-dimensional numbers such as the Knudsen number. The system of PDE's for Grad's approach are then obtained by taking the corresponding moments of Boltzmann's equation [75]:

$$\partial_t \underbrace{\left(\int \Psi(\xi) f \prod_{i=x,y,z} d\xi_i \right)}_{\Pi} + \nabla \cdot \underbrace{\left(\int \xi \Psi(\xi) f \prod_{i=x,y,z} d\xi_i \right)}_{\phi(\Pi)} + \int \Psi(\xi) F \cdot \nabla_{\xi} f \prod_{i=x,y,z} d\xi_i = \underbrace{\left(\int \Omega \Psi(\xi) f \prod_{i=x,y,z} d\xi_i \right)}_{S(\Pi)}, \quad (2.30)$$

where ϕ are the fluxes of moments Π and S are the effects of molecular collision (interaction). It can readily be observed that this system is not closed as it involves higher-order moments (in the convective term) of the distribution function and moments of the collision term.

To provide closure for the higher-order terms appearing in the balance equations, the distribution function is reconstructed using a truncated (of order N corresponding to the highest-order moments considered in the model) Hermite expansion as [76]:

$$f^{(N)} = f^{(eq)} \left(\sum_{n=0}^N \mathbf{a}_n : \mathcal{H}_n \right), \quad (2.31)$$

where \mathcal{H}_n and \mathbf{a}_n are the Hermite polynomials and coefficients tensors. Details of the theory of Hermite polynomials and expansion will be given in the next section to derive the lattice Boltzmann equations. The distribution function is then used to compute the higher-order moments as [75, 76]:

$$\phi(\Pi) = \int \xi \Psi(\xi) f^{(N)} \prod_{i=x,y,z} d\xi_i. \quad (2.32)$$

Another approach for the construction of the distribution function relies on the concept of entropy. In this approach the distribution function is found as the maximizer of the entropy density subject to constraints stemming from the considered system of moments [69]. In variational calculus this function can be found using Lagrange multipliers. This results in finding the extremum value of the following non-constrained functional:

$$\mathcal{L} = -k \int (f \ln f) d\xi - \sum_{\alpha} \lambda_{\alpha} \int \Psi_{\alpha} f d\xi \quad (2.33)$$

where λ_α are the Lagrange multipliers associated to each moment. The resulting distribution function is then introduced back into Eq. 2.29 to compute the values of the Lagrange multipliers.

2.2.2 Chapman-Enskog approach

As previously discussed, in the balance equations for the conserved moments of the distribution function there are additional terms such as the stress tensor and energy flux vector that need closure. One way to have a closed system of equation is through the so-called moments methods, of which Grad's approach is a popular example. Another approach, within the context of the kinetic theory was proposed by Enskog [77, 78] and Chapman [79, 80, 78]. Different from Grad's method, in this approach only balance equations for conserved moments are considered, i.e. $\mathbf{\Pi}_c = \{\rho, \mathbf{u}, \epsilon\}$ and closures for higher-order moments appearing in the balance equations are provided as functions of these conserved variables and their space derivatives. In practice this is achieved by approximating the distribution function as:

$$f^{(CE)} = f \left(\mathbf{\Pi}_c, \frac{\partial \mathbf{\Pi}_c}{\partial i}, \frac{\partial^2 \mathbf{\Pi}_c}{\partial i \partial j}, \dots \right), i, j \in \{x, y, z\}. \quad (2.34)$$

The basic idea is to expand the distribution function as a power series of a smallness parameter ε , tied to the Knudsen number:

$$f^{(CE)} = f^{(0)} + \varepsilon f^{(1)} + \varepsilon^2 f^{(2)} + \varepsilon^3 f^{(3)} + \dots \quad (2.35)$$

For the collision term in the Boltzmann equation to remain finite in the limit of vanishing Knudsen numbers one must have $f^{(0)} = f^{(eq)}$. As such, and considering that the first five moments are invariants of the collision operator, the expansion is subject to the following so-called compatibility conditions:

$$\int_{\boldsymbol{\xi}} f^{(i)}(\boldsymbol{\xi}) \prod_j d\xi_j = 0, \forall i \neq 0, \quad (2.36a)$$

$$\int_{\boldsymbol{\xi}} \boldsymbol{\xi} f^{(i)}(\boldsymbol{\xi}) \prod_j d\xi_j = 0, \forall i \neq 0, \quad (2.36b)$$

$$\int_{\boldsymbol{\xi}} \boldsymbol{\xi}^2 f^{(i)}(\boldsymbol{\xi}) \prod_j d\xi_j = 0, \forall i \neq 0. \quad (2.36c)$$

The CE approach consists of introducing the expansion of Eq. 2.35 along with expansions of the space and time derivatives into Boltzmann's equation to obtain the normal solutions for different orders of $f^{(i)}$ [81]. Given that this approach is thoroughly treated in subsection 3.1.1 to analyze the asymptotic behavior of the LBM, it will not be further detailed here.

2.3 Phase-space discretization and construction of discrete thermodynamic attractors

Looking at the continuous form of the Boltzmann equation supplemented with the linear BGK collision operator, it is observed that it comes with a 7-D phase-space (assuming that translational motion in 3-D space is the only degree of freedom in the Hamiltonian). As such, prior to discretization in space and time, additional phase-space variables (i.e. particle velocities space) need to be discretised. Given that the LBM is intended as a DNS solver for the NS system of equations, phase-space discretization is subject to a number of constraints, namely correct recovery of the moments appearing at the Euler and NS levels. A number of strategies have been devised to that effect during the past couple of years. Some of these strategies are reviewed in the next subsections.

2.3.1 Direct moment-matching methods

As clearly stated by its name, in this approach one tries to construct a discrete equilibrium by matching the moments appearing in the targeted macroscopic balance equations. Solvers based on this approach are also sometimes referred to as *Discrete Velocity Method* solvers [82].

To identify the constraints, one first uses the CE analysis. For example, a simple CE analysis at order ε shows that to correctly recover the NS and continuity equations, one needs to exactly match moments up to order three [83]. For example let us consider a 1-D system with only translational degrees of freedom. The following moments need to be correctly recovered:

$$\Pi_0 = \int_{\xi_x} \rho \sqrt{\frac{m}{2\pi k_B T}} \exp\left[-\frac{m(\xi_x - u_x)^2}{2k_B T}\right] d\xi_x = \rho, \quad (2.37a)$$

$$\Pi_x = \int_{\xi_x} \xi_x \rho \sqrt{\frac{m}{2\pi k_B T}} \exp\left[-\frac{m(\xi_x - u_x)^2}{2k_B T}\right] d\xi_x = \rho u_x, \quad (2.37b)$$

$$\Pi_{x^2} = \int_{\xi_x} \xi_x^2 \rho \sqrt{\frac{m}{2\pi k_B T}} \exp\left[-\frac{m(\xi_x - u_x)^2}{2k_B T}\right] d\xi_x = \rho \left(u_x^2 + \frac{k_B T}{m}\right), \quad (2.37c)$$

$$\Pi_{x^3} = \int_{\xi_x} \xi_x^3 \rho \sqrt{\frac{m}{2\pi k_B T}} \exp\left[-\frac{m(\xi_x - u_x)^2}{2k_B T}\right] d\xi_x = \rho u_x \left(u_x^2 + 3\frac{k_B T}{m}\right). \quad (2.37d)$$

In the second step of the discrete equilibrium state construction, one chooses a symmetrical stencil (set of discrete velocities) with a number of degrees of freedom equal to or greater than the number of constraints [84, 85, 86]. For example, in the case of the isothermal NS solver, one can either use a four-velocity model or a five-velocity model with an additional constraint to have a unique solution. The discrete equilibrium is then found by solving the

following system of equations:

$$\begin{bmatrix} 1 & 1 & 1 & 1 \\ c_0 & c_1 & c_2 & c_3 \\ c_0^2 & c_1^2 & c_2^2 & c_3^2 \\ c_0^3 & c_1^3 & c_2^3 & c_3^3 \end{bmatrix} \begin{bmatrix} f_0^{(eq)} \\ f_1^{(eq)} \\ f_2^{(eq)} \\ f_3^{(eq)} \end{bmatrix} = \begin{bmatrix} \rho \\ \rho u_x \\ \rho \left(u_x^2 + \frac{k_B T}{m} \right) \\ \rho u_x \left(u_x^2 + 3 \frac{k_B T}{m} \right) \end{bmatrix}, \quad (2.38)$$

where c_{0-3} are the discrete velocities in the stencil and $f_{0-3}^{(eq)}$ are the unknown discrete equilibria to be found by solving this system. The linear system formed using symmetrical stencils might not always be invertible. As such, for some models one might need to add non-symmetrical components to the system [87].

2.3.2 Quadrature-based methods: projection onto Hermite polynomials basis

One approach to discretise phase-space and derive the corresponding *discrete* EDF consists in expanding it in terms of Hermite polynomials and operating a truncation by using Gauss-Hermite quadratures [88, 89, 90].

Before starting the derivation, let us review the basic concepts of multi-variate Hermite polynomials. More details on the Hermite polynomials can be found in Appendix B. They are defined as [89]:

$$\mathcal{H}_n(\boldsymbol{\xi}) = \frac{(-1)^n}{w(\boldsymbol{\xi})} \nabla_{\boldsymbol{\xi}}^n w(\boldsymbol{\xi}), \quad (2.39)$$

where $w(\boldsymbol{\xi})$ is the normalized weight function defined as:

$$w(\boldsymbol{\xi}) = (2\pi)^{-D/2} \exp\left(-\frac{\boldsymbol{\xi}^2}{2}\right), \quad (2.40)$$

with D the dimension of $\boldsymbol{\xi}$. A function f can then be expanded in terms of Hermite polynomials as:

$$f = w(\boldsymbol{\xi}) \sum_{i=0}^{\infty} \frac{1}{n!} \mathbf{a}_n : \mathcal{H}_n(\boldsymbol{\xi}), \quad (2.41)$$

where “:” is the Frobenius inner product and the coefficients \mathbf{a}_n are computed as:

$$\mathbf{a}_n = \int \mathcal{H}_n(\boldsymbol{\xi}) f d\boldsymbol{\xi}. \quad (2.42)$$

The first step in the expansion is the choice of the non-dimensionalization strategy. While not necessary in the expansion, this choice is one of the most important steps in the construction of a discrete kinetic scheme as it will play a key role in the final numerical scheme’s behavior (especially higher-order moments errors). The recent development of LB models relying on non-symmetrical stencils and adaptive non-dimensionalization is a clear proof of the previous assertion. Some of these more advanced non-dimensionalization strategies leading

to shifted stencils or off-lattice propagation will be treated in details in the next chapters [91, 92, 93, 94, 95, 9]. For the sake of simplicity, in this section the continuous Maxwell-Boltzmann EDF is written in the following non-dimensional form as:

$$f^{(eq)}(\boldsymbol{\xi}, \rho, \mathbf{u}, \theta) = \rho(2\pi\theta)^{-D/2} \exp\left[-\frac{(\boldsymbol{\xi} - \mathbf{u})^2}{2\theta}\right], \quad (2.43)$$

where for the remainder of this subsection \mathbf{u} , and $\boldsymbol{\xi}$ are non-dimensionalized with a reference speed of sound c_s , $\theta = \frac{k_B T/m}{c_s^2}$ and $c_s = \frac{k_B T_0}{m_0}$, and T_0 and m_0 are respectively defined as the reference temperature and molecular mass. This results in the following first few Hermite polynomials:

$$\mathcal{H}_0 = 1, \quad (2.44a)$$

$$\mathcal{H}_{i_1} = \xi_{i_1}, \quad (2.44b)$$

$$\mathcal{H}_{i_1 i_2} = \xi_{i_1} \xi_{i_2} - \delta_{i_1 i_2}, \quad (2.44c)$$

$$\mathcal{H}_{i_1 i_2 i_3} = \xi_{i_1} \xi_{i_2} \xi_{i_3} - [\xi_{i_1} \delta_{i_2 i_3}]_{\text{cyc}}, \quad (2.44d)$$

$$\mathcal{H}_{i_1 i_2 i_3 i_4} = \xi_{i_1} \xi_{i_2} \xi_{i_3} \xi_{i_4} + [\delta_{i_1 i_2} \delta_{i_3 i_4}]_{\text{cyc}} - [\xi_{i_3} \xi_{i_4} \delta_{i_1 i_2}]_{\text{cyc}}, \quad (2.44e)$$

where $[\]_{\text{cyc}}$ designates cyclic permutations over the involved indexes, and corresponding *isothermal* ($\theta = 1$) Hermite coefficients:

$$a_0^{(eq)} = \rho, \quad (2.45a)$$

$$a_{i_1}^{(eq)} = \rho u_{i_1}, \quad (2.45b)$$

$$a_{i_1 i_2}^{(eq)} = \rho u_{i_1} u_{i_2}, \quad (2.45c)$$

$$a_{i_1 i_2 i_3}^{(eq)} = \rho u_{i_1} u_{i_2} u_{i_3}, \quad (2.45d)$$

$$a_{i_1 i_2 i_3 i_4}^{(eq)} = \rho u_{i_1} u_{i_2} u_{i_3} u_{i_4}. \quad (2.45e)$$

In the context of the classical LBM, the flow is assumed isothermal. The continuous EDF is then expanded as:

$$f^{(eq)}(\boldsymbol{\xi}, \rho, \mathbf{u}) = w(\boldsymbol{\xi}) \sum_{n=0}^{\infty} \frac{1}{n!} \mathbf{a}_n^{(eq)}(\rho, \mathbf{u}) : \mathcal{H}_n(\boldsymbol{\xi}). \quad (2.46)$$

As seen here, the expanded EDF still goes over the entire phase-space. Given the form of the EDF and the corresponding moments:

$$\Pi_{x^i y^j z^k} = \int \xi_x^i \xi_y^j \xi_z^k f^{(eq)}(\boldsymbol{\xi}, \rho, \mathbf{u}) d\boldsymbol{\xi}, \quad (2.47)$$

and using the Hermite expansion, it can be written as:

$$\Pi_{x^i y^j z^k} = \int P^\infty(\boldsymbol{\xi}, \rho, \mathbf{u}) w(\boldsymbol{\xi}) d\boldsymbol{\xi}, \quad (2.48)$$

where:

$$P^\infty(\boldsymbol{\xi}, \rho, \mathbf{u}) = \frac{\xi_x^i \xi_y^j \xi_z^k f^{(eq)}(\boldsymbol{\xi}, \rho, \mathbf{u})}{w(\boldsymbol{\xi})}, \quad (2.49)$$

and $P^\infty(\boldsymbol{\xi}, \rho, \mathbf{u})$ as defined here is a polynomial function of the variable $\boldsymbol{\xi}$ with order ∞ as the Hermite expansion has not yet been truncated. Given that the aim of the LB method is to solve the Boltzmann equation in the hydrodynamic regime one only needs to correctly recover the moments of the EDF involved in the hydrodynamic equations. Furthermore, Hermite polynomials are orthogonal functions and as such higher-order polynomials have no effect on lower-order terms. Given the previously cited arguments, one can limit the Hermite expansion of the EDF:

$$f^{(eq,N)}(\boldsymbol{\xi}, \rho, \mathbf{u}) = w(\boldsymbol{\xi}) \sum_{n=0}^N \frac{1}{n!} \mathbf{a}_n^{(eq)}(\rho, \mathbf{u},) : \mathcal{H}_n(\boldsymbol{\xi}), \quad (2.50)$$

where N corresponds to the highest-order moment involved in the targeted dynamics. For example, to correctly recover the NS equations for an isothermal flow one needs to correctly recover the third-order moment of the EDF. Now the polynomial P^∞ can be replaced with a finite-order polynomial:

$$P^M(\boldsymbol{\xi}, \rho, \mathbf{u}) = \frac{\xi_x^i \xi_y^j \xi_z^k f^{(eq),N}(\boldsymbol{\xi}, \rho, \boldsymbol{\xi})}{w(\boldsymbol{\xi})}, \quad (2.51)$$

where $M = 2N$. The integral of Eq. 2.48 can be evaluated using a discrete sum through a Gauss-Hermite quadrature as:

$$\int P^M(\boldsymbol{\xi}, \rho, \mathbf{u}) w(\boldsymbol{\xi}) d\boldsymbol{\xi} \cong \sum_{\alpha=0}^Q w_\alpha P^M(\mathbf{c}_\alpha, \rho, \mathbf{u}) \quad (2.52)$$

where \mathbf{c}_α are discrete non-dimensional abscissae used for the quadrature and w_α are the corresponding weights. According to the fundamental theorem of Gaussian quadratures, choosing the abscissae to be the roots of the orthogonal polynomial of the corresponding degree results in the maximum algebraic degree of precision, namely $2Q - 1$. To correctly recover the targeted moments one must have $M \leq 2Q - 1$. The third-order quadrature (designated by $E_{1,5}^3$ in 1-D) results in the following abscissae: $c_{\alpha,i} \in \{-\sqrt{3}, 0, \sqrt{3}\}$ corresponding to the following values $\{-\sqrt{3k_B T_0/m_0}, 0, \sqrt{3k_B T_0/m_0}\}$ in physical units. It is already clear that the third-order quadrature can not correctly recover all the moments appearing at the NS level. The corresponding weights are computed as:

$$w_\alpha = \frac{n!}{(\mathcal{H}_{n-1}(c_{\alpha,i}))^2}. \quad (2.53)$$

In the multi-variate case, the weights can be computed as the products of the weights in each dimension.

In the classical second-order EDF LB formulation (where only mass and momentum are

conserved), this discretization procedure results in the following discrete EDF:

$$\boxed{f_{\alpha}^{(eq,2)}(\mathbf{c}_{\alpha}, \rho, \mathbf{u}) = w_{\alpha} \rho \left(1 + \mathbf{c}_{\alpha} \cdot \mathbf{u} + \frac{(\mathbf{c}_{\alpha} \cdot \mathbf{u})^2}{2} - \frac{\mathbf{u}^2}{2} \right)}. \quad (2.54)$$

Computing the diagonal component of the second-order central moment of the EDF one gets the following pressure (in physical units):

$$p = \sum_{\alpha} c_{\alpha,i}^2 f_{\alpha}^{(eq,2)}(\mathbf{c}_{\alpha}, T_0) = \rho \frac{k_B T_0}{m_0}, \quad (2.55)$$

and therefore, the following isothermal speed of sound:

$$c_s = \sqrt{\left(\frac{\partial p}{\partial \rho} \right)_T} = \sqrt{\frac{k_B T_0}{m_0}}. \quad (2.56)$$

2.3.3 Entropic discrete equilibrium distribution functions

In the context of the entropic lattice Boltzmann method as described in [96], the discrete equilibrium state is found as the minimizer of a convex discrete entropy functional under mass and momentum conservation constraints. The derivation starts with the roots of the third-order Hermite polynomials as the discrete abscissae and considering the following conservation constraints:

$$\sum_{\alpha} f_{\alpha}^{(eq)} = \rho, \quad (2.57)$$

$$\sum_{\alpha} \mathbf{c}_{\alpha} f_{\alpha}^{(eq)} = \rho \mathbf{u}, \quad (2.58)$$

where notations follow those adopted in the previous subsection. The EDF is derived as the function extremizing the discrete entropy function:

$$H_{w_{\alpha}, c_{\alpha}} = \sum_{\alpha} f_{\alpha} \ln \left(\frac{f_{\alpha}}{w_{\alpha}} \right), \quad (2.59)$$

under the previously set constraints. Given the Galilean invariance of the weights the expression for the entropy function is also Galilean invariant [94]. The EDF can be expressed as:

$$f_{\alpha}^{(eq)} = w_{\alpha} \exp(\lambda_0) \prod_{i=1}^D \exp(c_{\alpha,i} \lambda_i), \quad (2.60)$$

where λ_0 and λ_i are the Lagrange multipliers associated with constraints on the zeroth and first-order moments. Introducing the following changes of variables, $X = \exp(-\lambda_0)$ and

$Z_i = \exp(\lambda_i)$ the EDF is re-written as:

$$f_\alpha^{(eq)} = w_\alpha X^{-1} \prod_{i=1}^D Z^{c_{\alpha,i}}. \quad (2.61)$$

Writing down the conservation equations using the new variables for the D2Q9 stencil, the following algebraic system of equations is obtained:

$$\rho X = \sum_{\alpha} w_{\alpha} \prod_{i=x,y} Z^{c_{\alpha,i}}, \quad (2.62a)$$

$$\rho u_x X = \sum_{\alpha} w_{\alpha} c_{\alpha,x} \prod_{i=x,y} Z^{c_{\alpha,i}}, \quad (2.62b)$$

$$\rho u_y X = \sum_{\alpha} w_{\alpha} c_{\alpha,y} \prod_{i=x,y} Z^{c_{\alpha,i}}. \quad (2.62c)$$

Solving this system of equation for Z_x , Z_y and X and keeping positive roots one gets:

$$Z_i = \frac{2u_i + \sqrt{u_i^2 + 1}}{1 - u_i}, \quad (2.63)$$

$$X^{-1} = \rho \prod_{i=x,y} \left(2 - \sqrt{u_i^2 + 1} \right), \quad (2.64)$$

and therefore can express the entropic discrete equilibrium as:

$$f_\alpha^{(eq)} = w_\alpha \rho \prod_{i=x,y} \left(2 - \sqrt{u_i^2 + 1} \right) \left(\frac{2u_i + \sqrt{u_i^2 + 1}}{1 - u_i} \right)^{c_{\alpha,i}}. \quad (2.65)$$

2.4 Space and time-discretization

2.4.1 Eulerian approaches

Considering any one of the phase-space discretized Boltzmann equations, i.e. Hermite polynomials, entropic and moment-matching, it can be observed that the system to be solved consists of a number of coupled hyperbolic PDEs. As such, to retain an acceptable CFL condition and prevent dispersion errors at large wave numbers (also referred to as Gibbs oscillations), one is limited to first-order upwind space discretization. Going to higher-order space accuracy would require non-linear operators, i.e. flux and slope limiters etc, to be added on top of the discretization. For example Beam and Warming's second-order scheme [97] has been extensively used with moment-matching-type discrete equilibrium construction techniques [82, 83, 84]. The ENO (Essentially Non-Oscillatory) class of solvers are also well suited for such hyperbolic systems of PDEs [98, 99, 100] and can, theoretically, reach relatively high orders of accuracy in space (in smooth regions). For example, with the WENO-5 scheme one can achieve fifth-order accuracy in smooth regions and third-order

accuracy near discontinuities [101]. However, it should be noted that the phase-space discretized Boltzmann PDEs discretized with classical Eulerian methods do not seem to present any advantage compared to macroscopic solvers. In fact, given that they rely on a larger number of variables they could be more costly than classical compressible solvers. The added value of this kind of approach might be more pronounced for simulations dealing with larger Knudsen numbers or considering non-equilibrium effects. As such they can be perceived as alternatives to higher-order PDEs such as Grad's moments method.

2.4.2 Lagrangian method with on-lattice propagation

Starting from the phase-space discretized form of the Boltzmann equation (a set of Q PDEs):

$$\partial_t f_\alpha + \mathbf{c}_\alpha \cdot \nabla f_\alpha = \Omega_\alpha, \quad (2.66)$$

the idea of the Lagrangian approach consists of integrating them along their respective characteristic lines, which contrary to Lagrangian solvers for the NS equations (given that fluid particle path-lines are space- and time-dependent), results in an exact solution for the advection term. As such integrating the equations from a time t to $t + \delta_t$ along the stencil directions one obtains:

$$f_\alpha(\mathbf{x} + \mathbf{c}_\alpha \delta_t, t + \delta_t) - f_\alpha(\mathbf{x}, t) = \int_t^{t+\delta_t} \Omega_\alpha(\mathbf{x}(t'), t') dt'. \quad (2.67)$$

Obviously within the context of the Lagrangian approach δ_x/δ_t is tied to the abscissae obtained from the Gauss-Hermite quadrature. In the case of the third-order quadrature:

$$c_{\alpha,i} = \sqrt{\frac{3k_B T_0}{m_0}} = \frac{\delta_x}{\delta_t}. \quad (2.68)$$

Coming back to Eq. 2.67, to get a second-order accurate scheme one can use the trapezoidal rule to evaluate the integral on the RHS:

$$\int_t^{t+\delta_t} \Omega_\alpha(\mathbf{x}(t'), t') dt' = \frac{\delta_t}{2} \Omega_\alpha(\mathbf{x}, t) + \frac{\delta_t}{2} \Omega_\alpha(\mathbf{x} + \mathbf{c}_\alpha \delta_t, t + \delta_t) + \mathcal{O}(\delta_t^3), \quad (2.69)$$

which in turn results in an implicit scheme. To take out the implicitness of the resulting equation, the following change of variables is introduced:

$$\bar{f}_\alpha = f_\alpha - \frac{\delta_t}{2} \Omega_\alpha, \quad (2.70)$$

$$\bar{f}_\alpha^{(eq)} = f_\alpha^{(eq)}, \quad (2.71)$$

$$\Omega_\alpha = \frac{1}{\tau + \delta_t/2} (\bar{f}_\alpha^{(eq)} - \bar{f}_\alpha). \quad (2.72)$$

Using this change of variable and Eqs. 2.67 and 2.69 one gets:

$$\begin{aligned} \bar{f}_\alpha(\mathbf{x} + \mathbf{c}_\alpha \delta_t, t + \delta_t) - \bar{f}_\alpha(\mathbf{x}, t) + \frac{\delta_t}{2} \Omega_\alpha(\mathbf{x} + \mathbf{c}_\alpha \delta_t, t + \delta_t) - \frac{\delta_t}{2} \Omega_\alpha(\mathbf{x}, t) = \\ \frac{\delta_t}{2} \Omega_\alpha(\mathbf{x} + \mathbf{c}_\alpha \delta_t, t + \delta_t) + \frac{\delta_t}{2} \Omega_\alpha(\mathbf{x}, t), \end{aligned} \quad (2.73)$$

which in turn using Eqs. 2.70–2.72 results in :

$$\boxed{\bar{f}_\alpha(\mathbf{x} + \mathbf{c}_\alpha \delta_t, t + \delta_t) - \bar{f}_\alpha(\mathbf{x}, t) = \frac{\delta_t}{\bar{\tau}} \left(\bar{f}_\alpha^{(eq,N)}(\mathbf{x}, t) - \bar{f}_\alpha(\mathbf{x}, t) \right)}, \quad (2.74)$$

where $\bar{\tau}$ is defined as:

$$\boxed{\bar{\tau} = \tau + \delta_t/2}. \quad (2.75)$$

It is also interesting to note that the new distribution functions have the following properties:

$$\sum_\alpha \bar{f}_\alpha = \sum_\alpha f_\alpha - \frac{\delta_t}{2} \sum_\alpha \Omega_\alpha = \rho, \quad (2.76)$$

$$\sum_\alpha \mathbf{c}_\alpha \bar{f}_\alpha = \sum_\alpha \mathbf{c}_\alpha f_\alpha - \frac{\delta_t}{2} \sum_\alpha \mathbf{c}_\alpha \Omega_\alpha = \rho \mathbf{u}, \quad (2.77)$$

and more generally for higher-order moments:

$$\sum_\alpha \mathcal{H}_n(\mathbf{c}_\alpha) \bar{f}_\alpha = \sum_\alpha \mathcal{H}_n(\mathbf{c}_\alpha) f_\alpha - \frac{\delta_t}{2} \sum_\alpha \mathcal{H}_n(\mathbf{c}_\alpha) \Omega_\alpha = \left(1 + \frac{\delta_t}{2\tau} \right) \mathbf{a}_n - \frac{\delta_t}{2\tau} \mathbf{a}_n^{(eq,N)}. \quad (2.78)$$

While to derive the previous scheme, particle streaming was restricted to be on-grid, it is not a necessary condition for working LB scheme. For the so-called semi-Lagrangian methods the restriction of Eq. 2.68 is relaxed, resulting in off-lattice propagation. As such, in this formulation the time-evolution operator of Eq. 2.74 is supplemented with an interpolation step to reconstruct the populations at the discrete grid-points:

$$\bar{f}_\alpha(\mathbf{x}, t + \delta_t) = \sum_{\mathbf{x}_i} A(\mathbf{x}, \mathbf{x}_i) \left[\bar{f}_\alpha(\mathbf{x}_i - \mathbf{c}_\alpha \delta_t, t) + \frac{\delta_t}{\bar{\tau}} \left(\bar{f}_\alpha^{(eq,N)}(\mathbf{x}_i - \mathbf{c}_\alpha \delta_t, t) - \bar{f}_\alpha(\mathbf{x}_i - \mathbf{c}_\alpha \delta_t, t) \right) \right], \quad (2.79)$$

where $A(\mathbf{x}, \mathbf{x}_i)$ are the coefficients involved in the interpolation process and \mathbf{x}_i are the interpolation stencil points. In practice, this approach has two main advantages: (a) it allows one to use quadratures of order four or five (since those result in non-space-filling stencils, they are unusable with the on-lattice solvers), (b) freedom over the choice of the time-step as the streaming does not need to fall on-grid [102, 103]. It also allows for the implementation of conforming meshes in the context of the LBM [104]. A more detailed analysis and discussion of such an approach is left to chapter 7.

The overbars on the re-defined discrete populations and relaxation time will be omitted during the rest of the manuscript for the sake of simplicity. Some of the discrete stencils

resulting from the space-time discretization process are listed in appendix C.

2.5 Enhanced collision operators for the LBM

It has been widely observed that in the limit of vanishing non-dimensional viscosities, the classical SRT collision operator with a second-order polynomial EDF leads to an almost unconditionally unstable scheme. To overcome this issue and facilitate under-resolved simulations with the LBM a number of more advanced models have been developed over the past decades. A number of the most widely used collision operators will be reviewed in this section.

2.5.1 Collision operator in momentum space

All modified BGK collision models in this category rely on the following main paradigm: Application of the equilibration operator in alternative spaces [105] as a way to de-alias the physical and ghost modes. It is interesting to note that such modal decompositions were also used in Shakhov's collision operator to allow for a variable Prandtl number. These alternative spaces are usually moments of the distribution function, chosen and tailored to suit specific properties. The following section will review some of the most well known collision models of this category.

2.5.1.1 Raw moments-based decomposition

The first category, developed and published in the early 2000s' is the so-called Multiple Relaxation Time (MRT) collision model [105, 55, 106, 107]. The idea behind this approach is to apply the collision step in momentum space, contrary to the classical SRT formulation where collision is carried out directly in phase-space. This allows for independent control over the relaxation rates of linearly independent moments, opening the door for a more flexible equilibration path [107, 106]. The added degrees of freedom can be useful both physically and numerically [108]. In this approach, the BGK collision operator is written as:

$$\Omega_{\alpha}^{(MRT)} = \mathbf{M}^{-1} \mathbf{S} \mathbf{M} (f_{\alpha}^{(eq)} - f_{\alpha}), \quad (2.80)$$

where \mathbf{M} is the transformation matrix such that:

$$\Pi_{\alpha} = \sum_{\beta} M_{\alpha,\beta} f_{\beta}, \quad (2.81)$$

where Π_{α} are the moments chosen for the application of the collision operation. For the remainder of this work, raw moments of the distribution function will be designated as $\Pi_{x^i y^j z^k}$, with:

$$\Pi_{x^i y^j z^k} = \sum_{\alpha} c_{\alpha,x}^i c_{\alpha,y}^j c_{\alpha,z}^k f_{\alpha}. \quad (2.82)$$

As seen in Eq. 2.80, using the transformation matrix \mathbf{M} the discrete populations are taken to momentum space. Then the relaxation matrix \mathbf{S} is applied and relaxed moments are converted back to discrete populations through \mathbf{M}^{-1} . For a typical DdQq stencil, q linearly independent moments are needed to span the phase-space. For example, given the properties of the Hermite polynomials, the first q linearly independent Hermite coefficients are an obvious choice. For the D2Q9 stencil, the following moments –Hermite coefficients– can be used:

$$\mathbf{\Pi} = \left\{ \Pi_0, \underbrace{\Pi_x, \Pi_y}_{a_1}, \underbrace{\Pi_{xy}, \Pi_{x^2} - c_s^2, \Pi_{y^2} - c_s^2}_{a_2}, \underbrace{\Pi_{x^2y} - c_s^2 \Pi_y, \Pi_{xy^2} - c_s^2 \Pi_x}_{a_3}, \underbrace{\Pi_{x^2y^2} - c_s^2 (\Pi_{x^2} + \Pi_{y^2}) + c_s^4}_{a_4} \right\}. \quad (2.83)$$

For this specific example, the corresponding equilibrium moments, assuming terms up to order two have been kept in the Hermite expansion, are:

$$\mathbf{\Pi}^{(eq)} = \{\rho, \rho u_x, \rho u_y, \rho u_x u_y, \rho u_x^2, \rho u_y^2, 0, 0, 0\}. \quad (2.84)$$

It is interesting to note that keeping Hermite polynomials up to order four, the discrete equilibrium moments match those of the continuous EDF. Another parameter appearing in Eq. 2.80 is the relaxation coefficients matrix, \mathbf{S} , mostly defined as a diagonal matrix with components $1/\tau_\alpha$ controlling the relaxation rate of their corresponding raw moment. Of the available nine relaxation coefficients in the D2Q9 stencil, three are tied to fluid viscosity (one to shear and two to bulk viscosities) as the corresponding moments appear in the viscous stress tensor and three are conserved moments; The rest can be tuned, for stability [55], optimal dispersion [109], fixing the boundary position for the half-way bounce-back boundary condition [30] etc.

As noted in [110, 111], using the full set of moments leads to a number of free parameters (the ghost moments relaxation coefficients), for which no formal physical closures exist. As previously mentioned, apart from the entropic argument, only *a posteriori* closures based on numerical arguments can be devised for these free parameters. Another way around this issue is to adopt targeted (on specific moments of the distribution function) minimalist MRT formulations. The TRT (Two Relaxation Time) collision operator developed and proposed by I. Ginzburg is an example of these minimalist models [112, 113, 51]. In this collision model the distribution function is decomposed into symmetrical, f_α^+ , and non-symmetrical parts, f_α^- , defined as [51]:

$$f_\alpha^+ = \frac{f_\alpha + f_{\bar{\alpha}}}{2}, \quad (2.85a)$$

$$f_\alpha^- = \frac{f_\alpha - f_{\bar{\alpha}}}{2}, \quad (2.85b)$$

resulting in two relaxation coefficients, τ^+ and τ^- , with the first one tied to the fluid viscosity. The BGK collision operator is then expressed as [113]:

$$\Omega_\alpha^{(TRT)} = \frac{1}{\tau^+} (f_\alpha^{(eq)+} - f_\alpha^+) + \frac{1}{\tau^-} (f_\alpha^{(eq)-} - f_\alpha^-). \quad (2.86)$$

As demonstrated in [114], judicious choices of the free parameter (the so-called “magic values”) can lead to, among other effects, the wall being placed exactly half-way when used with the half-way bounce-back boundary condition. Defining :

$$\Lambda = \left(\frac{\delta_t}{\tau^+} - \frac{1}{2} \right) \left(\frac{\delta_t}{\tau^-} - \frac{1}{2} \right), \quad (2.87)$$

it can be shown that setting $\Lambda = 3/16$ places the wall half-way [115], while $\Lambda = 1/6$ and $\Lambda = 1/12$ cancel out, respectively, the third- and fourth-order spatial error terms [116, 117] and $\Lambda = 1/4$ results in optimal stability [118].

Another example of a minimalist MRT scheme, studied later on in details, is that of the LKS [52, 119]. This collision model is a TRT scheme in the space of Hermite moments, where second-order moments are relaxed using the fluid viscosity while higher-order moments (three and four) are relaxed using a free parameter [54]. For the LKS the collision operator is written as [53, 52]:

$$\Omega_\alpha^{(\text{LKS})} = -\frac{1}{\lambda} (f_\alpha - f_\alpha^{(eq, \text{LKS})}). \quad (2.88)$$

The second relaxation coefficient λ is related to the SRT relaxation coefficient as [119]:

$$\lambda - A = \tau, \quad (2.89)$$

where A is a constant fixed by the choice of the free parameter. The EDF is then defined as [54]:

$$f_\alpha^{(eq, \text{LKS})} = f_\alpha^{(eq)} - \frac{A}{\tau} \frac{w_\alpha}{2} \mathbf{a}_2^{(neq)} : \mathcal{H}_{2, \alpha}. \quad (2.90)$$

The original regularized lattice Boltzmann method (RLBM) is an LKS solver where the free relaxation coefficient is set to 1 [54]. This collision operator has been applied to a variety of configurations ranging from multi-phase [120] to non-Newtonian flows [121] and advection-diffusion equations with variable diffusion coefficients [122, 123].

2.5.1.2 Central moments-based decomposition

In the Central Moments Multiple Relaxation Time (from here on referred to as CM-MRT) model, while the paradigm is quite similar to the MRT, a different set of moments are used: the central moments, designated by $\tilde{\Pi}_{x^i y^j z^k}$ and defined as [124, 125]:

$$\tilde{\Pi}_{x^i y^j z^k} = \sum_\alpha (c_{\alpha, x} - u_x)^i (c_{\alpha, y} - u_y)^j (c_{\alpha, z} - u_z)^k f_\alpha. \quad (2.91)$$

Taking again the example of the D2Q9 stencil with the Hermite coefficients as the projection space and a fourth-order expansion of the EDF results in the following central equilibrium moments [126]:

$$\tilde{\Pi}^{(eq)} = \{\rho, 0, 0, 0, 0, 0, 0, 0, 0\}. \quad (2.92)$$

Lower-order EDFs will result in a different set of equilibria with higher-order moments different from their continuous counter-parts [127]. As for the MRT, the collision operator is expressed as:

$$\Omega_\alpha = \mathbf{M}^{-1} \mathbf{N}^{-1} \mathbf{S} \mathbf{N} \mathbf{M} (f_\alpha^{(eq)} - f_\alpha) \quad (2.93)$$

where the additional matrix appearing in the equation, \mathbf{N} , converts raw moments to central moments:

$$\tilde{\mathbf{\Pi}} = \mathbf{N} \mathbf{\Pi}. \quad (2.94)$$

The different components of this matrix can be obtained using the binomial theorem. To illustrate the derivation of these matrices, a limited number of them are explicitly given in appendix D.

2.5.2 Pre-collision population reconstruction via regularization

Roughly speaking, the rationale behind regularized collision operators is to filter out higher-order components of the distribution functions (in the sense of the Chapman-Enskog expansion). It can be shown that first-order terms appear at the NS level, while higher-order terms intervene at the Burnett, super Burnett etc. scales (not of interest in the context of the LBM). In the context of the regularized collision approach the non-equilibrium part of the distribution function is reconstructed using only first-order contributions, $f_\alpha^{(neq)} \approx f_\alpha^{(1)}$. The discrete time-evolution equation can be re-expressed as [57, 128]:

$$f_\alpha(\mathbf{x} + \mathbf{c}_\alpha \delta_t, t + \delta_t) = f_\alpha^{(eq)}(\mathbf{x}, t) + \left(1 - \frac{\delta_t}{\tau}\right) f_\alpha^{(neq)}(\mathbf{x}, t). \quad (2.95)$$

Following the Hermite expansion used for the EDF, we can express the first-order component of the distribution function as:

$$f_\alpha^{(1)} = w_\alpha \sum_{n=2} \frac{1}{n!} \mathbf{a}_n^{(1)} : \mathcal{H}_n. \quad (2.96)$$

In the original regularized model [57] only the second-order Hermite polynomial was considered for the reconstruction process:

$$f_\alpha^{(1)} = w_\alpha \frac{\mathbf{a}_2^{(1)} : \mathcal{H}_2}{2}. \quad (2.97)$$

The only unknown in this equation is $\mathbf{a}_2^{(1)}$. In [57], this coefficient is computed as:

$$\mathbf{a}_2^{(1,PR)} \approx \mathbf{a}_2^{(neq)} = \sum_\alpha \mathcal{H}_2 : (f_\alpha - f_\alpha^{(eq)}). \quad (2.98)$$

In the context of the classical LB formulation with a second-order polynomial EDF, and given the orthogonality of the independent moments, this collision operator aimed at eliminating non-equilibrium effects of higher-order (kinetic) moments. It is interesting to note that this

formulation has a number of shortcomings: (a) Errors in all components of the third-order moments tensor of the EDF (given the absence of higher-order terms in the EDF), and (b) presence of higher-order effects (tied to $f_\alpha^{(i)}$ with $i \geq 2$) coming from the approximation used for $\mathbf{a}_2^{(1)}$. The latter can be, to some extent, cured using a CE-based closure for $\mathbf{a}_2^{(1)}$. Using this approach it can be shown that [58]:

$$\mathbf{a}_2^{(1,CE)} = -\rho c_s^2 \frac{\tau}{\delta t} (\nabla \mathbf{u} + \nabla \mathbf{u}^T). \quad (2.99)$$

This expression can be computed using classical FD approximations [129]. Additionally, recently published results seem to show that a weighted combination of both these closures can be effective in extending the stability domain of the scheme [129, 130]:

$$\mathbf{a}_2^{(1)} = \sigma \mathbf{a}_2^{(1,PR)} + (1 - \sigma) \mathbf{a}_2^{(1,CE)}, \quad (2.100)$$

where σ is the weight.

The first problem with the RLBM of [57], namely errors in the off-diagonal components of the third-order moments tensor can be accounted for by using third- (or fourth-) order terms in the EDF and using the recursive properties of the off-equilibrium Hermite coefficients [58], i.e.:

$$a_{n,ij\dots klm}^{(1)} = a_{n-1,ij\dots kl}^{(1)} u_m + \left[a_{lm}^{(1)} u_i u_j \dots u_k \right]_{\text{cyc}}. \quad (2.101)$$

For the D2Q9 stencil, assuming a fourth-order isothermal polynomial EDF the different non-equilibrium Hermite coefficients are computed as:

$$a_{xy^2}^{(1)} = u_x a_{y^2}^{(1)} + 2u_y a_{xy}^{(1)}, \quad (2.102a)$$

$$a_{x^2y}^{(1)} = u_y a_{2,x^2}^{(1)} + 2u_x a_{xy}^{(1)}, \quad (2.102b)$$

$$a_{x^2y^2}^{(1)} = u_y a_{x^2y}^{(1)} + u_x^2 a_{y^2}^{(1)} + u_x u_y a_{xy}^{(1)}. \quad (2.102c)$$

These coefficients are explicitly given here, as this model is considered in the extensive linear stability analysis of the next chapter.

2.5.3 Entropic lattice Boltzmann method

The original entropic LBM ensures stability of the solver by imposing a monotonous decrease of a discrete entropy function. While a number of different discrete entropy functionals have been proposed in the context of the ELBM [131, 132], the following form has gained the most attention [133, 134, 46, 135, 136]:

$$H = \sum_{\alpha} f_{\alpha} \ln \left(\frac{f_{\alpha}}{w_{\alpha}} \right). \quad (2.103)$$

2.5. Enhanced collision operators for the LBM

In practice, the monotonicity of the discrete entropy is enforced using a two-step linear reconstruction achieved through the following modified time-evolution equation [133, 134]:

$$f_\alpha(\mathbf{x} + \mathbf{c}_\alpha \delta_t, t + \delta_t) - f_\alpha(\mathbf{x}, t) = \beta \gamma (f_\alpha^{(eq, ELBM)}(\mathbf{x}, t) - f_\alpha(\mathbf{x}, t)), \quad (2.104)$$

where β is tied to the fluid viscosity as:

$$\beta = \frac{\delta_t}{2\tau + \delta_t}, \quad (2.105)$$

with $\tau = \nu/c_s^2$, while γ is obtained by solving the following system [137]:

$$H(f^*) = H(f), \quad (2.106)$$

with:

$$f_\alpha^* = f_\alpha + \gamma (f_\alpha^{(eq, ELBM)} - f_\alpha). \quad (2.107)$$

This two-step reconstruction procedure is illustrated in Fig. 2.1. In the first step, the equal entropy mirror state (relative to the equilibrium), f^* , is found by solving the non-linear equation shown in Eq. 2.106. As observed there γ is the maximum path length not resulting in an increase in entropy [138]. It is interesting to note that at thermodynamic equilibrium Eq. 2.106 has the non-trivial root $\gamma = 2$ which corresponds to the SRT collision operator [138]. In the second step, dissipation is introduced via the parameter β . The solution to

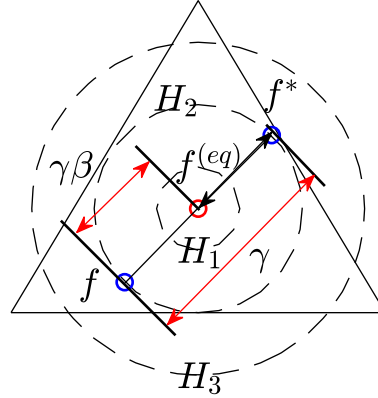


Figure 2.1: Schematic representation of the relaxation process in the ELBM. Dashed lines represent entropy levels while the triangle illustrates the positivity polytope.

Eq. 2.106 can be obtained using a Newton-Raphson iterative solver as:

$$\gamma^{n+1} = \gamma^n - \frac{G^n}{\partial_\gamma G^n}, \quad (2.108)$$

with:

$$G^n = H(f^{*n}) - H(f), \quad (2.109)$$

and:

$$\frac{\partial G^n}{\partial \gamma} = \sum_{\alpha} \left[1 + \ln \left(\frac{f^{*n}}{w_{\alpha}} \right) \right] (f_{\alpha}^{(eq,ELBM)} - f_{\alpha}), \quad (2.110)$$

where γ^n and γ^{n+1} are solutions obtained in the previous and current iterations. The iterative root-finding algorithm being rather expensive (especially when the populations get away from equilibrium) alternative approaches have been developed in recent years [133, 138]. These approximate solutions are also useful in the vicinity of equilibrium as the Newton-Raphson solver might diverge there.

The ELBM as described here relying on changing the effective viscosity to stabilize the simulation, and coming with non-negligible computational overhead, a modified version of it has been proposed relying on moments decomposition [111]. This approach is commonly referred to as the KBC model (short for Karlin-Bösch-Chikatamarla). This approach differs from the ELBM in the way the mirror state is constructed:

$$f_{\alpha}^* = 2f_{\alpha}^{(eq)} - f_{\alpha} + (\gamma - 2) (h_{\alpha}^{(eq)} - h_{\alpha}), \quad (2.111)$$

where h_{α} is the part of the distribution function containing ghost moments. As observed here the entropy-enforcing parameter γ now only affects ghost moments, theoretically allowing for the correct fluid viscosity to be enforced. This approach has been observed to be very effective in allowing for under-resolved simulations [139, 140, 141].

2.6 Summary

The aim of the present chapter was to introduce the theoretical background of the LBM. It is worth noting that all of the collision models presented in this chapter have been implemented in ALBORZ and will be used later in different sections of the present manuscript. The information to retain from this chapter is the discrete time-evolution equation for the LBM given in Eqs. 2.74 and 2.75. Furthermore, the discrete isothermal equilibrium attractors obtained through projection onto Hermite polynomial space and entropy extremization are given in Eqs. 2.54 and 2.65.

Apart from the discrete equilibrium state, it was shown that in order to achieve better numerical properties the equilibration path controlled by the collision operator can also be improved. Enhanced versions of the SRT collision operator derived in the LBM community intend to control higher-order ghost moments effect and prevent modal interaction by removing aliasing effects introduced by the collision operator. This argument prompted the development of models relying on relaxation in alternate spaces (e.g. raw moments, central moments, cumulants [142, 143] etc) instead of phase-space. While focusing on de-aliasing via modal decomposition, these models come with a large number of free parameters that can only be parametrized with *a posteriori* arguments such as linear stability analyses (as shown in the next chapter). Other classes of collision models such as the Regularized class aim at filtering out higher-order contribution by reconstructing the non-equilibrium part of the distribution function using CE analysis. The entropic model does not filter out higher-order contributions; It aims at keeping the scheme (and therefore higher-order contributions) dis-

sipative and hence guarantee non-linear stability by enforcing the H-theorem at the discrete level.

The next chapter will provide a more in-depth analysis of the physical and numerical properties of the isothermal LBM, along with the different enhanced collision models and their effects on the stability of the scheme.

Chapter 3

The isothermal lattice Boltzmann method: detailed study of properties

Contents

3.1	Bulk flow solver analysis : Asymptotic behavior	35
3.1.1	Asymptotic analysis : the Chapman–Enskog development	35
3.1.2	Asymptotic error analysis	37
3.2	Bulk flow solver analysis: non-vanishing wave-numbers	42
3.2.1	Methodology : The von Neumann formalism	43
3.2.2	Stability domain: Effect of equilibrium state	44
3.2.3	Equilibration strategy I: Filtering out higher-order contributions with regularization	47
3.2.4	Equilibration strategy II: Independent relaxation of ghost moments, the minimalist example of the LKS	49
3.2.5	Equilibration strategy III: Choice of basis moments, LKS vs TRT .	51
3.2.6	Equilibration strategy IV: central moments	52
3.3	Numerical applications	53
3.3.1	2-D periodic shear layer: Stability for under-resolved simulations .	54
3.3.2	3-D Taylor-Green vortex: Effect of ghost modes relaxation on under and moderately resolved features	56
3.4	Summary and closing remarks	59

Disclaimer

Part of this chapter has been published in:

- [1] S.A. Hosseini, N. Darabiha, and D. Thévenin. Theoretical and numerical analysis of the lattice kinetic scheme for complex flow simulations. *Physical Review E*, 99(2), p.023305, 2019.
- [2] S.A. Hosseini, C. Coreixas, N. Darabiha, and D. Thévenin. Stability of the lattice kinetic scheme and choice of the free relaxation parameter. *Physical Review E*, 99(6), p.063305, 2019.

3.1 Bulk flow solver analysis : Asymptotic behavior

In this first section, we are only interested in a continuum-level analysis of the classical isothermal LBM. The behavior and characteristics of different EDFs at this level are studied using first the Chapman-Enskog expansion and then by looking at the error in higher-order moments, especially those appearing at the NS level, in order to establish usability domains in terms of the Mach number.

3.1.1 Asymptotic analysis : the Chapman-Enskog development

The Chapman-Enskog analysis within the context of the LBM relies on concepts from perturbation analysis and the Taylor-McLaurin expansion to recover the macroscopic equations solved by the LBM at different time-scales. The first step is the introduction of a Taylor-McLaurin expansion to get space and time-continuous approximations to the discrete equation:

$$f_\alpha(\mathbf{x} + \mathbf{c}_\alpha \delta_t, t + \delta_t) = \sum_{n=0}^N \frac{\delta_t^n}{n!} (\partial_t + \mathbf{c}_\alpha \cdot \nabla)^n f_\alpha(\mathbf{x}, t), \quad (3.1)$$

which results in the following system of PDEs:

$$\sum_{n=1}^N \frac{\delta_t^n}{n!} (\partial_t + \mathbf{c}_\alpha \cdot \nabla)^n f_\alpha(\mathbf{x}, t) = \delta_t \Omega_\alpha(\mathbf{x}, t). \quad (3.2)$$

The next step is what one might perceive as a modal decomposition, by introducing different time-scales and expanding different parameters as power series of these scales:

$$\frac{\delta_t}{T} \partial_t = \sum_{i=1}^{\infty} \varepsilon^i \partial_t^{(i)}, \quad (3.3a)$$

$$f_\alpha = \sum_{i=0}^{\infty} \varepsilon^i f_\alpha^{(i)}, \quad (3.3b)$$

$$\frac{\delta_t}{T} \nabla = \varepsilon \nabla^{(1)}. \quad (3.3c)$$

This is achieved by non-dimensionalizing the equations using a characteristic time T , scale L and velocity $C = L/T$. This expansion results in a series of PDEs at these different time-scales (tracked through the parameter ε):

$$\varepsilon^0 : 0 = \frac{1}{\tau} (f_\alpha^{(eq)} - f_\alpha^{(0)}), \quad (3.4a)$$

$$\varepsilon^1 : \left(\partial_t^{(1)} + \mathbf{c}_\alpha \cdot \nabla^{(1)} \right) f_\alpha^{(0)} = -\frac{1}{\tau} f_\alpha^{(1)}, \quad (3.4b)$$

$$\varepsilon^2 : \partial_t^{(2)} f_\alpha^{(0)} + \left(\partial_t^{(1)} + \mathbf{c}_\alpha \cdot \nabla^{(1)} \right) f_\alpha^{(1)} + \frac{1}{2} \left(\partial_t^{(1)} + \mathbf{c}_\alpha \cdot \nabla^{(1)} \right)^2 f_\alpha^{(0)} = -\frac{1}{\tau} f_\alpha^{(2)}. \quad (3.4c)$$

3.1. Bulk flow solver analysis : Asymptotic behavior

Using these PDEs and solvability conditions (based on conservation properties of the collision operator):

$$\forall i > 0 : \sum_{\alpha} f_{\alpha}^{(i)} = 0, \quad (3.5a)$$

$$\forall i > 0 : \sum_{\alpha} \mathbf{c}_{\alpha} f_{\alpha}^{(i)} = 0, \quad (3.5b)$$

one can readily recover the corresponding macroscopic balance equations. For example at the Euler level (order ε^1) one gets the following mass and momentum balance equations:

$$\Pi_0, \varepsilon^1 : \partial_t^{(1)} \rho + \nabla^{(1)} \cdot \rho \mathbf{u} = 0, \quad (3.6a)$$

$$\Pi_1, \varepsilon^1 : \partial_t^{(1)} \rho \mathbf{u} + \nabla^{(1)} \cdot \rho \mathbf{u} \otimes \mathbf{u} + \nabla^{(1)} \cdot \mathbf{p} = 0, \quad (3.6b)$$

with $\mathbf{p} = p\mathbf{I} = \rho r_0 T_0 \mathbf{I}$, which correspond to a compressible isothermal flow.

At the NS level (order ε^2) while the mass balance is straightforward, getting the momentum conservation equations is a bit more tedious. After some algebra one gets the following PDE at this scale:

$$\varepsilon^2 : \partial_t^{(2)} f_{\alpha}^{(0)} + \left(\partial_t^{(1)} + \mathbf{c}_{\alpha} \cdot \nabla^{(1)} \right) \left(1 - \frac{\tau}{2} \right) f_{\alpha}^{(1)} = -\frac{1}{\tau} f_{\alpha}^{(2)}, \quad (3.7)$$

which in turn, taking the first-order moments results in:

$$\Pi_1, \varepsilon^2 : \partial_t^{(2)} \rho \mathbf{u} + \nabla^{(1)} \cdot \left(\frac{1}{2} - \tau \right) \left(\partial_t^{(1)} \Pi_2^{(eq)} + \nabla^{(1)} \cdot \Pi_3^{(eq)} \right) = 0. \quad (3.8)$$

One interesting issue to note is that, due to the limitations brought about by the quadrature, using a third-order stencil (first neighbor) introduces an aliasing between moments of order one and three:

$$\sum_{\alpha} c_{\alpha,i}^3 f_{\alpha}^{(eq)} = \sum_{\alpha} c_{\alpha,i} f_{\alpha}^{(eq)}. \quad (3.9)$$

This symmetry defect is the main reason behind Galilean invariance issues encountered at the NS level for moderate and large Mach number flows. While for the continuous Boltzmann equation one would get the following third-order moments tensor:

$$\Pi_{i_1 i_2 i_3}^{(eq)} = \rho u_{i_1} u_{i_2} u_{i_3} + \rho [u_{i_1} \delta_{i_2, i_3}]_{\text{cyc}}, \quad (3.10)$$

first-neighbor stencils in combination with a third-order Hermite expansion for the EDF result in the following:

$$\Pi_{i_1 i_2 i_3}^{(eq, N=3)} = \rho \delta_{i_1 i_2 i_3} [u_{i_1} \delta_{i_2, i_3}]_{\text{cyc}} + \rho (1 - \delta_{i_1 i_2 i_3}) \{ u_{i_1} u_{i_2} u_{i_3} + [u_{i_1} \delta_{i_2, i_3}]_{\text{cyc}} \}. \quad (3.11)$$

The next subsection will focus on the effect of local velocity (or Mach number) on such errors for different EDFs.

Using the CE formalism it can be shown that the addition of a correction term for the

third-order moments tensor can resolve this issue [9, 144, 145, 146]:

$$\Psi_\alpha = \left(1 - \frac{\delta_t}{2\tau}\right) \frac{w_\alpha}{2} (\nabla \otimes \mathcal{H}_{\alpha,2}) : \delta \mathbf{\Pi}_3^{(eq)}. \quad (3.12)$$

where $\delta \mathbf{\Pi}_3^{(eq)} = \mathbf{\Pi}_3^{(eq)} - \mathbf{\Pi}_3^{(eq,N)}$ reduces to its diagonal components for $N > 2$. A more thorough derivation and analysis of the correction for the third-order moments tensor will be provided in chapter 5.

3.1.2 Asymptotic error analysis

The previous CE analysis shows that LB formulations based on standard first-neighbor stencils do not exactly recover the NS level dynamics, i.e. the stress tensor. This comes from the fact that, due to lack of symmetry (tied to the order of the Gauss-Hermite quadrature), the third-order moments tensor does not correspond to its phase-space continuous counterpart. While including higher-order (third-order) components of the Hermite expansion in the EDF can help correct the deviatoric components, consistency of the diagonal components can only be re-established through additional correction terms. As such, to have a better measure of the applicability domain of the LB scheme, we will look at the deviations of these moments (for the isothermal case) from their continuous counterparts for varying Mach numbers. Although readily extendable to other stencils, the D2Q9 stencil will be considered here. Moments such as Π_{x^2} , Π_{y^2} , Π_{x^2y} , Π_{xy^2} , Π_{x^3} and Π_{y^3} , among others, will be studied through the normalized deviation defined as:

$$\delta = \left| 1 - \frac{\sum_\alpha c_{\alpha,x}^i c_{\alpha,y}^j f_\alpha^{(eq,N)}}{\Pi_{x^i y^j}^{(eq)}} \right|, \quad (3.13)$$

where $\Pi_{x^i y^j}^{(eq)}$ is the continuous moment and $\sum_\alpha c_{\alpha,x}^i c_{\alpha,y}^j f_\alpha^{(eq,N)}$ is the moment of the discrete EDF. The diagonal component of the second-order moment tensor for discrete and continuous EDFs are shown in Fig. 3.1. It is observed that including the second-order terms in the Hermite expansion leads to the correct second-order moments (diagonal components) regardless of the Mach number. While the continuous EDF recovers the following moment:

$$\Pi_{x^2} = \rho (u_x^2 + c_s^2), \quad (3.14)$$

for the first-order Hermite expansion and entropic EDF we respectively get:

$$\Pi_{x^2} = \rho c_s^2, \quad (3.15)$$

$$\Pi_{x^2} = \frac{\rho (12u_x^3 - 16u_x^2 + 8u_x - 4) + \rho (5u_x^2 - 10u_x + 1) \sqrt{u_x^2/c_s^2 + 1} + (u_x^2/c_s^2 + 1)^{3/2}}{6(u_x - 1)(2u_x + \sqrt{u_x^2/c_s^2 + 1})}. \quad (3.16)$$

It is also interesting to note that, while the entropic EDF does not exactly recover the correct diagonal components of the second-order moments tensor, the deviations from the

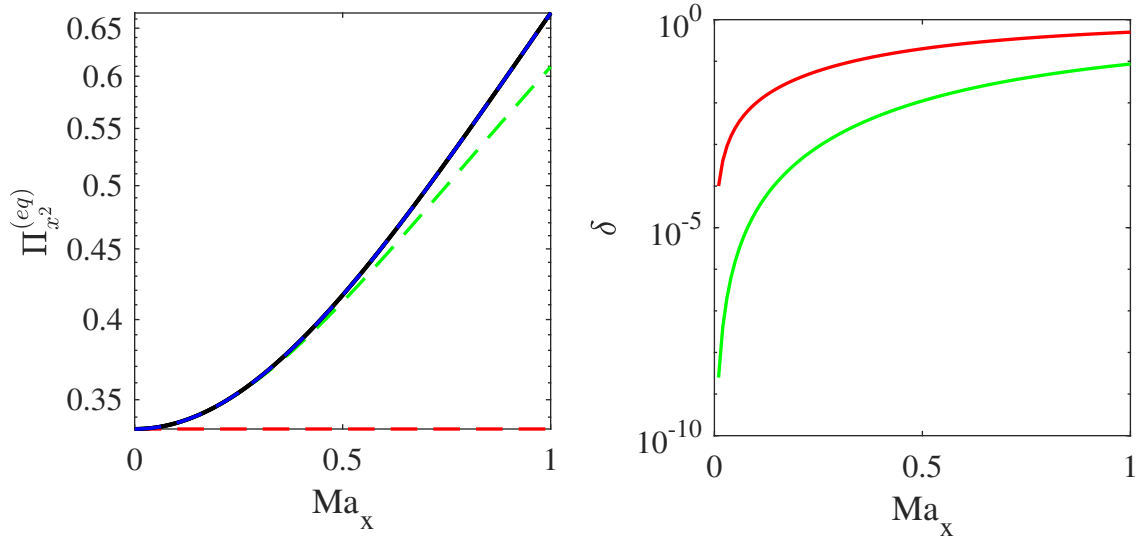


Figure 3.1: (left) $\Pi_{x^2}^{(eq)}$ moment and (right) relative deviations δ for (in red) first- and (in blue) second-order Hermite polynomial expansion and (in green) entropic EDF. The continuous moment is shown with black plain line. The third-order error line in the left plot is not visible as it is equal to zero.

continuous moment are much less pronounced than the first-order Hermite expansion, and even negligible for Mach numbers up to 0.4. As such the non-conservation of isothermal energy in the entropic EDF is not a restriction on the validity domain *per se*. Furthermore, all EDFs (even the first-order Hermite expansion) correctly recover the off-diagonal components of the second-order moments tensor.

As shown in the CE analysis, for the NS level dynamics to be correctly recovered, the components of the third-order moments tensor must also match those of the continuous EDF. However, as observed in Fig. 3.2, none of the EDFs are able to recover the correct diagonal components for this tensor. This shortcoming is not related to the equilibrium state but, as shown in the Hermite expansion section, to the limited order of the Gauss-Hermite quadrature used for first-neighbor stencils. In Fig. 3.2, it is observed that all three EDFs considered there (second- and third-order Hermite expansion and entropic) have the same moments. For the off-diagonal components of the third-order moments tensor however, as shown in Fig. 3.3, different EDFs result in different behaviors. While Hermite expansions of order higher than three exactly recover the correct moments, the second-order Hermite expansion and entropic EDFs show some deviations. Although not exactly recovering the correct moment the entropic EDF still closely follows its continuous counterpart even for large Mach numbers. This could, in part, explain why the entropic model exhibits less pronounced Galilean invariance problems as compared to the classical LBM with second-order EDF at moderate Mach numbers. As such, in agreement with the CE development, it is observed that in order to correctly recover the off-diagonal components of the third-order moments tensor in 2-D, the third-order terms of the Hermite expansion must be included. For the Fourier equation on the other hand, the components of the fourth-order moments

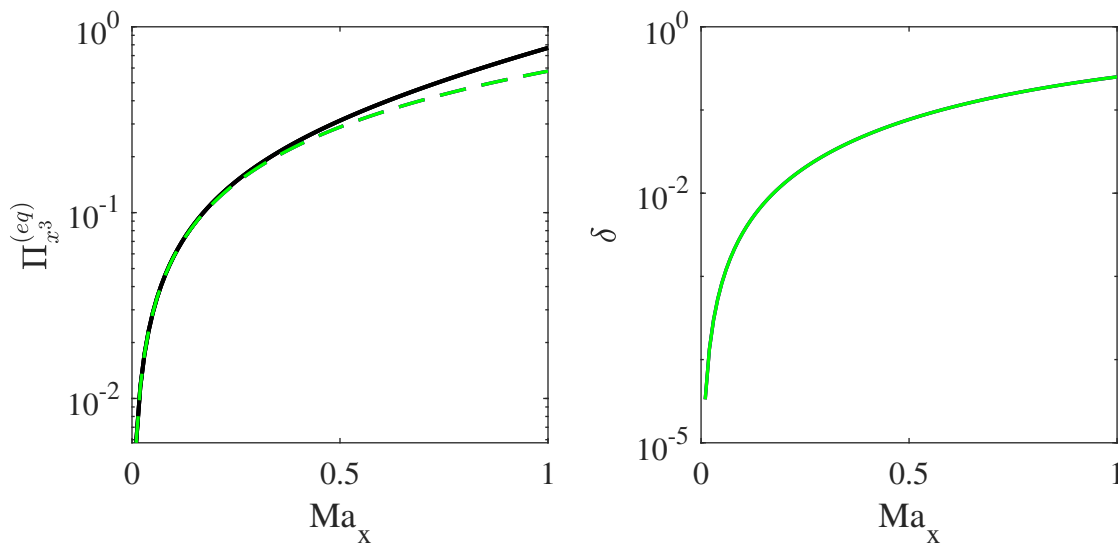


Figure 3.2: (left) $\Pi_{x^3}^{(eq)}$ moment and (right) relative deviations δ for (in red) second- and (in blue) third-order Hermite polynomial expansion and (in green) entropic EDF. The continuous moment is shown with black plain line. The red and blue lines are not visible as the green lines fall exactly on top of them.

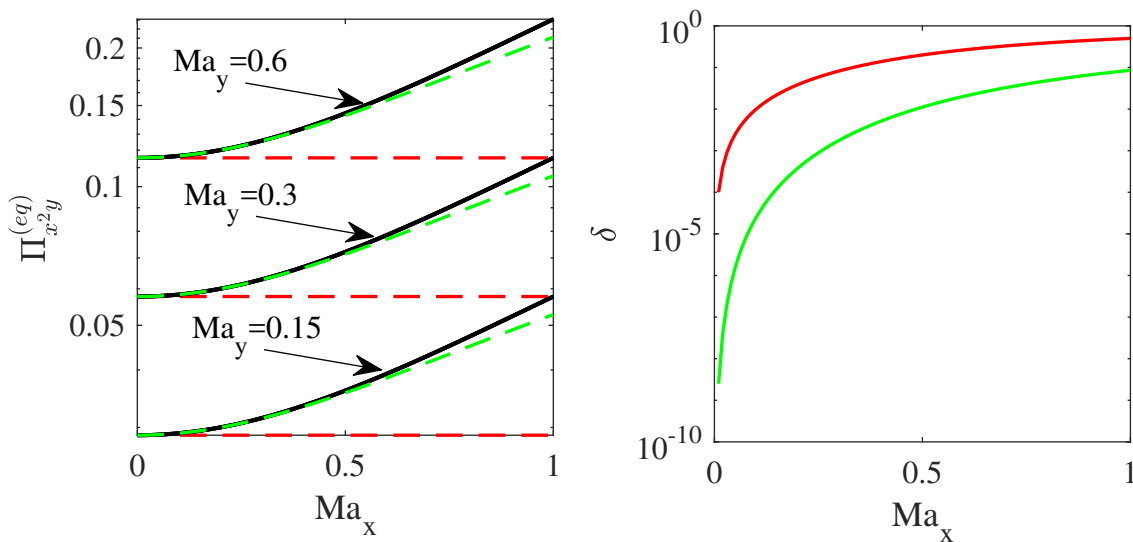


Figure 3.3: (left) $\Pi_{x^2y}^{(eq)}$ moment and (right) relative deviations δ for (in red) second- and (in blue) third-order Hermite polynomial expansion and (in green) entropic EDF. The continuous moment is shown with black plain line. The blue lines in the left plot fall exactly on the black plain lines. They are also not visible in the right plot as they are equal to zero.

tensor must also be correctly recovered. The diagonal components, i.e. $\Pi_{x^4}^{(eq)}$ are shown in Fig. 3.4. None of the EDFs considered here are able to follow the continuous curve for all Mach numbers. As for the diagonal components of the third-order moments tensor this is related to the limited degrees of freedom in the stencil. For the off-diagonal components of

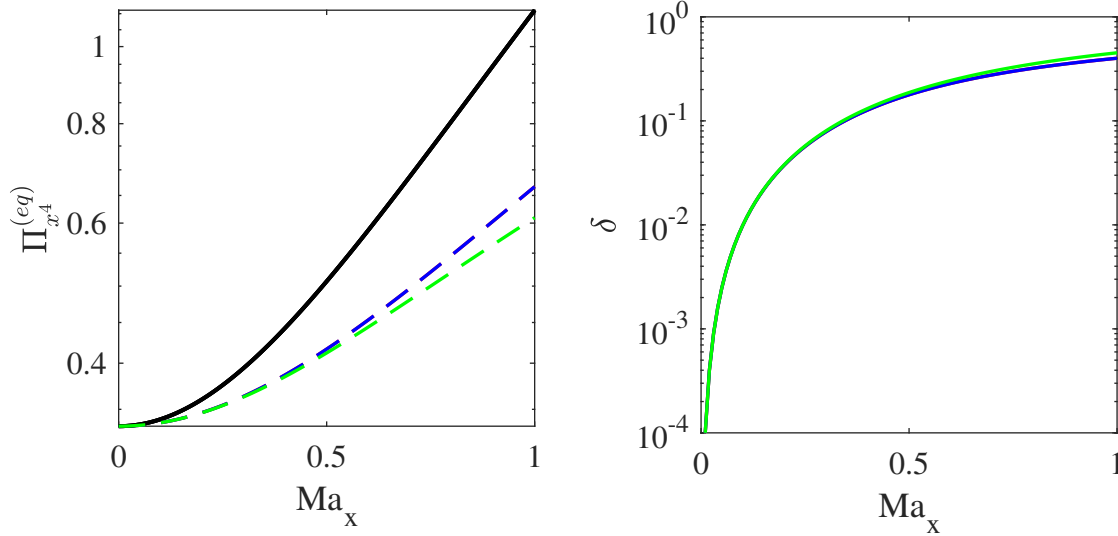


Figure 3.4: (left) $\Pi_{x^4}^{(eq)}$ moment and (right) relative deviations δ for (in red) second- and (in blue) third-order Hermite polynomial expansion and (in green) entropic EDF. The continuous moment is shown with black plain line. The red lines are not visible as they coincide with the blue ones.

the form $\Pi_{x^i y^j}^{(eq)}$ with both $i < 3$ and $j < 3$, only the fourth-order Hermite expansion is able to correctly recover the continuous moments. For the other components, the limited symmetry of the stencil results in discrepancies at moderate and high Mach numbers. Results are displayed in Figs. 3.5 and 3.6.

The simple study of the behavior of different higher-order moments of the EDFs appearing at different orders of the CE expansion clearly establishes the validity domain of the LB scheme based on standard first-neighbor stencils. This validity domain and aliasing effects between different moments caused by the quadrature are illustrated in Fig. 3.7. As shown there, for a solver intended for Euler-level dynamics (without conservation of energy) the second-order Hermite expansion is sufficient, while the entropic EDF needs corrections for the diagonal components of the second-order moments tensor. To correctly recover NS level dynamics (or Euler level with energy conservation) none of the considered EDFs can exactly match the stress tensor. The third-order Hermite expansion (the EDF that matches the larger number of components) still needs corrections for the diagonal components of the third-order moments tensor. Finally, for Burnett level dynamics (or NS level with energy conservation), as mentioned previously, even using the fourth-order Hermite expansion one would need to include corrections for all components involving directional moments of order higher than two.

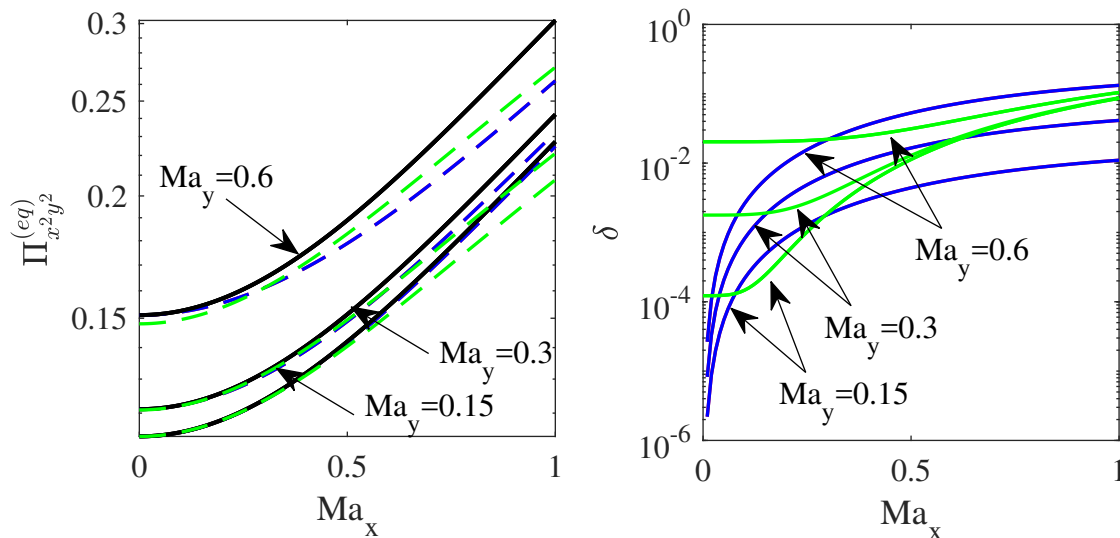


Figure 3.5: (left) $\Pi_{x^2y^2}^{(eq)}$ moment and (right) relative deviations δ for (in red) second- and (in blue) third-order Hermite polynomial expansion and (in green) entropic EDF. The continuous moment is shown with black plain line.

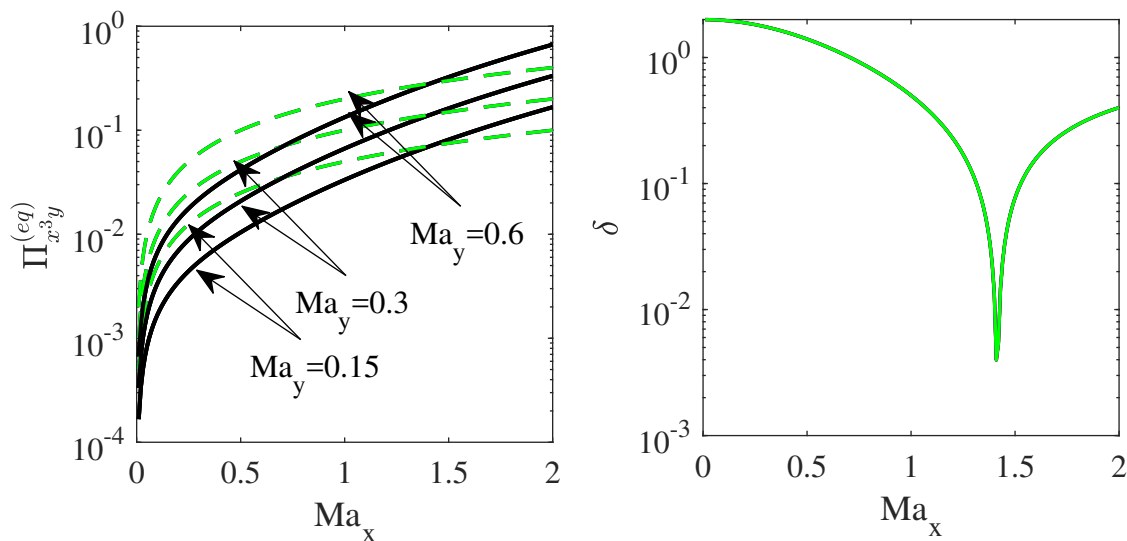


Figure 3.6: (left) $\Pi_{x^3y}^{(eq)}$ moment and (right) relative deviations δ for (in red) second- and (in blue) third-order-Hermite polynomial expansion and (in green) entropic EDF. The continuous moment is shown with black plain line. The red and blue lines are not visible as they coincide with the green lines.

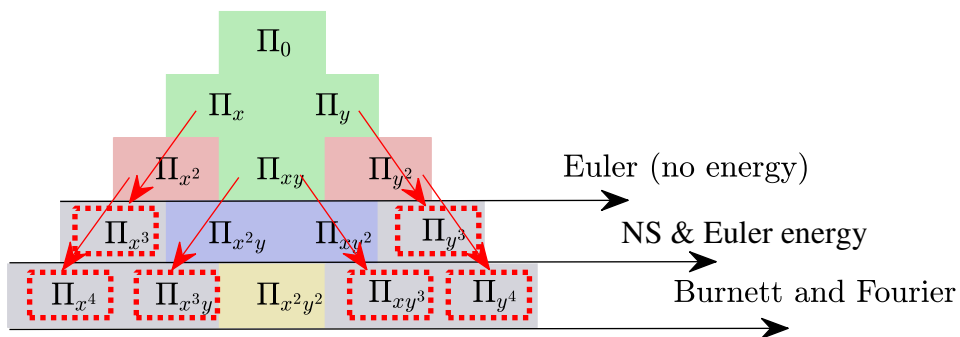


Figure 3.7: Hierarchy of moments on the D2Q9 stencil. Moments correctly recovered with (Green boxes) entropic, (Green+Red boxes) second, (Green+Red+Blue boxes) third and (Green+Red+Blue+Yellow boxes) fourth-order EDFs. Boxes in gray are moments that cannot be recovered on this stencil. Aliasing effects between moments induced by the quadrature are shown with red arrows.

3.2 Bulk flow solver analysis: non-vanishing wave-numbers

The von Neumann (VN) stability analysis aims at studying the time evolution of a perturbation f'_α that is injected into the linearized discrete time evolution equations. The perturbation is expanded as a combination of standing waves, whose propagation speed and attenuation rate will be obtained as a result of the VN analysis. A positive attenuation rate will result in a growth of the error at the corresponding wave-length and linear instability of the solver for the set of parameters considered (τ , Ma, etc). On the contrary, the scheme is linearly stable if it remains negative for all wave-numbers.

Furthermore, the spectral behavior and accuracy can be readily analyzed by comparing the spectral dispersions and dissipations to the theoretical modes obtained from the linearized NS equations. The NS theoretical modes for an isothermal flow can be expressed as [109]:

$$\omega^{\text{shear}} = \mathbf{u} \cdot \mathbf{k} - i\nu\mathbf{k}^2, \quad (3.17a)$$

$$\omega^{\text{acoustic}} = (\mathbf{u} \pm c_s) \cdot \mathbf{k} - i \left(\frac{D-1}{D}\nu + \frac{\eta}{2} \right) \nu\mathbf{k}^2, \quad (3.17b)$$

where D is the physical dimension of the system and \mathbf{k} the wave-number vector. As a consequence, the VN stability analysis can be used to evaluate the spectral behavior and linear stability domain of a LBM for a given set of parameters. As such it can be perceived as a tool to objectively evaluate the stabilization properties of different collision models, on the basis of necessary conditions. The latter comes from the fact that the analysis relies on a linearization step and as such gets the sufficient condition for stability only under the linear regime assumption (small amplitude perturbations). It has been widely used in the past to evaluate the stability properties of the lattice Boltzmann method. Interested readers are referred to [147, 148, 149, 150, 54, 151, 109], among other sources.

3.2.1 Methodology : The von Neumann formalism

Starting with a given set of coupled continuous/discretized PDEs, bound by periodic boundary conditions, defined as:

$$\mathcal{L}(f_\alpha, \mathbf{x}, t) = 0, \quad (3.18)$$

where \mathcal{L} is the time evolution operator, the equations have to be linearized in order to use the VN method. To achieve this for the LB system of equations one can expand (first-order Taylor-McLaurin expansion) the distribution function around a reference state $f_\alpha(\bar{\rho}, \bar{\mathbf{u}})$:

$$f_\alpha \approx \bar{f}_\alpha + f'_\alpha, \quad (3.19)$$

$$\delta_t \Omega_\alpha(f_\alpha) \approx \delta_t \Omega_\alpha|_{\bar{f}_\alpha} + J_{\alpha\beta} f'_\beta, \quad (3.20)$$

where Einstein's notation (summation) over β is used, and for the sake of clarity, $\bar{f}_\alpha = f_\alpha(\bar{\rho}, \bar{\mathbf{u}})$. Obviously, relying on a first-order expansion around the distribution function this expansion is only valid in the linear regime (i.e. small perturbations around the reference state). In addition, $J_{\alpha\beta}$ is the Jacobian of the collision operator evaluated about \bar{f}_β , i.e, $J_{\alpha\beta} = \partial_{f_\beta} \delta_t \Omega_\alpha|_{\bar{f}_\beta}$. Placing back these expressions into the discrete LB time-evolution equation:

$$f'_\alpha(\mathbf{x} + \mathbf{c}_\alpha \delta_t, t + \delta_t) - f'_\alpha(\mathbf{x}, t) = J_{\alpha\beta} f'_\beta(\mathbf{x}, t) - \underbrace{\left(\bar{f}_\alpha(\mathbf{x} + \mathbf{c}_\alpha \delta_t, t + \delta_t) - \bar{f}_\alpha(\mathbf{x}, t) - \delta_t \Omega_\alpha|_{\bar{f}_\alpha} \right)}_{=0}, \quad (3.21)$$

and taking out the last terms on the RHS one gets:

$$f'_\alpha(\mathbf{x} + \mathbf{c}_\alpha \delta_t, t + \delta_t) = (\delta_{\alpha\beta} + J_{\alpha\beta}) f'_\beta(\mathbf{x}, t), \quad (3.22)$$

where $\delta_{\alpha\beta}$ is the Kronecker delta function. Using the SRT collision operator for instance, we can then re-write the linearized time-evolution equation as:

$$f'_\alpha(\mathbf{x} + \mathbf{c}_\alpha \delta_t, t + \delta_t) = \left[\left(1 - \frac{\delta_t}{\tau} \right) \delta_{\alpha\beta} + \frac{\delta_t}{\tau} J_{\alpha\beta}^{(eq)} \right] f'_\beta(\mathbf{x}, t), \quad (3.23)$$

with $J_{\alpha\beta}^{(eq)} = \partial_{f_\beta} f_\alpha^{(eq)}|_{\bar{f}_\beta}$ and $\bar{f}_\beta = f_\beta^{(eq,N)}(\bar{\rho}, \bar{\mathbf{u}})$. To compute the Jacobian matrix of the EDF, knowing that $\partial_{f_\beta} f_\gamma = \delta_{\beta,\gamma}$, the following expressions can be used:

$$\partial_{f_\beta} \mathbf{a}_0^{(eq)} = \partial_{f_\beta}(\rho) = \sum_\gamma \delta_{\beta,\gamma} = 1, \quad (3.24)$$

$$\partial_{f_\beta} \mathbf{a}_1^{(eq)} = \partial_{f_\beta}(\rho \mathbf{u}) = \sum_\gamma \mathbf{c}_\gamma \delta_{\beta,\gamma} = \mathbf{c}_\beta. \quad (3.25)$$

Once re-written as a function of the conserved Hermite coefficients, computing the Jacobians of higher-order components of the Hermite expansion is straightforward. Let us consider the

second-order Hermite coefficient for example:

$$\partial_{f_\beta} \mathbf{a}_2^{(eq)} = \partial_{f_\beta} \frac{\mathbf{a}_1^{(eq)} \otimes \mathbf{a}_1^{(eq)}}{\mathbf{a}_0^{(eq)}} = -\frac{\mathbf{a}_1^{(eq)} \otimes \mathbf{a}_1^{(eq)}}{(\mathbf{a}_0^{(eq)})^2} + \frac{\mathbf{a}_1^{(eq)} \otimes \mathbf{c}_\beta + \left(\mathbf{a}_1^{(eq)} \otimes \mathbf{c}_\beta\right)^T}{\mathbf{a}_0^{(eq)}}. \quad (3.26)$$

Eventually, for the second-order EDF the Jacobian reads:

$$J_{\alpha\beta}^{(eq,2)} = w_\alpha \left(\mathcal{H}_{0,\alpha} + \mathcal{H}_{1,\alpha} : \partial_{f_\beta} \mathbf{a}_1^{(eq)} + \mathcal{H}_{2,\alpha} : \frac{\partial_{f_\beta} \mathbf{a}_2^{(eq)}}{2} \right). \quad (3.27)$$

Detailed expression for the Jacobians of the different EDFs and collision operators are found in appendix E. The last step of the VN analysis is to assume that perturbations f'_α are monochromatic plane waves :

$$f'_\alpha = F_\alpha \exp [i(\mathbf{k} \cdot \mathbf{x} - \omega_\alpha t)],$$

where F_α is the wave amplitude, i is the imaginary unit, $\|\mathbf{k}\| = k$ is the wave-number, and ω is the complex time frequency of the wave. k is related to the wave-length of f'_α , whereas $\Im(\omega)$ and $\Re(\omega)$ are related to its attenuation and propagation speed. By injecting these perturbations into Eq. (3.22) one obtains the following eigenvalue problem of size Q (the number of discrete velocities) :

$$\mathbf{M}\mathbf{F} = \exp(-i\omega_\alpha)\mathbf{F}, \quad (3.28)$$

where \mathbf{F} is the eigenvector composed of all amplitudes. It is related to the eigenvalue $\exp(-j\omega)$. \mathbf{M} is the matrix associated to Eq. (3.22). In the present work, this matrix can be expressed as :

$$\mathbf{M} = \mathbf{E}[\boldsymbol{\delta} + \mathbf{J}], \quad (3.29)$$

with

$$E_{\alpha\beta} = \exp[-i(\mathbf{c}_\alpha \cdot \mathbf{k})]\delta_{\alpha\beta}. \quad (3.30)$$

It is important to notice that the matrix \mathbf{M} and the eigenvalue problem (3.28) depend on the mean flow $(\bar{\rho}, \bar{\mathbf{u}})$, the wave-number (k_x and k_y in 2D) and the relaxation coefficient τ , or equivalently the kinematic viscosity ν . This means that for each set of these parameters the eigenvalue problem needs to be solved to obtain the corresponding values of $\Re(\omega)$ and $\Im(\omega)$. Doing so, the spectral properties (dispersion and dissipation) can be obtained for any given collision model.

3.2.2 Stability domain: Effect of equilibrium state

As mentioned previously, the equilibrium state is one of the most important components of a kinetic scheme and controls, for the most part, the leading-order dynamics of the system (i.e. the macroscopic PDEs of interest), but also the behavior of higher-order (errors, ghost modes) terms. The effects of the EDF on leading-order terms were studied in previous sections. In

this subsection, using the VN formalism we look at the effect of the EDF on the linear stability domain. To do so the eigenvalue problem of the VN equations is solved for different values of non-dimensional viscosities, over the entire wave-number space, i.e. k_x and k_y with a resolution of 100 points in each direction. The highest Mach number resulting in negative dissipation rates over all wave-numbers is retained as the linear stability limit. These limits are shown in Fig. 3.8. Looking at those results a number of points are worth noting: For

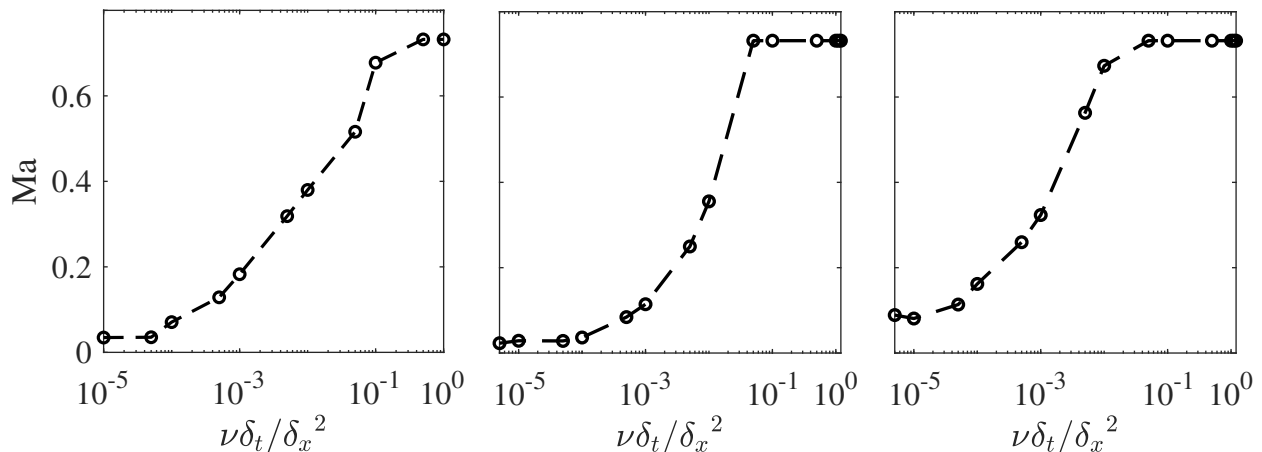


Figure 3.8: Linear stability domains of SRT collision operator with EDFs of orders (from left to right) two, three and four

all of these EDFs, regardless of the value of the non-dimensional viscosity (Fourier number), the maximum stable Mach number never goes beyond $\text{Ma} = \sqrt{3} - 1 \approx 0.732$. Furthermore while the addition of third-order components appears not to have a large effect on the stability domain, the fourth-order component (which does not affect the terms appearing at the NS level) extends it. It is also worth noting that the entropic EDF, not illustrated here but detailed in [152], was found to be linearly stable for all values of the Mach number supported by the stencil, i.e. $\text{Ma} = \sqrt{3}$, even for vanishing viscosities. An illustration of the corresponding linear stability domain can be found in Fig. 7.5 in chapter 7. This in turn confirms the effectiveness of the discrete EDF construction approach in guaranteeing linear stability (by enforcing a discrete H-theorem).

Apart from extending the linear stability domain, the addition of the fourth-order component results in more isotropic behavior especially for small values of the non-dimensional viscosity. The directional stability domains obtained with different orders of the EDF are shown in Fig. 3.9. Finally, one can readily confirm the assertion made in the previous subsections concerning the effect of third-order Hermite terms on the deviatoric components of the third-order moments tensor by looking at the spectral dissipation of physical modes. The spectral dissipation of the shear modes of the third and second-order EDF for three different Mach numbers are shown in Fig. 3.10. It is clearly observed that for the third-order EDF, in the limit of vanishing wave-numbers, the obtained dissipations converge to the correct value regardless of the Mach number. However for the second-order EDF signs of Galilean invariance problems are clearly observed as the continuum limit of shear mode dissipation changes with the Mach number.

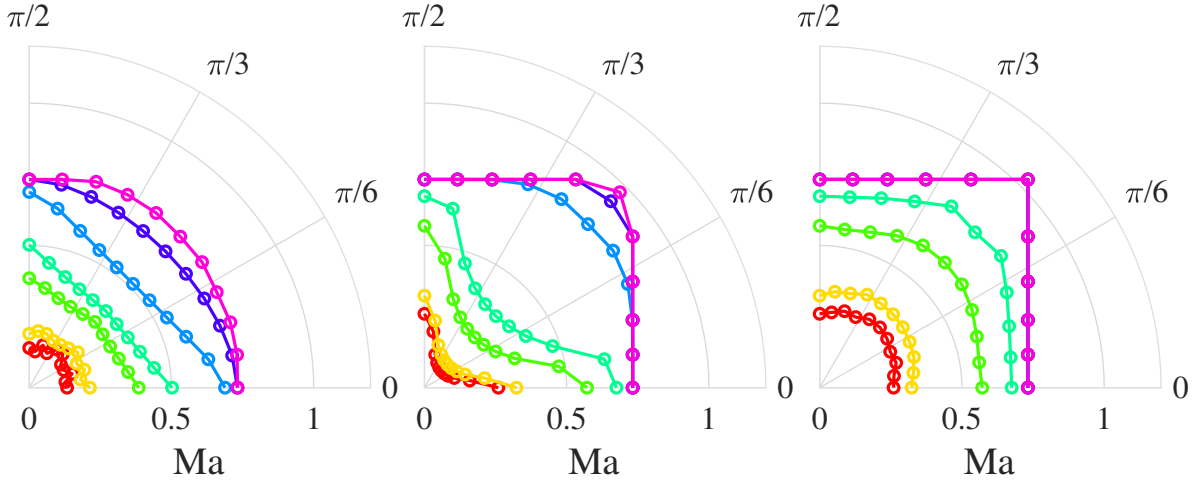


Figure 3.9: Illustration of anisotropy of linear stability domains for EDFs of orders (from left to right) two, three and four, and for seven different non-dimensional kinematic viscosities, i.e. (—) 5×10^{-4} , (—) 1×10^{-3} , (—) 5×10^{-3} , (—) 0.01, (—) 0.05, (—) 0.1, (—) 0.5.

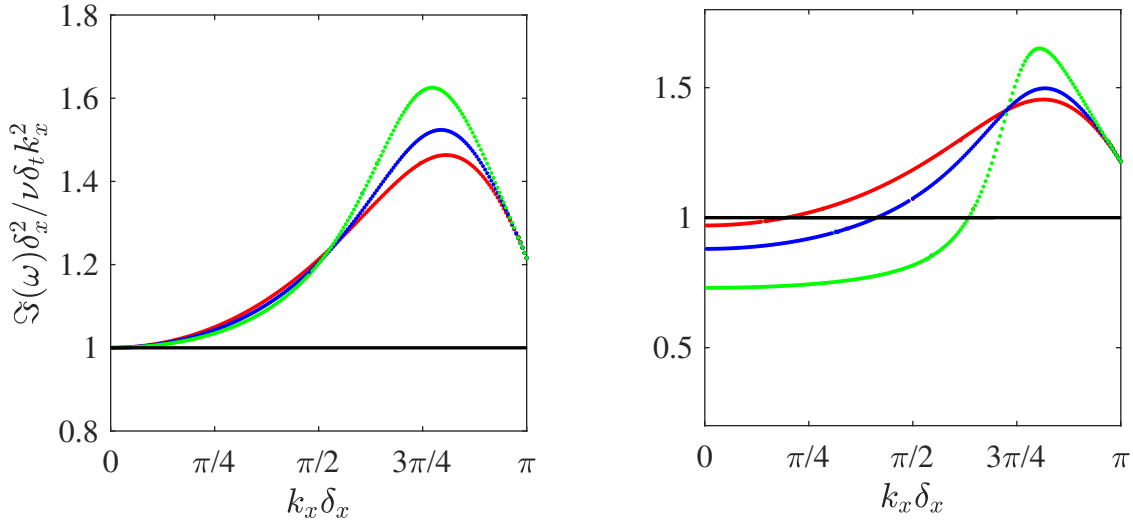


Figure 3.10: Shear mode dissipation rate (normalized by its physical counterpart) for (left) third- and (right) second-order EDF for three different Mach numbers, i.e. (in red) 0.1, (in blue) 0.2 and (in green) 0.3. The continuum reference is shown with a plain black line.

The results obtained in this subsection also point to the fact that the SRT collision operator becomes practically unusable below non-dimensional viscosities of $10^{-3} - 10^{-4}$. Different strategies, detailed in the first chapter, have been developed to allow simulations at lower non-dimensional viscosities. We will analyze the spectral properties of some of these models in the next subsections.

3.2.3 Equilibration strategy I: Filtering out higher-order contributions with regularization

As discussed in the second chapter, the regularization of the distribution function is an approach developed to extend the stability domain of the SRT collision operator and enhance the overall accuracy of the scheme. In order to evaluate the effect of the regularization step on stability, both projection (second-order) and recursive regularization (third and fourth-order) have been studied using the VN method. The linear stability domains are shown in Fig. 3.11 and compared to the SRT. The second-order projection regularized collision model does not

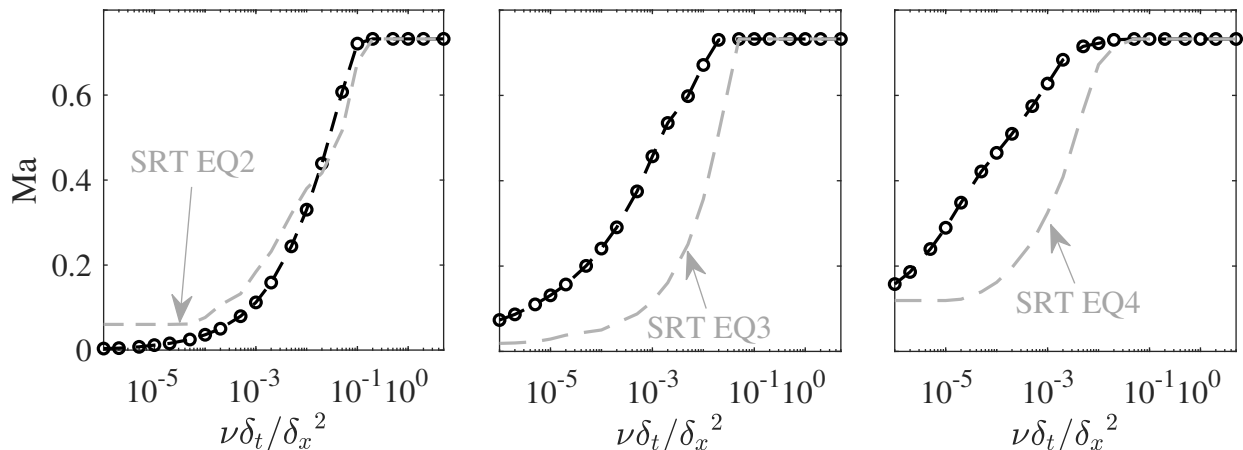


Figure 3.11: Linear stability domains of (from left to right) second-order projection, third and fourth-order recursive regularized collision operators. Stability domains of corresponding SRT operators are shown with grey dashed lines.

seem to extend the stability domain of the scheme. On the contrary, in the limit of vanishing non-dimensional viscosities it results in a reduced stability domain (as compared to its SRT counterpart). However, the recursive regularized operators (both third and fourth-order) significantly increase the maximum stable velocities for mid-range non-dimensional viscosities (i.e. $10^{-5} < \nu\delta_t/\delta_x^2 < 5 \times 10^{-2}$). At smaller viscosities the stability domains converge back to those of their SRT counterparts. Alongside its effect on the linear stability domain, the regularization step can also be observed to have a positive impact on the isotropy of the collision operator. This effect can be observed in Fig. 3.12. The recursive regularization is observed to counter-balance the presence of deviatoric (and absence of diagonal) components of the third-order moments tensor and the resulting pronounced anisotropy along the x - and y -axes.

To have a better understanding of how stabilization is achieved and which modes are affected one can look at the spectral dissipation rates. While it is clear that ghost modes are over-relaxed (by setting them directly to their equilibrium), it is unclear how physical modes are affected by regularization. The spectral dissipation of second-order projection and third-order recursive regularized collision models are shown in Fig. 3.13. While for the second-order projection regularized collision operator the shear mode dissipation rate changes sign past a threshold Mach number and becomes unstable, for the regularized operator the

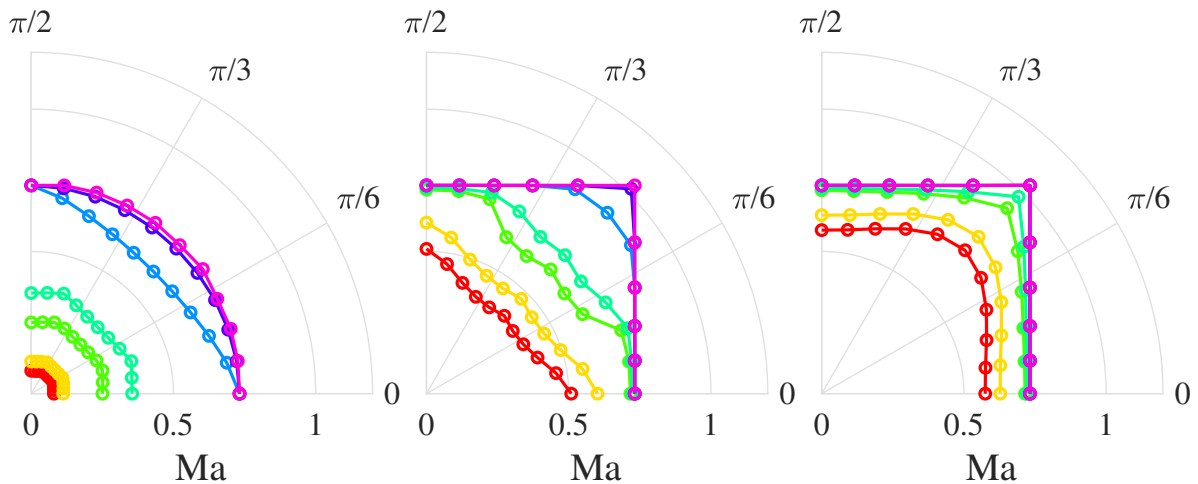


Figure 3.12: Orientation-dependence of stability domains for (from left to right) second-order projection, third and fourth-order recursive regularized collision operators. Considered non-dimensional viscosities are: (—) 5×10^{-4} , (—) 1×10^{-3} , (—) 5×10^{-3} , (—) 0.01, (—) 0.05, (—) 0.1, (—) 0.5.

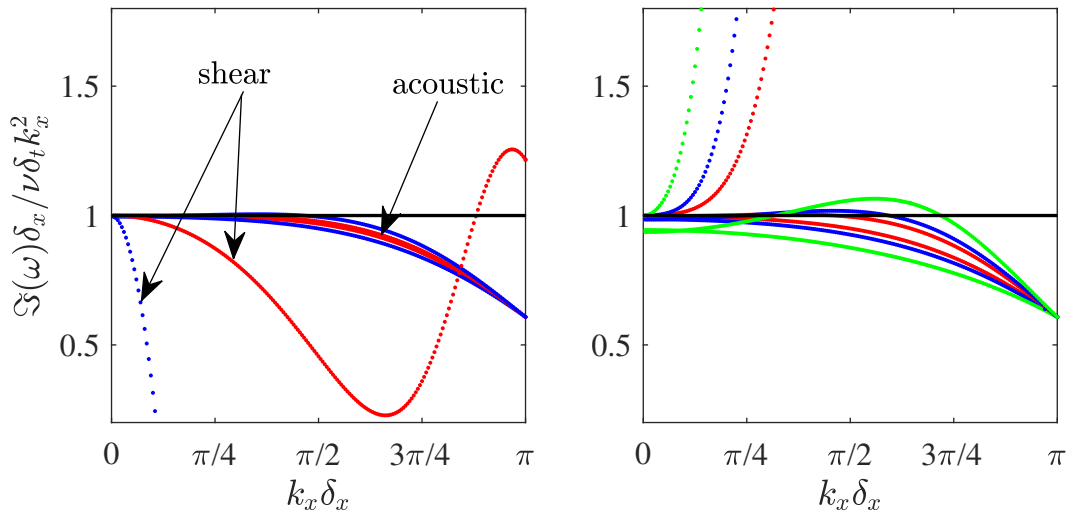


Figure 3.13: Spectral dissipation of physical modes for (left) second-order project and (right) third-order recursive regularized models with $\nu \delta_t / \delta_x^2 = 10^{-5}$ for three Mach numbers: (in red) 0.05, (in blue) 0.1 and (in green) 0.2.

filtering is observed to clearly work. As the velocity increases, the filtering decreases to lower wave-numbers. This way wave-numbers at which modal interactions occur are filtered-out and eigen-mode collisions are prevented [151]. This process however comes with very large over-dissipation of moderately resolved features. For example at a Mach number of 0.05, as shown in Fig. 3.13 flow structures resolved with 16 points or less experience at least a 50 percent increase in dissipation rate (as compared to the intended physical dissipation).

3.2.4 Equilibration strategy II: Independent relaxation of ghost moments, the minimalist example of the LKS

As a minimalist illustration of the concept of Generalized BGK collision operators we consider the effect of the previously introduced LKS on stability. In this collision model, while the second-order Hermite coefficients relax at a rate τ tied to the fluid viscosity, other moments are relaxed at a separate rate λ tied, for the purposes of this section, to a separate viscosity η as:

$$\lambda = \frac{\eta}{c_s^2} + \frac{\delta_t}{2}. \quad (3.31)$$

In order to clarify the effect of this parameter on linear stability, a systematic VN study with a wide range of parameters have been performed. The results are shown in Fig. 3.14. These plots also provide comparison with the SRT and projection regularized collision operators. As observed there, setting $\lambda = 1$, or $\frac{\eta\delta_t}{\delta_x^2} = \frac{1}{6}$ (equivalent to regularization of the second-order moments via projection), systematically lowers the stability limits, even compared to the SRT.

It can be observed that the added degree of freedom in the model can help improve the

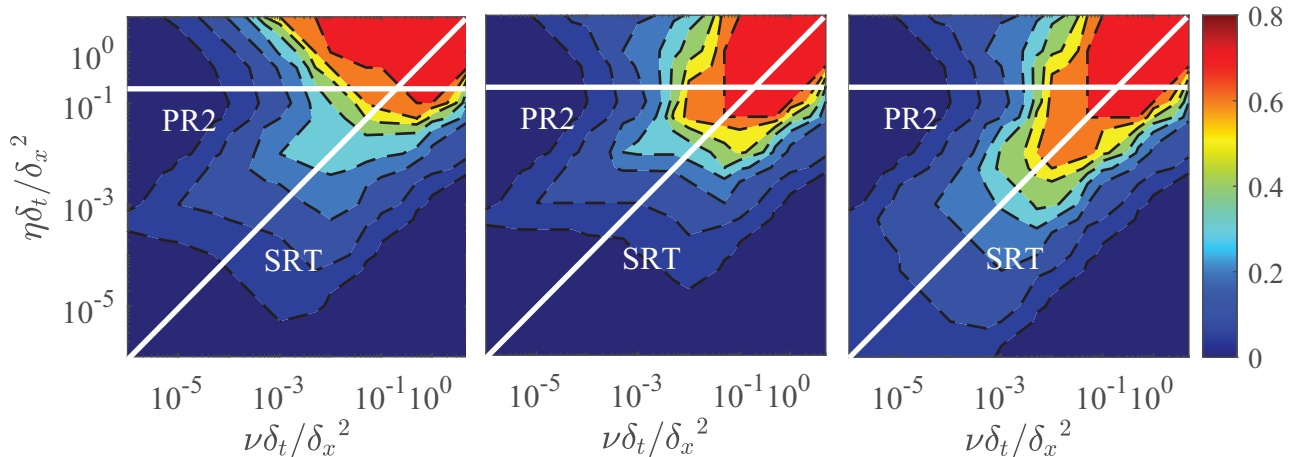


Figure 3.14: Linear stability domain iso-contours of the LKS with EDFs of orders (from left to right) two, three and four. The color bar shows the maximum achievable Mach number.

stability domain to some extent. It is also interesting to note that with an optimized value of this parameter the LKS outperforms the second-order projection regularized model (equivalent to $\lambda = 1$).

It is also worth mentioning that the LKS (while resulting in marginal improvement of the stability domain) does not affect the acoustic modes dissipation. As noted by P. Dellar, a number of MRT models improve stability by over-damping acoustic modes, and therefore modifying a physical parameter, namely the bulk viscosity coefficient [108]. The *modus operandi* of the LKS is illustrated in Fig. 3.15 through the spectral dissipation of different modes. The choice of higher second relaxation coefficient values mainly affects the ghost modes (that are over-dissipated). This is in agreement with the basic principle of the regu-

3.2. Bulk flow solver analysis: non-vanishing wave-numbers

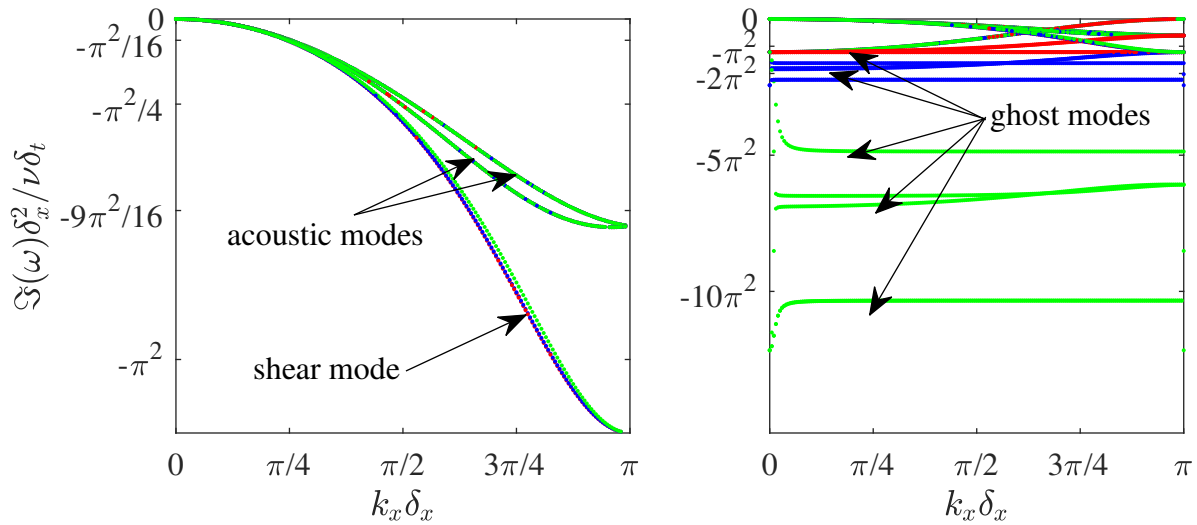


Figure 3.15: Effects of the second relaxation coefficient for $\nu\delta_t/\delta_x^2 = 5 \times 10^{-4}$ and $\text{Ma}=0.1$ on (from left to right) dissipation of acoustic and shear modes, and dissipation of hydrodynamic and kinetic modes. The dissipation curves of shear and acoustic modes for all values of $\eta\delta_t/\delta_x^2$ can not be clearly distinguished as they exactly fall onto each other.

larized collision operator. Furthermore, it can be seen that the second relaxation coefficient does not affect the dissipation rate of acoustic modes.

This last assertion can be further shown by simulating dissipating acoustic waves in the linear regime. Using a domain of size 64×2 , and setting $\rho_0 = 1\text{kg/m}^3$ and $\delta\rho = 10^{-6}\text{kg/m}^3$ the dissipation rate of the acoustic modes were measured for different values of the second relaxation coefficient and values of $\text{Kn}=\text{Ma}/\text{Re}$. The obtained results are depicted in Fig. 3.16. As expected, and in agreement with spectral dissipation results the choice of the

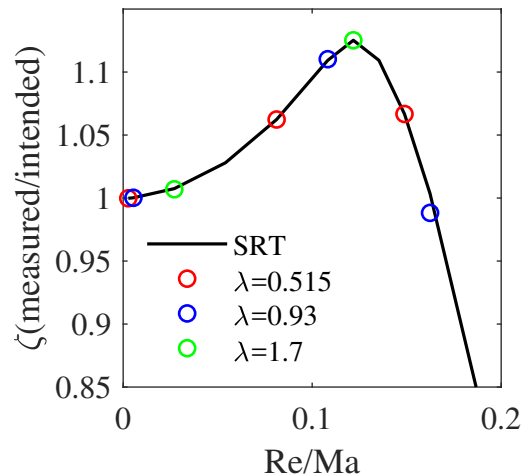


Figure 3.16: Dissipation rate of acoustic modes using the LKS with different values of the second relaxation coefficient versus SRT, obtained using the decaying acoustic wave test-case.

second relaxation coefficient does not affect the behavior of acoustic modes, as they exactly follow their SRT counterparts.

3.2.5 Equilibration strategy III: Choice of basis moments, LKS vs TRT

In the second chapter, it was mentioned that the choice of the basis moments in the context of MRT collision operators can affect the behavior of the solver and its numerical properties. To illustrate this effect, following the analysis of the LKS in the previous subsection, we present corresponding results for the TRT. The linear stability domains for various orders of the EDF and second relaxation coefficients are given in Fig. 3.17. For the sake of uniformity of the analysis presented in this chapter, the notations used for the LKS are also adopted for the TRT; The relaxation coefficient of odd moments is tied to a secondary viscosity coefficient η as in Eq. 3.31. It is interesting to note that in the LKS, moments tied to Hermite polynomials

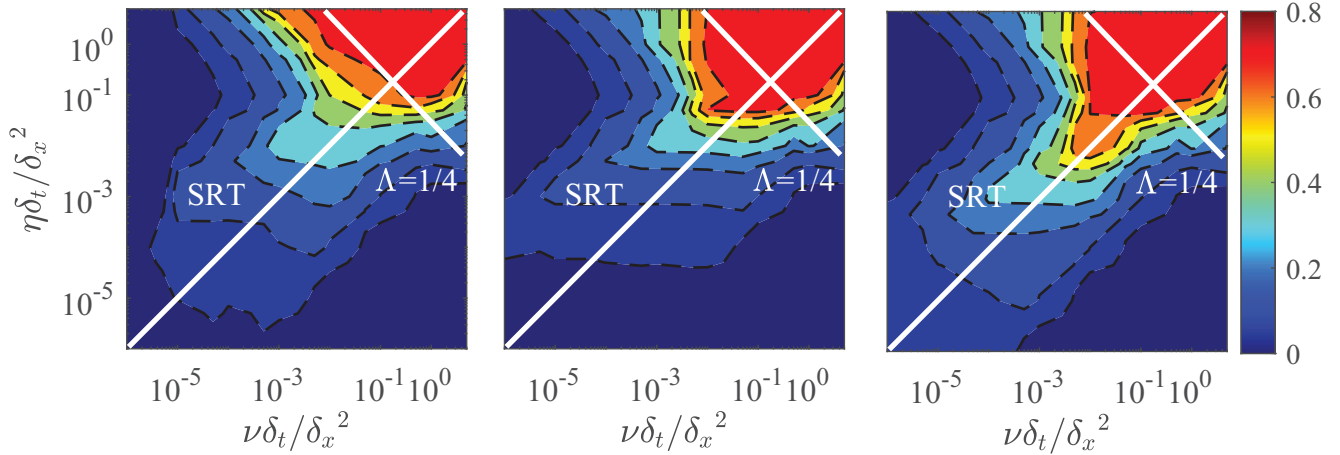


Figure 3.17: Linear stability domain of the TRT collision operator for EDF of orders (from left to right) two, three and four. The color bar shows the maximum achievable Mach number.

$\mathcal{H}_n \in \{\mathcal{H}_0, \mathcal{H}_x, \mathcal{H}_y, \mathcal{H}_{x^2y}, \mathcal{H}_{xy^2}, \mathcal{H}_{x^2y^2}\}$ relax with viscosity η while for $\mathcal{H}_n \in \{\mathcal{H}_{x^2}, \mathcal{H}_{y^2}, \mathcal{H}_{xy}\}$, they are tied to ν . For the TRT on the other hand, $\mathcal{H}_n \in \{\mathcal{H}_0, \mathcal{H}_{x^2}, \mathcal{H}_{y^2}, \mathcal{H}_{xy}, \mathcal{H}_{x^2y^2}\}$ are tied to the physical viscosity while $\mathcal{H}_n \in \{\mathcal{H}_x, \mathcal{H}_y, \mathcal{H}_{x^2y}, \mathcal{H}_{xy^2}\}$ relax with the second relaxation coefficient. As such, similar to the LKS one expects the TRT not to affect acoustic modes dissipation (This is readily confirmed by looking at Fig. 3.18 where acoustic modes of both collision operators coincide). However, one expects to see differences in the ghost moments $\Pi_{x^2y^2}$, Π_x and Π_y . This is confirmed by the spectral dissipation rates shown in Fig. 3.18. The control of all products of the form $\Lambda = c_s^4 (\tau^{(odd)} - 1/2) (\tau^{(even)} - 1/2)$, where $\tau^{(odd)}$ and $\tau^{(even)}$ are the relaxation coefficients of any odd and even-order moment through the specific decomposition operated in the TRT allows it to control the position of the wall when used with the bounce-back rule. In the case of the LKS, the decomposition in Hermite space does not allow for this using only two relaxation coefficients. For any modal decomposition

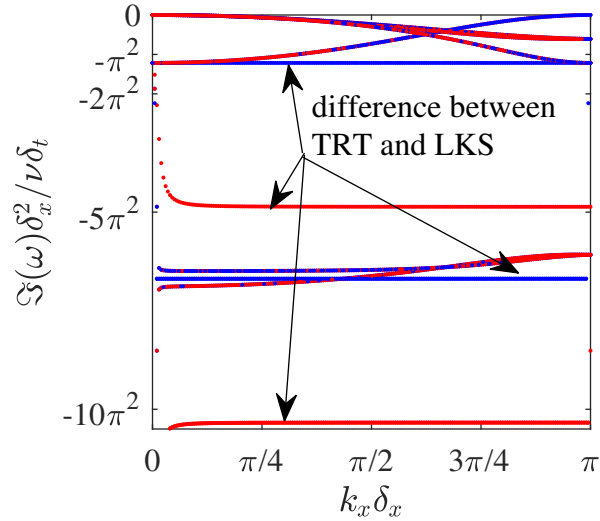


Figure 3.18: Effects of the second relaxation coefficient for $\nu\delta_t/\delta_x^2 = 5 \times 10^{-4}$ and $\text{Ma}=0.1$ on different modes using the (in blue) TRT and (in red) LKS models. The second relaxation coefficient is set to 5×10^{-5} for both models.

other than the one operated in the TRT, one would have to use the full set of independent moments in order to control the wall position in the bounce-back rule. A detailed analysis of this point can be found in [53].

3.2.6 Equilibration strategy IV: central moments

Central moments decomposition of phase-space (instead of raw moments) for the collision operator, as detailed in the previous chapter, has been shown to allow for wider stability domains [56, 153]. While reducing the Galilean invariance tied to higher orders, it is more effective in de-aliasing relaxation of the different moments. Just as for the MRT collision operator, a number of authors have argued that apart from the relaxation coefficient of non-physical modes the choice of the moments space is a determining factor in the stability and accuracy of the scheme [154]. Given that the effect of the moments basis has been treated in previous sections, it will not be studied here anymore. With the emergence of the central moments-based MRT operator another parameter (or free component) of the collision operator gained attention: The order of the EDF. A number of authors argued that instead of computing the corresponding equilibrium moments of the chosen basis (from the discrete second-order EDF) one can use moments of the continuous Maxwell-Boltzmann distribution in the collision operator to improve stability. This in turn was later shown to be equivalent to using a higher-order Hermite expansion in the discrete EDF [127]. To clarify some of these points, the linear stability domains of collision operators based on raw and central moments were computed. Hermite polynomials were chosen as the moments basis and all non-relevant (ghost) modes were relaxed at the same rate (independent from the viscosity). In effect this is equivalent to the LKS collision operator applied in the local fluid velocity frame (instead of a frame at rest). As such the free parameter controlling ghost

moments relaxation is designated using the same variables. The obtained results are shown in Fig. 3.19. It can be observed that by setting $\frac{\eta\delta_t}{\delta_x^2} = \frac{\nu\delta_t}{\delta_x^2}$ one recovers the stability domain of

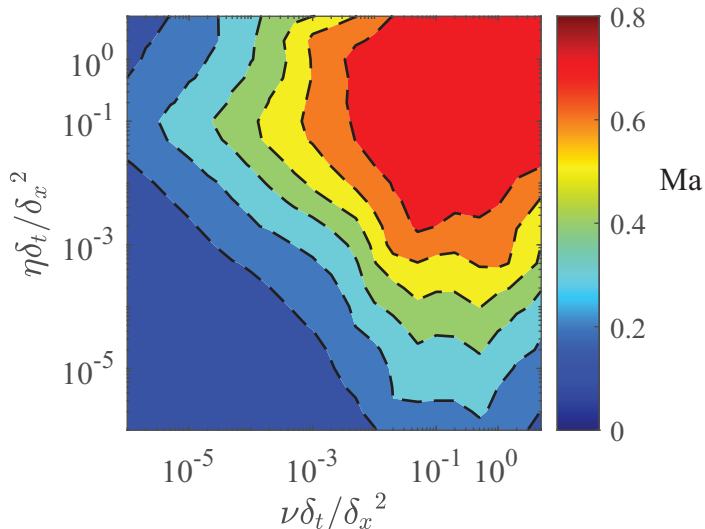


Figure 3.19: Stability domain of a two relaxation time collision operator (similar to the LKS) based on central moments instead of raw moments.

the SRT collision operator with fourth-order EDF. Furthermore, the optimal linear stability domain is achieved when setting the relaxation coefficient of ghost moments to one, which would be equivalent to regularization in the fluid frame. However, it is important to note that the previous assertion only holds for the reduced search-space considered here, i.e. relaxing all ghost moments at the same rate. To better understand the effect of applying the collision operator in the fluid frame the stability domains of the (projection) regularized scheme in the static (at rest) and fluid frame are compared in Fig. 3.20. One can clearly observe that the transition to central moments has a rather pronounced effect on the stability domain at small non-dimensional viscosities. Another observation is that the use of the full set of Hermite polynomials in the EDF (fourth-order in the case of the D2Q9 stencil) does further extend the stability domain.

Coreixas et al. [154] noted that a central moments collision operator in Hermite polynomial space where all ghost modes are set to equilibrium is equivalent to the recursive regularized scheme of the same order. This fact can also be observed in Fig. 3.20. The stability domain of the central moments collision operator with fourth-order EDF corresponds to the one found earlier for the recursive regularized model in Fig. 3.11.

3.3 Numerical applications

To better analyze and understand the operation mode of different collision operators studied in this chapter two classical test-cases are considered in this section: (a) the 2-D periodic shear layer and (b) the 3-D Taylor-Green vortex. Through these test-cases it will be shown

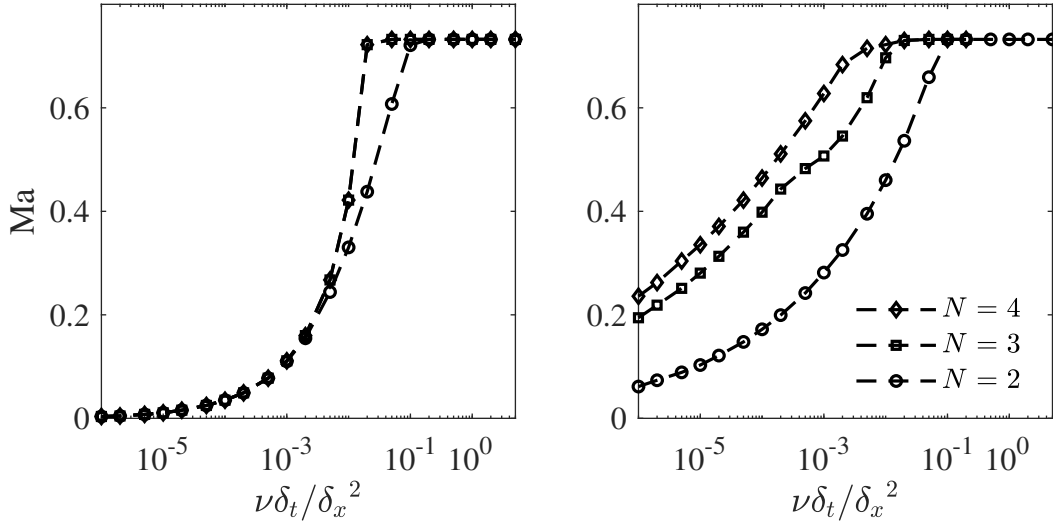


Figure 3.20: Stability limits of (left) raw and (right) central multiple relaxation time collision operator (Hermite coefficients are the chosen moments basis) for different orders of the EDF (N). All relaxation coefficients except those tied to the shear and bulk viscosity are set to one.

that aiming solely for the scheme maximizing the stability domain does not guarantee reliable under-resolved simulations.

3.3.1 2-D periodic shear layer: Stability for under-resolved simulations

The periodic shear layer test-case is an interesting 2-D configuration to assess the stability and dispersion errors of a numerical scheme [155, 156]. As such, the ability of different collision models to cope with under-resolved features will be studied through this test-case here. This 2-D case is made up of two longitudinal shear layers, located at $y = L/4$ and $y = 3L/4$, that evolve in a fully-periodic simulation domain of size $L \times L$. Periodicity allows to study the stability properties of the bulk solver without any effects from boundary conditions [157]. As a result of a small perturbation introduced in the velocity field, the shear layers roll-up –due to a Kelvin-Helmholtz instability– and eventually generate two counter-rotating vortices. For many numerical schemes, the under-resolved simulations of this test-case results in additional spurious vortices, ultimately leading to divergence (in some cases the additional vortices are effectively dissipated and do not lead to blow-up). Given that the formation of the additional vortices have been identified as non-linear effects, cases leading to numerical blow-ups through these numerical artifacts are interesting to study (especially when instabilities are not predicted by the linear analysis). The velocity field is initialized through the following functions:

$$u_x = u_0 \tanh \left[\alpha \left(0.25 - \left| \frac{y}{L} - 0.5 \right| \right) \right], \quad \forall y \quad (3.32a)$$

$$u_y = u_0 \delta \sin \left[2\pi \left(\frac{x}{L} + 0.25 \right) \right], \quad \forall x \quad (3.32b)$$

where u_0 is the mean flow speed, α controls the thickness of the shear layer and δ determines the amplitude of the perturbation. All simulations are performed at $\text{Re}=30,000$, at three different resolutions, namely 32×32 , 64×64 and 128×128 . For all simulations the initial velocity is set to $u_0 = 0.04$, while the perturbation amplitude and shear layer thickness are respectively set to $\delta = 0.05$ and $\alpha = 80$. Four different models are considered here: (a) second-order projection regularized, (b) third-order recursive regularized, (c) fourth-order LKS with free parameter optimized for widest stability domain and, (d) MRT based on central Hermite moments (with all relaxation coefficients set to one except those affecting viscosity). The vorticity fields obtained at $t = t_c = L/u_0$ are shown in Fig. 3.21, where L is the size of the box here equal to the number of grid-points in each dimension. Contrary

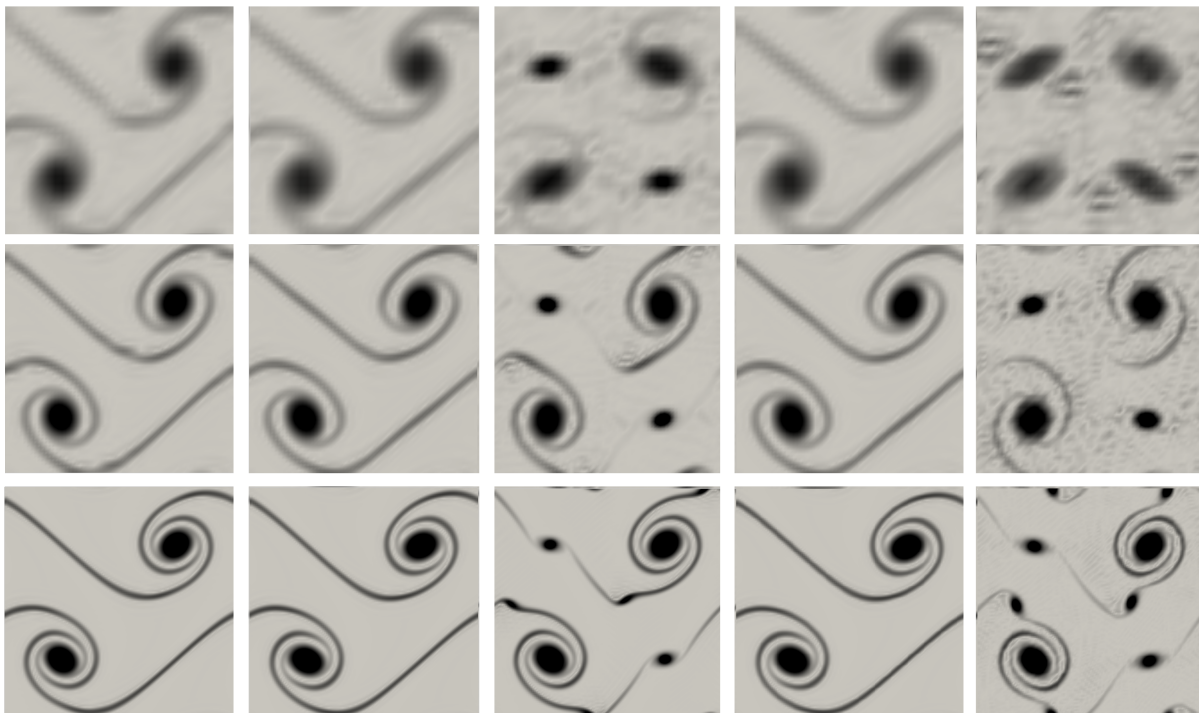


Figure 3.21: Vorticity fields for the periodic shear layer case at $t = t_c$ using (from left to right) second-order projection regularized, third-order recursive regularized, LKS with fourth-order EDF and MRT with central Hermite polynomials at three different resolutions (from top to bottom): 32×32 , 64×64 and 128×128

to the SRT collision operator (unstable for all considered resolutions), all models used in this section were stable for all resolutions. The LKS (in resting frame), however, led to two additional spurious vortices. The appearance of these spurious vortices is tied to dispersion errors at large wave-numbers. While these dispersion errors, as shown previously, exist for all collision models, they are filtered out due to the large hyper-viscosity introduced at those wave-lengths for the other models. This effect will be studied in more details in the next subsection. The formation of these additional vortices can also be observed in the time evolution curves of the kinetic energy, E_k , as shown in Fig. 3.22. At approximately $t = 0.5t_c$

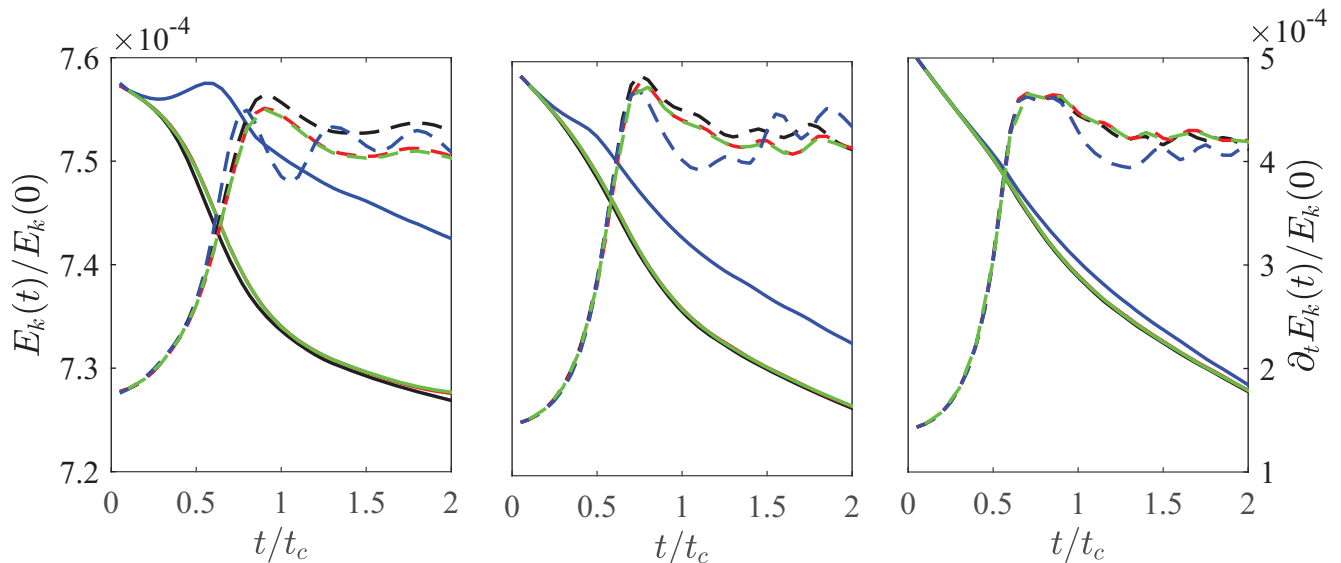


Figure 3.22: Normalized (left axes and plain lines) kinetic energy and (right axes and dashed lines) kinetic energy dissipation rates at three different resolutions: (from left to right) 32×32 , 64×64 and 128×128 using four different collision models: (in black) second-order projection regularized, (in red) third-order recursive regularized, (in blue) fourth-order LKS and (in green) central Hermite MRT.

a jump in the kinetic energy associated to the formation of these vortices can be observed (for the LKS). This effect is less visible in the simulation at 128 as the simulation domain is bigger and the overall kinetic energy is a global parameter. It can also be observed that the central MRT and recursive regularized collision operators reproduce almost exactly the same behavior.

It seems surprising that the second-order projection regularized operator is stable for all these configurations, as referring to the VN analyses one would expect linear instabilities. The absence of linear instabilities for this operator can be explained by a number of facts: (a) small amplification factors, even though unstable, would require a very large number of time-steps to lead to a blow up; (b) the fluid velocity not being above the stability threshold at all domain points, low-velocity areas act as energy sinks by dissipating modes that are unstable in larger velocity areas; (c) the reduced number of grid points itself operates as a filter, limiting the maximum number of modes by the number of grid points. As such, unstable modes not resolved by the simulation do not appear and result in a stable simulation. This last assertion can readily be confirmed by performing VN analyses with different resolutions as shown in Fig. 3.23.

3.3.2 3-D Taylor-Green vortex: Effect of ghost modes relaxation on under and moderately resolved features

In order to study the effect of ghost modes relaxation rates on dissipation and dispersion errors at moderate and large wave-numbers (structures resolved with four points or less)

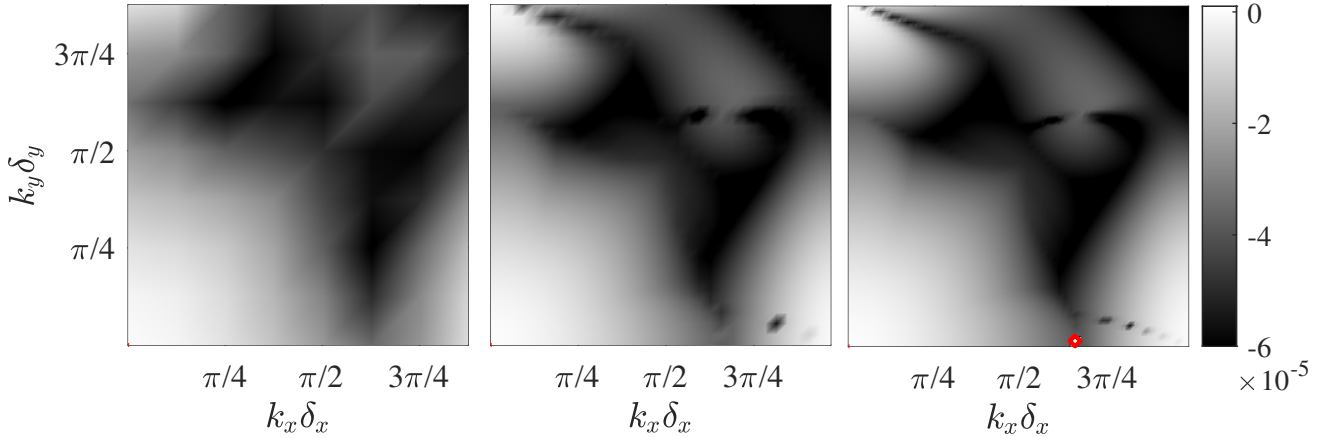


Figure 3.23: Effect of resolution on stability: maximum amplification $\max[\mathfrak{S}(\omega) \delta_x^2 / \delta_t]$ in the $k_x - k_y$ space obtained using SRT collision operator with second-order EDF for three different resolutions, (from left to right) 16×16 , 64×64 and 128×128 points. Unstable wave-numbers are shown with red contour lines, only visible as a very small dot in the right-most figure.

the 3-D Taylor-Green vortex is studied here. This problem consist of an all-around periodic cubic simulation domain, initialized using the following equations:

$$u_x = u_0 \sin \frac{x}{L} \cos \frac{y}{L} \cos \frac{z}{L}, \quad (3.33a)$$

$$u_y = -u_0 \cos \frac{x}{L} \sin \frac{y}{L} \cos \frac{z}{L}, \quad (3.33b)$$

$$u_z = 0, \quad (3.33c)$$

$$p = p_0 + \frac{\rho_0 u_0^2}{16} \left(\cos \frac{2z}{L} + 2 \right) \left(\cos \frac{2x}{L} + \cos \frac{2y}{L} \right), \quad (3.33d)$$

where L is the size of the box. For the purposes of the present study, the Reynolds number is set to $\text{Re}=1600$ and u_0 to 0.1. The simulations are performed at three different resolutions, i.e. 32^3 , 64^3 and 128^3 . The LKS with a fourth-order EDF is used and different values of the second relaxation coefficient are considered. The obtained results are then compared to a well-resolved simulations (i.e. 512^3) performed using the SRT collision models with a fourth-order EDF. The energy spectra obtained from these simulations are summarized in Fig. 3.24. Zoomed-in curves are shown in Fig. 3.25. These energy spectra clearly illustrate the effect of the relaxation of higher-order moments on dissipation errors. For $\lambda = 1$ (i.e. second-order projection regularization) under-resolved flow features are consistently over-damped regardless of the considered resolutions. This over-dissipation is observed to affect even moderately resolved flow features. While lower values of the second relaxation coefficient result in higher energy concentration at higher wave-numbers, they do not necessarily guarantee correct dispersion. The dispersion error can be observed by looking at the vorticity iso-surfaces displayed in Fig. 3.26. Indeed, for smaller values of the free parameter, the flow field is polluted by large wave-number features caused by dispersion error of small-scale under-resolved features. To better distinguish structures caused by dispersion errors from physical ones, the same field is shown in Fig. 3.27 for the reference simulation. Given that

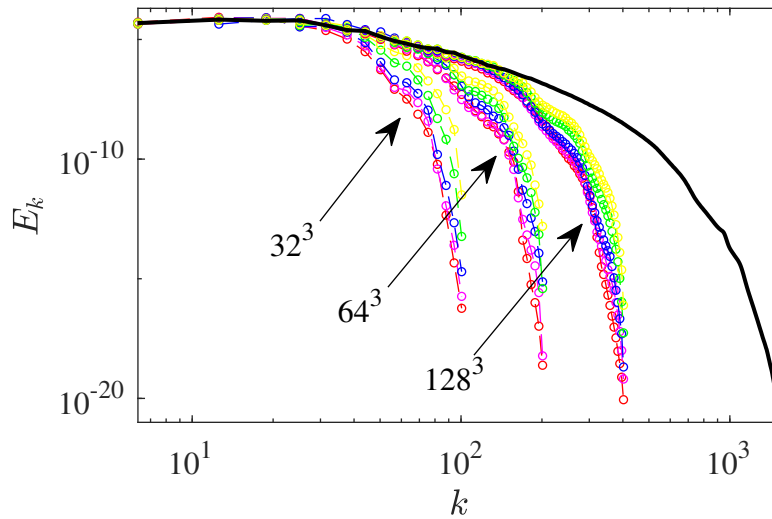


Figure 3.24: Energy spectra at $t = 10t_c$ as obtained with different resolutions. The reference result at 512^3 using the SRT collision operator is shown with a black plain line.

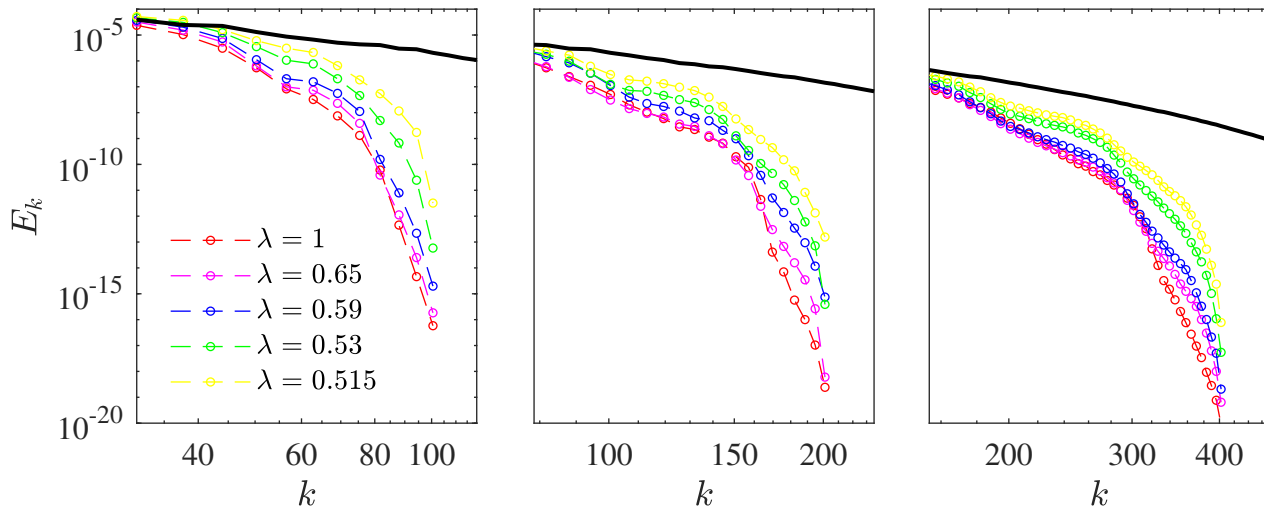


Figure 3.25: Energy spectra at $t = 10t_c$ as obtained with (from left to right) 32^3 , 64^3 and 128^3 using the LKS collision model. The reference result at 512^3 using the SRT collision operator is shown with a black plain line.

for all three considered resolutions the grid-size is larger than the smallest scale, large wave-number features (under-resolved with $k \geq \pi/2$) are created and – if not dissipated – will pollute numerically the flow field. This assertion is corroborated by the spectral dispersion of the solver at viscosities and Mach numbers corresponding to those of the simulations, as illustrated in Fig. 3.28. Above $\pi/2$, corresponding to features resolved with four points or less, there is a five percent error in the shear mode velocity experienced by the signal.

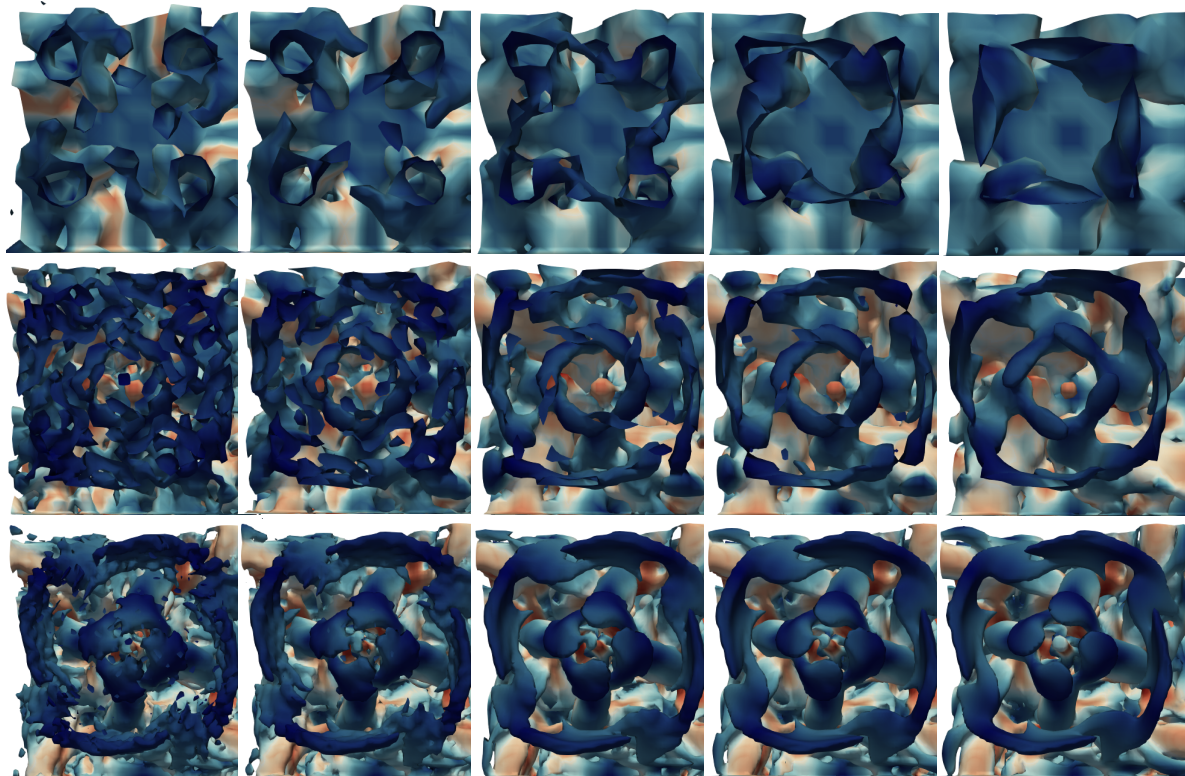


Figure 3.26: Iso-surfaces of the z -component of vorticity $\omega_z = 0$ (bottom view in the z -direction, only the upper left quadrant –of the full domain as shown in Fig. 3.27– is shown) at $t = 10t_c$ obtained using the LKS at three different resolutions (from top to bottom): 32^3 , 64^3 , 128^3 with five different values for the free parameter (from left to right): $\lambda = 0.515, 0.53, 0.59, 0.65, 1$.

3.4 Summary and closing remarks

When using a lattice Boltzmann solver on a stencil based on third-order quadratures there are a number of key parameters to carefully consider:

- The choice of the order of the discrete EDF,
- The Galilean invariance for the dissipation rate of the acoustic modes,
- The choice of the collision operator.
- The choice of the free parameters in the different collision models (i.e. relaxation rates and moments basis).

The choice of the order of the discrete EDF can be important with respect to different aspects. The use of the classical second-order EDF leads to Galilean invariance in the dissipation rate of the shear mode. This error becomes more and more important at intermediate and high Mach numbers. As shown by the CE and higher-order moments error analysis, this problem

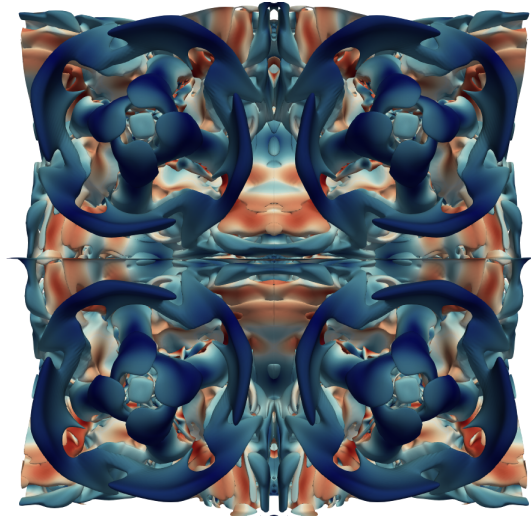


Figure 3.27: Iso-surfaces of the z -component of vorticity $\omega_z = 0$ (bottom view in the z -direction) at $t = 10t_c$ obtained using the SRT at resolutions 512^3 as the reference solution.

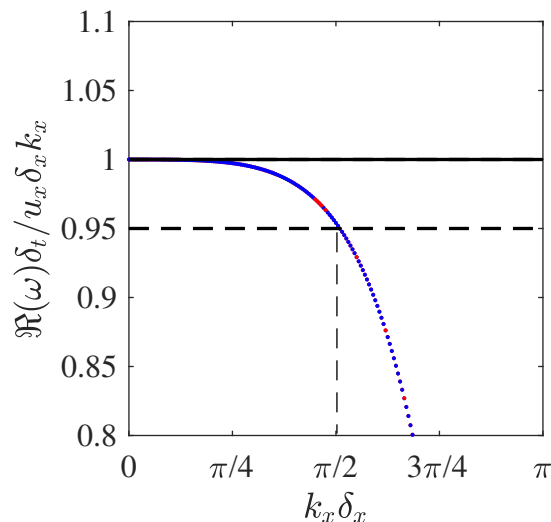


Figure 3.28: Spectral dispersion of the shear mode using the SRT with fourth-order EDF, for $Ma = 0.172$ and viscosities corresponding to TGV simulation with (in red) 32^3 and (in blue) 128^3 grid points. Reference is shown with black plain line.

is tied to the fact that the deviatoric components of the third-order moments tensor are not correctly recovered. The addition of the fourth-order component of the EDF does not have any effect on the stress tensor at the NS level. However, as shown by the spectral dissipation and stability curves, it can have a non-negligible effect on the linear stability domain of the solver regardless of the collision model.

The limited order of the quadratures does not allow first neighbor stencils to correctly recover diagonal components of the third-order moments tensor. These components are tied to the dissipation rate of normal (acoustic) modes. As such, regardless of the order of the

EDF or the collision model, there is a Galilean invariance issue with the dissipation rate of these modes. This error can only be removed (at the NS level) through the addition of a correction term. Therefore, the presence of third-order components of the EDF along with this correction term are necessary for acoustic studies.

Among the different collision operators studied in this chapter, the central moments MRT and fourth-order recursive regularized schemes has the widest linear stability domains. This is not surprising as by setting the moments basis to central Hermite polynomials and filtering out ghost modes (by setting the corresponding relaxation coefficient to one) one recovers the recursive regularized model. The central moments formulation, however, has the additional advantage of allowing for variable relaxation of the ghost moments. As observed in the parametric study of the LKS, fine tuning the free relaxation coefficients can extend the stability domain and/or reduce the hyper-viscosity by the model. Reducing the hyper-viscosity and allowing structures with larger wave-numbers to persist can also lead to the presence of spurious oscillations coming from spectral dispersion inconsistency at these wave-numbers. Furthermore, as opposed to the recursive regularized one, the central moments formulation can also allows to eliminate the viscosity-dependence of the position of the wall in the half-way bounce-back boundary condition, by correctly setting the values of the corresponding relaxation coefficients.

Now that the properties of the basic isothermal LB formulation, and all more advanced collision operators have been clarified, the next chapter will focus on presenting LB-based solvers for the species and energy balance equations.

Chapter 4

Species and Energy balance

Contents

4.1	Introduction to macroscopic equations	65
4.1.1	Species mass balance equations	65
4.1.1.1	Production rate	65
4.1.1.2	Diffusion velocity	66
4.1.2	Energy balance equation	68
4.1.3	Parameter evaluation	70
4.2	Modified advection-diffusion LB solver for energy balance equation	71
4.2.1	Theoretical background	71
4.2.1.1	Brief overview of different LB formulations for energy balance	71
4.2.1.2	CE analysis: shortcomings of the advection-diffusion LB model	73
4.2.1.3	Advection-diffusion model for the mixture-averaged energy balance equation	74
4.2.2	Numerical application and validation	78
4.2.2.1	Heat diffusion with variable thermal conductivity	78
4.2.2.2	Transient diffusion with variable specific heat capacity	78
4.2.2.3	Validation of viscous heating term: 2-D thermal Couette flow	79
4.2.2.4	2-D channel flow with heated obstacles	80
4.2.2.5	Heated lid-driven cavity with variable thermo-physical properties	82
4.2.2.6	Turbulent flow over a multi-layered wall-mounted cube	85
4.3	Species mass balance equations	88

4.3.1	Background and theory	88
4.3.1.1	Brief overview of the literature with a focus on low-order models	88
4.3.1.2	Overcoming issues in the advection-diffusion model: advanced diffusion models and variable density	91
4.3.2	Validation of the proposed model	93
4.3.3	Hirschfelder-Curtiss diffusion: pseudo 1-D diffusion	93
4.3.4	Validation of mass corrector: 2-D counterflow Propane/air flame .	95
4.3.5	Validation of mass corrector: 3-D counterflow non-premixed Ozone/air reacting flow	99
4.4	Final remarks	100

Disclaimer

Part of this chapter has been published in:

- [1] S.A. Hosseini, A. Eshghinejadfard, N. Darabiha, and D. Thévenin. Weakly compressible Lattice Boltzmann simulations of reacting flows with detailed thermo-chemical models. *Computers & Mathematics with Applications*, 79(1), pp.141-158, 2020.
- [2] S.A. Hosseini, N. Darabiha, and D. Thévenin. Mass-conserving advection-diffusion Lattice Boltzmann model for multi-species reacting flows. *Physica A: Statistical Mechanics and its Applications*, 499, pp.40-57, 2018.
- [3] S.A. Hosseini, N. Darabiha, and D. Thévenin. Lattice Boltzmann advection-diffusion model for conjugate heat transfer in heterogeneous media. *International Journal of Heat and Mass Transfer*, 132, pp.906-919, 2019.

4.1 Introduction to macroscopic equations

Before going into the details of the LB solvers for the energy and species mass balance equations, let us introduce the macroscopic descriptions for multi-species reactive flows and corresponding target equations.

4.1.1 Species mass balance equations

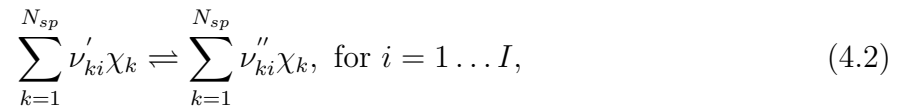
At the macroscopic level, similar to total mass and momentum, one can write balance equations for each species in the following form:

$$\partial_t \rho Y_k + \nabla \cdot \rho Y_k (\mathbf{u} + \mathbf{V}_k) = M_k \dot{\omega}_k, \quad (4.1)$$

where $Y_k = \rho_k/\rho$ is the k^{th} species mass fraction, M_k the k^{th} species molar mass, $\dot{\omega}_k$ the production rate (through chemical reactions) per unit volume and \mathbf{V}_k the diffusion velocity, associated to non-equilibrium effects.

4.1.1.1 Production rate

The species production rate is a key component needing closure in the balance equation. Let us consider a reactive gaseous flow consisting of N_{sp} species χ_k , $k = 1, \dots, N_{sp}$. Chemical reactions can be represented by a detailed chemical scheme involving I elementary reactions represented in the form:



where ν'_{ki} and ν''_{ki} are the i^{th} reaction stoichiometric coefficients. These coefficients verify the mass conservation through the following equation:

$$\sum_{k=1}^{N_{sp}} \nu'_{ki} M_k = \sum_{k=1}^{N_{sp}} \nu''_{ki} M_k. \quad (4.3)$$

The production rate of the k^{th} species $\dot{\omega}_k$ can be computed from the reactions progress rates q_i as:

$$\dot{\omega}_k = \sum_{i=1}^I \nu_{ki} q_i, \quad (4.4)$$

with:

$$\nu_{ki} = \nu''_{ki} - \nu'_{ki}. \quad (4.5)$$

The mass conservation can easily be shown by summing the species production rates and

using Eq. 4.3:

$$\sum_{k=1}^{N_{sp}} M_k \dot{\omega}_k = \sum_{i=1}^I \sum_{k=1}^{N_{sp}} M_k (\nu''_{ki} - \nu'_{ki}) q_i = 0. \quad (4.6)$$

The progress rate of the i^{th} reaction, q_i , reads:

$$q_i = k_{fi} \prod_{k=1}^{N_{sp}} [\chi_k]^{\nu'_{ki}} - k_{ri} \prod_{k=1}^{N_{sp}} [\chi_k]^{\nu''_{ki}}, \quad (4.7)$$

and involves the molar concentration of k^{th} species, $[\chi_k] = \rho Y_k / M_k$. The forward and reverse reaction rate constants, k_{fi} and k_{ri} , are expressed by an Arrhenius-type function. The forward rate is:

$$k_{fi} = A_i T^{\beta_i} \exp\left(\frac{-E_i}{\mathcal{R}T}\right), \quad (4.8)$$

where A_i is the pre-exponential factor, β_i the temperature exponent, E_i the activation energy of the i^{th} reaction and \mathcal{R} the universal gas constant. The reverse reaction rate k_{ri} is computed using the equilibrium constant k_i^{eq} as:

$$k_{ri} = \frac{k_{fi}}{k_i^{eq}}. \quad (4.9)$$

The equilibrium constant is defined as [158]:

$$k_i^{eq} = \left(\frac{p_0}{\mathcal{R}T}\right)^{\sum_{k=1}^{N_{sp}} \nu_{ki}} \exp\left(\frac{\Delta S_i^0}{\mathcal{R}} - \frac{\Delta H_i^0}{\mathcal{R}T}\right), \quad (4.10)$$

where p_0 is the reference pressure, ΔH_i^0 and ΔS_i^0 are the enthalpy and entropy changes for the i^{th} reaction:

$$\Delta H_i^0 = \sum_{k=1}^{N_{sp}} \nu_{ki} M_k h_k(T), \quad (4.11)$$

$$\Delta S_i^0 = \sum_{k=1}^{N_{sp}} \nu_{ki} M_k s_k(T), \quad (4.12)$$

where s_k and h_k are respectively the entropy and total enthalpy (taking into account sensible and chemical contributions) of the k^{th} species.

4.1.1.2 Diffusion velocity

First, it is useful to notice that by summing up Eq. 4.1 over all involved species:

$$\underbrace{\partial_t \rho \left(\sum_{k=1}^{N_{sp}} Y_k \right)}_{\partial_t \rho} + \underbrace{\nabla \cdot \rho \mathbf{u} \left(\sum_{k=1}^{N_{sp}} Y_k \right)}_{\nabla \cdot \rho \mathbf{u}} + \nabla \rho \cdot \left(\sum_{k=1}^{N_{sp}} Y_k \mathbf{V}_k \right) = \underbrace{\sum_{k=1}^{N_{sp}} M_k \dot{\omega}_k}_{=0}. \quad (4.13)$$

and comparing to total mass balance equation, one can easily show that the total diffusion mass flux must vanish:

$$\sum_{k=1}^{N_{sp}} Y_k \mathbf{V}_k = 0. \quad (4.14)$$

Based on the Maxwell-Stefan kinetic theory, the diffusion velocities \mathbf{V}_k should satisfy the following system of equations [159, 160]:

$$\sum_{k'=1}^{N_{sp}} \frac{X_k X_{k'}}{\mathcal{D}_{kk'}} (\mathbf{V}_{k'} - \mathbf{V}_k) = \mathbf{d}_k + \sum_{k'=1}^{N_{sp}} \frac{X_k X_{k'}}{\rho \mathcal{D}_{kk'}} \left(\frac{D_k^T}{Y_k} - \frac{D_{k'}^T}{Y_{k'}} \right) \frac{\nabla T}{T}. \quad (4.15)$$

where $\mathcal{D}_{kk'}$ is the binary diffusion coefficient, and X_k is the k^{th} species mole fraction, related to mass fraction Y_k by:

$$X_k = \frac{\bar{M}}{M_k} Y_k. \quad (4.16)$$

In this equation, \bar{M} represents the mixture-averaged molar mass computed as:

$$\bar{M} = \sum_{k=1}^{N_{sp}} M_k X_k = \frac{1}{\sum_{k=1}^{N_{sp}} Y_k / M_k}. \quad (4.17)$$

In Eq. 4.15, \mathbf{d}_k corresponds to the species diffusion driven forces:

$$\mathbf{d}_k = \nabla X_k + (X_k - Y_k) \frac{\nabla p}{p} + \frac{\rho}{p} \sum_{k'=1}^{N_{sp}} Y_k Y_{k'} (\mathbf{F}_{k'} - \mathbf{F}_k), \quad (4.18)$$

with F_k the external force exerted on the k^{th} species. The last term on RHS of Eq. 4.15 corresponds to the Soert effect with D_k^T the Ludwig-Soret diffusion coefficient of the k^{th} species. Finally, the system of Eqs. 4.15 (rank of $N_{sp} - 1$) combined with Eq. 4.14 can be inverted to obtain the diffusion velocities \mathbf{V}_k . It should however be underlined that, in reactive flow simulations, the inversion should be done at each point of space and time, which will be very CPU time consuming when the gas flow consists of several tens of species. Simplified diffusion are therefore employed for complex reactive flow systems such as:

- *Hirschfelder-Curtiss approximation*: This model is generally used in the combustion community [161]:

$$Y_k \mathbf{V}_k = -D_k \frac{M_k}{\bar{M}} \nabla X_k, \quad (4.19)$$

where D_k is the mixture-averaged diffusion coefficient, which can be modeled as:

$$D_k = \frac{1 - Y_k}{\sum_{k' \neq k} X_{k'} / \mathcal{D}_{kk'}}. \quad (4.20)$$

The approximation introduces a number of shortcomings including, among others, non conservation of overall mass. Indeed, when the species diffusion coefficients and/or molar mass are very different, this approximation does not conserve overall mass through Eq. 4.14. A correction velocity \mathbf{V}^c is therefore employed to overcome this difficulty [162] :

$$Y_k \mathbf{V}_k = -D_k \frac{M_k}{M} \nabla X_k + Y_k \mathbf{V}^c, \quad (4.21)$$

with

$$\mathbf{V}^c = \sum_{k'=1}^{N_{sp}} D_{k'} \frac{M_{k'}}{M} \nabla X_{k'} \quad (4.22)$$

- *Fick approximation*: One of the simplest models is the so-called generalized Fick approximation [162]:

$$Y_k \mathbf{V}_k = -D_k \nabla Y_k, \quad (4.23)$$

where D_k is an effective species diffusion coefficient. Here again mass conservation is obtained only if all species have the same diffusion coefficient, $D_k = D$. The overall mass conservation issue is usually dealt with using one of the two following approaches[162]: (a) solving the species mass balance equation for $N_{sp} - 1$ species and computing the mass fraction of the last species, with index N_{sp} at each point as:

$$Y_{N_{sp}} = 1 - \sum_{k=1}^{N_{sp}-1} Y_k, \quad (4.24)$$

or (b) introducing a so-called correction velocity \mathbf{V}^c [162] to explicitly enforce mass conservation:

$$Y_k \mathbf{V}_k = -D_k \nabla Y_k + Y_k \mathbf{V}^c, \quad (4.25)$$

with

$$\mathbf{V}^c = \sum_{k'=1}^{N_{sp}} D_{k'} \nabla Y_{k'}. \quad (4.26)$$

4.1.2 Energy balance equation

Let us now introduce the macroscopic energy equations, i.e. its different forms, in this subsection. Following [162], starting with the total energy, $\epsilon_t = \epsilon + \mathbf{u}^2/2$, with ϵ the internal energy, one gets:

$$\partial_t \rho \epsilon_t + \nabla \cdot \rho \epsilon_t \mathbf{u} + \nabla \cdot \mathbf{q} + \nabla \cdot p \mathbf{u} - \nabla \otimes \mathbf{u} : \mathcal{T} = 0, \quad (4.27)$$

In this equation, \mathcal{T} is the stress tensor, and \mathbf{q} is the heat flux:

$$\mathbf{q} = -\lambda \nabla T + \sum_{k=1}^{N_{sp}} \rho_k h_k \mathbf{V}_k, \quad (4.28)$$

with λ the thermal conductivity. The last term in Eq. 4.28 expresses energy transport due to diffusion of species with different enthalpies h_k . Making use of the relation between energy and enthalpy, $h_t = \epsilon_t + p/\rho$, with $h_t = h + \mathbf{u}^2/2$, one can write:

$$\partial_t \rho h_t + \nabla \cdot \rho h_t \mathbf{u} - \partial_t p + \nabla \cdot \mathbf{q} - \nabla \otimes \mathbf{u} : \mathcal{T} = 0. \quad (4.29)$$

Subtracting the kinetic energy $\mathbf{u}^2/2$ from Eqs. 4.27 and 4.29, one can get the balance equations for respectively the internal energy and enthalpy:

$$\partial_t \rho \epsilon + \nabla \cdot \rho \epsilon \mathbf{u} + \nabla \cdot \mathbf{q} + p \nabla \cdot \mathbf{u} - \mathcal{T} : \nabla \otimes \mathbf{u} = 0, \quad (4.30)$$

$$\partial_t \rho h + \nabla \cdot \rho h \mathbf{u} - \partial_t p - \mathbf{u} \cdot \nabla p + \nabla \cdot \mathbf{q} - \mathcal{T} : \nabla \otimes \mathbf{u} = 0. \quad (4.31)$$

Finally, for flows involving multiple species and chemical reactions, more suitable forms of the balance equations are found by relying on the concepts of sensible energy and enthalpy, defined as:

$$\epsilon_s = \epsilon - \sum_{k=1}^{N_{sp}} \Delta \epsilon_k^0 Y_k \quad \text{and} \quad h_s = h - \sum_{k=1}^{N_{sp}} \Delta h_k^0 Y_k,$$

and using

$$\epsilon_s = \int_{T_0}^T c_v dT - \bar{r} T_0 \quad \text{and} \quad h_s = \int_{T_0}^T c_p dT.$$

In these equations T_0 is a reference temperature and $\Delta \epsilon^0$ and Δh_k^0 are respectively the energy and enthalpy of formation at this temperature and $\bar{r} = \mathcal{R}/\bar{M}$. Heat capacities, enthalpy and internal energy are calculated as:

$$c_v = \sum_{k=1}^{N_{sp}} Y_k c_{vk} \quad \text{and} \quad c_p = \sum_{k=1}^{N_{sp}} Y_k c_{pk},$$

$$\epsilon = \sum_{k=1}^{N_{sp}} Y_k \epsilon_k \quad \text{and} \quad h = \sum_{k=1}^{N_{sp}} Y_k h_k.$$

The resulting balance equations are obtained as [162]:

$$\partial_t \rho \epsilon_s + \nabla \cdot \rho \epsilon_s \mathbf{u} + p \nabla \cdot \mathbf{u} - \nabla \cdot \lambda \nabla T + \nabla \cdot \left(\sum_{k=1}^{N_{sp}} \rho_k h_{s,k} \mathbf{V}_k \right) - \mathcal{T} : \nabla \otimes \mathbf{u} = \dot{\omega}_T, \quad (4.32)$$

and

$$\partial_t \rho h_s + \nabla \cdot \rho h_s \mathbf{u} - \partial_t p - \mathbf{u} \cdot \nabla p - \nabla \cdot \lambda \nabla T + \nabla \cdot \left(\sum_{k=1}^{N_{sp}} \rho_k h_{s,k} \mathbf{V}_k \right) - \mathcal{T} : \nabla \otimes \mathbf{u} = \dot{\omega}_T, \quad (4.33)$$

with

$$\dot{\omega}_T = - \sum_{k=1}^{N_{sp}} \Delta h_k^0 M_k \dot{\omega}_k.$$

In addition to these two equations, balance equations for sensible total energy (also referred to as *total non-chemical* energy) and enthalpy can also be written as:

$$\partial_t \rho \epsilon_{t,s} + \nabla \cdot \rho \epsilon_{t,s} \mathbf{u} + \nabla \cdot p \mathbf{u} - \nabla \cdot \lambda \nabla T + \nabla \cdot \left(\sum_{k=1}^{N_{sp}} \rho_k h_{s,k} \mathbf{V}_k \right) - \nabla \otimes \mathbf{u} : \mathcal{T} = \dot{\omega}_T, \quad (4.34)$$

and:

$$\partial_t \rho h_{t,s} + \nabla \cdot \rho h_{t,s} \mathbf{u} - \partial_t p - \nabla \cdot \lambda \nabla T + \nabla \cdot \left(\sum_{k=1}^{N_{sp}} \rho_k h_{s,k} \mathbf{V}_k \right) - \nabla \otimes \mathbf{u} : \mathcal{T} = \dot{\omega}_T. \quad (4.35)$$

Given that the interest of the present thesis lies in multi-species flows, the last four forms of the energy balance equation, as expressed in Eqs. 4.32–4.35 will be used in the remainder of the manuscript, and considered to be the target macroscopic equations for the developed LB models.

4.1.3 Parameter evaluation

For detailed mixture-averaged simulations pure substance thermodynamic parameters such as specific heat capacities and enthalpies are extracted from NASA's Chemical Equilibrium with Application (CEA) database, expressed as polynomials of the temperature [163]:

$$\frac{M_k c_{p,k}}{\mathcal{R}} = \sum_{n=1}^5 a_{n,k} T^{(n-1)}, \quad (4.36a)$$

$$\frac{h_k}{\mathcal{R}T} = \frac{a_{6,k}}{T} + \sum_{n=1}^5 \frac{a_{n,k}}{n} T^{(n-1)}, \quad (4.36b)$$

which can then be used to compute the mixture-average specific heat capacity as:

$$\bar{c}_p = \sum_{k=1}^{N_{sp}} c_{p,k} Y_k. \quad (4.37)$$

The specific heat capacity at constant volume can readily be computed from the constant pressure one, for an ideal gas, as:

$$c_{v,k} = c_{p,k} - \frac{\mathcal{R}}{M_k}, \quad (4.38)$$

leading to the following expression for the mixture-averaged capacity:

$$\bar{c}_v = \bar{c}_p - \frac{\mathcal{R}}{\bar{M}}. \quad (4.39)$$

The mixture-average fluid viscosity is computed using Wilke's semi-empirical formula [164] later modified by Bird [165]:

$$\bar{\mu} = \sum_{k=1}^{N_{sp}} \frac{X_k \mu_k}{\sum_{k'=1}^{N_{sp}} X_{k'} \Phi_{kk'}}, \quad (4.40)$$

with:

$$\Phi_{kk'} = \frac{1}{\sqrt{8}} \left(1 + \frac{M_k}{M_{k'}}\right)^{-1/2} \left(1 + \left(\frac{\mu_k}{\mu_{k'}}\right)^{1/2} \left(\frac{M_{k'}}{M_k}\right)^{1/4}\right)^2. \quad (4.41)$$

The mixture-averaged thermal conductivity is computed using averaging formulae proposed by Burgoyne and Weinberg [166, 167, 168, 160]:

$$\bar{\lambda} = \frac{1}{2} \sum_{k=1}^{N_{sp}} X_k \lambda_k + \frac{1}{2} \left(\sum_{k=1}^{N_{sp}} X_k / \lambda_k \right)^{-1}. \quad (4.42)$$

4.2 Modified advection-diffusion LB solver for energy balance equation

4.2.1 Theoretical background

After a thorough analysis of the properties and limitations of the isothermal LB flow solver, this section will focus on developing the necessary tools in the context of the LB formulation to solve the energy balance equations. The aim is to develop the simplest numerical scheme appropriate for the targeted applications.

4.2.1.1 Brief overview of different LB formulations for energy balance

As explained in details in Chapter 2, the standard first-neighbor stencils based on third-order quadrature are unable to correctly recover the moments involved in the energy balance equation at the Euler and NS levels. To overcome these issues, there are two possible approaches: (a) coupled and (b) decoupled; The first approach, called *coupled* here, is a straight-forward extension of the discrete kinetic solver construction methods detailed in Chapter 2. It consists in taking into account the additional constraints on higher-order moments stemming from the energy balance equations at the Euler and NS levels and using larger stencils to satisfy them. Given that the derivation of such formulations does not involve new concepts (compared to the isothermal construction of Chapter 2) and that they are not pursued in the present work, they will not be further detailed here. Interested readers are referred to [169, 170, 171], among other sources.

The decoupled formulation consists in using the LB flow solver for mass and momentum balances and introducing an additional set of distribution functions for the energy balance equation [172, 173, 174, 175, 176, 177, 178], reason why it also referred to as the double-distribution formulation. This can be achieved through a mesoscopically-consistent approach where the new distribution function is defined as (if one chooses to model internal energy):

$$g = \frac{(\boldsymbol{\xi} - \mathbf{u})^2}{2} f. \quad (4.43)$$

Using Boltzmann's equation and the new distribution function one can then derive a time-evolution equation:

$$\partial_t g + \boldsymbol{\xi} \cdot \nabla g + f(\mathbf{u} - \boldsymbol{\xi})(\partial_t + \boldsymbol{\xi} \cdot \nabla) \mathbf{u} = \frac{(\boldsymbol{\xi} - \mathbf{u})^2}{2} \Omega, \quad (4.44)$$

which can in turn, be discretized in phase-space and then in physical space and time to yield a collision-streaming equation similar to that of the flow field. In its simplest form, this approach reduces to a formulation usually referred to as the *advection-diffusion* or *passive scalar* approach [175]. In this approach, similar to the classical LBM, the following discrete time-evolution equation is used:

$$g_\alpha(\mathbf{x} + \mathbf{c}_\alpha \delta_t, t + \delta_t) = \left(1 - \frac{\delta_t}{\tau_T}\right) g_\alpha(\mathbf{x}, t) + \frac{\delta_t}{\tau_T} g_\alpha^{(eq)}(\mathbf{x}, t) + \delta_t w_\alpha \frac{\dot{\omega}_T}{\rho c_p}, \quad (4.45)$$

where both the discrete equilibrium state $g_\alpha^{(eq)}$ and collision time τ_T can be readily determined through the CE expansion, as shown in the next subsection. In the limit of incompressible flows the EDF is usually defined as:

$$g_\alpha^{(eq)}(T, \mathbf{u}) = w_\alpha T \left(1 + \frac{\mathbf{c}_\alpha \cdot \mathbf{u}}{c_s^2} + \frac{(\mathbf{c}_\alpha \cdot \mathbf{u})^2}{2c_s^4} - \frac{\mathbf{u}^2}{2c_s^2}\right), \quad (4.46)$$

while the relaxation time is computed as:

$$\tau_T = \frac{\lambda/\rho c_p}{c_s^2} + \frac{\delta_t}{2}. \quad (4.47)$$

While widely used in the literature for many different applications, especially under the incompressible flow assumption [179, 180, 181], it is not well-suited for flows targeted in the present work, i.e. flows involving variable density and thermodynamic properties. The shortcomings of this model will be reviewed in the next subsection through a brief CE analysis.

4.2.1.2 CE analysis: shortcomings of the advection-diffusion LB model

Using the same formalism as that used in subsection 3.1.1, at order ε^1 one gets:

$$\varepsilon^1 : \partial_t^{(1)}T + \nabla^{(1)} \cdot \mathbf{u}T = 0. \quad (4.48)$$

At order ε^2 , for a linear EDF:

$$\varepsilon^2 : \partial_t^{(2)}T + \nabla^{(1)} \cdot \left(\frac{1}{2} - \tau_T \right) \{ \partial_t^{(1)}\mathbf{u}T + \nabla^{(1)}c_s^2T \} = \frac{\dot{\omega}_T^{(2)}}{\rho c_p}, \quad (4.49)$$

while a quadratic EDF would result in:

$$\varepsilon^2 : \partial_t^{(2)}T + \nabla^{(1)} \cdot \left(\frac{1}{2} - \tau_T \right) \{ \partial_t^{(1)}\mathbf{u}T + \nabla^{(1)}c_s^2T + \nabla^{(1)} \cdot T(\mathbf{u} \otimes \mathbf{u}) \} = \frac{\dot{\omega}_T^{(2)}}{\rho c_p}. \quad (4.50)$$

Summing up the equations at order ε^1 and ε^2 one gets the following PDE, recovered by the advection-diffusion scheme:

$$\partial_t T + \nabla \cdot \mathbf{u}T - \nabla \cdot \frac{\lambda}{\rho c_p} \nabla T - \nabla \cdot \frac{\lambda}{c_s^2 \rho c_p} \partial_t \mathbf{u}T + \mathcal{O}(\varepsilon^3) = \frac{\dot{\omega}_T}{\rho c_p}. \quad (4.51)$$

Comparing this equation with any one of the different forms of the energy balance equations a number of shortcomings are observed:

- Variable density: Assuming constant specific heat capacity, and that one intends to recover the energy balance equation in its non-conservative form, the advection term recovered by the LB scheme is different from what it should be, i.e. $\mathbf{u} \cdot \nabla T$. An additional error is found in the diffusion term as it should be $\frac{1}{\rho} \nabla \cdot \frac{\lambda}{c_p} \nabla T$. Given that c_p is assumed to be constant it is taken inside the first space-derivative to mimic the expression in Eq. 4.51.
- Variable specific heat capacity: Lifting the assumption of a constant specific heat capacity, the diffusion term should be $\frac{1}{\rho c_p} \nabla \cdot \lambda \nabla T$.
- The solver is only second-order accurate under diffusive scaling. Under acoustic scaling, there is an error term, i.e. last term on the LHS, of the form $\nabla \cdot \frac{\lambda}{c_s^2 \rho c_p} \partial_t \mathbf{u}T$.

Taking all those issues into account, to correctly recover the energy balance equation for variable density and heat capacity, the time-evolution equation must include a correction term Φ_α defined as:

$$\Phi_\alpha = w_\alpha \left\{ T \nabla \cdot \mathbf{u} + \lambda \nabla T \cdot \nabla \frac{1}{\rho c_p} \right\}. \quad (4.52)$$

Introducing this correction term in the CE expansion via:

$$\Phi_\alpha = \underbrace{\varepsilon w_\alpha T \nabla^{(1)} \cdot \mathbf{u}}_{\Phi_\alpha^{(1)}} + \underbrace{\varepsilon^2 w_\alpha \lambda \nabla T \cdot \nabla \frac{1}{\rho c_p}}_{\Phi_\alpha^{(2)}}, \quad (4.53)$$

the PDE recovered at the Euler and NS levels changes to (under diffusive scaling):

$$\partial_t T + \mathbf{u} \cdot \nabla T - \frac{1}{\rho c_p} \nabla \cdot \lambda \nabla T + \mathcal{O}(\varepsilon^3) = \frac{\dot{\omega}_T}{\rho c_p}. \quad (4.54)$$

While leading to the correct macroscopic equation, this approach is not computationally attractive as it involves non-local operators and complicated additional terms. Furthermore, while correctly recovering the compressible form of the energy balance equation, the internal energy formulation as proposed in [176, 177, 178] would need a number of complicated non-conservative correction terms coming from the mixture-averaged nature of the targeted balance equations. As such, in the next part, a LB model adapted to the mixture-averaged formulation will be presented.

4.2.1.3 Advection-diffusion model for the mixture-averaged energy balance equation

For applications targeted in the present work, the balance of total sensible energy seems to be the best choice, as all involved terms are in the conservative form, and easily recovered with the LB scheme by correctly defining the discrete equilibrium state.

Before going into the details of the model, we must introduce non-dimensionalization factors for the involved variables. As for the LB flow solver, the non-dimensionalization strategy is essential to a stable scheme and controlled higher-order errors. As shown in [150] in the limit of vanishing diffusion coefficient, the linear stability domain of the advection-diffusion models tends towards the positivity area of the EDF. Given that the intent of the present section is to recover the correct PDE by modifying the second-order moment of the EDF, via EDFs of the general form:

$$g_\alpha^{(eq)} = w_\alpha \left[a_0^{(eq)} + \frac{1}{c_s^2} \mathbf{a}_1^{(eq)} \cdot \boldsymbol{\mathcal{H}}_{1,\alpha} + \frac{1}{2c_s^2} \sum_{i=x,y,z} a_{i2}^{(eq)} \mathcal{H}_{i2,\alpha} \right], \quad (4.55)$$

it is clear that for the resting population to remain positive one must have:

$$\frac{1}{D} \geq \frac{a_{i2}^{(eq)}}{a_0^{(eq)}}, \quad (4.56)$$

where D is the physical dimension of the flow. For moving populations, the following condi-

tion guarantees positivity of all EDFs:

$$c_s^2 \left[1 + \frac{1 - D c_s^2 a_{ii}^{(eq)}}{2 c_s^2 a_0^{(eq)}} \right] \geq \frac{\|a_1^{(eq)}\|}{a_0^{(eq)}}. \quad (4.57)$$

As such we introduce a reference energy per unit volume E^{ref} with units J/m^3 , and a reference temperature T^{ref} , not to be confused with the reference temperature T_0 tied to the lattice spacing and time-step. Therefore, the energy, temperature and pressure as employed in this section are tied to their dimensional counterparts as:

$$\rho' \epsilon'_{t,s} = \frac{\rho \epsilon_{t,s}}{E^{\text{ref}}}, \quad (4.58a)$$

$$p' = \frac{p}{E^{\text{ref}}}, \quad (4.58b)$$

$$T' = \frac{T}{T^{\text{ref}}}. \quad (4.58c)$$

For the remainder of this subsection all energies and temperatures, unless stated otherwise, are in non-dimensional form. The prime symbol is dropped for the sake of readability.

To correctly recover the target PDE, the transported variable, also zeroth-order moment of the EDF, is:

$$\sum_{\alpha} g_{\alpha} = \rho \epsilon_{t,s} = \rho \left(\frac{\mathbf{u}^2}{2} + \int_{T_0}^T \bar{c}_v dT \right), \quad (4.59)$$

while the first-order moment should be:

$$\sum_{\alpha} \mathbf{c}_{\alpha} g_{\alpha} = \rho (\epsilon_{t,s} + p/\rho). \quad (4.60)$$

and the second-order moment:

$$\sum_{\alpha} c_{\alpha,i}^2 g_{\alpha} = c_s^2 T. \quad (4.61)$$

Based on these three conditions and the orthogonality of Hermite polynomials one can readily define a second-order discrete equilibrium state as:

$$g_{\alpha}^{(eq)} = w_{\alpha} \left[\underbrace{\rho \epsilon_{t,s}}_{a_0^{(eq)}} + \underbrace{(\rho \epsilon_{t,s} + p) \mathbf{u}}_{\mathbf{a}_1^{(eq)}} \cdot \frac{\mathcal{H}_{1,\alpha}}{c_s^2} + \underbrace{(T - \rho \epsilon_{t,s})}_{a_{i^2}^{(eq)}} \frac{1}{2 c_s^2} \sum_{i=x,y,z} \mathcal{H}_{i^2,\alpha} \right]. \quad (4.62)$$

Going back to the reference energy and temperature, the following restriction would have to be met to guarantee positivity of resting populations:

$$\frac{D+1}{D} \geq \frac{T}{\rho \epsilon_{t,s}} \frac{E^{\text{ref}}}{T^{\text{ref}}}. \quad (4.63)$$

Given the temperature-dependence of the sensible energy/enthalpy, a root-finding algorithm must be employed to compute the temperature. The root of the following equation:

$$\epsilon_{t,s} - \frac{\mathbf{u}^2}{2} - \int_{T_0}^T \bar{c}_v(T) dT = 0, \quad (4.64)$$

is computed using the Newton-Raphson method where the $n + 1^{\text{th}}$ iteration is given as:

$$T^{n+1} = T^n + \frac{\epsilon_{t,s} - \frac{\mathbf{u}^2}{2} - \int_{T_0}^{T^n} \bar{c}_v(T^n) dT}{\bar{c}_v(T^n)}. \quad (4.65)$$

In practice, starting with the temperature at the previous time-step as the first guess, it takes on average only two iterations to get a converged value for the new temperature.

Using the CE analysis introduced in the previous section, at order ε^1 one recovers the following balance equation for the proposed EDF:

$$\varepsilon^1 : \partial_t^{(1)} \rho \epsilon_{t,s} + \nabla^{(1)} \cdot (\rho \epsilon_{t,s} + p) \mathbf{u} = 0, \quad (4.66)$$

while at order ε^2 the following PDE is found:

$$\varepsilon^2 : \partial_t^{(2)} \rho \epsilon_{t,s} + \nabla^{(1)} \cdot \left(\frac{1}{2} - \tau_T \right) \{ \nabla^{(1)} c_s^2 T + \partial_t^{(1)} (\epsilon_{t,s} + p) \mathbf{u} \} = \dot{\omega}_T^{(2)}. \quad (4.67)$$

The last term, as shown in [182] can be accounted for via a correction defined as:

$$\Phi_\alpha = \frac{w_\alpha}{c_s^2} \left(1 - \frac{\delta_t}{2\tau_T} \right) \mathbf{c}_\alpha \cdot \underbrace{\partial_t (\rho \epsilon_{t,s} + p) \mathbf{u}}_{\mathbf{a}_1^{(eq)}}. \quad (4.68)$$

Furthermore, the relaxation coefficient is found to be:

$$\tau_T = \frac{\lambda T^{\text{ref}}}{c_s^2 E^{\text{ref}}} + \frac{\delta_t}{2}. \quad (4.69)$$

To account for viscous dissipation heating, we introduce a source term, Ξ , such that:

$$\Xi_\alpha = \varepsilon \Xi_\alpha^{(1)} + \varepsilon^2 \Xi_\alpha^{(2)} + \mathcal{O}(\varepsilon^3). \quad (4.70)$$

This expansion is justified by the fact that viscous dissipation is a non-equilibrium effect. Being a non-equilibrium effect, it should not affect the energy balance equation at the Euler level. Therefore:

$$\sum_\alpha \Xi_\alpha^{(1)} = 0. \quad (4.71)$$

Taking this new term into account and using the previously-listed restrictions on it, Eq. 4.67

changes into:

$$\varepsilon^2 : \partial_t^{(2)} \rho \epsilon_{t,s} + \nabla^{(1)} \cdot \left(\frac{1}{2} - \tau_T \right) \{ \nabla^{(1)} c_s^2 T + \partial_t^{(1)} (\rho \epsilon_{t,s} + p) \mathbf{u} \} + \nabla^{(1)} \cdot \left(\tau_T \sum_{\alpha} \mathbf{c}_{\alpha} \Xi_{\alpha}^{(1)} \right) = \dot{\omega}_T^{(2)}. \quad (4.72)$$

This in turn results in a new restriction on Ξ_{α} , i.e.:

$$\sum_{\alpha} \tau_T \mathbf{c}_{\alpha} \Xi_{\alpha}^{(1)} = \mathbf{u} \left(\frac{1}{2} - \tau \right) \{ \partial_t^{(1)} \mathbf{\Pi}_2^{(0)}(f_{\alpha}) + \nabla^{(1)} \cdot \mathbf{\Pi}_3^{(0)}(f_{\alpha}) \}. \quad (4.73)$$

where $\mathbf{\Pi}_2^{(0)}(f_{\alpha})$ and $\mathbf{\Pi}_3^{(0)}(f_{\alpha})$ are the moments of the flow field distribution function and τ is the fluid solver relaxation coefficient. To satisfy all restrictions on this term, it can be defined as:

$$\Xi_{\alpha} = \frac{1 - 1/2\tau}{\tau_T} \mathbf{u} \cdot \mathbf{c}_{\alpha} (f_{\alpha} - f_{\alpha}^{(eq)}), \quad (4.74)$$

which can also be written in a more efficient way as:

$$\Xi_{\alpha}(\mathbf{x}, t) = \frac{1 - 2\tau}{2\tau_T} \mathbf{u}(\mathbf{x}, t) \cdot \mathbf{c}_{\alpha} [f_{\alpha}(\mathbf{x} + \mathbf{c}_{\alpha} \delta_t, t + \delta_t) - f_{\alpha}(\mathbf{x}, t)]. \quad (4.75)$$

To sum up, the time-evolution equation for the proposed model can be expressed as:

$$g_{\alpha}(\mathbf{x} + \mathbf{c}_{\alpha} \delta_t, t + \delta_t) - g_{\alpha}(\mathbf{x}, t) = \frac{\delta_t}{\tau_T} (g_{\alpha}^{(eq)}(\mathbf{x}, t) - g_{\alpha}(\mathbf{x}, t)) + \Xi_{\alpha} + \Phi_{\alpha} + \delta_t w_{\alpha} \dot{\omega}_T, \quad (4.76)$$

where the expressions for the EDF, source terms Φ_{α} and Ξ_{α} are respectively given by Eqs. 4.62, 4.68 and 4.75.

It is also worth mentioning that in some cases, to have better control over higher-order errors and wider stability domains the MRT collision operator is used. The independent Hermite coefficients are used as the moments basis. For example, on the D2Q5 stencil, the following moments are used as basis:

$$\Pi = \{ \Pi_0, \Pi_x, \Pi_y, \Pi_{x^2}, \Pi_{y^2} \}, \quad (4.77)$$

resulting in the following equilibrium moments:

$$\Pi^{(eq)} = \{ \rho \epsilon_{t,s}, \rho(\epsilon_{t,s} + p/\rho) u_x, \rho(\epsilon_{t,s} + p/\rho) u_y, c_s^2(T - \rho \epsilon_{t,s}), c_s^2(T - \rho \epsilon_{t,s}) \}. \quad (4.78)$$

The transformation matrices on different stencils are detailed in appendix D. The proposed model along with the different source terms will be assessed in the next subsection through a variety of numerical applications.

4.2.2 Numerical application and validation

4.2.2.1 Heat diffusion with variable thermal conductivity

As first validation cases, two pseudo 1-D configurations involving variable thermal conductivities are studied: (a) solid two-layer medium and (b) single layer slab with temperature-dependent conductivity. In the first configuration, the simulation domain is composed of two regions, of lengths $L_1 = L/2$ and $L_2 = L/2$, with the same heat capacities and densities but different thermal diffusion coefficients, i.e. $\lambda_1 = 0.1$ and $\lambda_2 = 0.2$ W/m.K. In the second configuration the thermal conductivity is defined as a linear function of the temperature as:

$$\lambda(T) = \lambda(T^*) \frac{T}{T^*}, \quad (4.79)$$

where $T^* = 300$ K and $\lambda(T^*) = 0.1$ W/m.K. In both cases the domain size is set to $L = 100$ m, fixed temperatures are enforced at the top and bottom boundaries, i.e. $T_h = 1000$ and $T_c = 300$ K respectively, while periodic boundary conditions are applied in the x -direction. The governing equations are:

$$\begin{cases} \partial_t T - \partial_y \lambda(T, y) \partial_y T = 0, \\ T(y = 0) = T_c, \\ T(y = L) = T_h. \end{cases} \quad (4.80)$$

The analytical steady-state solution for the two-block configuration can be found to be:

$$T(y) = \begin{cases} \frac{T_h - T_c}{\lambda_1 \left(\frac{L_1}{\lambda_1} + \frac{L - L_1}{\lambda_2} \right)} y + T_c, & y < L_1 \\ \frac{T_h - T_c}{\lambda_2 \left(\frac{L_1}{\lambda_1} + \frac{L - L_1}{\lambda_2} \right)} y + T_h - \frac{(T_h - T_c)L}{\lambda_2 \left(\frac{L_1}{\lambda_1} + \frac{L - L_1}{\lambda_2} \right)}, & L_1 \leq y \leq L, \end{cases} \quad (4.81)$$

while for the second configuration one gets:

$$T(y) = \sqrt{\left(\frac{y}{L} T_h^2 + \frac{(L - y)}{L} T_c^2 \right)}. \quad (4.82)$$

For both cases the grid and time-step sizes are set to unity. The steady-state solutions obtained using the proposed solver are compared to their analytical counterparts in Fig. 4.1. As expected the solver is in excellent agreement with analytical solutions.

4.2.2.2 Transient diffusion with variable specific heat capacity

Previous test-cases have shown that the proposed scheme is able to model heat diffusion with variable thermal conductivity. This next configuration is used to prove that it is also able to deal with diffusion with variable specific heat capacities and densities. It consists of a domain of height $L = 3$ m, with three regions of lengths L_1 , L_2 and L_3 , all set to $L/3$ in the present study. At the upper and lower boundaries constant temperatures, respectively $T_c = 300$ K

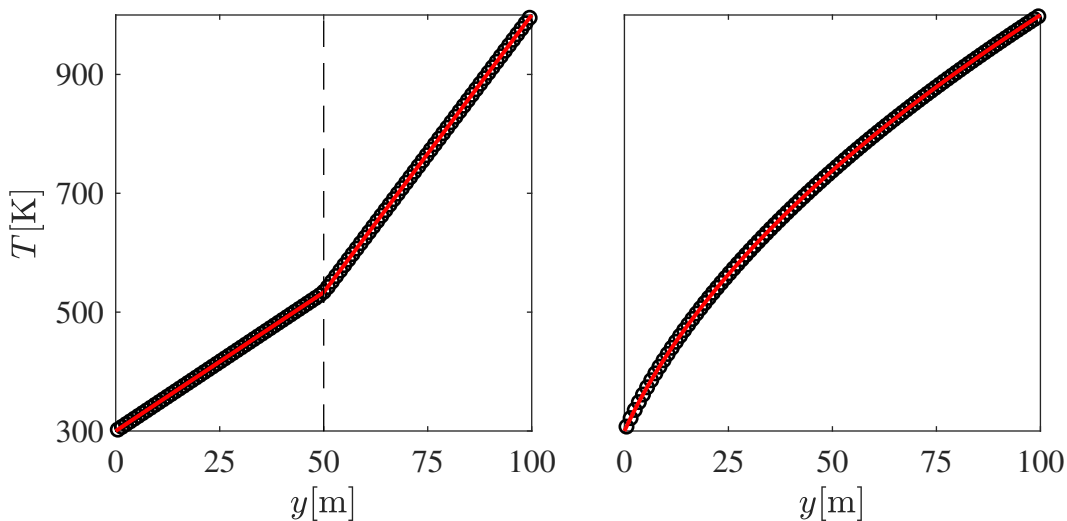


Figure 4.1: Steady-state (red plain line) analytical and (black symbols) numerical solutions, obtained using the proposed model, for the (left) two-block and (right) temperature-dependent thermal conductivity test-cases.

and $T_h = 1000\text{K}$, are enforced. The specific heat capacities and thermal conductivities of each region are shown in Table 4.1. The simulation is performed setting $\delta_x = 3 \times 10^{-2}\text{m}$ and

	$\lambda[\text{W/m.K}]$	$c_p[\text{J/kg.K}]$	$L[\text{m}]$
Zone 1	1.	1.	1.
Zone 2	0.1	0.033	1.
Zone 3	1.	1.	1.

Table 4.1: Simulation parameters for unsteady three-block media test-case [183]

$\delta_t = 1 \times 10^{-4}\text{s}$. Initially the temperature in the domain is set to T_c . Temperature profiles obtained at different times are compared to reference results from a spectral simulation reported in [183]. The results are displayed in Fig. 4.2. The unsteady temperature profiles at four different times are compared in Fig. 4.2. As for previous configurations, it is observed that the temperature profiles obtained with the proposed model are in excellent agreement with reference solutions.

4.2.2.3 Validation of viscous heating term: 2-D thermal Couette flow

To assess the validity of the viscous heating term as proposed in Eq. 4.75 in combination with the anti-bounce-back equation, the thermal Couette flow is considered. The configuration consists of a 2-D channel of height L bounded by a stagnant wall (at the bottom) at temperature T_c (set to 300 K here) and a moving wall (at the top), at velocity u_0 (set to 0.05 m/s) and temperature T_h (set to 300.002 K). The Reynolds number for this flow is defined as $\text{Re} = \frac{u_0 L}{\nu}$. The flow is governed by the Brinkman number, i.e. $\text{Br} = \text{PrEc}$, where the Prandtl number is defined as $\text{Pr} = \frac{\rho c_p \nu}{\lambda}$ and the Eckert number as $\text{Ec} = \frac{u_0^2}{c_v(T_h - T_c)}$. Using

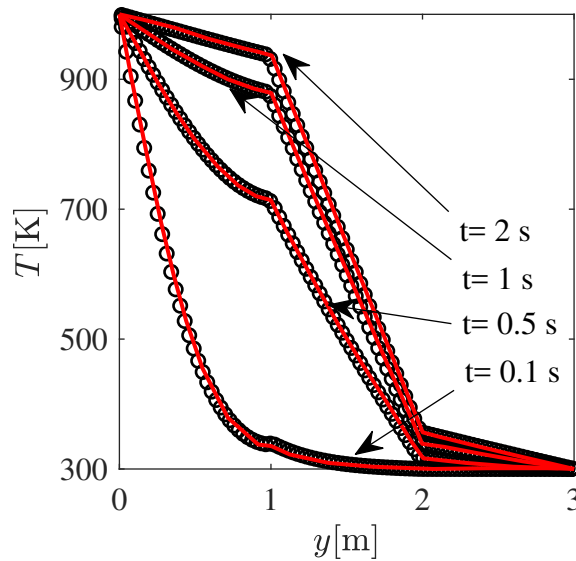


Figure 4.2: Unsteady (red plain line) spectral and (black symbols) numerical solutions, obtained using the proposed model, at different times for the three-block media configuration.

this non-dimensional number the analytical solution can be expressed as [184, 185, 9]:

$$T(y) = T_c + \frac{y}{L} \left[1 + \frac{\text{Br}}{2} \left(1 - \frac{y}{L} \right) \right] (T_h - T_c). \quad (4.83)$$

To validate the ability of the proposed model to capture viscous heating, this configuration was modeled for different Brinkman numbers. Obtained results are compared to analytical solutions in Fig. 4.3. Simulation are performed, as for previous cases, on the D2Q9 stencil, using 50 grid-points in the y -direction. As observed in Fig. 4.3 the obtained temperature profiles are in excellent agreement with analytical solutions.

4.2.2.4 2-D channel flow with heated obstacles

To confront the model to more realistic configurations and showcase the ability of the model to capture conjugate heat transfer, a 2-D channel flow with heated square obstacles on both upper and lower walls is considered here [3, 186]. The geometrical configuration and boundary conditions are shown in Fig. 4.4. This test-case has been studied in details in [3, 186] at different Reynolds numbers ranging from 400 to 2000 with different solid-to-fluid thermal conductivity ratios. In the present work a Reynolds number of 400 is considered, where the Reynolds number is defined as:

$$\text{Re} = \frac{D_h \bar{u}_0}{\nu}, \quad (4.84)$$

where D_h is the hydraulic diameter defined as $D_h = 2H$ and \bar{u}_0 is the average inlet velocity (a Poiseuille profile is imposed at the inlet). The Prandtl number is set to 0.71 and the solid-to-fluid thermal conductivity ratio, λ_s/λ_f to 10. The kinematic viscosity was taken

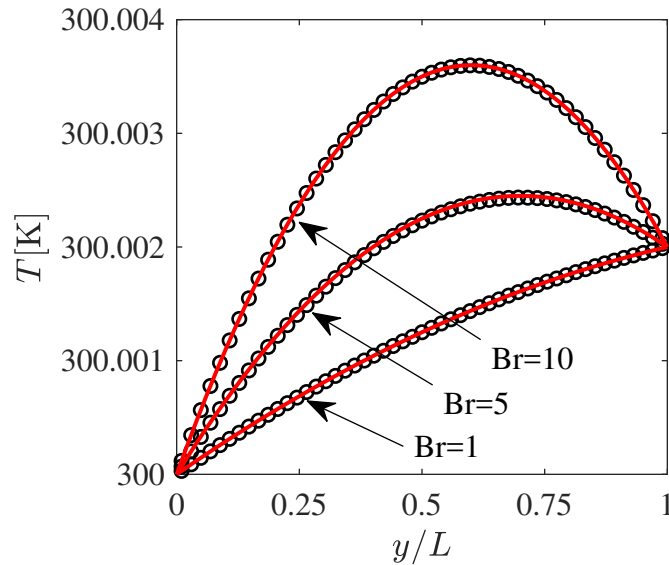


Figure 4.3: Steady-state (red plain line) analytical and (black symbols) numerical solutions, obtained using the proposed model, for the thermal 2-D Couette flow.

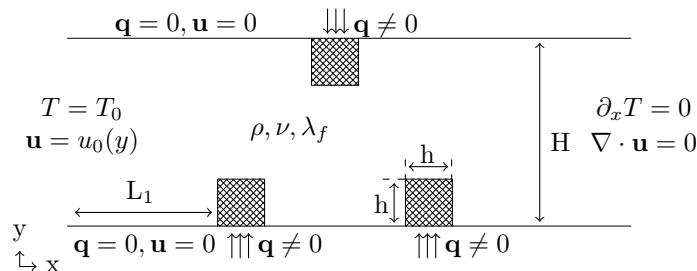


Figure 4.4: Configuration for 2-D channel flow with heated obstacles mounted on upper and lower walls

as $1.568 \times 10^{-5} \text{m}^2/\text{s}$ (corresponding to that of air), while thermal conductivity, density and specific heat capacity in the fluid were respectively set to $0.0262 \text{W}\cdot\text{m}^{-1}\text{K}^{-1}$, $1.177 \text{kg}/\text{m}^3$ and $1004.9 \text{J}/\text{kg}\cdot\text{K}$. Following [3, 186], the density and specific heat capacity of the solid obstacle have been set equal to that of the fluid. Furthermore, the channel height H is set to 1mm and $\bar{u}_0 = 3.136 \text{m}/\text{s}$. The heat flux at the base of each obstacle, q is set to $436.7 \text{W}\cdot\text{m}^{-2}$.

Adiabatic, fixed-temperature, and fixed-velocity boundary conditions are applied using the anti-bounce-back formulation. Non-zero constant-flux boundary condition at the base of the solid obstacles is enforced following [187], where missing populations are computed as:

$$g_\alpha(\mathbf{x}, t) = (w_\alpha + w_{\bar{\alpha}}) T_w - g_{\bar{\alpha}}^*(\mathbf{x}, t - \delta_t), \quad (4.85)$$

where g_α^* is the post-collision population and T_w is computed as:

$$T_w = \frac{2q(\mathbf{x}, t)}{\lambda(\mathbf{x}, t)} + T(\mathbf{x}, t - \delta_t). \quad (4.86)$$

To minimize boundary effects from the inlet and outlet, the first obstacle is placed at a distance of $L_1 = 5H$ from the inlet while L_{out} , the horizontal distance between the last obstacle and the outlet boundary is set to $20H$. The simulation is performed on a grid of size 80×2100 , with H resolved with 80 grid-points and h with 20, δ_x is set to 1.25×10^{-5} m and δ_t to 4.7×10^{-8} s. The center-to-center horizontal distance between the bottom obstacles is $2h$. The streamlines obtained at steady-state are shown in Fig. 4.5. The non-dimensional

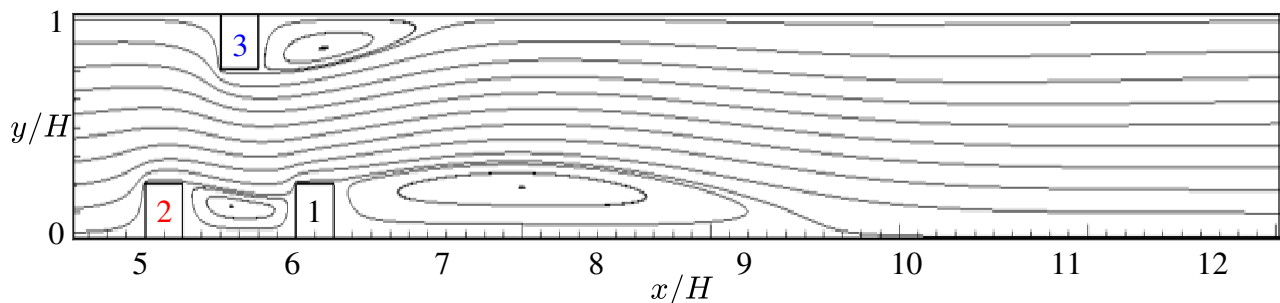


Figure 4.5: Steady-state streamlines for the 2-D channel flow with heated obstacles at $Re=400$.

temperature distributions, defined as:

$$\theta = \frac{T - T_0}{qH/\lambda_f}, \quad (4.87)$$

on the surfaces of all obstacles are also compared to reference data from [3, 186] in Fig. 4.6. Comparing the non-dimensional temperature distribution on the surfaces of the obstacles, as a function of the peripheral distance, it is observed that the proposed scheme is able to correctly model conjugate heat transfer.

4.2.2.5 Heated lid-driven cavity with variable thermo-physical properties

The next test-case is based on a classical configuration within the LBM community: The 2-D lid-driven cavity. In its isothermal form, this case consists of a rectangular domain of size $L_x \times L_y$ bounded by three static and one moving wall. In the present study, additional degrees of complexity in the form of heat transfer and variable thermo-physical properties are considered. While the temperature at the static walls is fixed at $T_c = 300K$, a temperature of $T_h = 1500K$ is enforced at the moving wall. The overall configuration of the studied case is illustrated in Fig .4.7. The specific heat capacity is temperature-dependent and defined as:

$$c_p(T) = a_1T + a_0, \quad (4.88)$$

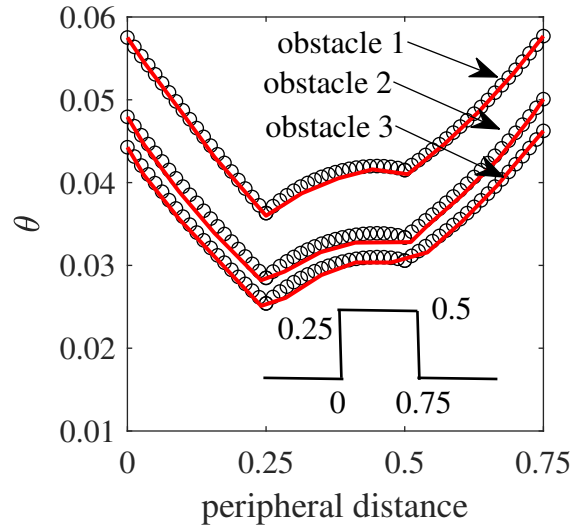


Figure 4.6: Non-dimensional temperature distribution on the surfaces of the three heated obstacles. Red plain lines represent reference data from [3] while black symbols designate results from the present work.

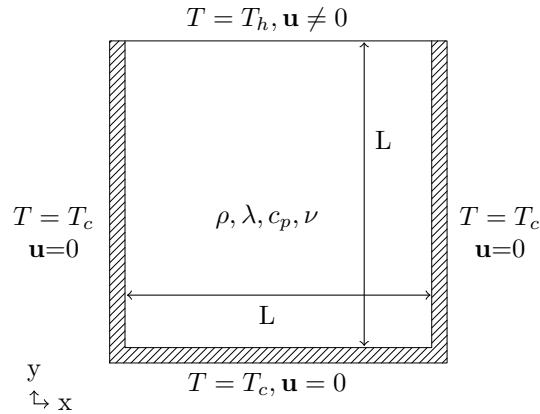


Figure 4.7: Heated lid-driven cavity configuration.

with $a_1 = 0.00187733\text{J/K}^2.\text{kg}$ and $a_0 = 1.9368\text{J/K.kg}$. The fluid thermal conductivity is computed as:

$$\lambda(T) = 8.333 \times 10^{-5}T, \quad (4.89)$$

while the kinematic viscosity is expressed as:

$$\nu(T) = 4.167 \times 10^{-5}T. \quad (4.90)$$

For the results presented here, $L_x = L_y = L = 200$ m. To validate the proposed numerical method, simulations are performed using both LB and ANSYS Fluent on a 200×200 grid, with $\delta_x = 1$ m, and steady-state results are compared. The obtained velocity and temperature profiles along the horizontal and vertical centerlines are shown in Figs. 4.8 and 4.9. As

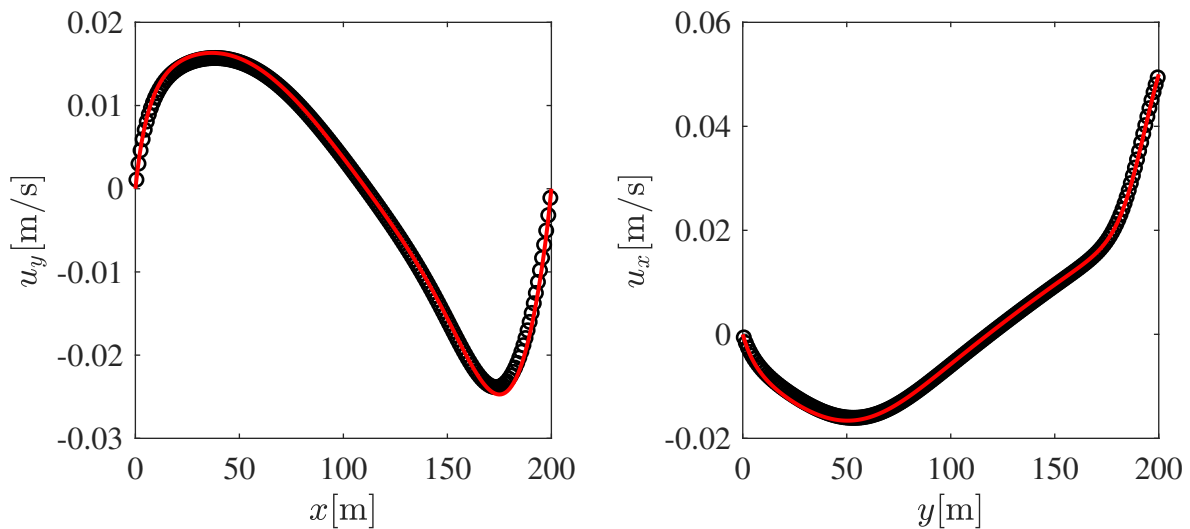


Figure 4.8: Steady-state velocity profiles along the (left) horizontal and (right) vertical centerlines, obtained using (red plain lines) Fluent and (black symbols) the LB solver.

observed in those figures, the agreement between the two schemes is excellent, putting forward the ability of the proposed solver to model thermal flows with variable thermo-physical properties.

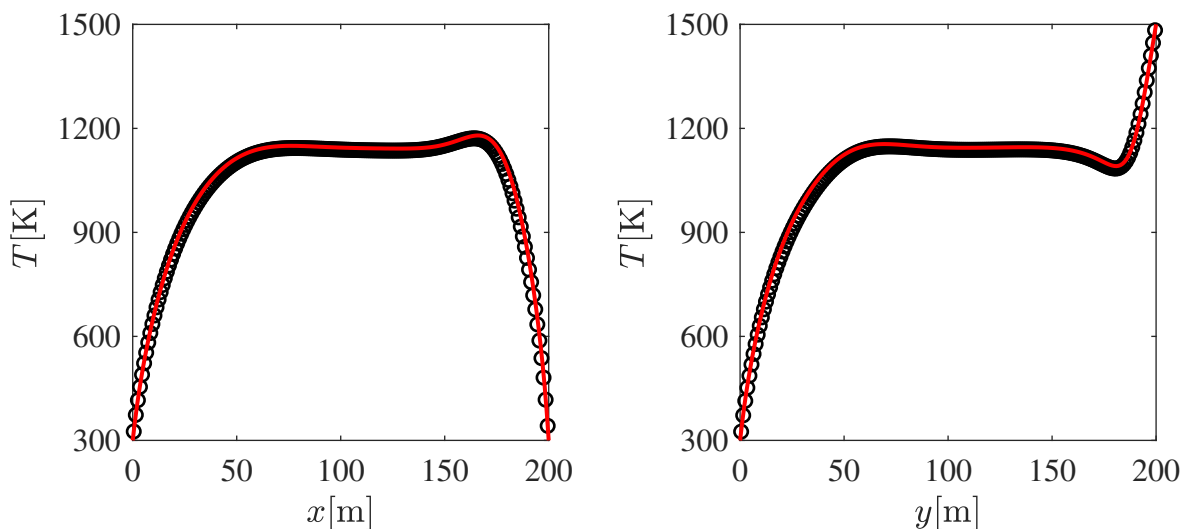


Figure 4.9: Steady-state temperature profiles along the (left) horizontal and (right) vertical centerlines, obtained using (red plain lines) Fluent and (black symbols) the LB solver.

As mentioned in the first sections, one of the advantages of more complex and dissipative collision models such as the MRT (using either raw or central moments) is the possibility to perform under-resolved simulations. To illustrate the robustness of the proposed solver in the face of under-resolved features, simulations were performed using a number of different resolutions, i.e. 200×200 , 100×100 and 50×50 . While the raw moments MRT collision

operator was used for energy, central moments were used for the flow solver. The results obtained using the three different resolutions are compared in Fig. 4.10. It is interesting

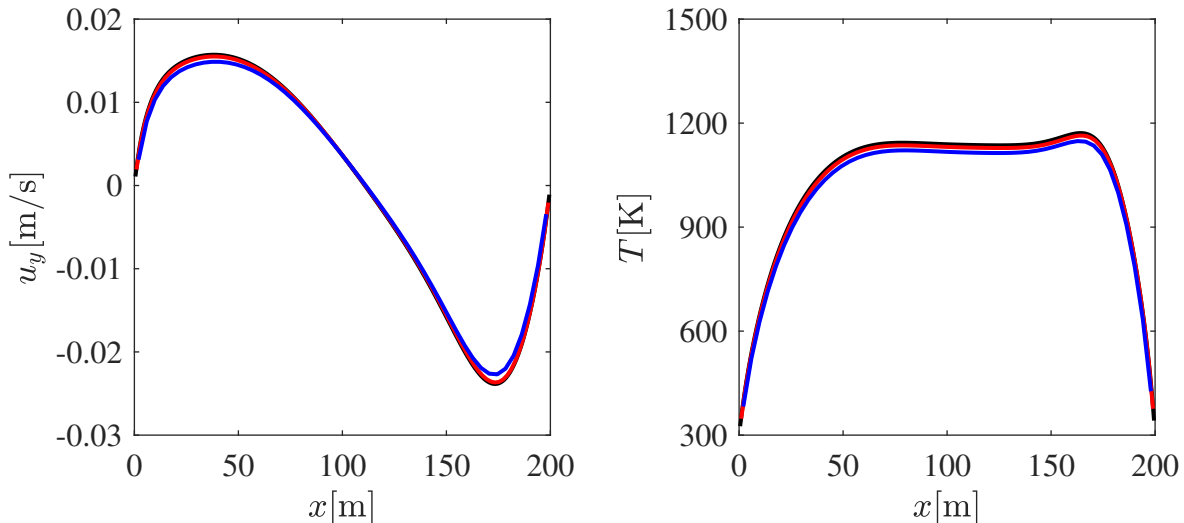


Figure 4.10: Steady-state (left) velocity and (right) temperature profiles along the horizontal centerlines at different resolutions: (in black) 200×200 , (in red) 100×100 and (in blue) 50×50 .

to observe that while a scheme relying on SRT collision operators for both fields would have resulted in numerical instabilities at low resolutions, the proposed scheme is stable. Furthermore, even at the lowest resolution, i.e. only 50 grid-points in each direction, the flow features and fields are well-captured.

4.2.2.6 Turbulent flow over a multi-layered wall-mounted cube

The last configuration studied using the proposed model for energy balance is the heated wall-mounted cube subject to a turbulent velocity field. In [5], the turbulent flow structure and surface heat transfer from a heated cube placed in a spatially periodic array of cubes mounted on one of the walls of a plane channel was studied. To better understand the physics, numerical studies on an equivalent configuration were conducted. In the numerical study, to reduce computation costs, a single heated cube of size h was mounted at the center of the bottom wall and surrounded by periodic boundary conditions (only applied to the flow field) in both span- and stream-wise directions. Given that in the original configuration none of the other cubes were heated, the energy field was subjected to constant temperature (at 293.15 K) at the inlet and zero-gradient boundary conditions at the outlet in the stream-wise direction [4]. The cube placed at the center of the bottom wall, in agreement with the experimental configuration, consisted of a smaller constant temperature cube of size $0.8h$ and temperature 348.15 K wrapped in a thin layer of epoxy of thickness $0.1h$ [4]. At the top and bottom walls adiabatic boundary conditions were imposed on the temperature field. The overall geometrical configuration is shown in Fig. 4.11. Following [4], the flow was studied at $Re_h=3854$ with $Re_h = \frac{hU_0}{\nu}$, where U_0 is the average velocity deduced from the imposed

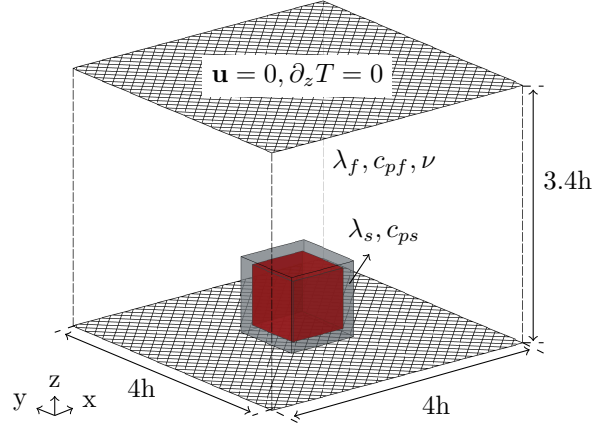


Figure 4.11: Geometrical configuration of channel flow with heated multi-layered wall-mounted obstacle.

flow rate. The physical parameters of the working fluid and epoxy are given in Tables 4.2 and 4.3.

ρ_f [kg/m ³]	λ_f [W/m.K]	c_{pf} [J/kg.K]	ν [m ² /s]
1.16	0.0257	1007.0	1.567×10^{-5}

Table 4.2: Simulation parameters for turbulent channel flow with heated obstacle: fluid properties

ρ_s kg/m ³	λ_s [W/m.K]	c_{ps} [J/kg.K]
1150	0.236	1668.5

Table 4.3: Simulation parameters for turbulent channel flow with heated obstacle: solid properties

The simulation was performed on a $600 \times 600 \times 510$ grid, leading to $\delta_x = 10^{-4}$ m. The time-step δ_t was set to 2.48×10^{-6} s, leading to $\tau = 0.51168$ and $\frac{\bar{U}_0 \delta_t}{\delta_x} = 0.1$. The flow field was modeled on a D3Q19 stencil while a D3Q7 stencil was used for the energy field. Both fields were modeled using the SRT collision operators. To maintain the flow at $Re_h=3854$, a background uniform pressure gradient was applied in the stream-wise direction. The additional pressure gradient $\vec{\nabla} \cdot p_0(t)$ to apply at each time-step was computed as as:

$$\vec{\nabla} \cdot p_0(t) = (\rho_f U_0 - \rho \bar{u}_x(t)), \quad (4.91)$$

where $\rho \bar{u}_x$ is averaged over the entire domain at each time-step. According to [4], the vortex shedding period is approximately 15000 time-steps (based on the chosen time-step size). As such after a transition period of 225,000 steps, equivalent to 15 shedding cycles average fields were taken over 25 shedding periods, equivalent to 375,000 steps. During the course

of the transition period, the diffusion coefficient of the fluid, initially set to a higher value to accelerate convergence, was changed back to its original value after 50,000 steps[4]. The simulation was initialized with a fluid at $T=293.15$ K. The simulation was carried out on 900 processing units clocked at 2.4 GHz on the Neumann cluster at the “Otto-von-Guericke” university of Magdeburg.

The flow structure is illustrated via averaged vorticity iso-surfaces in Fig. 4.12 and instantaneous velocity and temperature fields in Fig. 4.13. Looking at the overall flow structure,

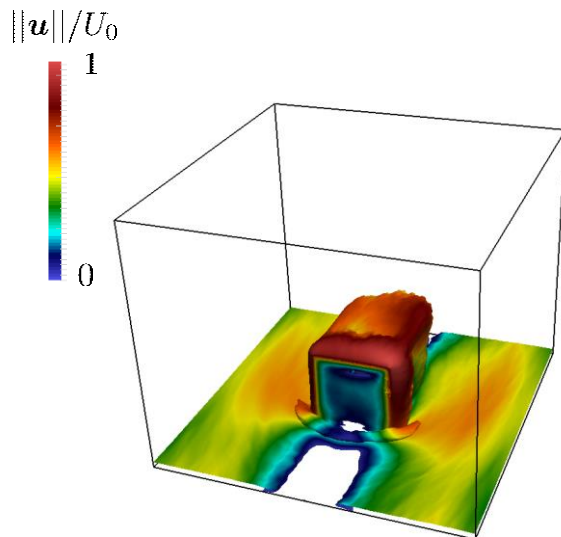


Figure 4.12: Iso-surface of the average vorticity magnitude. The iso-surface value is fixed at 3% of the maximum value

one can observe a large horseshoe-shaped re-circulating zone in front of the obstacle which is in agreement with reported results from both LES [4] and KBC [6] simulations. The turbulent velocity field is further assessed by looking at average stream-wise velocity and the stream-wise and span-wise diagonal components of the Reynolds stress tensor in Fig. 4.14. Two sets of reference data are shown with those from the present study in this figure: (a) Experimental data from [5] and LES results from [4]. While minor differences are observed, overall the results from the present study are in good agreement with the reference data. It is worth mentioning that in the LB study a maximum non-dimensional velocity of 0.15 was reached, which can affect the flow field in the form of compressibility error. Furthermore, given the use of the bounce-back boundary condition on the walls in parallel with the D3Q19 stencils and a body force, errors are to be expected close to the obstacle in the flow field [188, 189]. Furthermore, results from the present study are closer to experimental data compared to LES results in the core and near the upper wall. This might be due to the use of finer grids in the present study in those regions.

The temperature profiles on the surface of the obstacle obtained through the present study are shown in Figs. 4.15 and 4.16. In both figures, the obtained data is benchmarked against three sets of data: (a) experimental [5], (b) Large-Eddy [4] and (c) ELBM simulation [6].

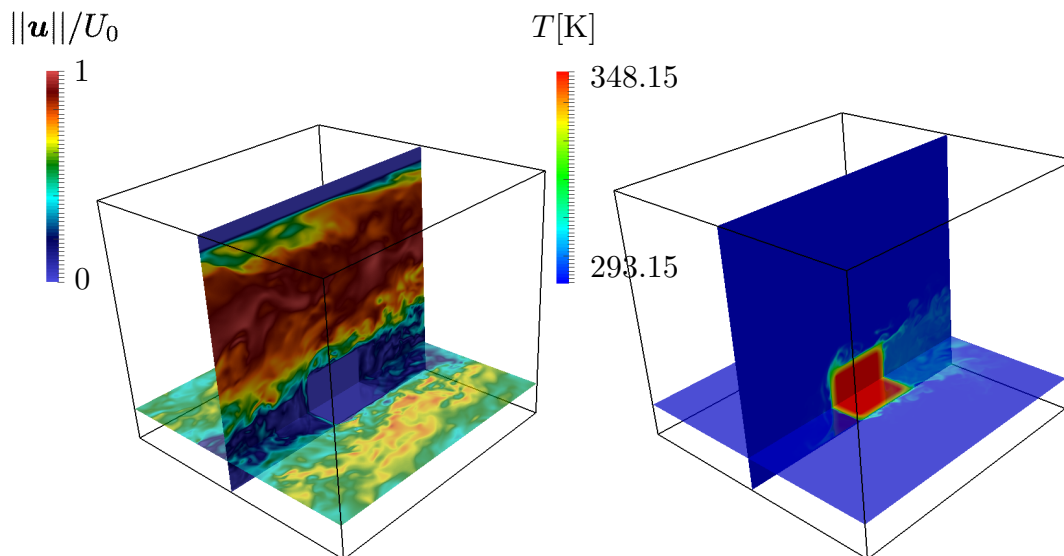


Figure 4.13: Instantaneous (left) velocity and (right) temperature fields for the turbulent channel flow with a heated obstacles.

Both figures show that the results obtained in the present study are within an acceptable range from previously reported data from either simulations or experiments. The large differences close to the bottom wall of the channel can be explained by the type of boundary condition used in the present simulation. The zero-gradient boundary condition only enforces zero-flux in the direction perpendicular to the wall, thus allowing for heat transfer on the surface of the boundary itself. This issue can be dealt with by using a full bounce-back boundary condition for the energy field.

Overall, through a variety of different test-cases, involving different levels of complexity, it was shown that the proposed scheme can properly model the energy balance equation with variable density and heat capacities. The next section will focus on proposing and validating a model for species mass balance.

4.3 Species mass balance equations

As for the previous section, first the theory behind the proposed model for species mass balance is presented. Next, the developed model is validated through a variety of test-cases.

4.3.1 Background and theory

4.3.1.1 Brief overview of the literature with a focus on low-order models

A number of multi-component models relying on the linear BGK relaxation collision operator satisfying non-negativity of density and the second law of thermodynamics have been proposed over the past decades, the most notables of which can be split in two main categories:

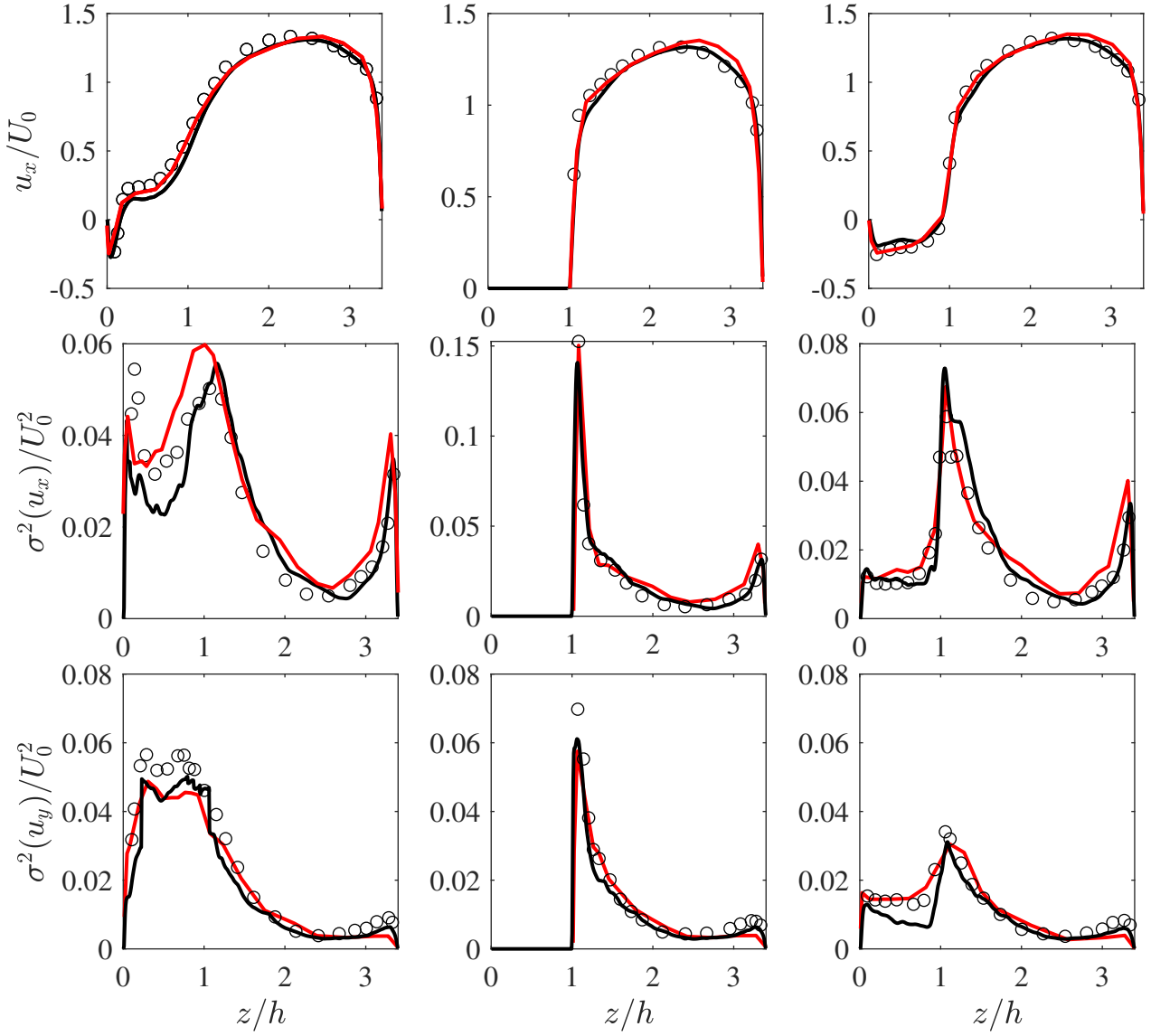


Figure 4.14: Normalized time-averaged turbulent velocity profiles along three vertical lines on the vertical plane located at $y/h=2$. From left to right: $x/h=1.2$, 1.8 and $x/h=2.8$. From top to bottom: average stream-wise velocity, stream-wise diagonal component of Reynolds stress tensor and span-wise diagonal component of Reynolds stress tensor respectively. Symbols: Black solid line: present study, red solid line: LES [4] and black symbols: experimental [5]

(a) models relying on a sum of linear BGK collision operators written as:

$$\Omega_k = \sum_{k'=1}^{N_{sp}} \frac{1}{\tau_{kk'}} \left(f_{kk'}^{(eq)} - f_k \right), \quad (4.92)$$

where Ω_k is the collision term appearing in the Boltzmann equation, f_k is the distribution function of species k and $\tau_{kk'}$ is the relaxation coefficient associated to the cross-collision of

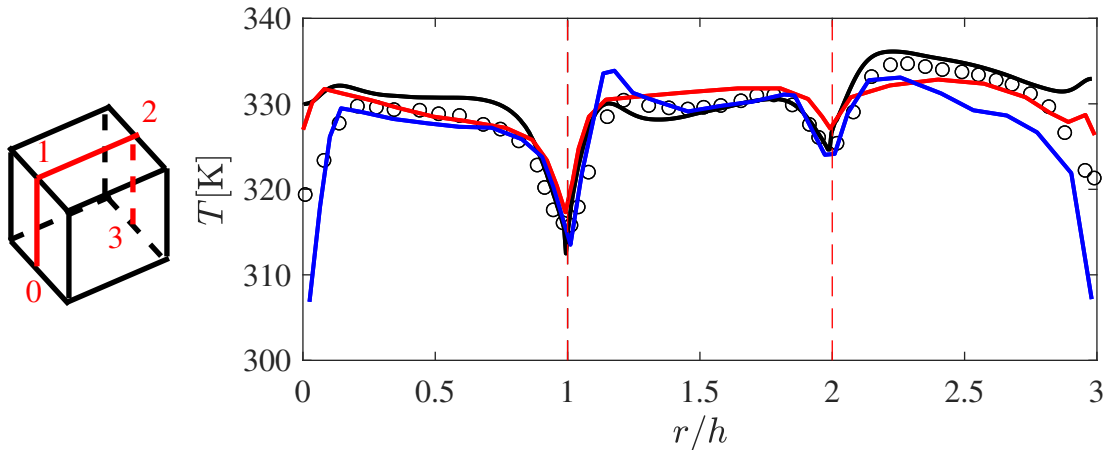


Figure 4.15: Surface temperature distribution along the 0–1–2–3 path-line on a vertical plane at $y/h=2$. Black solid line: present study, red solid line: LES [4], blue solid line: KBC [6] and black symbols: experimental [5]

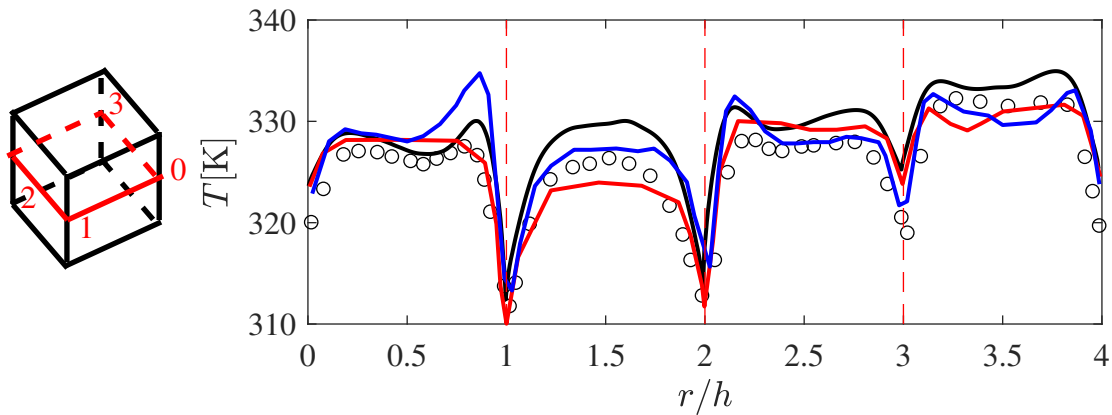


Figure 4.16: Surface temperature distribution along the 0–1–2–3–0 path-line on a horizontal plane at $z/h=0.5$. Black solid line: present study, red solid line: LES [4], blue solid line: KBC [6] and black symbols: experimental [5]

species k and k' . Each term in the summation models collision between one couple of species and $f_{kk'}^{(eq)}$ can be interpreted as pseudo-equilibria around temperature $T_{kk'}$ and velocity $\mathbf{u}_{kk'}$ defined so as to satisfy the appropriate conservation laws [190, 191].

(b) models relying on a single relaxation operator to model all collisions in the system and therefore using a general equilibrium [192, 193]. The latter have the additional property of satisfying the indifferentiability principle [193]. A number of reduced LB solvers based on these kinetic models have been developed in the past couple of years. Given that such models would require at least third-order quadratures for each species distribution function (for an isothermal flow), they are not further pursued here. Interested readers are, among other source, referred to [36, 82, 194, 195, 32, 196, 34, 197].

As for the energy balance equation, going back to the simplest model, namely the advection-

4.3. Species mass balance equations

diffusion LB scheme for species mass balance equation, it relies on an equilibrium distribution function defined as:

$$g_{\alpha,k}^{(eq)} = w_\alpha Y_k \left(1 + \frac{\mathbf{c}_\alpha \cdot \mathbf{u}}{c_s^2} + \frac{(\mathbf{c}_\alpha \cdot \mathbf{u})^2}{2c_s^4} - \frac{\mathbf{u}^2}{2c_s^2} \right), \quad (4.93)$$

where the quadratic terms can be taken out. The relaxation coefficient is also defined as:

$$\tau_k = \frac{c_s^2 D_k \delta_t}{\delta_x^2} + \frac{\delta_t}{2}. \quad (4.94)$$

Using the CE expansion, it can be easily shown that this scheme leads to the following PDE up to second-order in ε^2 :

$$\partial_t Y_k + \nabla \cdot Y_k \mathbf{u} - \nabla \cdot D_k \nabla Y_k - \nabla \cdot \frac{D_k}{c_s^2} \partial_t Y_k \mathbf{u} = \frac{M_k \dot{\omega}_k}{\rho}. \quad (4.95)$$

This form of the species mass balance is not convenient in many aspects:

- Variable density: The advection term recovered by the LB scheme is different from what it should be, i.e. $\mathbf{u} \cdot \nabla Y_k$.
- Diffusion model: The scheme recovers the generalized Fick approximation without the mass corrector. As such it is not well-suited for configurations involving non-premixed combustion, and if written for all species it does not conserve overall mass.
- The solver is only second-order accurate under diffusive scaling. Under acoustic scaling, there is an error term, i.e. last term on the LHS of Eg. 4.95, of the form $\nabla \cdot \frac{D_k}{c_s^2} \partial_t Y_k \mathbf{u}$.

Following the approach used in the first section of this chapter for the energy balance equation, a modified scheme will be proposed in the next subsection to overcome these issues.

4.3.1.2 Overcoming issues in the advection-diffusion model: advanced diffusion models and variable density

To overcome the restriction on density, and the diffusion model, let us redefine the EDF as:

$$g_{\alpha,k}^{(eq)} = w_\alpha \left[a_{0,k}^{(eq)} + \frac{1}{c_s^2} \mathcal{H}_\alpha \cdot a_{1,k}^{(eq)} + \frac{1}{2c_s^2} \sum_{i=x,y,z} \mathcal{H}_{i^2,\alpha} a_{i^2,k}^{(eq)} \right], \quad (4.96)$$

where to recover the compressible form of the balance equation with the Hirschfelder-Curtiss approximation the coefficients are set to:

$$a_{0,k}^{(eq)} = \rho_k = \rho Y_k, \quad (4.97a)$$

$$a_i^{(eq)} = \rho_k u_i, \quad (4.97b)$$

$$a_{i^2}^{(eq)} = X_k / \Gamma^{\text{ref}} - \rho_k. \quad (4.97c)$$

4.3. Species mass balance equations

Similar to the model for energy balance, to guarantee positivity of the EDF, physical parameters must be re-scaled by *reference state* parameters. As such the non-dimensional density as appearing in the EDF is defined as:

$$\rho'_k = \frac{\rho_k}{\rho^{\text{ref}}}, \quad (4.98)$$

while the mole fraction in the EDF, has been re-scaled by a reference species to average molar mass ratio, i.e. $\Gamma^{\text{ref}} = \bar{M}^{\text{ref}}/M_k$. As for the previous subsection, for the sake of readability the prime symbol will be dropped. In that case the relaxation time is defined as $\tau_k = \frac{\delta_t^2}{\delta_x^2 c_s^2} \frac{\rho D_k \Gamma}{\rho^{\text{ref}} \bar{M}/M_k} + \frac{\delta_t}{2}$. These re-definitions lead to the following positivity condition for resting populations:

$$\frac{D+1}{D} \geq \frac{\bar{M}/M_k}{\rho} \frac{\rho^{\text{ref}}}{\bar{M}^{\text{ref}}/M_k}, \quad (4.99)$$

which can be used to set the reference state. To recover the Fick approximation the coefficients must be defined as:

$$a_{0,k}^{(eq)} = \rho_k = \rho Y_k, \quad (4.100a)$$

$$a_i^{(eq)} = \rho_k u_i, \quad (4.100b)$$

$$a_{i^2}^{(eq)} = Y_k - \rho_k, \quad (4.100c)$$

and $\tau_k = \frac{\delta_t^2}{\delta_x^2 c_s^2} \frac{\rho}{\rho^{\text{ref}}} D_k + \frac{\delta_t}{2}$.

The next point is to introduce the mass corrector in the LB model; This term can readily be taken into account by introducing it into the EDF as proposed by the author in [63]. However, being a non-equilibrium effect it can also be introduced into the solver following the approach proposed for viscous heating in the previous section. Let us define the source term $\mathcal{V}_{\alpha,k}^c$ supposed to recover the correction velocity. Being tied to the non-equilibrium part of the species distribution functions it is clear that it can be expanded as:

$$\mathcal{V}_{\alpha,k}^c = \varepsilon \mathcal{V}_{\alpha,k}^{c(1)} + \varepsilon^2 \mathcal{V}_{\alpha,k}^{c(2)} + \mathcal{O}(\varepsilon^3), \quad (4.101)$$

in the context of the CE analysis. At the Euler level, taking this term into account one gets:

$$\varepsilon^1 : \partial_t^{(1)} \rho_k + \nabla^{(1)} \cdot \rho_k \mathbf{u} = \sum_{\alpha} \mathcal{V}_{\alpha,k}^{c(1)}, \quad (4.102)$$

resulting in the first constraint on $\mathcal{V}_{\alpha,k}^c$, i.e.:

$$\sum_{\alpha} \mathcal{V}_{\alpha,k}^c = 0. \quad (4.103)$$

4.3. Species mass balance equations

At the NS level the following equation is obtained after some simple algebra:

$$\varepsilon^2 : \partial_t^{(2)} \rho_k + \nabla^{(1)} \cdot \left(\frac{1}{2} - \tau_k \right) \{ \partial_t^{(1)} \rho_k \mathbf{u} + \nabla^{(1)} c_s^2 X_k \} + \nabla^{(1)} \cdot \tau_k \sum_{\alpha} \mathbf{c}_{\alpha} \mathcal{V}_{\alpha,k}^c{}^{(1)} = M_k \dot{\omega}_k^{(2)}, \quad (4.104)$$

which leads to the following restriction:

$$\sum_{\alpha} \mathbf{c}_{\alpha} \mathcal{V}_{\alpha,k}^c{}^{(1)} = \frac{Y_k}{\tau_k} \sum_{k'=1}^{N_{sp}} \frac{D_{k'} M_{k'}}{M} \nabla^{(1)} X_{k'}. \quad (4.105)$$

Considering these restriction the following expression for $\mathcal{V}_{\alpha,k}^c$ is proposed:

$$\mathcal{V}_{\alpha,k}^c = -\frac{Y_k}{\tau_k} \sum_{k'=1}^{N_{sp}} \left(1 - \frac{1}{2\tau_{k'}} \right) \left[g_{\alpha,k'} - g_{\alpha,k'}^{(eq)} \right], \quad (4.106)$$

which can be re-written as:

$$\mathcal{V}_{\alpha,k}^c = -\frac{Y_k}{\tau_k} \sum_{k'=1}^{N_{sp}} \left(\frac{1}{2} - \tau_{k'} \right) \left[g_{\alpha,k'}(\mathbf{x} + \mathbf{c}_{\alpha} \delta_t, t + \delta_t) - g_{\alpha,k'}(\mathbf{x}, t) \right]. \quad (4.107)$$

Following the same approach, an expression for the Ludwig-Soret effect can also be derived as:

$$\Theta_{\alpha,k} = \frac{\mathcal{D}_T \delta_t}{\tau_k T \delta_x^2} \left[g_{\alpha}(\mathbf{x} + \mathbf{c}_{\alpha} \delta_t, t + \delta_t) - g_{\alpha}(\mathbf{x}, t) \right]. \quad (4.108)$$

To sum up the proposed model relies on a discrete time-evolution equation defined as:

$$g_{\alpha,k}(\mathbf{x} + \mathbf{c}_{\alpha} \delta_t, t + \delta_t) - g_{\alpha,k}(\mathbf{x}, t) = \frac{\delta_t}{\tau_k} \left(g_{\alpha,k}^{(eq)}(\mathbf{x}, t) - g_{\alpha,k}(\mathbf{x}, t) \right) + \mathcal{V}_{\alpha,k}^c + \Theta_{\alpha,k} + \Phi_{\alpha,k} + \delta_t w_{\alpha} M_k \dot{\omega}_k, \quad (4.109)$$

where the expressions for the EDF and correction terms have been derived and presented respectively in Eqs. 4.96-4.100, 4.107 and 4.108. The proposed model will be used to study a variety of multi-species flows and benchmarked against reference solutions in the next subsection.

4.3.2 Validation of the proposed model

4.3.3 Hirschfelder-Curtiss diffusion: pseudo 1-D diffusion

As a first validation, pseudo 1-D pure diffusion mixing of a system consisting of three species is considered: C_6H_{14} , N_2 and H_2 . Given that large molar mass ratios can lead to unstable schemes, these species have been chosen to prove the robustness of the model. The domain is initially divided into two halves with $Y_{H_2} = 0.2$, $Y_{N_2} = 0.8$ and $Y_{C_6H_{14}} = 0$ in the bottom half and $Y_{H_2} = 0$, $Y_{N_2} = 0.8$ and $Y_{C_6H_{14}} = 0.2$ in the top half. Both boundaries (top and bottom) are set to zero-gradient. Simulations are performed using both the proposed LB scheme and

4.3. Species mass balance equations

a second-order finite-difference solver, with $\delta_x = 1 \times 10^{-3}\text{m}$ and $\delta_t = 1 \times 10^{-3}\text{s}$ on a domain of size $L = 0.1\text{m}$. For both solvers the Hirschfelder-Curtiss approximation without the mass corrector is used. The effective diffusion coefficients for species are computed as [198]:

$$D_k = \frac{1 - Y_k}{\sum_{k' \neq k} \mathcal{D}_{kk'} / Y_{k'}}, \quad (4.110)$$

where the binary diffusion coefficient are computed using Chapman and Enskog's model as [198]:

$$\mathcal{D}_{AB} = \frac{0.00266T^{3/2}}{p\sqrt{M_{AB}}\sigma_{AB}^2\Omega_{AB}}, \quad (4.111)$$

where σ_{AB} is the interaction characteristic length in Å, Ω_{AB} the dimensionless collision integral and $M_{AB} = \frac{2}{1/M_A + 1/M_B}$. The collision integral can be computed using the approximation proposed by Neufield et al. as [199, 198]:

$$\Omega_{AB} = \frac{1.06036}{k_B T / \varepsilon_{AB}^{0.1561}} + \frac{0.193}{\exp(0.47635 k_B T / \varepsilon_{AB})} + \frac{1.03587}{\exp(1.52996 k_B T / \varepsilon_{AB})} + \frac{1.76474}{\exp(1.03587 k_B T / \varepsilon_{AB})}, \quad (4.112)$$

where assuming a Lennard-Jones interaction potential:

$$\varepsilon_{AB} = \sqrt{\varepsilon_A \varepsilon_B}, \quad (4.113)$$

and:

$$\sigma_{AB} = \frac{\sigma_A + \sigma_B}{2}. \quad (4.114)$$

The list of properties needed to evaluate the binary diffusion coefficient of the considered species are given in Table 4.4.

Species	M [kg/mol]	σ [Å]	ε/k_B
C ₆ H ₁₄	0.086178	399.3	5.949
N ₂	0.028	71.4	3.798
H ₂	0.002	59.7	2.827

Table 4.4: List of properties used to evaluate binary diffusion coefficients.

Using the properties listed in Table 4.4 and assuming the mixture to be at $T = 300\text{K}$ and a pressure of 1 bar one obtains the following binary coefficients: $\mathcal{D}_{\text{H}_2-\text{N}_2} = 7.0958 \times 10^{-5}\text{m}^2/\text{s}$, $\mathcal{D}_{\text{C}_6\text{H}_{14}-\text{H}_2} = 4.52 \times 10^{-6}\text{m}^2/\text{s}$ and $\mathcal{D}_{\text{C}_6\text{H}_{14}-\text{N}_2} = 1.1277 \times 10^{-6}\text{m}^2/\text{s}$.

The simulations using both solvers were performed for 1000 time-steps. The obtained species profiles at $t=1\text{s}$ are displayed in Fig. 4.17. As observed here, the proposed scheme is able to correctly reproduce the target diffusion term, i.e. the Hirschfelder-Curtiss approximation, even in the presence of species with large molar mass discrepancies.

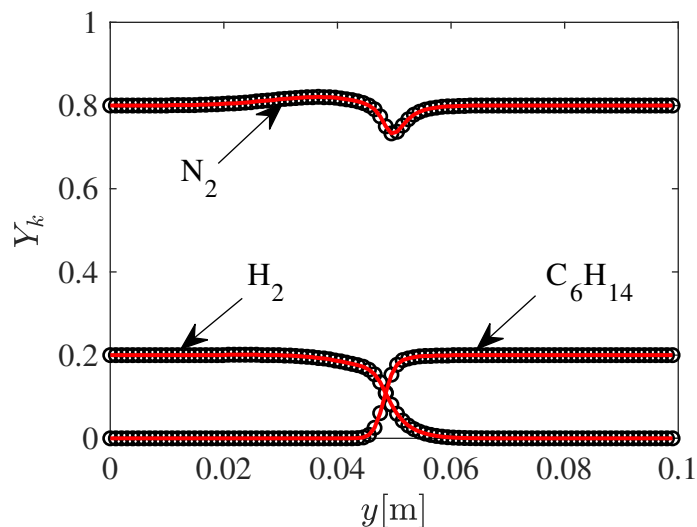


Figure 4.17: Species profiles for the $C_6H_{14}/N_2/H_2$ pure diffusion test-case at $t=1s$. Red plain lines have been obtained using a FD solver while black symbols represent results from the proposed LB solver.

4.3.4 Validation of mass corrector: 2-D counterflow Propane/air flame

To validate the mass corrector, we consider a premixed 2-D Propane/air counterflow flame under the cold flame assumption. It must be noted that by *cold flame* assumption, we refer to the fact that dilatation effects are not taken into account. The geometrical configuration is depicted in Fig. 4.18. The test-case involves two inlets with uniform velocity distribution at opposing ends of the simulation domain, denoted BC1 and BC2, and two outlets with constant pressure, perpendicular to the inlets, written BC3 and BC4. At both inlets, constant temperature and chemical composition are imposed, while at the outlets zero-gradient boundary conditions are used for both species and temperature. Following the test-case presented by Yamamoto [7], the equivalence ratio of the incoming gas mixture is set to $\phi = 0.6$. The inlet velocity, temperature and mass fractions are listed in Table 4.5.

u_{in} [m/s]	T_{in} [K]	$Y_{C_3H_8,in}$	$Y_{O_2,in}$	$Y_{N_2,in}$
0.2	300	0.037	0.2245	0.7385

Table 4.5: Imposed values at inlet boundaries for Propane/air counterflow flame.

The grid spacing and time-step have been respectively set to $\delta_x = 3.5 \times 10^{-5}$ m and $\delta_t = 1 \times 10^{-5}$ s. The initial temperature and chemical composition are set to those of the inlet boundary conditions. In order to start the reaction, at $t = 0$, in the region referred to as “reaction initiation zone” in Fig. 4.18, the initial temperature is set to 1200 K, to ignite the Propane/air mixture.

4.3. Species mass balance equations

The chemical scheme involves 5 species and a single-step global reaction defined as:



Following the case as set in [7], under the assumption of a diluted flame, the diffusion coefficients (for species, heat and momentum) differ from each other, but are taken to be constant over time and space. The list of species along with their properties are presented in Table 4.6.

Species	D [m^2/s]
C_3H_8	1.1×10^{-5}
O_2	2.1×10^{-5}
N_2	2.2×10^{-5}
H_2O	2.2×10^{-5}
CO_2	1.6×10^{-5}

Table 4.6: List of species with corresponding molecular diffusion coefficient

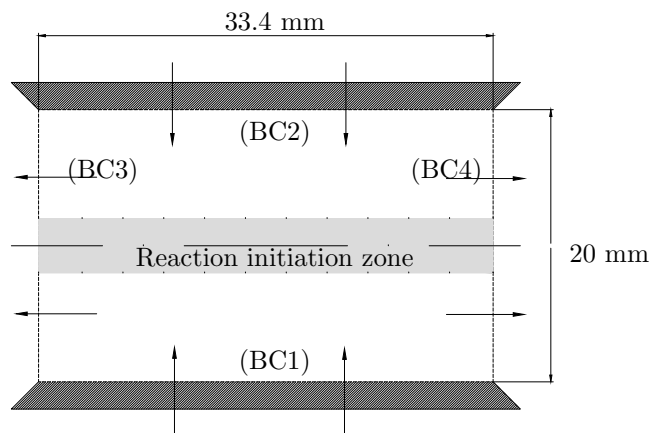


Figure 4.18: Geometrical configuration 2-D counterflow Propane/air flame.

At the beginning of the simulation, slowly dissipating pressure waves appear in the numerical domain. To accelerate convergence and dissipate acoustic waves, for the present study simple low-pass filters are used at the outflow boundaries. Details of the implemented filter along with corresponding parameters can be found in [200]. To further accelerate convergence to steady-state the simulation starts with a pre-conditioning step where only the flow field is modeled. During this phase, filtered boundary conditions are used. Once the flow field has reached a prescribed convergence level the full simulation, involving species and temperature, starts and boundary filters are turned off. The pre-conditioning phase starts with a uniform density of $1 \text{ kg}/\text{m}^3$ and zero velocity.

The steady-state velocity profiles are compared to those from [7] in Fig. 4.19. As shown

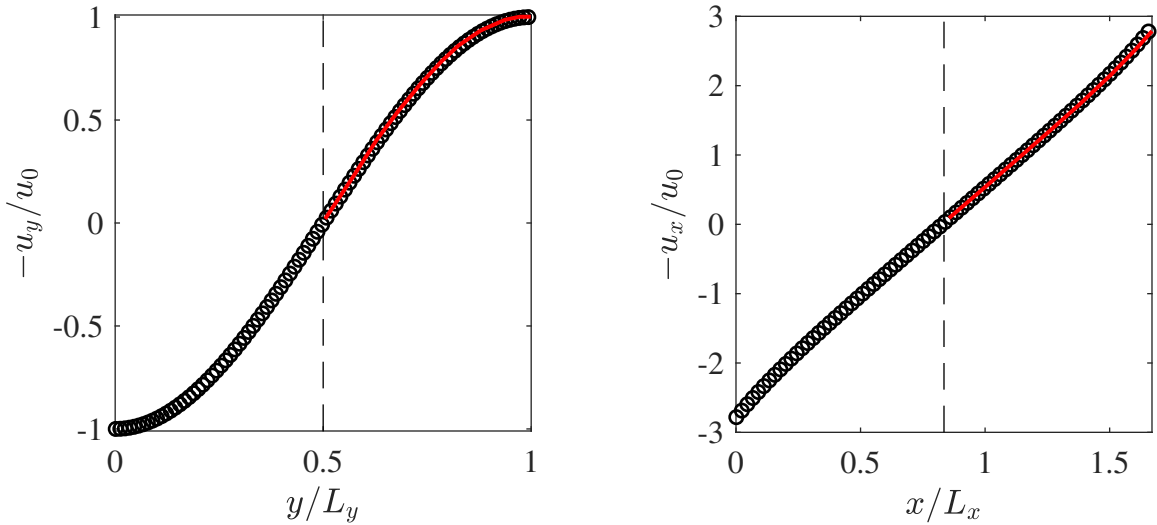


Figure 4.19: Velocity distribution along (left) vertical and (right) horizontal centerlines from (plain red line) [7] and (black symbols) current study.

in Fig. 4.19 the velocity profiles along both lines are in perfect agreement with the published data. In his study, Yamamoto solved the advection-diffusion equation only for the species involved in the reaction, meaning that all the inconsistencies stemming from both the numerical scheme and the diffusion velocity-induced non-conservation of mass were absorbed into the diluting species, i.e. N_2 . In the context of the present work, three sets of simulations were run in order to clarify the effect of each modification onto the original advection-diffusion scheme: (1) Using the original LB advection-diffusion scheme without any modification; (2) Using the original LB advection-diffusion model with the mass corrector; 3) Finally using the modified model (dilatable) taking into account the correction velocity. In all cases, the advection-diffusion equations are solved for all species, including N_2 . The species mass fraction and temperature profiles along the vertical centerline are shown in Fig. 4.20. As previously for the velocity profiles, the obtained results agree with the reference. This agreement was expected as all thermo-chemical properties employed in this case are fixed and homogeneous in space; therefore, they do not depend on local composition or temperature. Additionally, the flame is diluted, reducing the importance of density gradients and molecular diffusion. It is now interesting to look at the effect of the three different models on overall mass conservation. The total mass fraction $Y_{tot} = \sum_{k=1}^{N_{sp}} Y_k$ is plotted along the vertical centerline in Fig. 4.21 for all three approaches. As shown in Fig. 4.21, the total mass fraction in the classical AD-LB not only admits fluctuations similar to the mixture density, it is also subject to additional loss of mass at the diffusion/reaction fronts. Errors observed in areas subject to mixing can be attributed to the diffusion operator. This can be further confirmed by looking at the total mass fraction profile for the second approach, classical AD-LB with correction velocity. The two sharp minima appearing at the flame fronts are completely canceled out. Finally, the overall mass profile from the third solver introduced in this work, shows no significant deviation from the target value, 1. The overall mass loss/gain observed in the classical AD-LB model has been canceled out by using the approach presented in this

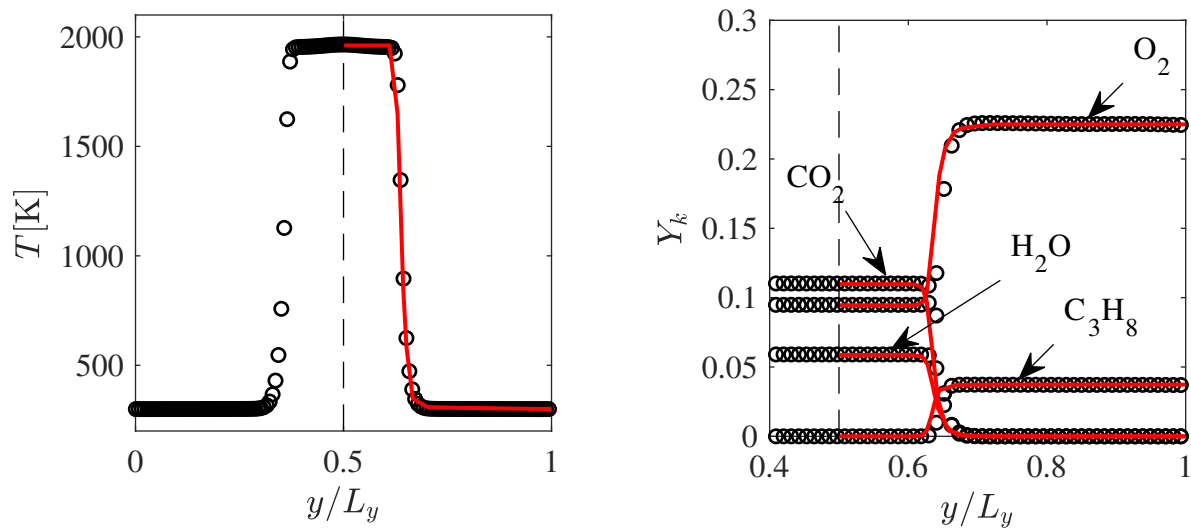


Figure 4.20: Comparison of (left) temperature and (right) species profiles along vertical centerlines from (plain red line) [7] and (black symbols) current study.

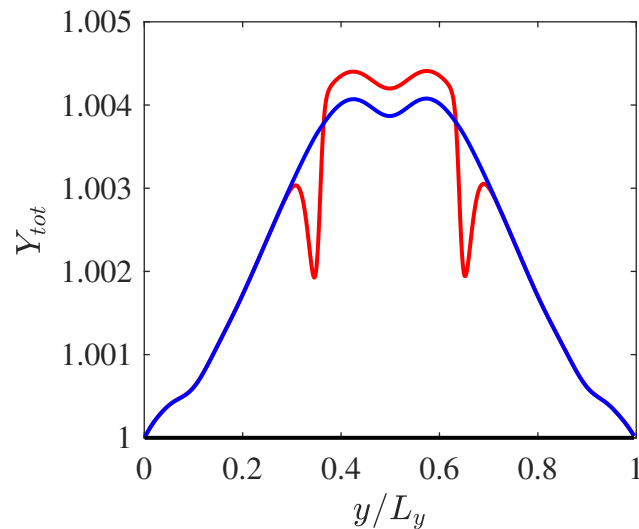


Figure 4.21: Overall mass fraction along vertical centerline obtained using (red) classical advection-diffusion formulation, (blue) classical model with mass corrector and (black) proposed model with mass corrector.

work. In this test-case, even before correction the non-conservation of mass was below 0.5 %, which can be considered to be negligible. This is partly due to the fact that the mixtures are diluted in N_2 . As previously mentioned, the inconsistency stemming from the diffusion velocity is not grid-dependent, it is mainly function of the involved species diffusion coefficients and mass fractions; the larger the discrepancies in effective diffusion coefficient the larger the non-conservation of mass. For example one would expect to have more pronounced effects for non-diluted cases, mixtures involving species with large discrepancies in binary diffusion coefficient, large temperature and/or density gradients...

4.3.5 Validation of mass corrector: 3-D counterflow non-premixed Ozone/air reacting flow

The last case studied is noticeably more complex, a 3-D counterflow non-premixed Ozone/air reacting flow. Only the modified AD-LB with the correction velocity is employed here. The detailed chemical scheme consists of 4 species (O_2 , O_3 , O and N_2) along with 18 elementary reactions. Further information can be found in [168, 1]. The list of involved reactions can be found in Appendix F. The multi-component thermo-chemical and transport properties are all computed locally using REGATH as a function of temperature, pressure and composition [201]. The geometry along with the dimensions and boundary conditions are shown in Fig. 4.22. The physical domain has been discretized using a $400 \times 400 \times 400$ grid, while the

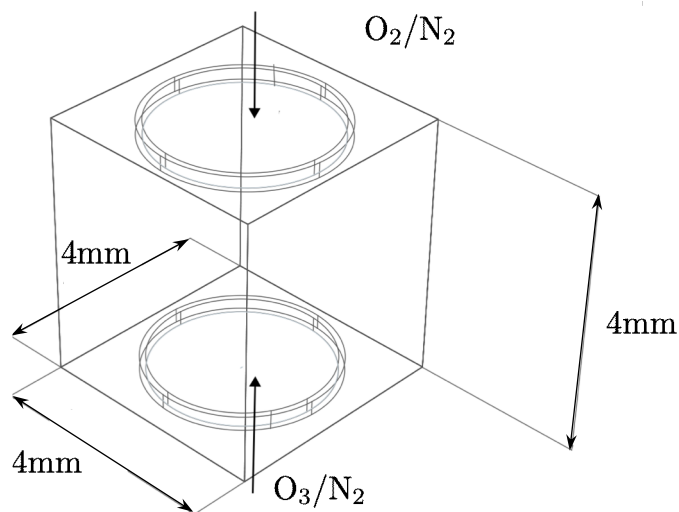


Figure 4.22: Geometrical configuration of 3-D counterflow non-premixed Ozone/air reacting flow.

time-step was set to 6×10^{-7} s. The flow field is modeled on the D3Q19 stencil, while the D3Q7 stencil is used for the temperature and species fields. Both solvers use SRT collision operators. Contrary to the flow field solver, the species solver only conserves one macroscopic property; as such a smaller number of velocities are sufficient. All boundaries are defined as constant pressure, adiabatic, and zero-gradient for the species, except for the two opposite circular inlets on the upper and lower surfaces. These two inlets are defined with constant velocity (Poiseuille distribution), temperature and composition. The values corresponding to the inlet boundaries are listed in Table 4.7.

	u_{in}^{max} [m/s]	T_{in} [K]	$Y_{O_2,in}$	$Y_{N_2,in}$	$Y_{O_3,in}$
Lower	0.3	300	0	0.767	0.233
Upper	-0.3	300	0.233	0.767	0

Table 4.7: Imposed values at inlet boundaries for the counterflow Ozone/air flow.

The simulation is repeated for both the original AD-LB and the modified model with the correction velocity. As for the previous case, the simulation starts with a pre-conditioning step. The validity of the obtained solutions is first checked by comparing the profiles along the centerline oriented in the z -axis with a reference steady-state implicit finite-difference solver, REGATH-1D. The reference solver uses the same thermo-chemical library and parameter evaluation algorithms as LB. Details of the governing equations and numerical method for the reference solver can be found in [201]. The z -component of the velocity along the vertical centerline is compared to the solution from the reference solver in Fig. 4.23. The species mass

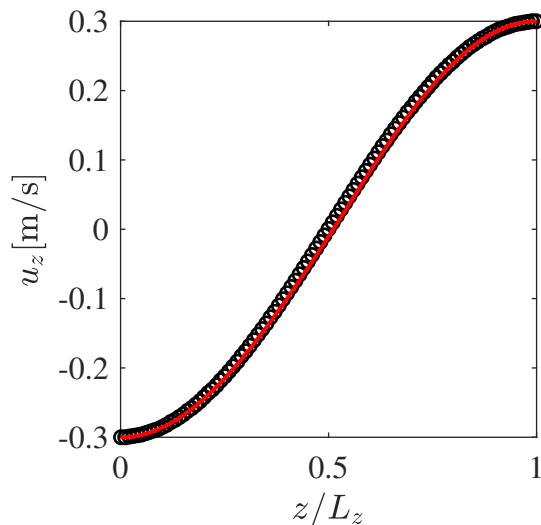


Figure 4.23: Velocity profile along vertical (z -direction) centerline from (plain red line) REGATH and (black symbols) current study.

fraction profiles are shown in Fig. 4.24. These figures demonstrate that the LB solver recovers the solution from the reference finite-difference solver. To demonstrate the effectiveness of the proposed formulation in dealing with the non-conservation of mass, even in cases involving variable diffusion coefficients, the total mass $Y_{tot} = \sum_{k=1}^{N_{sp}} Y_k$ obtained with classical AD-LB (without correction velocity) and with our improved formulation (including correction velocity and releasing the incompressibility assumption) are compared in Fig. 4.25. As seen in Fig. 4.25, the improved formulation proposed in this work is able to conserve total mass much better than the standard approach, although mass loss/gain were small even before correction. As previously stated, this effect becomes much more pronounced in non-diluted mixtures and flows subject to large variations in temperature and/or density.

4.4 Final remarks

During the course of this chapter, a number of modified LB schemes based on the advection-diffusion formulation, only conserving the zeroth-order moment, appropriate for energy and species balance equations with variable thermo-physical properties were derived. Furthermore, expressions for higher-order coupling terms such as the Ludwig-Soret effect or viscous

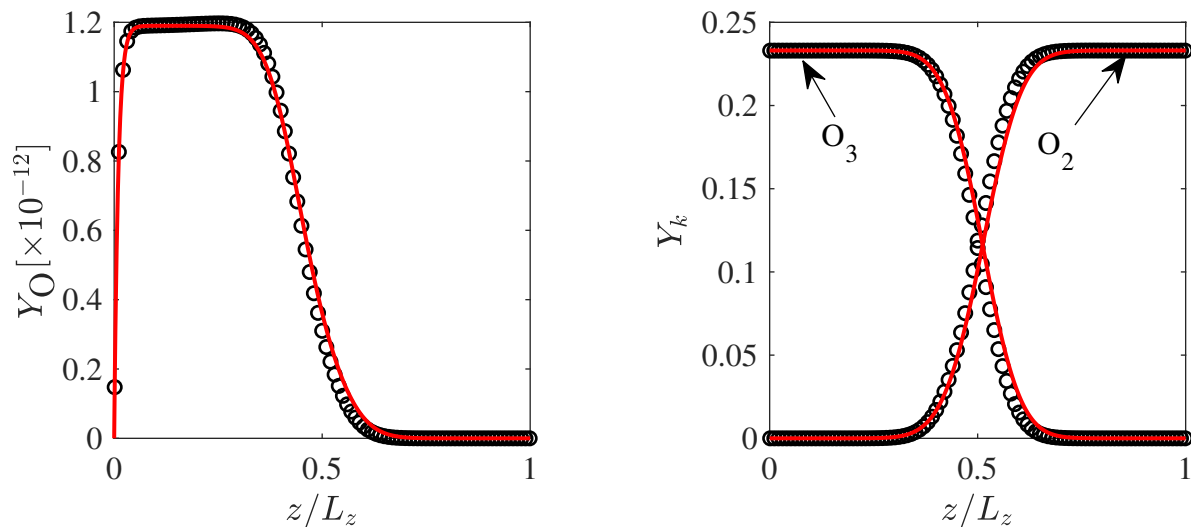


Figure 4.24: Species profiles along vertical (z -direction) centerline from (plain red line) RE-GATH and (black symbols) current study.

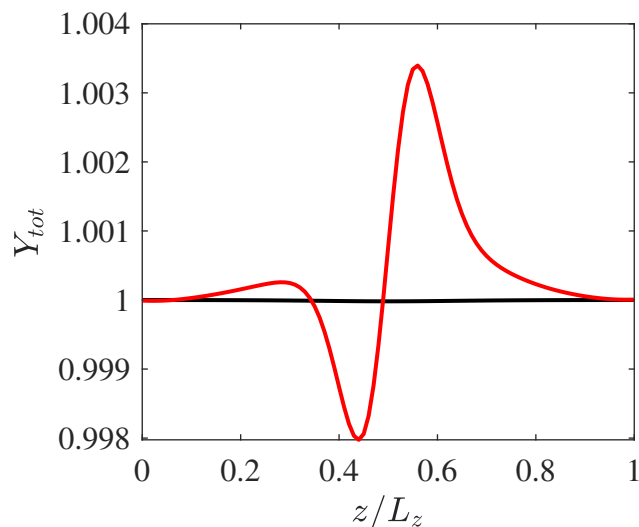


Figure 4.25: Overall mass fraction along vertical (z -direction) centerline with (red) classical AD-LB and (black) the proposed model.

dissipation heating were derived and validated. It was shown that the proposed models, which can be interpreted as DNS for the target macroscopic equations, were able to recover the proper physics while relying on reduced stencils, i.e. D2Q5 in 2-D and D3Q7 in 3-D. Furthermore, to reduce errors coming from higher-order moments and extend the stability domain of the solvers, appropriate non-dimensionalization schemes and corresponding MRT formulations were given.

Now that appropriate solvers for the energy and species mass balance equations have been proposed and validated, the next chapter will focus on introducing dilatation/compressibility effects into the flow solver.

Chapter 5

Thermo-compressibility on standard stencils

Contents

5.1	Beyond Boussinesq: Low Mach number approximation	105
5.1.1	Model formalism	105
5.1.1.1	Decoupling of density: introducing hydrodynamic pressure	106
5.1.1.2	Introducing thermo-compressibility: Evaluation of velocity divergence	107
5.1.1.3	Space and time-discretized equations	108
5.1.2	Validation and numerical application	109
5.1.2.1	Natural convection in a 2-D heated cavity with large temperature ratios	109
5.1.2.2	Three-dimensional thermo-compressible Taylor-Green vortex with species	111
5.2	Implicit approach: Thermal discrete equilibrium	114
5.2.1	Equilibrium distribution function: Thermal Hermite expansion . .	115
5.2.2	Chapman-Enskog analysis	115
5.2.3	Further extension of stability domain: temperature-scaled central moments	117
5.2.4	Validation and numerical application	118
5.2.5	Galilean invariance: sound speed, acoustic and shear wave dissipation rate	119
5.2.5.1	Low Mach number viscous 1-D Sod shock tube	121
5.3	Spectral analysis of the implicit scheme	123
5.3.1	Effect of EDF order	123
5.3.2	Advanced collision model: effect of regularization	124

5.3.3	Central moments MRT versus temperature-scaled central moments	124
5.3.4	Effect of correction term	126
5.4	Concluding remarks	127

Disclaimer

Part of this chapter has been published in:

[1] S.A. Hosseini, N. Darabiha, and D. Thévenin. Compressibility in lattice Boltzmann on standard stencils : effects of deviation from reference temperature, Phil. Trans. A.

The classical LB solver of chapter 3 was derived assuming an isothermal flow and as such is unable to reproduce dilatation effects. The aim of the present chapter is to introduce these effects into the solver in order to model flames without the cold flame assumption. Two different approaches will be introduced and analyzed in this chapter: (a) A model similar to the low Mach number approximation used in classical combustion simulations and (b) a compressible formulation based on the extension of the Hermite expansion to thermal flows. Both of the considered models rely on standard first-neighbor stencils and are intended for low Mach flows.

5.1 Beyond Boussinesq: Low Mach number approximation

5.1.1 Model formalism

The idea behind the zero-Mach limit formulation of the compressible fluid system of equations consists of operating a multi-scale perturbation analysis as a function of the Mach number. This in turn decouples the flow from acoustics and can allow for much larger time-steps. Considering a low Mach number flow, the different independent variables governing the fluid flow are expanded in terms of the Mach number (a very small parameter) [202]:

$$p = p^{(0)} + \text{Ma } p^{(1)} + \text{Ma}^2 p^{(2)} + \mathcal{O}(\text{Ma}^3), \quad (5.1a)$$

$$\mathbf{u} = \mathbf{u}^{(0)} + \text{Ma } \mathbf{u}^{(1)} + \mathcal{O}(\text{Ma}^2), \quad (5.1b)$$

$$\rho = \rho^{(0)} + \text{Ma } \rho^{(1)} + \mathcal{O}(\text{Ma}^2), \quad (5.1c)$$

$$T = T^{(0)} + \text{Ma } T^{(1)} + \mathcal{O}(\text{Ma}^2). \quad (5.1d)$$

Upon introduction of these expansions into the PDEs one finds the following equations at order zero:

$$\nabla p^{(0)} = 0, \quad (5.2a)$$

$$\partial_t \rho^{(0)} + \nabla \cdot \rho^{(0)} \mathbf{u}^{(0)} = 0, \quad (5.2b)$$

$$\begin{aligned} & \partial_t \rho^{(0)} \mathbf{u}^{(0)} + \nabla \cdot \rho^{(0)} \mathbf{u}^{(0)} \otimes \mathbf{u}^{(0)} + \nabla p^{(1)} \\ & - \nabla \cdot \mu \left(\nabla \otimes \mathbf{u}^{(0)} + \nabla \otimes \mathbf{u}^{(0)T} - \frac{2}{3} \nabla \mathbf{u}^{(0)} \mathbf{I} \right) = 0 \end{aligned} \quad (5.2c)$$

$$p^{(0)} = \rho^{(0)} \bar{r} T^{(0)}, \quad (5.2d)$$

where $p^{(0)}$ is the thermodynamic pressure, uniformly distributed in space, and $p^{(1)}$ the hydrodynamic pressure admitting fluctuations in time and space. In practice, the acoustics are filtered by operating a Helmholtz-Hodge decomposition of the velocity vector field into a solenoidal and irrotational field. Reconstruction of purely hydrodynamic effects through a divergence-free velocity field allows to filter out acoustic effects while the second component of the decomposition (non-solenoidal field) introduces dilatation effects. The fluid density

is determined through the EoS and the uniform thermodynamic pressure. The aim of the next section is to propose a LB-based model capable to represent this low Mach number formulation.

5.1.1.1 Decoupling of density: introducing hydrodynamic pressure

Over the past score years, a number of attempts have been made at developing models for combustion simulation based (partially or entirely) on LB solvers. A number of these models based their developments on low Mach (decoupled) formulations [37, 38, 43]. However none of these proposed models have gone beyond simple steady configurations. The present part of the thesis will introduce a pressure/density decoupling approach initially developed for simulation of multi-phase flows with large density ratios, see for instance [203, 204]. This formulation was later extended and used (under different assumptions) for 2-D thermo-compressible flows in [48, 205, 206]. The main idea behind the development of a LB-based solver for thermo-compressible flows, following the previously introduced philosophy of low Mach formulations is to decouple the flow density from velocity and hydrodynamic pressure space fluctuations. To achieve this decoupling, and given that the *thermodynamic* pressure tied to density through the EoS, equal to $p = \rho c_s^2$ in the LBM, is assumed to be uniform in space, the first step is to introduce a *hydrodynamic* pressure independent from the local density, at the Euler level. This is achieved by introducing a body force defined as [44]:

$$\mathbf{F} = \nabla \rho c_s^2 - \nabla p_h + \mathbf{F}_b, \quad (5.3)$$

where \mathbf{F}_b designates other external body forces such as gravity. While this body force modifies the pressure term at the Euler level, it does not eliminate the velocity-dependence of the local fluid density; Furthermore, since the hydrodynamic pressure does not appear in the Boltzmann equation (except in the introduced body force), it needs closure. To recover the hydrodynamic pressure as the zeroth-order moment and completely decouple the flow density from hydrodynamics the following new distribution function is introduced:

$$g'_\alpha = c_s^2 f_\alpha + w_\alpha (p_h - \rho c_s^2). \quad (5.4)$$

It can readily be observed that the zeroth-order moment of this new distribution function is p_h . Introducing this new distribution back into Boltzmann's equation the following continuous time-evolution PDE is obtained:

$$\begin{aligned} \partial_t g'_\alpha + \mathbf{c}_\alpha \cdot \nabla g'_\alpha = & \frac{1}{\tau} \left(g_\alpha^{(eq)'} - g'_\alpha \right) + w_\alpha (\partial_t p_h + \mathbf{c}_\alpha \cdot \nabla p_h) \\ & - w_\alpha c_s^2 (\partial_t \rho + \mathbf{c}_\alpha \cdot \nabla \rho) - \mathbf{F} \cdot \nabla_{\mathbf{c}_\alpha} f_\alpha, \end{aligned} \quad (5.5)$$

where $\partial_t \rho + \mathbf{c}_\alpha \cdot \nabla \rho$ can be re-written using the continuity equation as:

$$\partial_t \rho + \mathbf{c}_\alpha \cdot \nabla \rho = (\mathbf{c}_\alpha - \mathbf{u}) \cdot \nabla \rho - \rho \nabla \cdot \mathbf{u}. \quad (5.6)$$

Furthermore, the last term on the RHS of Eq. 5.5 can be approximated as [204]:

$$\mathbf{F} \cdot \nabla_{\mathbf{c}_\alpha} f_\alpha = -\mathbf{F} \cdot \frac{\mathbf{c}_\alpha - \mathbf{u}}{\rho c_s^2} f_\alpha^{(eq)}, \quad (5.7)$$

and terms of the form $\partial_t p_h$ and $\mathbf{u}^j \cdot \nabla p_h$, with $j \geq 1$, can be neglected as they are third-order in non-dimensional velocity. Eventually, before discretization in space and time the following PDE is recovered:

$$\begin{aligned} \partial_t g'_\alpha + \mathbf{c}_\alpha \cdot \nabla g'_\alpha = & \frac{1}{\tau} \left(g_\alpha^{(eq)'} - g'_\alpha \right) + c_s^2 \left(\frac{f_\alpha^{(eq)}}{\rho} - w_\alpha \right) (\mathbf{c}_\alpha - \mathbf{u}) \cdot \nabla \rho + w_\alpha c_s^2 \rho \nabla \cdot \mathbf{u} \\ & + \mathbf{F}_b \cdot (\mathbf{c}_\alpha - \mathbf{u}) \frac{f_\alpha^{(eq)}}{\rho}. \end{aligned} \quad (5.8)$$

5.1.1.2 Introducing thermo-compressibility: Evaluation of velocity divergence

The previously introduced formalism decoupled the density from the flow field, i.e. velocity and hydrodynamic pressure field. However, it also eliminated the implicit equation of state in the original LB formulation. Furthermore, the zeroth-order moment of the distribution function being the hydrodynamic pressure, the continuity equation is not imposed in the model anymore. Following the original low Mach formulation, the density is now computed using the thermodynamic pressure, local temperature and EoS as:

$$\rho = \frac{p_{th}}{\bar{r}T}. \quad (5.9)$$

Furthermore, for the model to satisfy the continuity equation, it is used to evaluate the velocity divergence appearing in Eq. 5.8 as:

$$\nabla \cdot \mathbf{u} = -\frac{\partial_t \rho + \mathbf{u} \cdot \nabla \rho}{\rho}, \quad (5.10)$$

and further developed using the EoS as:

$$\nabla \cdot \mathbf{u} = -\frac{\partial_t p_{th} + \mathbf{u} \cdot \nabla p_{th}}{p_{th}} - \frac{\partial_t \frac{1}{T} + \mathbf{u} \cdot \nabla \frac{1}{T}}{\frac{1}{T}} - \frac{\partial_t \frac{1}{\bar{r}} + \mathbf{u} \cdot \nabla \frac{1}{\bar{r}}}{\frac{1}{\bar{r}}}. \quad (5.11)$$

The space-derivative of p_{th} cancels out as it is assumed to be uniform. Furthermore the second term on the LHS can be re-written as:

$$-\frac{\partial_t \frac{1}{T} + \mathbf{u} \cdot \nabla \frac{1}{T}}{\frac{1}{T}} = \frac{\partial_t T + \mathbf{u} \cdot \nabla T}{T}, \quad (5.12)$$

while the third one is readily developed as:

$$-\frac{\partial_t \frac{1}{\bar{r}} + \mathbf{u} \cdot \nabla \frac{1}{\bar{r}}}{\frac{1}{\bar{r}}} = \sum_{k=1}^{N_{sp}} \frac{\bar{M}}{M_k} (\partial_t Y_k + \mathbf{u} \cdot \nabla Y_k), \quad (5.13)$$

where we have used $\bar{r} = \mathcal{R} \sum_{k=1}^{N_{sp}} Y_k / M_k$. Putting all these terms back together one gets:

$$\nabla \cdot \mathbf{u} = -\frac{\partial_t p_{th}}{p_{th}} + \frac{\partial_t T + \mathbf{u} \cdot \nabla T}{T} + \sum_{k=1}^{N_{sp}} \frac{\bar{M}}{M_k} (\partial_t Y_k + \mathbf{u} \cdot \nabla Y_k), \quad (5.14)$$

for a multi-species flow. The previous equation along with Eqs. 5.8 and 5.10 and:

$$\sum_{\alpha} g_{\alpha} = p_h, \quad (5.15a)$$

$$\sum_{\alpha} \mathbf{c}_{\alpha} g_{\alpha} = \rho c_s^2 \mathbf{u}, \quad (5.15b)$$

constitute the main equations for the LB-based low Mach model for thermo-compressible flows.

Using the CE formalism introduced in subsection 3.1.1, it can readily be observed that at order ε^1 the following PDE is recovered for the hydrodynamic pressure:

$$\frac{1}{\rho c_s^2} \partial_t^{(1)} p_h + \nabla^{(1)} \cdot \mathbf{u} = -\frac{\partial_t^{(1)} p_{th}}{p_{th}} + \frac{\partial_t^{(1)} T + \mathbf{u} \cdot \nabla^{(1)} T}{T} + \sum_{k=1}^{N_{sp}} \frac{\bar{M}}{M_k} \left(\partial_t^{(1)} Y_k + \mathbf{u} \cdot \nabla^{(1)} Y_k \right). \quad (5.16)$$

While this LB-based low Mach formulation does not exactly impose the intended velocity divergence, the error term $\frac{1}{\rho c_s^2} \partial_t^{(1)} p_h$ is of order $\mathcal{O}\left(\frac{u^3}{(\delta_x / \delta_t)^3}\right)$ and therefore negligible for small non-dimensional velocities. This argument is further comforted by the restrictive CFL condition on different collision operators (especially SRT) in the limit of vanishing non-dimensional viscosities (relaxation coefficients).

5.1.1.3 Space and time-discretized equations

Given that the space discretization process relying on integration along characteristic lines has been thoroughly detailed in subsection 2.4.2 for the classical LB formulation, re-deriving the discrete equations for the previously-introduced model would be redundant. As such only the final equations are given here. The discrete collision-streaming equation for the new distribution function is:

$$\begin{aligned} g'_{\alpha}(\mathbf{x} + \mathbf{c}_{\alpha} \delta_t, t + \delta_t) - g'_{\alpha}(\mathbf{x}, t) &= \frac{\delta_t}{\tau} \left(g^{(eq)'}_{\alpha}(\mathbf{x}, t) - g'_{\alpha}(\mathbf{x}, t) \right) + \left(1 - \frac{\delta_t}{2\tau} \right) w_{\alpha} c_s^2 \rho \nabla \cdot \mathbf{u} \\ &+ \left(1 - \frac{\delta_t}{2\tau} \right) (\mathbf{c}_{\alpha} - \mathbf{u}) \left(\frac{f_{\alpha}^{(eq)}}{\rho} - w_{\alpha} \right) c_s^2 \nabla \rho + F_{\alpha,b}, \end{aligned} \quad (5.17)$$

where we have dropped the overbar of the post-discretization distribution function for the sake of simplicity and $F_{\alpha,b}$ is the contribution of the external body forces, e.g. gravity, which can be evaluated through anyone of the available LB forcing schemes. It is interesting to note that apart from the presence of species, the model as used here is different from those proposed in [48, 205] as it includes a factor $1 - \frac{\delta_t}{2\tau}$. The absence of this factor, also needed for the correction term of the compressible scheme in the next section, leads to serious stability issues. The moments of the distribution function are defined as:

$$\sum_{\alpha} g_{\alpha} = p_h - \frac{c_s^2 \delta_t}{2} (\rho \nabla \cdot \mathbf{u} + \mathbf{u} \cdot \nabla \rho), \quad (5.18a)$$

$$\sum_{\alpha} \mathbf{c}_{\alpha} g_{\alpha} = \rho c_s^2 \mathbf{u} - \frac{c_s^2 \delta_t}{2} \mathbf{F}_b. \quad (5.18b)$$

It is also worth mentioning that this formulation where the temperature is defined through the EoS, which would need the local temperature and composition, can not be used in combination with solvers for the conservative form of the energy and species mass balance equations with explicit coupling. Given that in the conservative form extensive forms of variables are transported, to get to the intensive parameters one needs the local density. The local density on the other hand in this low Mach formulation is unknown and determined through the EoS and local intensive variables, i.e. temperature and mass fractions. Therefore, to only correct way to couple these two solvers is implicit, and involves an iterative solver. As such for the remainder of this study, the low Mach formulation is always used in combination with a finite-difference solver for the non-conservative form of the energy and species balance equations. Furthermore, given that in this model the thermodynamic pressure is supposed to be uniform in space, for energy balance, the sensible enthalpy formulation is used and the space gradient of pressure is set to zero.

5.1.2 Validation and numerical application

To showcase the ability of the scheme to capture thermo-compressibility effects and its robustness in the face of under-resolved simulations, it is now used to model two different test-cases involving 2 and 3-D flows.

5.1.2.1 Natural convection in a 2-D heated cavity with large temperature ratios

As a natural candidate for the validation of thermo-compressibility effects in the low Mach number model and proper coupling with the temperature field, natural convection in a heated 2-D cavity is studied here. Different from configurations studied using incompressible solvers supplemented with the Boussinesq force, the cases studied here involve large temperature variations and as such do not fall in the validity domain of the Boussinesq approximation. This test-case involves a rectangular domain of size $L \times L$, surrounded with static walls. The top and bottom walls are insulators and therefore modeled using zero-flux boundary conditions while the left and right walls are maintained at constant temperatures, respectively $T_h = 960\text{K}$ and $T_c = 240\text{K}$. Given the large variations in temperature, temperature-

dependence of the fluid viscosity is taken into account via Sutherland's correlation:

$$\mu(T) = \mu(T^*) \left(\frac{T}{T^*} \right)^{3/2} \frac{T^* + S}{T + S}, \quad (5.19)$$

where $S = 110.5\text{K}$, $T^* = 273\text{K}$ and $\mu(T^*) = 1.68 \times 10^{-5}\text{kg/m.s}$. The dynamics of this flow are governed by one non-dimensional number, namely the Rayleigh number defined as:

$$\text{Ra} = \frac{\text{Pr}g\rho_0^2(T_h - T_c)L^3}{\mu_0^2T_0}, \quad (5.20)$$

where $g = 9.81\text{m/s}^2$, $\text{Pr}=0.71$, T_0 is the reference temperature set to $T_0 = \frac{T_h+T_c}{2} = 600\text{K}$, and ρ_0 and μ_0 are the density and dynamic viscosities at this temperature. This configuration has been extensively studied for a wide range of Ra numbers in [8] and used for validation in a large number of models, e.g. [177, 146, 207, 48]. For the present validation, two different Rayleigh numbers are modeled: 10^4 and 10^6 . In both cases, the simulations are performed on a 100×100 domain. Ra number, reference temperature, left and right wall temperature, gravity and Pr number are kept constant while the domain size is modified. At $\text{Ra}=10^4$, δ_x is set to $1.4454 \times 10^{-4}\text{m}$ and δ_t to 10^{-5}s while for $\text{Ra}=10^6$, δ_x and δ_t are respectively set to 6.7067×10^{-4} and $5 \times 10^{-5}\text{s}$. The steady-state non-dimensional velocity profiles along the horizontal and vertical centerlines are compared to reference values from [8] in Fig. 5.1. The

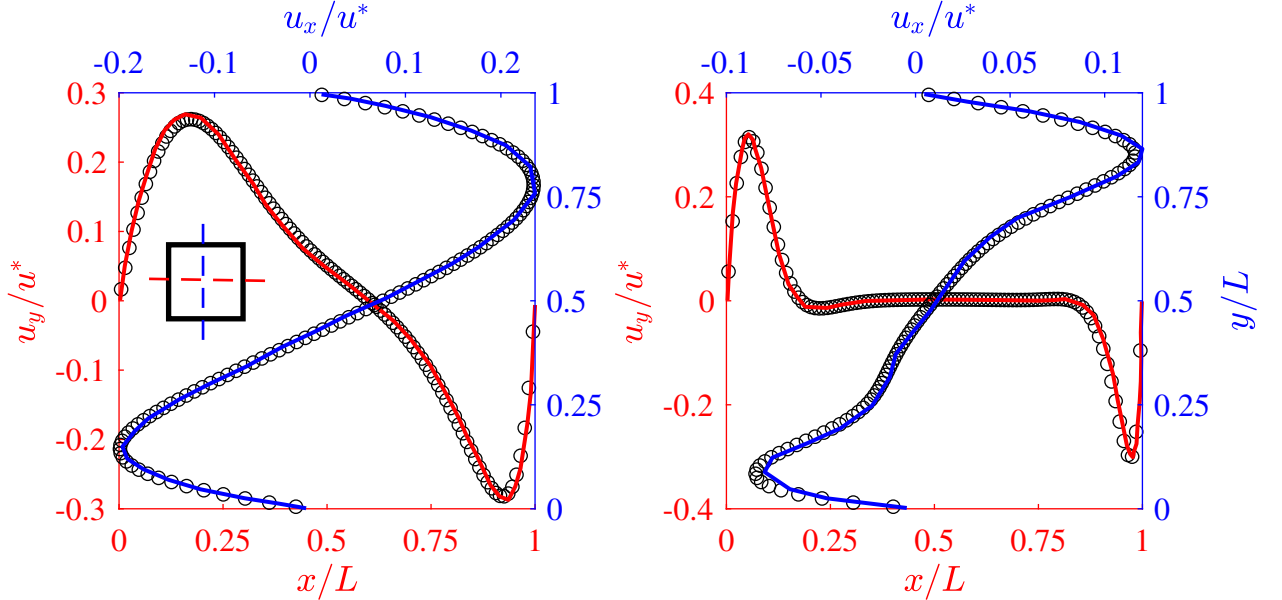


Figure 5.1: Steady-state velocity profiles along the (red) horizontal and (blue) vertical centerlines for (left) $\text{Ra}=10^4$ and (right) $\text{Ra}=10^6$ obtained from (red and blue plain lines) [8] and (black symbols) the LB solver.

velocities are non-dimensionalized using a characteristic velocity defined as:

$$u^* = \frac{\mu_0 \sqrt{\text{Ra}}}{\rho_0 L}. \quad (5.21)$$

Furthermore, the temperature distribution along three horizontal lines at $y/L = 0, 0.5$ and 1 are shown in Fig. 5.2. All data are in excellent agreement with the reference solutions. To

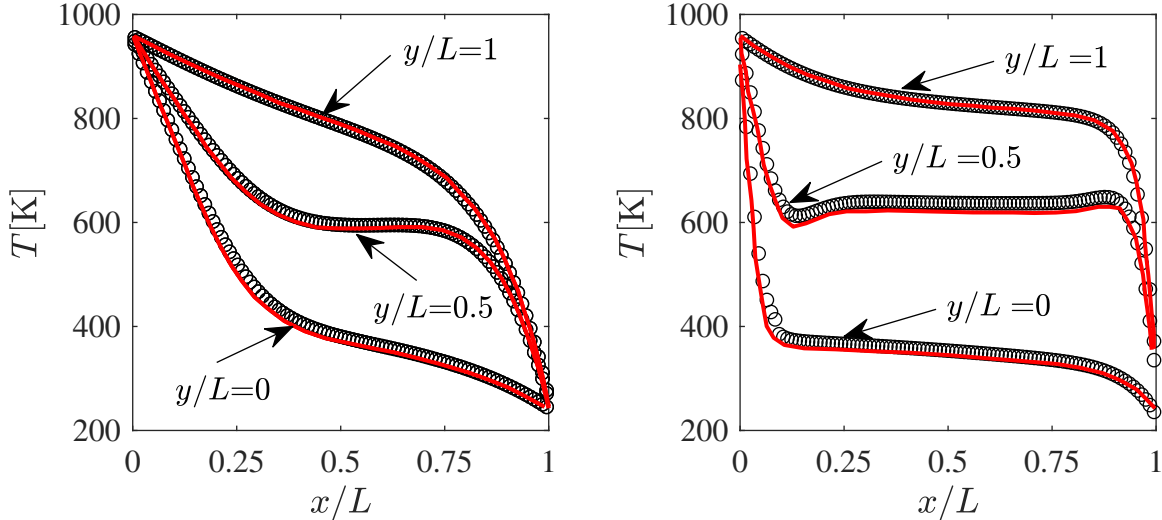


Figure 5.2: Steady-state temperature profiles along three horizontal lines for (left) $\text{Ra}=10^4$ and (right) $\text{Ra}=10^6$ obtained from (red plain lines) [8] and (black symbols) the LB solver.

better illustrate the flow structure, the temperature field along with iso-contours for both studied configurations are shown in Fig. 5.3.

5.1.2.2 Three-dimensional thermo-compressible Taylor-Green vortex with species

As a second test-case, to put forward the ability of the scheme to deal with large temperature discrepancies in the domain and its robustness in the face of complex flows we study a modified thermo-compressible Taylor-Green vortex in 3-D. The test-case was first proposed and used within the context of the ‘‘Verification and Validation of Combustion DNS’’ workshop at the 17th International Conference on Numerical Combustion to validate and benchmark high-order codes for DNS of combustion [208, 209]. The flow field is initialized using the same equations as the classical Taylor-Green case in a fully periodic box of size $L_x = L_y = L_z = 2\pi\text{mm}$. The initial velocity field can be found in subsection 3.3.2. At the difference of the classical Taylor-Green case, here the fluid consists of a gaseous mixture of three species, i.e. H_2 , O_2 and N_2 , and takes into account heat transfer. The temperature field is initialized as:

$$T(x) = T_c + (T_h - T_c)\psi_T(x), \quad (5.22)$$

where:

$$\psi_T(x) = \text{sgn}(R_d - R) \tanh \left[\frac{c(R_d - R)}{R} \right], \quad (5.23)$$

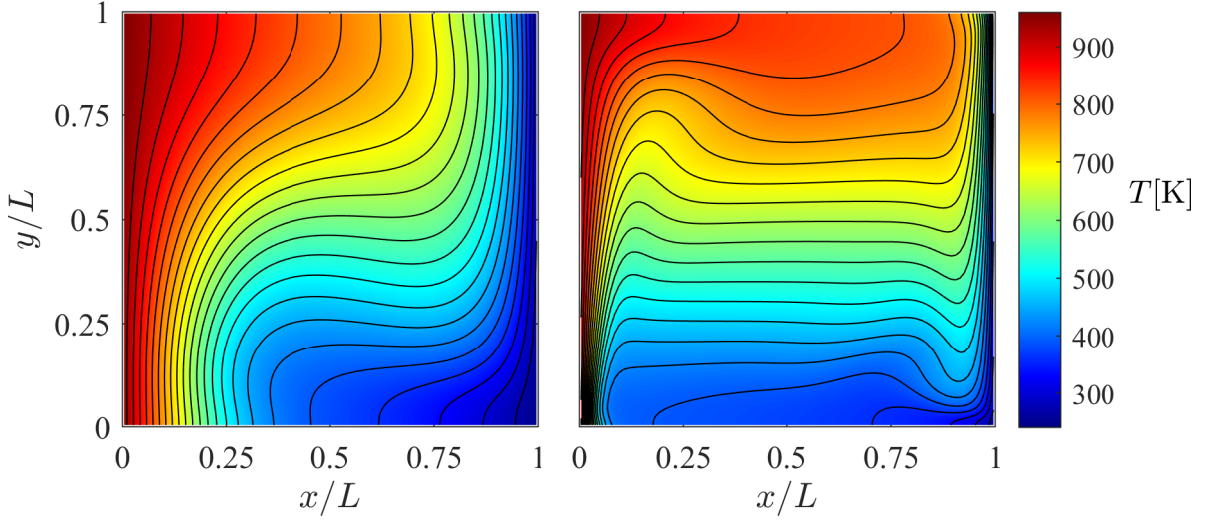


Figure 5.3: Temperature field and iso-contours for (left) $Ra=10^4$ and (right) $Ra=10^6$. Iso-contours go from $T = 240\text{K}$ to 960K with $\delta T = 30\text{K}$.

and:

$$R_d = \sqrt{(x - L_x/2)^2}. \quad (5.24)$$

For the species on the other hand, the initial conditions are defined through:

$$Y_{\text{O}_2}(x) = Y_{\text{O}_2,0}\psi(x), \quad (5.25a)$$

$$Y_{\text{H}_2}(x) = Y_{\text{H}_2,0}(1 - \psi(x)), \quad (5.25b)$$

$$Y_{\text{N}_2}(x) = 1 - Y_{\text{H}_2}(x) - Y_{\text{O}_2}(x), \quad (5.25c)$$

with:

$$\psi(x) = \frac{1 + \tanh\left[\frac{c(R_d - R)}{R}\right]}{2}, \quad (5.26)$$

where $Y_{\text{O}_2,0} = 0.232918$, $Y_{\text{H}_2,0} = 0.055604$, $R = 0.785\text{mm}$, $c = 3$ and $u_0 = 4\text{m/s}$. Furthermore, while the fluid viscosity, thermal conductivity and specific heat capacities are evaluated using mixture-average formulation, detailed in the previous chapter, the species diffusion coefficients are set by fixing the corresponding Lewis numbers: $Le_{\text{H}_2} = 0.329$, $Le_{\text{O}_2} = 1.2703$ and $Le_{\text{N}_2} = 1.8268$. It is also worth mentioning that species diffusion is approximated using the Hirschfelder-Curtiss model with the mass corrector. To put forward the ability of the model to simulate dilatation/flow structure interactions and robustness in the face of under-resolved features, the test-case was run on a $128 \times 128 \times 128$ grid and δ_t was set to 10^{-7}s . To better illustrate the dynamics of the flow and the interactions between the different fields, they are shown in Fig. 5.4 at different times from $t = 0$ to 1.5ms , as obtained from LB simulations. As observed there, the species and energy distributions undergo diffusion

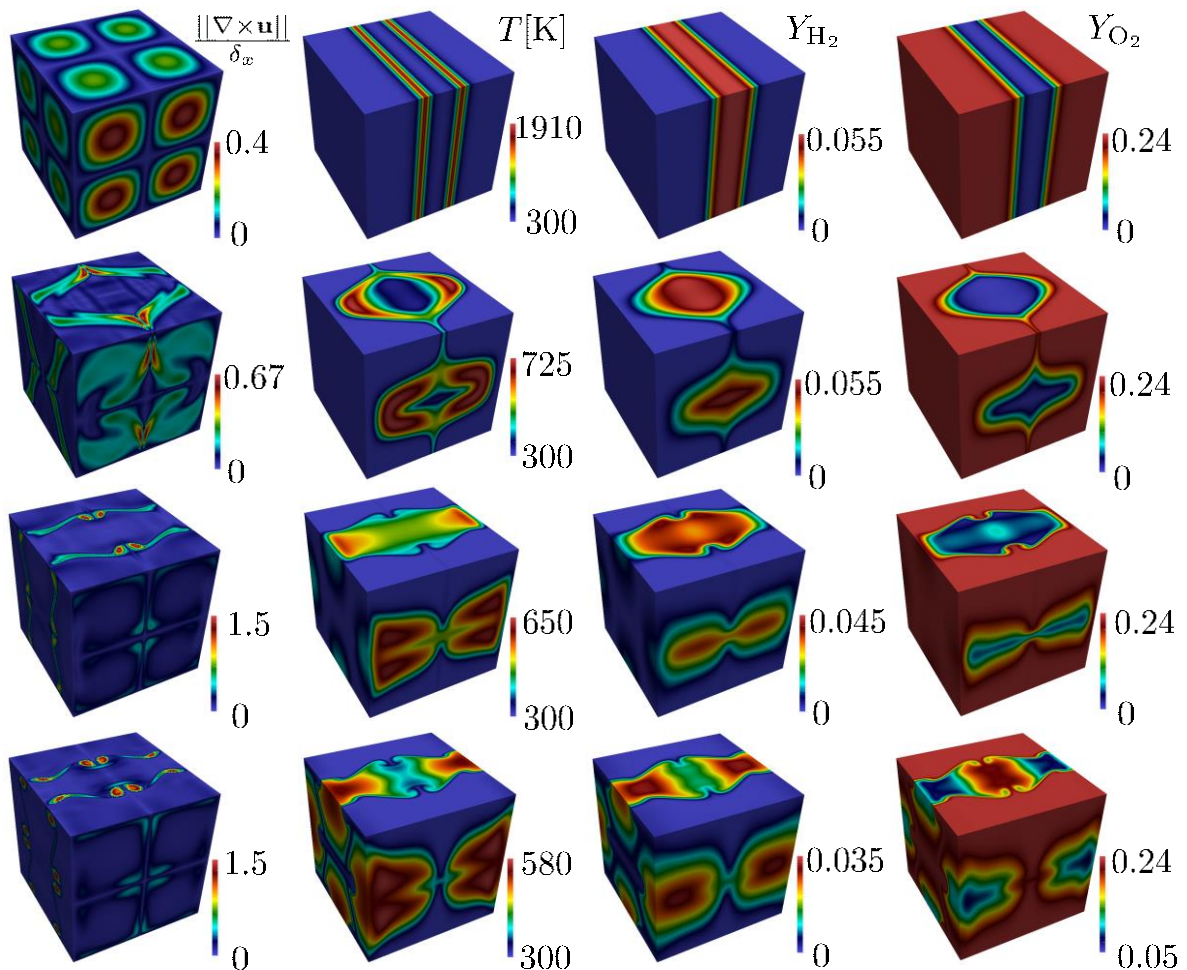


Figure 5.4: Flow state at different times for the thermal Taylor-Green vortex. From left to right: vorticity magnitude, temperature, H_2 and O_2 mass fractions. From top to bottom: $t = 0, 0.5, 1, 1.5$ ms.

and are convected by the vortices in the flow field. The presence of vortical structure in the flow field, as observed here, mimics turbulent mixing of the species and temperature fields. The results obtained at $t = 0.5$ ms, are compared to reference solutions obtained using the DNS tool DINO [210] on a $256 \times 256 \times 256$ grid in Figs. 5.5 and 5.6. The grid-size of the reference solution along with discretization order of the solver (sixth-order in space [210]) clearly illustrates the fact that the LB simulation is under-resolved, explaining the small discrepancies observed in Fig. 5.5. However, it can be observed that the agreement between the two solutions is very good. The same observation holds for the species mass fractions and the time-evolution of maximum temperature in the domain shown in Fig. 5.6.

As mentioned at the beginning of this chapter, apart from the presented low Mach formulation, one can go about modeling compressible flows on standard stencils by using the thermal Hermite expansion to discretize phase-space. This alternative is detailed in the next section.

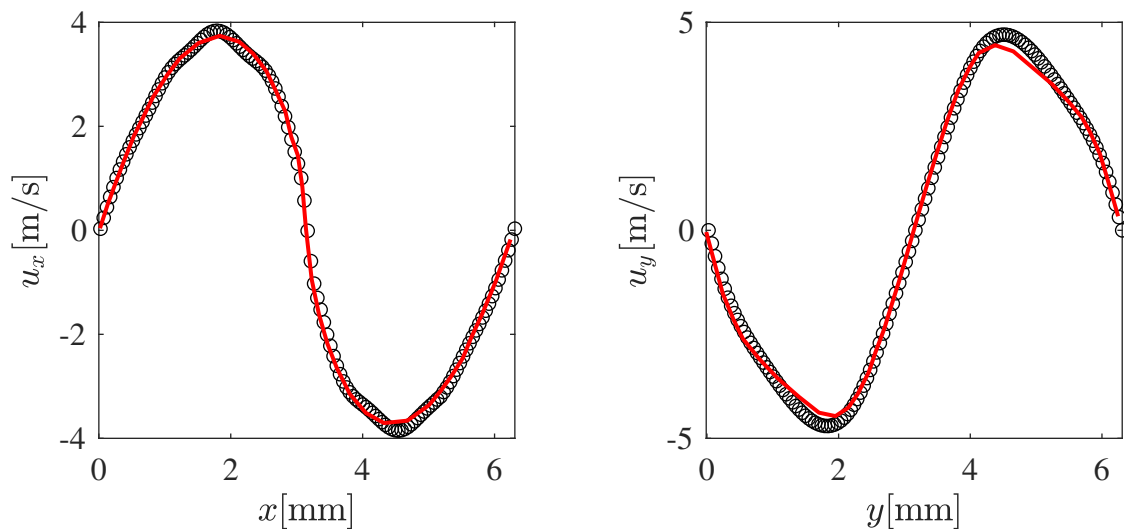


Figure 5.5: (left) Velocity profiles along the x -direction at $y = N_y/2$ and $z = N_z/2$ and (right) along the y -direction at $x = N_x/2$ and $z = N_z/2$. Results obtained through the proposed model are shown with black symbols while reference solutions from DINO are plotted with plain red lines.

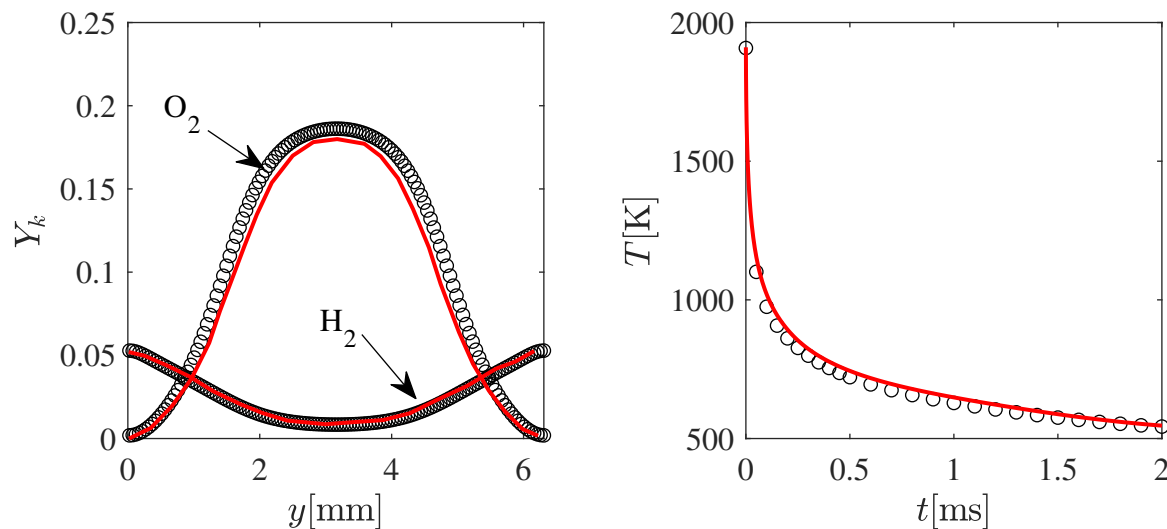


Figure 5.6: (left) Species mass fraction profiles along the x -direction at $y = N_y/2$ and $z = N_z/2$ and (right) variations of maximum temperature in the domain with time. Results obtained through the proposed model are shown with black symbols while reference solutions from DINO are plotted with plain red lines.

5.2 Implicit approach: Thermal discrete equilibrium

The second approach to introducing dilatation effects into the flow solver is to lift the isothermal assumption in the Hermite expansion of the EDF. This section will introduce the corresponding theoretical background and validate the resulting solver.

5.2.1 Equilibrium distribution function: Thermal Hermite expansion

To go from the classical isothermal Hermite expansion of the continuous EDF used in the classical LB formulation to one incorporating a thermal ideal EoS, one just needs to lift the isothermal assumption in the expansion of the continuous EDF:

$$f^{(eq)}(\boldsymbol{\xi}, \theta) = \rho(2\pi\theta)^{-D/2} \exp\left[-\frac{(\boldsymbol{\xi} - \mathbf{u})^2}{2\theta}\right]. \quad (5.27)$$

While Hermite polynomials as shown in Eq. 2.44 remain unchanged, the corresponding coefficients are modified. The first four orders (supported by the D2Q9 stencil, and post discretization in space and time) are defined as:

$$a_0^{(eq)} = \rho, \quad (5.28a)$$

$$a_{i_1}^{(eq)} = \rho u_{i_1}, \quad (5.28b)$$

$$a_{i_1 i_2}^{(eq)} = \rho u_{i_1} u_{i_2} + \rho c_s^2 (\theta - 1) \delta_{i_1 i_2}, \quad (5.28c)$$

$$a_{i_1 i_2 i_3}^{(eq)} = \rho u_{i_1} u_{i_2} u_{i_3} + \rho c_s^2 (\theta - 1) [u_{i_1} \delta_{i_2 i_3}]_{\text{cyc}}, \quad (5.28d)$$

$$a_{i_1 i_2 i_3 i_4}^{(eq)} = \rho u_{i_1} u_{i_2} u_{i_3} u_{i_4} + \rho c_s^4 (\theta - 1)^2 [\delta_{i_1 i_2} \delta_{i_3 i_4}]_{\text{cyc}} + \rho c_s^2 (\theta - 1) [u_{i_1} u_{i_2} \delta_{i_3 i_4}]_{\text{cyc}}, \quad (5.28e)$$

resulting in, for example, the following second-order EDF:

$$f_{\alpha}^{(eq,2)}(\mathbf{c}_{\alpha}, \rho, \mathbf{u}, \theta) = w_{\alpha} \rho \left(1 + \frac{\mathbf{c}_{\alpha} \cdot \mathbf{u}}{c_s^2} + \frac{(\mathbf{c}_{\alpha} \cdot \mathbf{u})^2}{2c_s^4} - \frac{\mathbf{u}^2}{2c_s^2} + \frac{(\mathbf{c}_{\alpha}^2 - D)(\theta - 1)}{2c_s^4} \right). \quad (5.29)$$

Different from the isothermal formulation, here the constant temperature speed of sound is not function of the reference temperature:

$$\sqrt{\left(\frac{\partial p}{\partial \rho}\right)_T} = \sqrt{\frac{k_B T}{m}}. \quad (5.30)$$

To better understand the changes induced by the introduction of temperature into the discrete EDF the resulting macroscopic PDEs at the Euler and NS levels need to be evaluated.

5.2.2 Chapman-Enskog analysis

Following the development introduced in subsection 3.1.1, and including a correction term for the diagonal components of the third-order moments tensor (to be defined from this analysis) one gets:

$$\sum_{n=1}^N \frac{\delta_t^n}{n!} (\partial_t + \mathbf{c}_{\alpha} \cdot \nabla)^n f_{\alpha}(\mathbf{x}, t) = \delta_t \Omega_{\alpha}(\mathbf{x}, t) + C, \quad (5.31)$$

where ref is the correction term. Operating the multi-scale expansion, with the addition of the following:

$$\Psi_\alpha = \varepsilon \Psi_\alpha^{(1)}, \quad (5.32)$$

where we have used the fact that this error involves a first-order space derivative to make the expansion, it can be readily shown that the following PDEs are recovered at order ε^1 for the previously-introduced thermal model:

$$\Pi_0, \varepsilon^1 : \partial_t^{(1)} \rho + \nabla^{(1)} \cdot \rho \mathbf{u} = \sum_\alpha \Psi_\alpha^{(1)}, \quad (5.33a)$$

$$\Pi_1, \varepsilon^1 : \partial_t^{(1)} \rho \mathbf{u} + \nabla^{(1)} \cdot \rho \mathbf{u} \otimes \mathbf{u} + \nabla^{(1)} \cdot \mathbf{p} = \sum_\alpha \mathbf{c}_\alpha \Psi_\alpha^{(1)}, \quad (5.33b)$$

where the pressure is now $p = \rho \frac{k_B T}{m}$. At the NS level, i.e. ε^2 , one gets:

$$\Pi_0, \varepsilon^2 : \partial_t^{(2)} \rho = 0, \quad (5.34a)$$

$$\begin{aligned} \Pi_1, \varepsilon^2 : \partial_t^{(1)} \rho \mathbf{u} + \nabla^{(1)} \cdot \left(\frac{1}{2} - \tau \right) \left(\partial_t^{(1)} \mathbf{\Pi}_2^{(eq)} + \nabla^{(1)} \cdot \mathbf{\Pi}_3^{(eq)} \right) \\ + \nabla^{(1)} \cdot \tau \left(\sum_\alpha \mathbf{c}_\alpha \otimes \mathbf{c}_\alpha \Psi_\alpha^{(1)} \right) + \partial_t^{(1)} \left(\sum_\alpha \mathbf{c}_\alpha \Psi_\alpha^{(1)} \right) = 0. \end{aligned} \quad (5.34b)$$

Based on Eqs. 5.33 and 5.34, Ψ_α should satisfy the following conditions:

$$\sum_\alpha \Psi_\alpha = 0, \quad (5.35a)$$

$$\sum_\alpha \mathbf{c}_\alpha \Psi_\alpha = 0, \quad (5.35b)$$

$$\sum_\alpha \mathbf{c}_\alpha \otimes \mathbf{c}_\alpha \Psi_\alpha = \left(1 - \frac{\delta_t}{2\tau} \right) \nabla \cdot \left(\delta \mathbf{\Pi}_3^{(eq)} \right). \quad (5.35c)$$

More precisely, the third condition can be detailed as:

$$\sum_\alpha c_{\alpha, i_1}^2 \Psi_\alpha = \left(1 - \frac{\delta_t}{2\tau} \right) \partial_x [\rho u_{i_1} (u_{i_1}^2 + 1 - 3\theta)], \quad (5.36a)$$

$$\sum_\alpha c_{\alpha, i_1} c_{\alpha, i_2} \Psi_\alpha = 0. \quad (5.36b)$$

This system can be solved through either one of these two approaches: (a) Solving the corresponding system of equations consisting of the above-cited constraints [9, 144, 211], (b) using the properties of Hermite polynomials (namely the fact that they are mutually ortho-normal [146, 145, 130, 212, 207, 177]). The latter leads to the following expression for

the correction term:

$$\Psi_\alpha = \frac{1}{2} \left(1 - \frac{\delta_t}{2\tau} \right) \sum_{i=x,y,z} \mathcal{H}_{i^2} \partial_i \delta \Pi_{i^3}. \quad (5.37)$$

While similar to the expression used in the literature, the correction term used in the present work differs from those proposed for instance in [146, 145, 130, 212] in that it has a factor $(1 - \frac{\delta_t}{2\tau})$. The necessity of this factor to both stability and recovery of correct acoustic modes dissipation will be further demonstrated in the next section through spectral analysis.

To further illustrate the errors in the moments of the discrete EDFs, they are plotted in Fig. 5.7 as a function of the non-dimensional temperature. It is clear that the error goes to

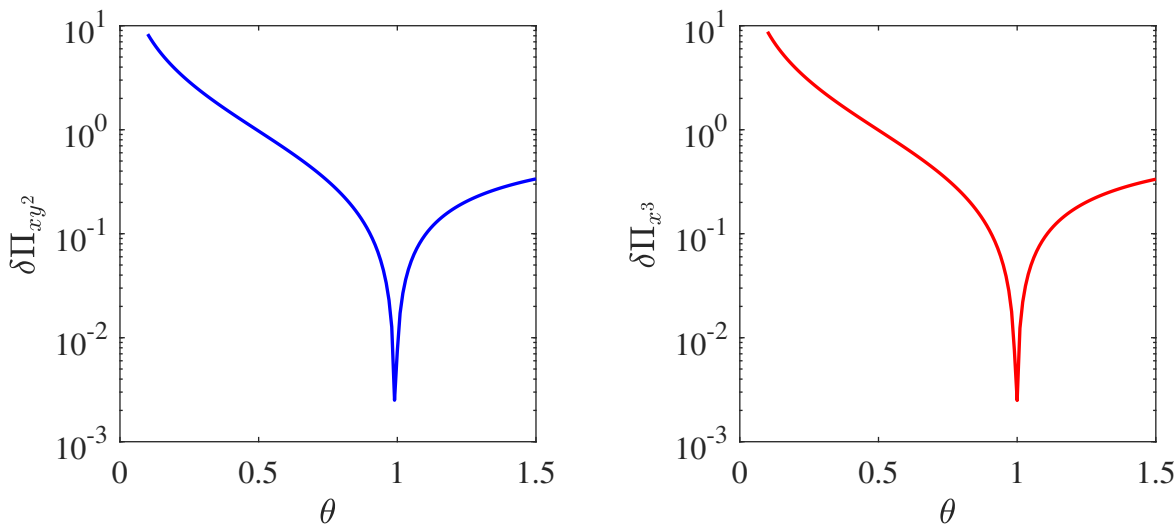


Figure 5.7: Error in (left) the deviatoric component of the third-order moments tensor for a second-order EDF and (right) in the diagonal components for a third-order EDF, both shown as a function of local temperature.

zero at $\theta = 1$, i.e. the reference temperature, while deviations from this state result in very pronounced errors in third-order moments.

The introduction of the thermal Hermite expansion into the LBM does not introduce any changes to the scheme and space-time and phase-space discretization strategy. As such all of the advanced collision models reviewed in section 2.5 can still be used with very little changes. However, as will be shown later in this chapter, while approaches such as the MRT based on central moments effectively increase the stability domain of the isothermal LBM, they do not lead to the widest interval of usable non-dimensional temperatures. As such, a temperature-scaled central moments formulation will be introduced in the next part.

5.2.3 Further extension of stability domain: temperature-scaled central moments

Similar to the cascaded approach, one can perform the collision step in the space of central temperature-scaled moments. This concept was, for the first time used in [171], to extend

the regularized collision model stability domain on higher-order stencils. The idea consists in taking the populations to the temperature-scaled moments space, defined as:

$$\tilde{\Pi}_{\theta, x^i y^j z^k} = \sum_{\alpha} \left(\frac{c_{\alpha, x} - u_x}{\sqrt{\theta}} \right)^i \left(\frac{c_{\alpha, y} - u_y}{\sqrt{\theta}} \right)^j \left(\frac{c_{\alpha, z} - u_z}{\sqrt{\theta}} \right)^k f_{\alpha}, \quad (5.38)$$

performing the collision and then transforming the moments back to discrete populations. This leads to the following collision operator:

$$\Omega_{\alpha} = \mathbf{M}_{\theta}^{-1} \mathbf{N}_{\theta}^{-1} \mathbf{S} \mathbf{N}_{\theta} \mathbf{M}_{\theta} (f_{\alpha}^{(eq)} - f_{\alpha}), \quad (5.39)$$

resulting in the following discrete time-evolution equations:

$$f_{\alpha}(\mathbf{x} + \mathbf{c}_{\alpha} \delta t, t + \delta t) = \mathbf{M}_{\theta}^{-1} \mathbf{N}_{\theta}^{-1} (\mathbf{I} - \mathbf{S}) \tilde{\Pi}_{\theta} + \mathbf{M}_{\theta}^{-1} \mathbf{N}_{\theta}^{-1} \mathbf{S} \tilde{\Pi}_{\theta}^{(eq)} + \mathbf{M}_{\theta}^{-1} \mathbf{N}_{\theta}^{-1} \tilde{\mathcal{F}}_{\theta}, \quad (5.40)$$

where $\tilde{\mathcal{F}}_{\theta}$ is the external body force. Choosing for example the scaled central Hermite coefficients as the moments basis, one gets the following equilibrium moments (for a fourth-order EDF):

$$\tilde{\Pi}_{\theta}^{(eq)} = \{\rho, 0, 0, 0, 0, 0, 0, 0, 0\}, \quad (5.41)$$

instead of:

$$\tilde{\Pi}^{(eq)} = \{\rho, 0, 0, 0, \rho c_s^2 (\theta - 1), \rho c_s^2 (\theta - 1), 0, 0, \rho c_s^4 (\theta - 1)^2\}, \quad (5.42)$$

for the corresponding central moments MRT formulation. The forcing term, \mathcal{F} , using the exact differences formulation [213, 214] becomes:

$$\tilde{\mathcal{F}}_{\theta} = \left\{ 0, \frac{F_x}{\sqrt{\theta}}, \frac{F_y}{\sqrt{\theta}}, \frac{F_x F_y}{\theta}, \frac{F_x^2}{\theta}, \frac{F_y^2}{\theta}, \frac{F_x^2 F_y}{\theta^{3/2}}, \frac{F_x F_y^2}{\theta^{3/2}}, \frac{F_x^2 F_y^2}{\theta^2} \right\}, \quad (5.43)$$

while with Guo's approach [49] one gets:

$$\tilde{\mathcal{F}}_{\theta} = \left\{ 0, (1 - \delta_t/2\tau) \frac{F_x}{\sqrt{\theta}}, (1 - \delta_t/2\tau) \frac{F_y}{\sqrt{\theta}}, 0, 0, 0, 0, 0, 0 \right\}. \quad (5.44)$$

The effect of this collision model on the linear stability domain will be studied with more details in the next section using the von Neumann analysis. For the remainder of this manuscript, all simulations performed using the compressible formulation rely on this collision operator.

Before going into a detailed analysis of the numerical properties of the compressible solver, the effect of the correction term and thermal Hermite expansion are assessed through a number of simple test-cases.

5.2.4 Validation and numerical application

The aim of this part is to validate the physical behavior of the model, through simple test-cases. As such, correct dissipation rates and sound speeds are first validated using acoustic

and shear waves dissipation and propagation. Then, to validate compressibility, a low Mach version of the Sod shock-tube is simulated. All simulations use previously-derived LB solvers for the energy balance equation (the total sensible energy formulation).

5.2.5 Galilean invariance: sound speed, acoustic and shear wave dissipation rate

In order to validate the temperature-dependence of sound speed in the compressible model, following [9], a pseudo 1-D domain is separated into two regions with the same temperature and initial velocity and a pressure difference of $\Delta p = 10^{-4} \text{J/m}^3$ between them. The system is left to evolve and the shock front is tracked in time to compute the speed of sound. The simulations are performed for different specific heat ratios, i.e. $\gamma = 1.4, 2$ and 3 , and non-dimensional temperatures. The obtained results are shown in Fig. 5.8. They are compared to the theoretical isentropic sound speed, $c_{s,T} = \sqrt{\gamma k_B T/m}$.

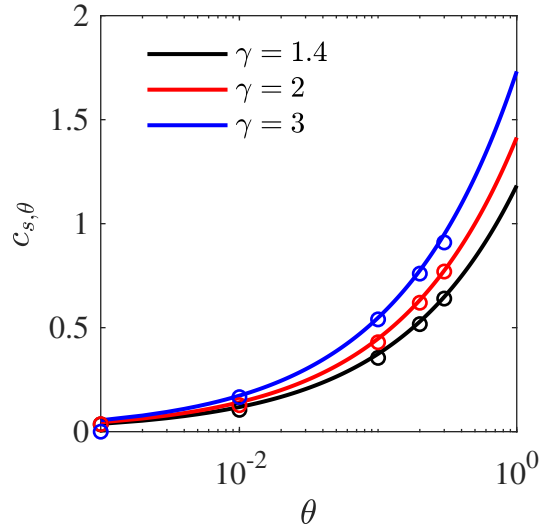


Figure 5.8: Isentropic sound speeds obtained using the compressible model for different non-dimensional temperatures and specific heat ratios. Reference sound speed are shown with plain lines while simulations results are represented with symbols.

In order to validate the effects of the correction terms, a decaying shear wave is modeled. While the third-order thermal equilibrium correctly recovers shear mode dissipations, the second-order EDF needs correction terms for the off-diagonal components of the third-order moments tensor. As such, to validate these corrections a domain of size $2 \times N_y$ (with

$N_y = 200$) is used to perform a simulation with the following initial conditions [9]:

$$\rho(x, y) = 1, \quad (5.45a)$$

$$u_x(x, y) = 1 \times 10^{-4} \sin\left(\frac{2\pi y}{N_y}\right), \quad (5.45b)$$

$$u_y(x, y) = 0, \quad (5.45c)$$

$$\theta = \theta_0. \quad (5.45d)$$

The kinematic viscosity is set to $\nu = 0.1\text{m}^2/\text{s}$. The simulations are performed over 50,000 time steps using second- (both with and without the correction for off-diagonal components) and third-order EDFs for $\theta \in [0.1 - 1.2]$. By monitoring the time evolution of the maximum velocity of this wave and fitting an exponential function to it, the effective numerical kinetic viscosities are then measured. The obtained results are displayed in Fig. 5.9. As

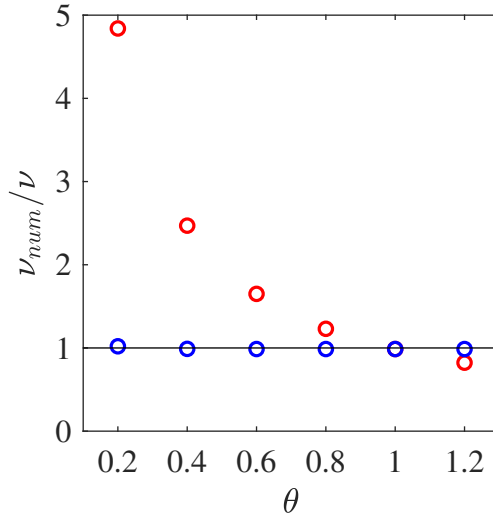


Figure 5.9: Effective dissipation rate of the shear mode for the (in black) third- and second-order EDF (in blue) with and (in red) without the correction term obtained for the decaying shear wave test-case. The reference viscosity is shown with a plain line.

observed in this figure, the second-order EDF is unable to correctly dissipate shear waves. At lower temperatures, the deviations from the reference temperature result in pronounced over-dissipation of the waves. It can also be observed that the addition of the off-diagonal components correction restores the appropriate dissipation rate for the second-order EDF.

To assess the accuracy of the acoustic modes dissipation, the test-case presented in [108] is used. This case having already been used to investigate the effect of the second relaxation coefficient in the LKS in subsection 3.2.4 it will not be detailed again. In the context of this study, $N_x = 200$, $\rho_0 = 1\text{kg}/\text{m}^3$ and $\delta\rho = 10^{-6}\text{kg}/\text{m}^3$ are used. As with the previous case, different temperatures are considered with a third-order equilibrium both with and without the correction term. The results are shown in Fig. 5.10. It can be clearly observed that the correction term restores the appropriate acoustic mode dissipation rate into the solver.

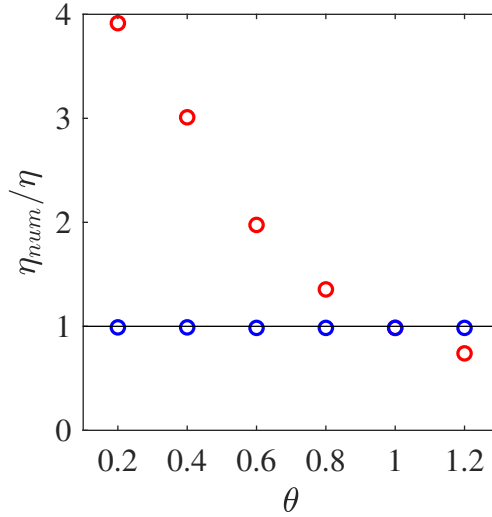


Figure 5.10: Effective dissipation rate of the acoustic modes for the third-order EDF (in blue) with and (in red) without the correction term obtained for the decaying acoustic wave test-case. The reference viscosity is shown with a plain line. Black symbols are not visible as they fall exactly on top of the blue ones.

The three test-cases presented in this part have clearly established that by using a third-order EDF along with the appropriate correction term for the diagonal components of the third-order moment tensor one can effectively restore the Galilean invariance in the dissipation rates of acoustic and shear modes.

5.2.5.1 Low Mach number viscous 1-D Sod shock tube

In order to both validate the scheme and illustrate its ability to model compressible flows a low Mach version of the Sod shock tube configuration is considered [9, 207]. The test-case as used in this subsection is taken from [9]. The simulation is initialized by dividing a pseudo 1-D domain into two separate halves, with:

$$\{\rho, u_x, T\} = \{0.5, 0, 0.2\}, \quad \forall x : x/L \leq 0.5, \quad (5.46a)$$

$$\{\rho, u_x, p\} = \{2, 0, 0.025\} \quad \forall x : x/L > 0.5. \quad (5.46b)$$

Following [9], the simulation is performed over 1287 time-steps, setting $\delta_x = 1\text{m}$, $\delta_t = 1\text{s}$, $\mu = 0.025\text{kg/m.s}$ and $c_v = 1\text{J/kg.K}$ ($\gamma = 2$). The obtained results (using the temperature-scaled central moments formulation) are compared to their analytical counterparts in Fig. 5.11. It can be observed that the analytical solution agrees very well with results from the simulation.

A similar configuration is modeled in [207], where the authors use a central moments formulation based on the following basis, $\tilde{\Pi} = \{\tilde{\Pi}_0, \tilde{\Pi}_x, \tilde{\Pi}_y, \tilde{\Pi}_{x^2} + \tilde{\Pi}_{y^2}, \tilde{\Pi}_{x^2} - \tilde{\Pi}_{y^2}, \tilde{\Pi}_{xy}, \tilde{\Pi}_{x^2y}, \tilde{\Pi}_{xy^2}, \tilde{\Pi}_{x^2y^2}\}$, and set all relaxation parameters to 1, except the one tied to shear viscosity, set to $\nu\delta_t/\delta_x^2 = 0.01$. It is interesting to note that in this test-case the value of shear viscosity has no effect on the simulation, as it is a pseudo 1-D case with only normal modes. As such by setting the relaxation coefficient of the acoustic mode to 1, the effective viscosity is fixed at $\nu\delta_t/\delta_x^2 = 0.167$

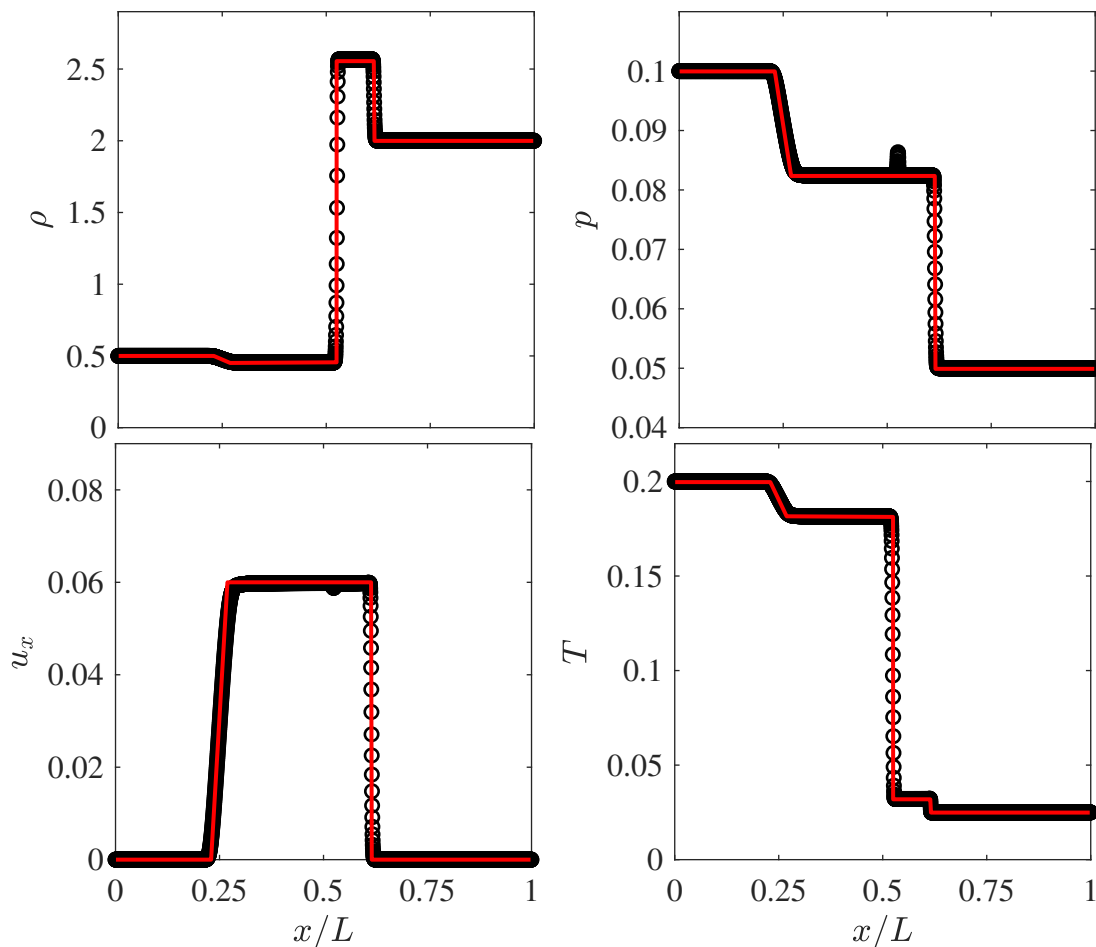


Figure 5.11: Sod shock tube simulation results at $t = 1273\delta_t$. Black symbols represents results obtained through the LB simulation while the red lines are the reference profiles from [9].

(as done in [207]).

The simulations performed in this section illustrated the ability of this formulation to correctly capture compressibility effects. However, it has been observed that deviation of the temperature in the EDF from the reference temperature leads to errors in higher-order moments, which in turn can affect both accuracy and linear stability domain. As such the next section, similar to the analysis of section 3.2, will focus on analyzing the effect of local temperature and different collision operators on the linear stability domain. Furthermore, the correction term as derived in this section will be further validated through an analysis of the spectral dissipation.

5.3 Spectral analysis of the implicit scheme

In order to quantify the effects of temperature deviation from the reference state of the stencil, as in section 3.2, the VN analysis will be used to determine the linear stability domain in terms of the temperature, analyze spectral properties of the solver for fluid temperatures different from the stencil reference temperature, and validate the form of the correction term as derived in the previous section.

5.3.1 Effect of EDF order

As for the isothermal formulation, the order of the Hermite expansion used in the EDF can affect the linear stability domain and spectral properties. While a second-order EDF leads to velocity and temperature-dependent error in the dissipation of the shear mode, the third- and fourth-order EDFs have virtually the same spectral properties (for physical modes). However, while not affecting NS level dynamics the fourth-order term can improve the stability domain of the scheme, as for the isothermal formulation. To that end, the linear stability domains of the SRT collision operator with different orders of the EDF were evaluated. The results (maximum achievable non-dimensional velocities) are shown in Fig. 5.12. As expected from

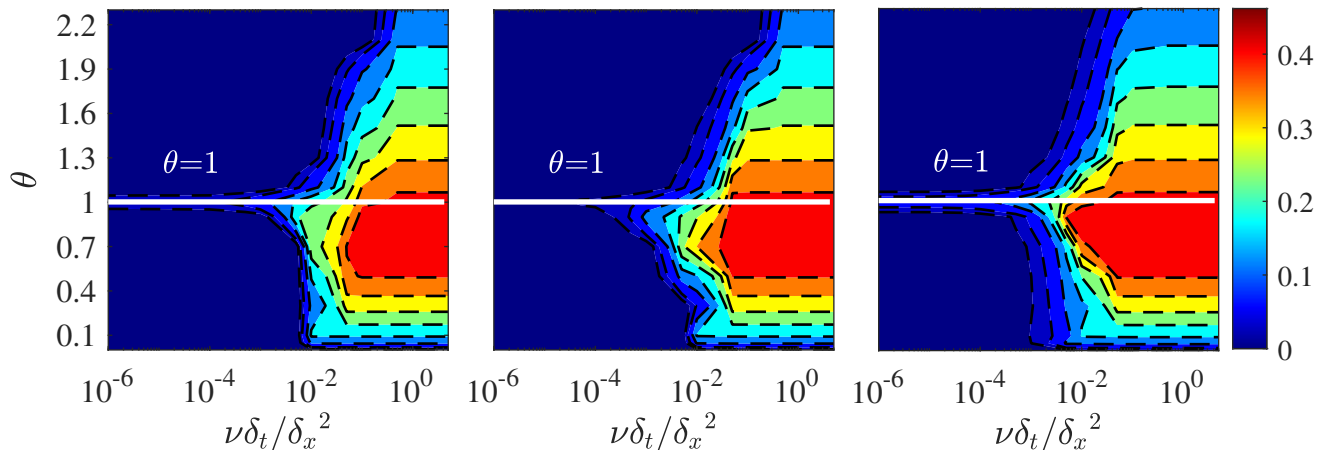


Figure 5.12: Stability domain (in the $\theta - \nu\delta_t/\delta_x^2$ space) of the SRT collision operator with (from left to right) second, third and fourth-order EDFs. The colorbar shows the maximum achievable velocity, i.e. $\frac{u}{\delta_x/\delta_t}$.

the LB development and continuum error analysis, at $\theta = 1$, the solver exhibits a much wider *usability domain* (in terms of non-dimensional viscosity). It is also interesting to note that close to $\theta = 0$ the scheme becomes unconditionally unstable for any value of the non-dimensional viscosity. While the addition of third-order components does not have any major impact on the stability domain (especially for small non-dimensional viscosities), the fourth-order EDF extends it, making the solver usable for non-dimensional viscosities as small as $\nu\delta_t/\delta_x^2 = 10^{-3}$ at $\theta = 0.1$ (from $\nu\delta_t/\delta_x^2 = 10^{-2}$ for the second- and third-order EDFs).

To better illustrate the limitations stemming from the obtained linear stability domain,

it is interesting to consider a typical configuration encountered in combustion involving temperatures going from 300 to 3000 K: setting the reference temperature to 3000 K, $0.1 < \theta < 1$, the fourth-order EDF is stable for $10^{-3} < \nu\delta_t/\delta_x^2$.

5.3.2 Advanced collision model: effect of regularization

The use of the regularized family of collision models is also observed to further extend the stability domain. The expressions and discrete time-evolution equations for different orders of this class of models were detailed in subsection 2.5.2. The only difference between the expressions presented there and the thermal version lies in the expression of $a_{x^2y^2}$ [170]:

$$a_{x^2y^2}^{(1)} = u_x^2 a_{y^2}^{(1)} + u_y^2 a_{x^2}^{(1)} + 4u_x u_y a_{xy}^{(1)} + (\theta - 1) \left(a_{y^2}^{(1)} + a_{x^2}^{(1)} \right). \quad (5.47)$$

The obtained results, from the VN analysis, are illustrated in Fig. 5.13. Although the fourth-order recursive regularized scheme, as expected, allows to achieve the highest non-dimensional velocities for $\theta \in [0.5, 1.5]$ it is outperformed by the classical second-order regularized collision operator for $\theta < 0.5$. Although showing good linear stability properties at

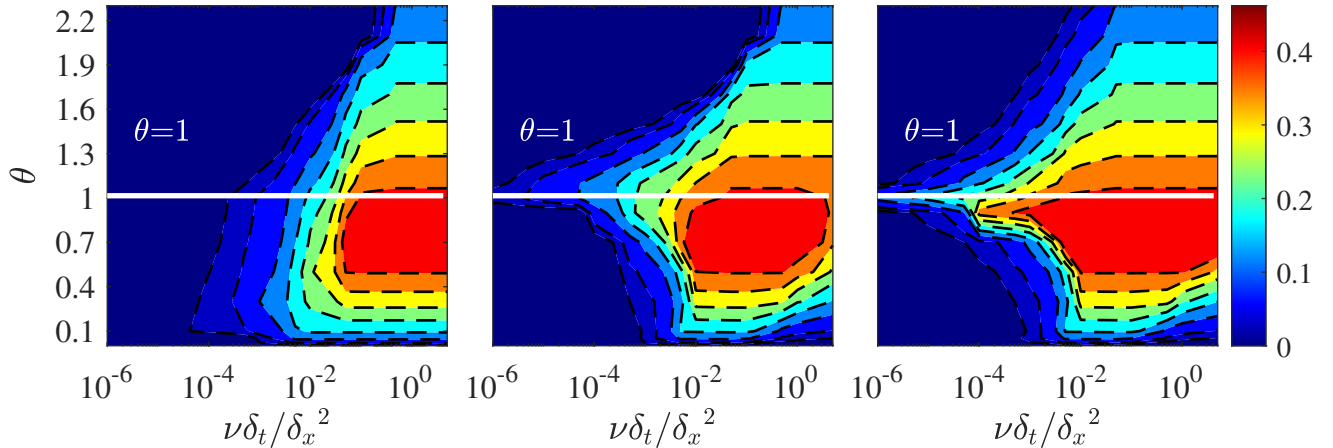


Figure 5.13: Stability domain (in the $\theta - \nu\delta_t/\delta_x^2$ space) of the regularized collision operator of different order, (from left to right) second-, third- and fourth-order. The color bar shows the maximum achievable velocity, i.e. $\frac{u}{\delta_x/\delta_t}$.

low non-dimensional temperatures, it must be noted that the second-order expansion used in the classical regularized collision model results in over-dissipation of all physical modes (both shear and acoustic) even at the continuum limit, as observed in Fig. 5.9. This over-dissipation is also one of the reasons it is exhibiting an unexpectedly wide stability domain.

5.3.3 Central moments MRT versus temperature-scaled central moments

As seen in section 3.2, performing the collision operation in central moments space can have a considerable effect on the linear stability domain for the isothermal LBM. How-

ever, it is unclear whether this collision operator would also have a pronounced impact on the stability domain in terms of the fluid temperature. To clarify its effect, and showcase the performances of previously-introduced temperature-scaled central moments the linear stability domain of both operators using Hermite polynomials as the moments space were studied, setting the ghost relaxation coefficients to one. The obtained stability domains are illustrated in Fig. 5.14. Comparing the stability domains it can be observed that using

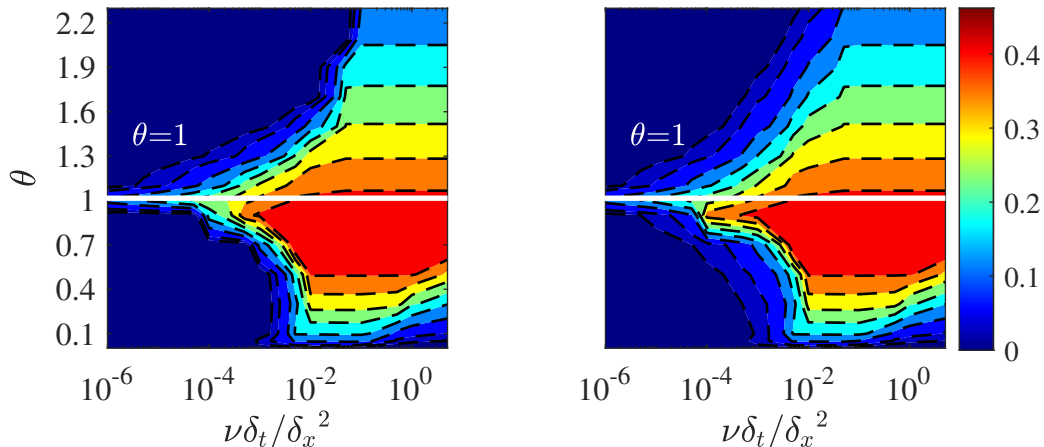


Figure 5.14: Stability domain (in the $\theta - \nu\delta_t/\delta_x^2$ space) of (left) central moments and (right) temperature-scaled central moments MRT collision operators. The color bar shows the maximum achievable velocity, i.e. $\frac{u}{\delta_x/\delta_t}$.

temperature-scaled central moments widens the stability domain to smaller non-dimensional viscosities. As previously mentioned and shown in [154] using central Hermite polynomials in a MRT collision model and setting ghost relaxation coefficients to one, the isothermal recursive regularized collision operator is recovered. Looking at the stability domains in Figs. 5.13 and 5.14, and through some standard algebra it can be shown that switching to temperature-scaled moments and setting ghost moments relaxations to one, the thermal recursive regularized collision model is recovered.

The temperature-scaled central moments MRT, however, has the advantages of: (a) allowing for tunable relaxation coefficients for ghost moments and, therefore, potentially independent control on the over-dissipation effects and (b) being computationally more efficient; Finally, while in 2-D a fourth-order recursive regularized collision operator is equivalent to the temperature-scaled MRT model, in 3-D on a D3Q27 one would have to recursively regularize moments up to order six to match the performances of the temperature-scaled operator.

As such, of all collision models studied in this section, and more generally in this thesis, the temperature-scaled central moment MRT model is more adapted to thermal flows.

As a final step in the spectral analysis of the compressible model, the next section will study the spectral dissipation properties of the bare and corrected models to corroborate the expression previously obtained for this correction term.

5.3.4 Effect of correction term

To validate the correction term expression as obtained in the previous section, the derivatives are approximated using a second-order central-differences scheme at first, and used to get the spectral dissipation rates of all physical modes for a given set of parameters, i.e. temperature and velocity. The obtained results using the third-order EDF both with and without the correction are displayed in Fig. 5.15. The flow velocity vector is in the x -direction and only results on the k_x axis are shown. While, as shown there, one observes over-dissipation of the acoustic modes at $\theta = 0.5$, the introduction of the correction term restores the correct dissipation rate (independent of temperature) at the continuum limit. Given the effect of

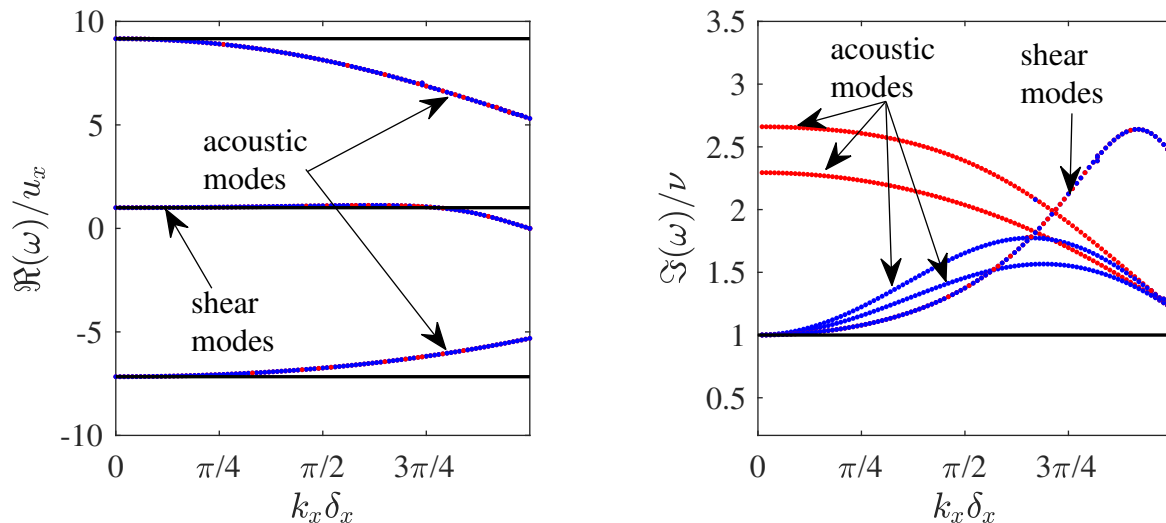


Figure 5.15: (left) Dispersion and (right) dissipation of the acoustic and shear modes for a third-order EDF (in blue) with and (in red) without the correction term at $u_x = 0.05$ and $\theta = 0.5$ for $\nu\delta_t/\delta_x^2 = 1 \times 10^{-4}$. Plain black lines are the reference spectral dispersion and dissipation curves.

the correction term on the dissipation of acoustic modes at low wave-numbers, it might also be interesting to see whether higher-order evaluations of the correction term would lead to enhanced results. This effect is illustrated in Fig. 5.16, where the gradient in the correction term is computed using second-, fourth- and sixth-order central-differences for two different fluid temperatures, i.e. $\theta = 0.05$ and 1.4 . The coefficients of the corresponding finite-differences approximations are given in Table 5.1. As observed in Fig. 5.16, for $\theta <$

Table 5.1: Coefficients for finite-differences approximations

Order	$x - 3\delta_x$	$x - 2\delta_x$	$x - \delta_x$	$x + \delta_x$	$x + 2\delta_x$	$x + 3\delta_x$
2	0	0	$-1/2$	$1/2$	0	0
4	0	$1/12$	$-2/3$	$2/3$	$-1/12$	0
6	$-1/60$	$3/20$	$-3/4$	$3/4$	$-3/20$	$1/60$

1, the use of higher-order approximations reduces the over-dissipation observed at higher

wave-numbers. For $\theta > 1$ on the other hand, higher-order approximations are observed to introduce dissipation into the system (while getting closer to the physical dissipation rate) and can potentially be beneficial to the stability of the solver. In conclusion, the

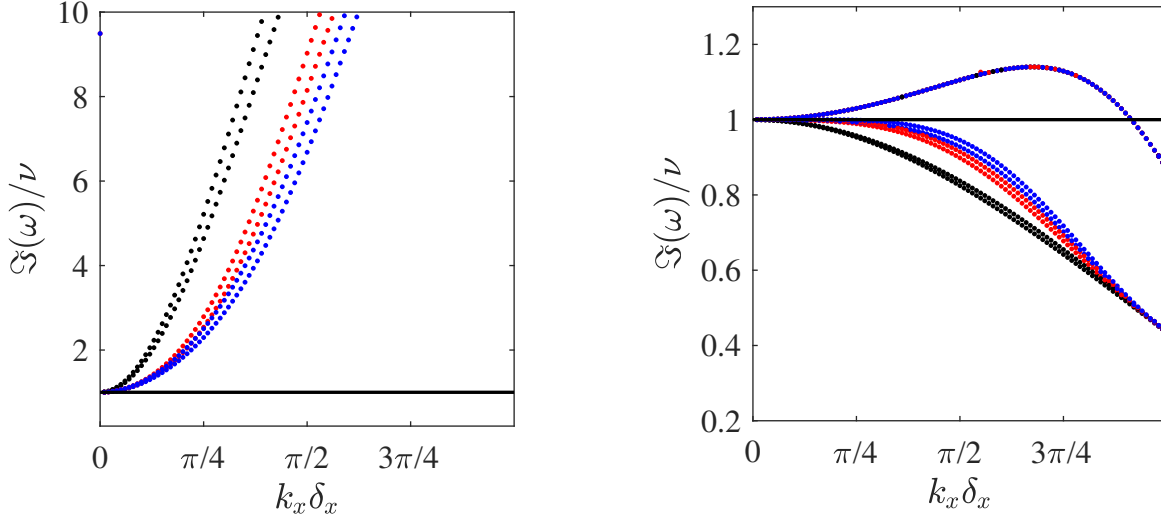


Figure 5.16: Spectral dissipation of the acoustic modes using a third-order EDF and the correction term evaluated using (in black) second-, (in red) fourth-, and (in blue) sixth-order central-differences for (left) $\theta = 0.05$ and (right) $\theta = 1.4$. Plain black lines are the reference spectral dispersion and dissipation curves.

spectral analysis of the dissipation of acoustic modes showed that the correction as derived in this section restores the correct physical acoustic dissipation in the limit of vanishing wave numbers (continuum). Furthermore, the order of the approximation used for the derivatives in the correction term affects the dissipation rate at higher wave-numbers. As such, while leading to additional communication overhead in parallel codes, the use of a fourth-order central-differences approximation can be useful to increase both the accuracy and stability of the solver.

5.4 Concluding remarks

The present chapter was dedicated to the last theoretical step in the development of a mixture-averaged single-fluid LB-based solver intended for low Mach number combustion simulation: the introduction of dilatation effects into the flow solver. To that end, two different approaches have been proposed, detailed and validated: a low Mach thermo-compressible formulation relying on decoupling density and hydrodynamic pressure, and a compressible formulation based on a thermal Hermite expansion of the distribution function. The former was shown to correctly capture dilatation effects through configurations such as the heated cavity with large temperature differences. Given the fact that the fluid density in this model is evaluated using local temperature and thermodynamic pressure, it can only efficiently be coupled with discrete solvers for the non-conservative forms of the species and

energy balance equations. The LB solvers for energy and species mass balance proposed in the previous chapter are not good matches for this thermo-compressible solver. Therefore, it is coupled to a finite-differences solver implemented in ALBORZ, with the possibility to choose between different space-discretization strategies for the convection term, e.g. second- and fourth-order central, first- and third-order upwind, and finally third- and fifth-order Weighted Essentially Non-Oscillatory [215, 100].

The latter, i.e. compressible solver, was also shown to correctly capture all physical properties of the compressible flow such as sound speed and dissipation rate of shear and acoustic modes. Furthermore, it was shown to accurately model compressible configurations such as the Sod shock tube. Contrary to the first approach, this compressible solver was coupled to LB-based solvers for the energy and species balance equations. This solver however, similar to the isothermal LBM is subject to stability issues when the local temperature deviates from the reference temperature. The effect of fluid temperature on stability along with different collision models were studied through systematic von Neumann analyses. A temperature-scaled central moments MRT collision operator, shown to be equivalent to a thermal fourth-order recursive regularized collision operator on the D2Q9 stencil was observed to have the widest stability domain. As such it is chosen as the collision operator used in the next chapter to perform combustion simulations.

The models developed and analyzed in chapters 1 through 5 are used to model different configurations involving low Mach number combustion in the next chapter.

Chapter 6

Numerical application: Combustion simulation

Contents

6.1	Employed code and models	131
6.2	Numerical applications and validation	133
6.2.1	1-D flame simulations	134
6.2.1.1	First validation case: 1-D premixed Propane/air flame with simple thermo-chemistry	134
6.2.1.2	Order of accuracy: Methane/Air 1-D freely-propagating flame with BFER scheme	136
6.2.2	Complex configurations	138
6.2.2.1	Premixed Propane/air 2-D counterflow flame with simple chemistry	139
6.2.2.2	Premixed Propane/air counterflow flame with simple chemistry in 3-D	140
6.2.2.3	Methane/air 2-D coflow diffusion flame with two-step chemistry	141
6.2.2.4	Flame/vortex interaction	143
6.3	Concluding remarks	148

Disclaimer

Part of this chapter has been published in:

[1] S.A. Hosseini, H. Safari, N. Darabiha, D. Thévenin, and M. Krafczyk. Hybrid lattice Boltzmann-finite difference model for low Mach number combustion simulation. *Combustion and Flame*, 209, pp.394-404, 2019.

The aim of the present chapter is to validate the previously developed/proposed approaches to combustion simulation. As such it is organised into three main sections, namely a first section introducing the overall structure of the used codes, a second section illustrating the accuracy and ability of the code to model combustion through a multitude of test-cases and finally a third section with final remarks and conclusions.

6.1 Employed code and models

The examples shown in what follows have been compiled at different stages of this project, and thus rely on different libraries implemented in the code. In general, the employed numerical tool combines three main components: (a) Solver for mixture-averaged continuity and momentum balance equations; (b) solvers for the energy and species mass balance equations; and (c) a module for thermo-physical parameters and chemistry evaluation.

For the flow solver, as mentioned in the previous chapter, two different formulations have been used: (a) low Mach number dilatible solver of section 5.1; and (b) compressible solver of section 5.2. For the species mass and energy balance equations, they can be solved either using the LB formulation introduced in chapter 3 or in combination with classical FD solvers. Furthermore, depending on the type of flow, i.e. compressible or low Mach dilatible, the energy balance equation is solved for either the total sensible energy or total sensible enthalpy. Due to the the coupling possibilities and limitations of each solver, three different schemes are used in this chapter:

- Low Mach dilatible LB solver coupled to FD solver for energy and species mass balance (Approach I): In this approach, the flow field is modeled through the low Mach formulation of section 5.1. Coupling of this code to solvers for the conservative form of the transport equations for energy and species requiring an iterative process, FD solvers are used. The FD solvers, while readily extendable to higher orders, rely here only on a first-order Euler discretization in time. Furthermore, given that the flow solver is only dilatible, sensible enthalpy is used for the energy field, while the space-derivative of pressure is set to zero (given the assumption of uniform thermodynamic pressure). For all solvers in this section the thermo-chemical parameters are computed using REGATH. The overall structure of this approach is illustrated in Fig. 6.1.
- Compressible LB solver coupled to FD solver for energy and species mass balance (Approach II): The second approach relies on the compressible flow solver of section 5.2 while using FD, as for the previous solver, for energy and species mass balance. Different from the previous solver, given the compressible nature of the flow solver, the sensible energy form of the energy balance equation is solved. The sensible energy is used instead of the total energy as the FD solver can handle non-conservative terms. The overall algorithm of this approach is displayed in Fig. 6.2.
- Compressible LB solver coupled to LB solvers for energy and species mass balance (Approach III): The last approach, completely based on LB, relies on the compressible

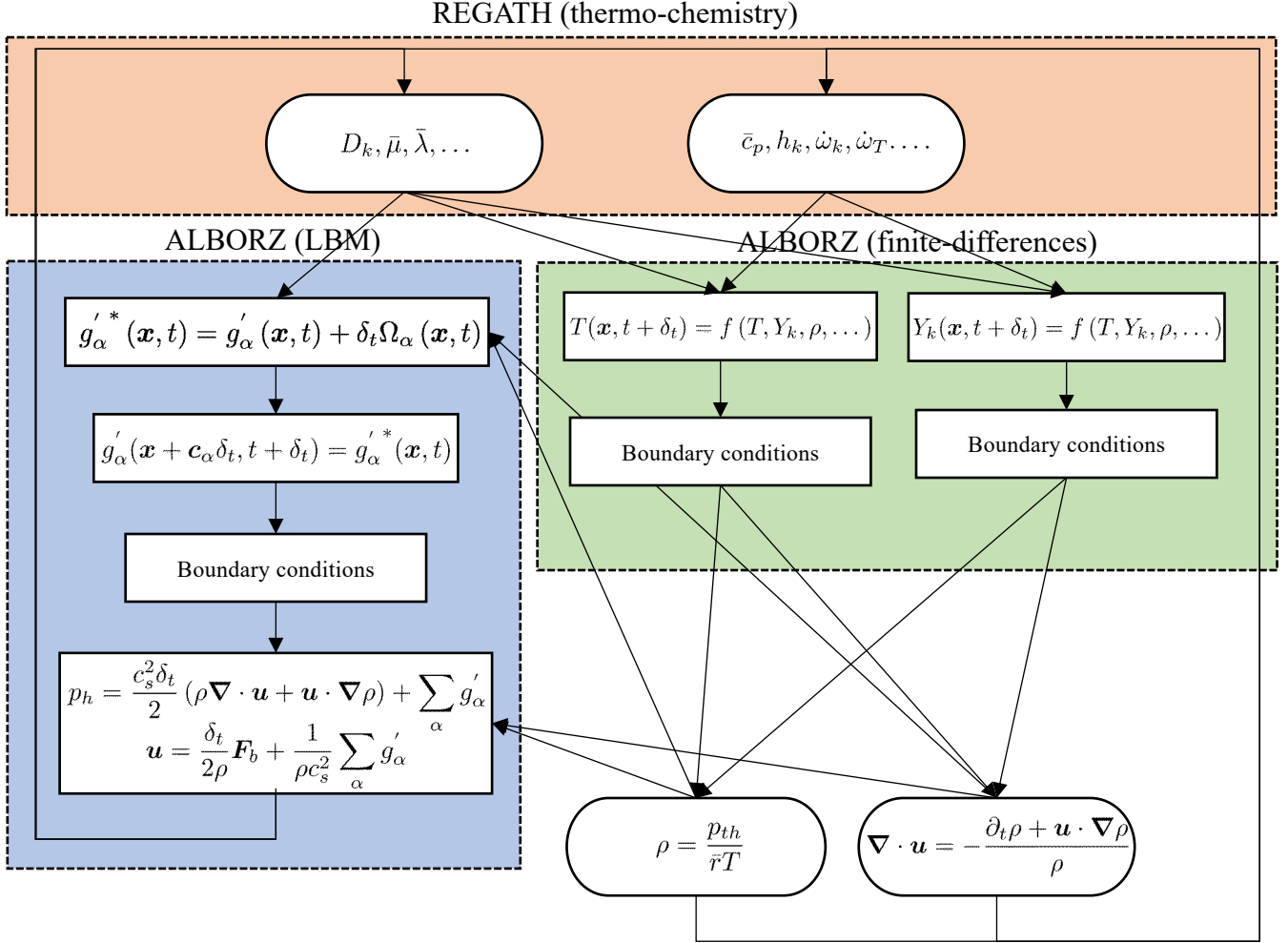


Figure 6.1: Overall algorithm structure and communication scheme for the low Mach formulation coupled to a finite-difference solver (Approach I).

flow solver of section 5.2, as for the second one, while using the modified LB-based advection-diffusion solvers of chapter 3. Apart from the discrete solver, the main difference between this approach and the previous one is the form of the solved PDEs: while the FD approach solves the non-conservative form of the balance equations, here the LB solvers rely on the conservative form. Furthermore, given this limitation on the form of the terms, the total sensible energy is considered for the energy field (mainly to recover the pressure and viscous heating terms in conservative form). The corresponding algorithm is shown in Fig. 6.3.

While slightly different in the forms of the considered balance equations and flow field solver, given that low Mach number flows are considered in this section, we do not expect to observe major discrepancies between the different approaches.

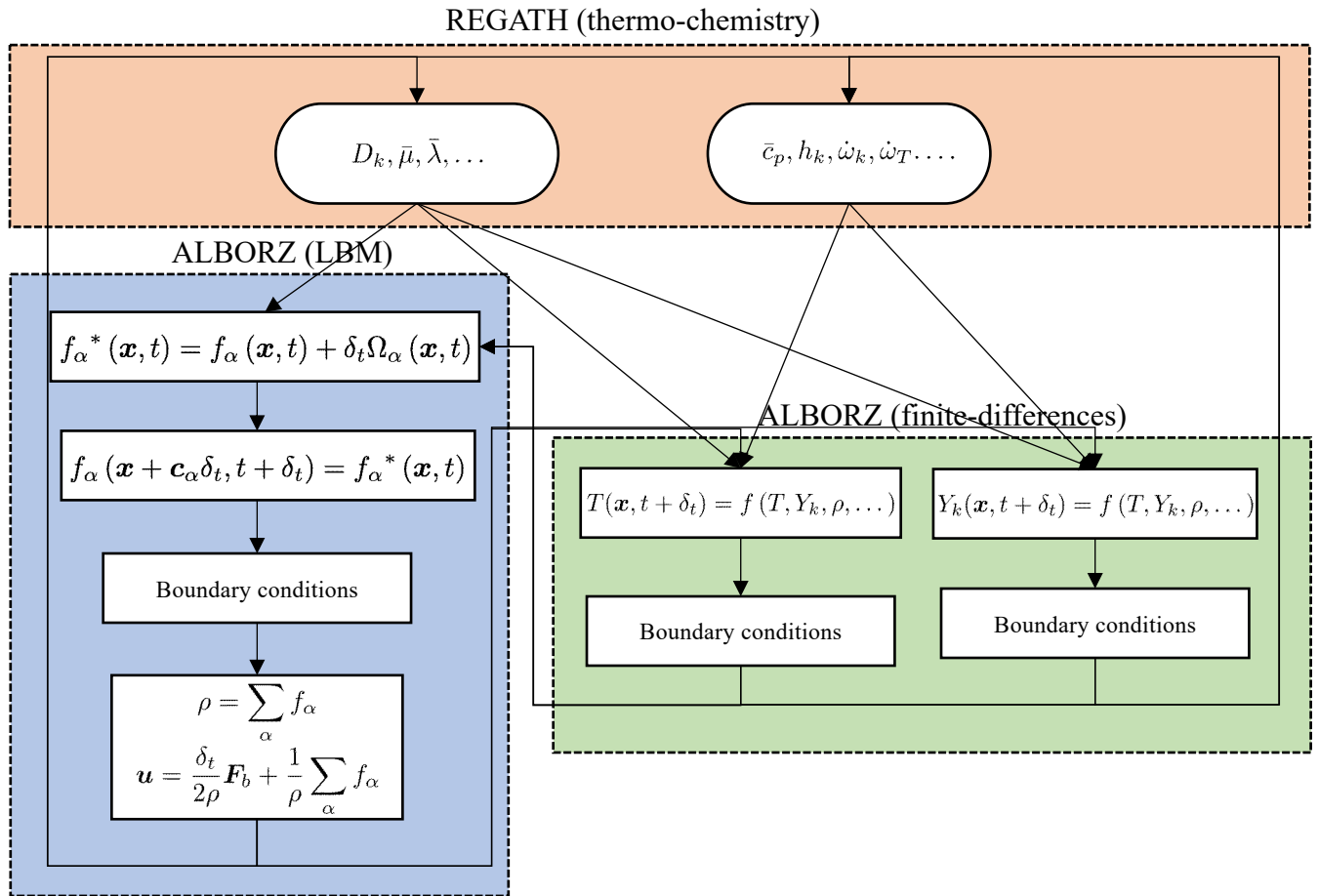


Figure 6.2: Overall algorithm structure and communication scheme for the compressible LBM coupled to a FD solver (Approach II).

6.2 Numerical applications and validation

Two classes of numerical applications are considered in this section: (a) simple 1-D flames and (b) more complex multi-dimensional cases. While the latter are used to showcase the ability of the models to handle complex configurations, the former are mainly used to evaluate the order of convergence of the different schemes. Although performed with all three approaches, in the second part, for the sake of readability only results obtained using the most efficient method (approach I) will be shown and compared to reference data.

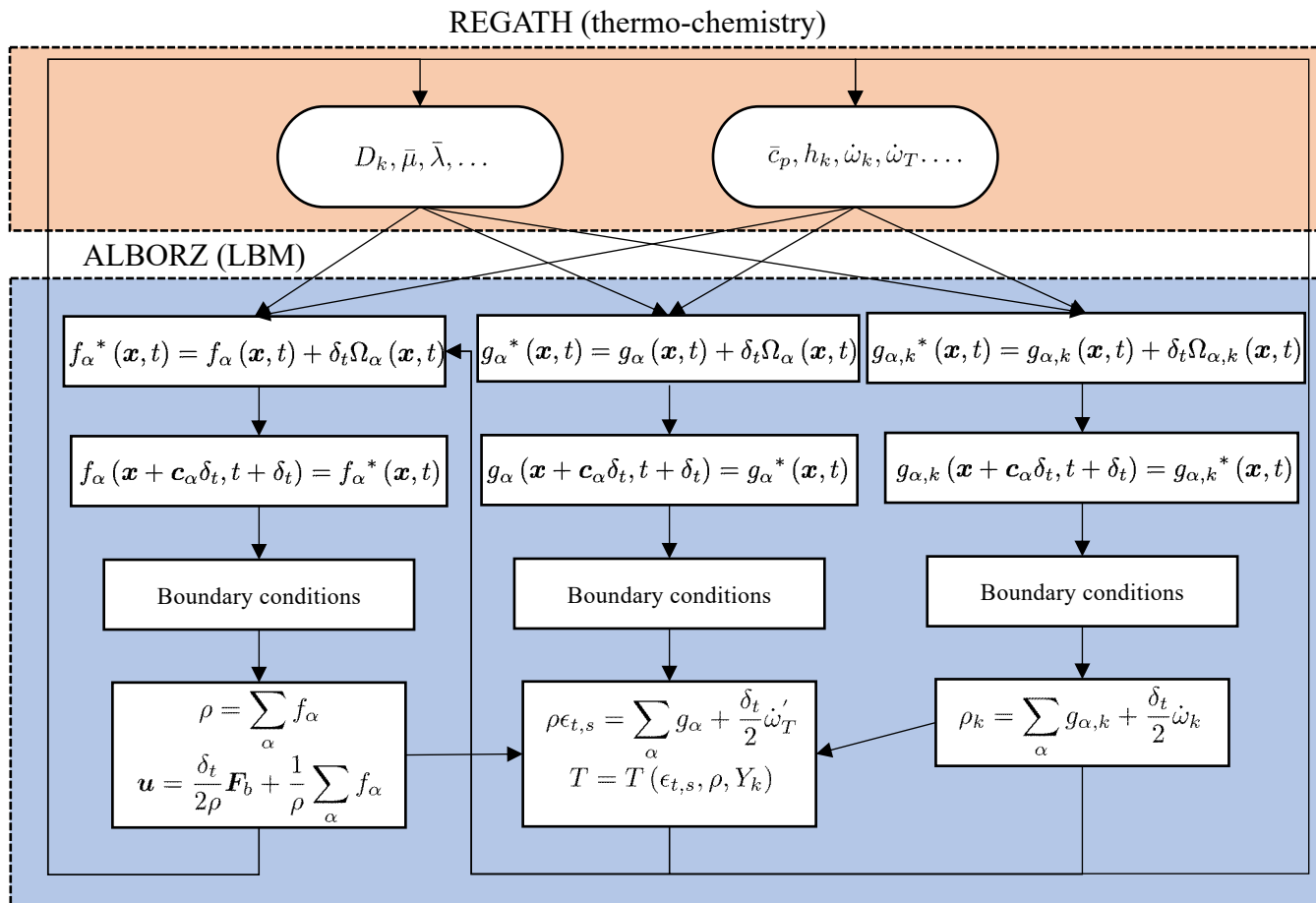


Figure 6.3: Overall algorithm structure and communication scheme for the compressible LBM coupled to LB advection-diffusion solvers for the energy and species mass balance (Approach III).

6.2.1 1-D flame simulations

6.2.1.1 First validation case: 1-D premixed Propane/air flame with simple thermo-chemistry

As a first validation study, the case of a pseudo 1-D freely-propagating premixed Propane/air flame is considered. This configuration consists of a 2-D simulation domain bounded by an inlet and outlet boundary condition in the x -direction and periodic boundary conditions (with only two grid-points) in the y -direction. At the inlet, a given mass flow-rate with a fixed temperature and composition is imposed through a fixed-velocity boundary condition on the flow solver and a set of Dirichlet boundary conditions on the temperature and species

solvers. These boundary conditions correspond to the fresh gas composition. At the outlet, Neumann first-order zero-gradient boundary conditions are imposed on all fields.

The simulations are initialized by imposing respectively fresh and burnt gas compositions, temperature and density on the left and right halves of the domain. Following [216, 47] the dynamic viscosity is approximated through a Sutherland model:

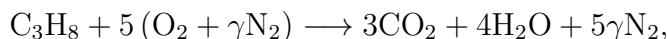
$$\mu = \mu(T^*) \left(\frac{T}{T^*} \right)^\beta, \quad (6.1)$$

where T^* is a reference temperature set to 298K here, $\mu(T^*)$ the dynamic viscosity at this temperature, set to 1.782×10^{-5} kg/m.s and β is a parameter set to 0.69 [216]. The thermal and species diffusion coefficients are determined through fixed Prandtl and Schmidt numbers given in Table 6.1.

Parameter	value
Pr	0.682
$Sc_{C_3H_8}$	1.241
Sc_{O_2}	0.728
Sc_{H_2O}	0.941
Sc_{CO_2}	0.537
Sc_{N_2}	0.682

Table 6.1: Prandtl and Schmidt numbers used in the 1-D Propane/air simulations

To reproduce the test-case as studied in [216], the mixture heat capacity is taken to be constant and equal to 1008 J/kg.K. The chemistry is described through a one-step global reaction:



where $\gamma = 3.76$, and the reaction rate constant k , the activation energy E_a and the temperature exponent β are respectively set to 9.9×10^{-7} m³.mol⁻¹s⁻¹, 125520 J and 0. Furthermore, the overall heat of reaction is taken to be equal to 2.0×10^6 J/mol [216, 7].

An interesting point to discuss here is the choice of δ_x and δ_t with regards to the restrictions on linear stability of each solver. Considering a configuration leading to the highest temperature ratio, i.e. $\phi = 1$, one expects to have a minimum and maximum temperature of 300 and 3070K in the domain leading to $\nu \in [1.52 \times 10^{-5}; 7.68 \times 10^{-4}]$ m²/s, while the maximum velocity in the domain is expected not to exceed 6m/s. As such, for the compressible solver we choose the reference temperature to be 1820K, leading to $\theta \in [0.16; 1.7]$. Setting $\delta_x = 5 \times 10^{-5}$ m, the chosen temperature leads to $\delta_t = 4 \times 10^{-8}$ s. The low Mach number formulation on the other hand can take larger time-steps. The settings are expected to be stable for other equivalence ratios (as other values of ϕ would lead to lower adiabatic temperatures), and as such are used for all simulations reported in this part. Simulations were ran for equivalence ratios, $\phi = \frac{(Y_{C_3H_8}/Y_{O_2})}{(Y_{C_3H_8}/Y_{O_2})_{st}}$, going from 0.5 to 1. The flame front speed is computed by recording its position at different time-steps. Once the speed reaches a steady

value it is recorded as the flame laminar speed. The flame front speed and temperature at different equivalence ratios, as obtained from the three different solvers are compared to reference results obtained using Cantera [217] in Fig. 6.4. It can be observed that apart from

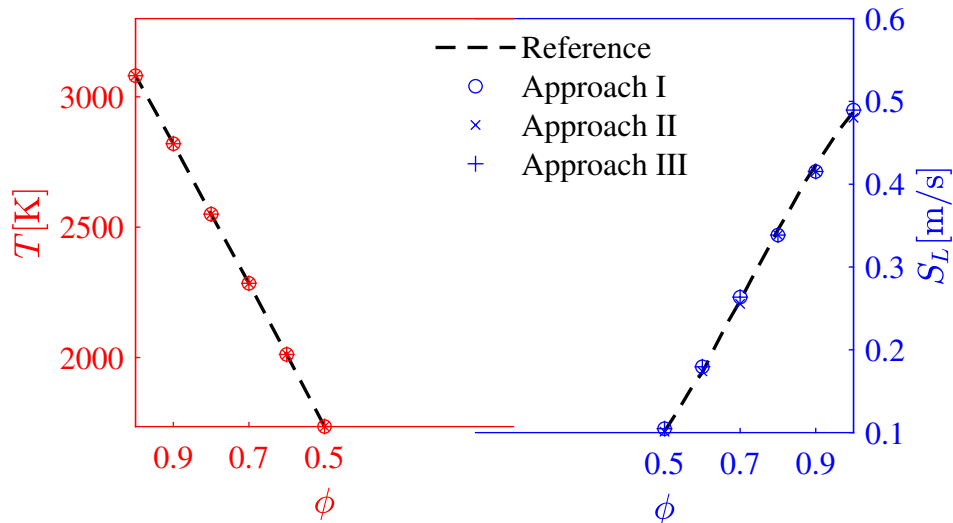
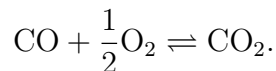
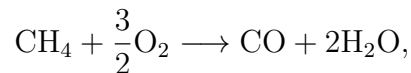


Figure 6.4: Propane/air laminar flame speed and adiabatic temperature obtained using the different approaches.

very minor differences between the three solvers, they are all able to reproduce the correct laminar flame speeds. To better understand the differences between the different schemes their orders of convergence are studied in the next part.

6.2.1.2 Order of accuracy: Methane/Air 1-D freely-propagating flame with BFER scheme

To assess the overall order of accuracy of the proposed solvers, a 1-D freely-propagating Methane/air flame (similar to the previous test-case) is modeled using the BFER 2-step chemistry model [218]. The two steps in this scheme are defined as:



Corresponding reaction rates can be found in appendix F. Detailed transport and thermodynamic properties are used for this simulation. The physical size of the domain is 1 cm. Initially, the domain is divided into two equal size sections. The left-hand side is initialized using fresh gas while the right-hand side is filled with burnt gas. The initial conditions are given in Table 6.2. Similar to the previous test-cases, at the inlet fresh gas composition, temperature and density are imposed along with constant velocity, while the outlet is modeled using zero-gradient boundary conditions.

Simulations were performed using five different grid-sizes, namely 10^{-5} , 1.5×10^{-5} , 2×10^{-5} ,

Parameter	fresh gas	burnt
T [K]	800	2230
u [m/s]	0	0
Y_{CH_4}	0.0393	0
Y_{O_2}	0.2239	0.0682
$Y_{\text{H}_2\text{O}}$	0	0.0883
Y_{CO_2}	0	0.1046
Y_{CO}	0	2.01×10^{-3}
Y_{N_2}	0.7368	0.73689

Table 6.2: Methane/air BFER free flame initial conditions.

3×10^{-5} and 4×10^{-5} m. Given the order of accuracy of the FD time integration scheme employed for the hybrid solvers, a diffusive scaling for the time-step is preferred. However, given the restriction on fluid temperature deviations from the stencil reference temperature, for approaches II and III an acoustic scaling is chosen. The resulting time-step sizes are listed in Table 6.3. After convergence, the flame front propagation speeds were measured

Scheme/ δ_x	10^{-5} m	1.5×10^{-5} m	2×10^{-5} m	3×10^{-5} m	4×10^{-5} m
δ_t I	10^{-5} s	2.25×10^{-5} s	4×10^{-5} s	9×10^{-5} s	1.6×10^{-4} s
δ_t II and III	10^{-5} s	1.5×10^{-5} s	2×10^{-5} s	3×10^{-5} s	4×10^{-5} s

Table 6.3: Grid and time-step sizes used for the different schemes for the Methane/air free flame.

and corresponding errors (as compared to a reference Cantera simulation) were computed. The obtained results are shown in Fig. 6.5. As observed there the first approach is close to second-order accuracy under diffusive scaling. This is to be expected as both the FD solvers and low Mach LB solver are second-order under diffusive scaling. The second approach on the other hand is only first-order accurate under acoustic scaling. As for the previous scheme, this behavior was to be expected as the FD solver is only first-order in time. The third approach is close to second-order accuracy under acoustic scaling. This is because the species and energy balance equations are modeled using LB solvers which using the appropriate correction terms, as used here, are supposed to be second-order accurate under acoustic scaling. It is also worth noting that while second-order accurate, the first approach exhibits larger errors. This can partially be explained by the larger time-step sizes (as compared to approaches II and III) used to perform the simulations. The species and flow field profiles as obtained from the simulation with the highest resolution are shown in Fig. 6.6. To have a full picture of the performances of all approaches, their respective computational times are discussed later in the conclusions. Before that, a number of simulation results in 2- and 3-D are presented in the next subsection.

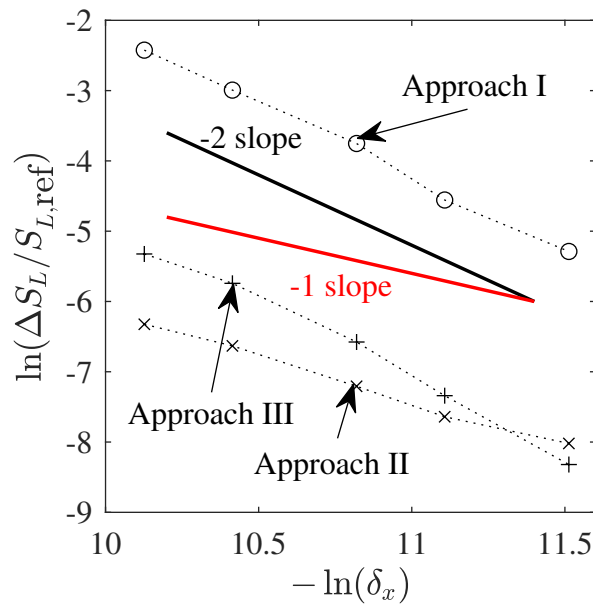


Figure 6.5: Convergence of the different approaches for the Methane/air free flame.

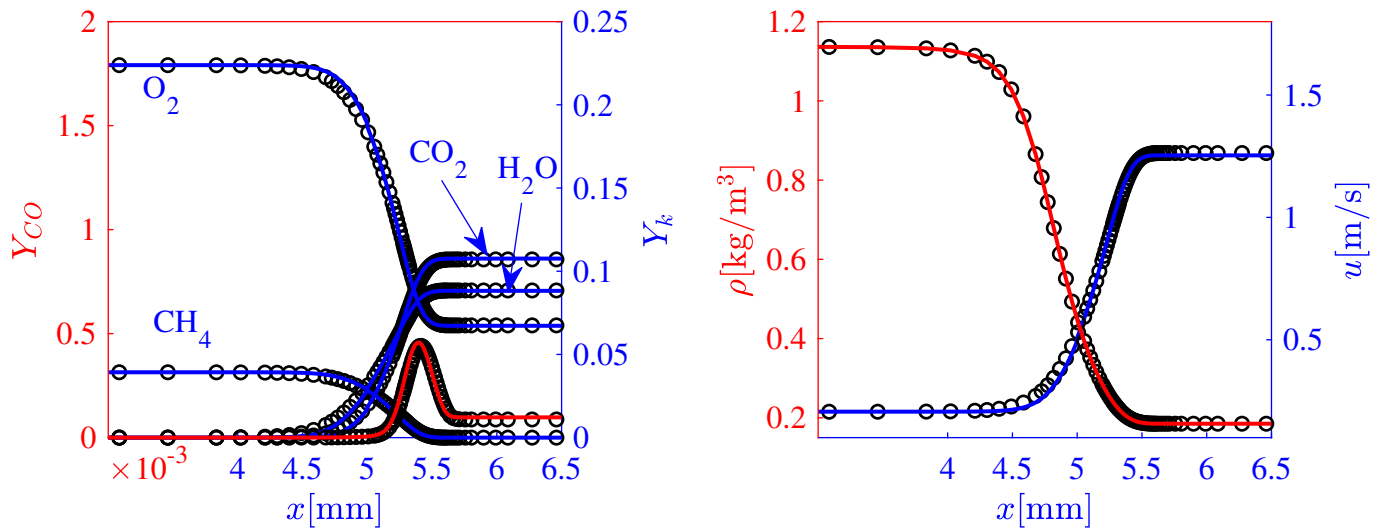


Figure 6.6: (left) species mass fraction and (right) density and velocity profiles at the flame front for the Methane/air 1-D freely propagating flame. Results from the LB simulation (with approach III) with the highest resolution are shown with black symbols while reference profiles from Cantera are shown with plain lines.

6.2.2 Complex configurations

A number of more complex configurations are modeled in this subsection to illustrate the versatility of the solver and its ability to deal with configurations typically encountered in low Mach combustion. For the sake of clarity, unless stated otherwise, only results obtained using approach I are shown.

6.2.2.1 Premixed Propane/air 2-D counterflow flame with simple chemistry

The test-case considered here, is that of a 2-D premixed counterflow burner, similar to the one studied in [7]. The corresponding geometry is shown in Fig. 6.7. As shown there, at

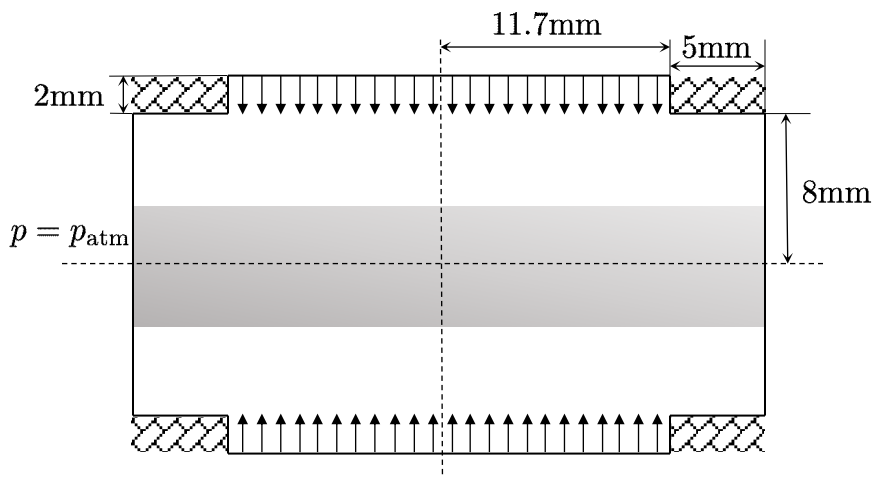


Figure 6.7: Geometrical configuration of the 2-D counterflow premixed Propane/air flame.

the top and bottom inlets, the fresh gas mixture is injected at a constant velocity, at an equivalence ratio of $\phi = 0.6$ and a constant temperature of 300 K, and at the outlets (left and right) a constant pressure is imposed on the flow field while the species and temperature fields are subjected to zero-gradient boundary conditions. At solid walls, zero-gradient BCs are imposed on both temperature and species fields. The simulation is initialized with fresh gas in the blank region in Fig. 6.7 while the grey-colored region is filled with burnt gas. Due to the symmetrical configuration of the burner, only the upper right quadrant is considered in the simulations. The chemical scheme, thermodynamic and transport properties follow those

Parameter	fresh gas	burnt
T [K]	300	1970
ρ [kg/m ³]	1.17	0.162
u [m/s]	0	0
$Y_{\text{C}_3\text{H}_8}$	0.037	0
Y_{O_2}	0.224	0.089
$Y_{\text{H}_2\text{O}}$	0	0.061
Y_{CO_2}	0	0.111
Y_{N_2}	0.739	0.739

Table 6.4: 2-D counterflow burner initial conditions.

set in part 6.2.1.1. The test-case is modeled using both the LB solver and the commercial CFD solver ANSYS-Fluent for comparison. The initial conditions are given in Table 6.4.

Both simulations were performed at atmospheric pressure.

In Fluent, the pressure-based solver is used to model the previously defined flow on a uniform grid of size $\delta x = 2 \times 10^{-5}$ m. The inlet and outlet are respectively modeled using the constant velocity and outflow boundary conditions.

In the LB solver the grid and time-step sizes are respectively set to $\delta x = 5.55 \times 10^{-5}$ m and $\delta t = 5 \times 10^{-7}$ s. It is interesting to note that for approaches II and III to be stable, δt had to be set to $= 4 \times 10^{-8}$ s.

At steady-state, the solutions obtained using both Fluent and the LB solver are compared. First, to quantify the position of the flame front the density and Propane net production rates are compared in Fig. 6.8. As shown in this figure, there is an excellent agreement

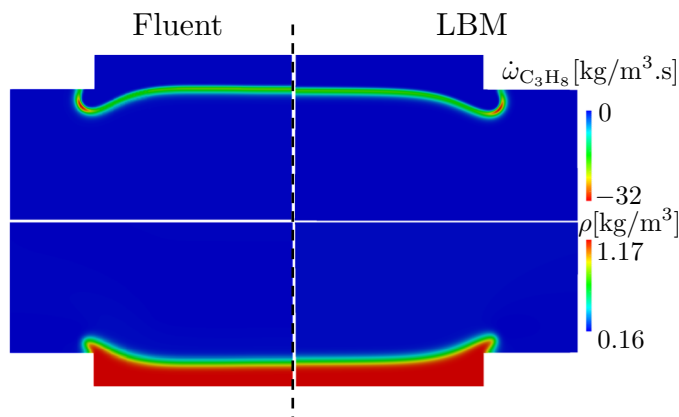


Figure 6.8: Density and Propane consumption rate fields at steady-state as obtained from LBM and Fluent.

concerning position and shape of the flame fronts for both solvers. Furthermore, to verify that the thermal dilatation effect is correctly captured, the y -component of the velocity vectors along the vertical centerline are compared in Fig. 6.9. It is readily observed that the LB solver is able to correctly capture the flow field, and associated dilatation effects.

6.2.2.2 Premixed Propane/air counterflow flame with simple chemistry in 3-D

As an extension to the previous case and to illustrate the ability of the solver to handle 3-D flows, the 3-D version of the previously discussed 2-D counterflow premixed flame is modeled here. All parameters and boundary conditions are similar to the previous case. The geometry in 3-D is shown in Fig 6.10. The simulations are performed on a D3Q27 stencil while the grid and time-step sizes are respectively set to $\delta x = 1.67 \times 10^{-4}$ m and $\delta t = 6 \times 10^{-6}$ s, leading to a simulation domain of $200 \times 200 \times 120$ grid points. The steady-state fields obtained from the LB simulation are displayed in Fig 6.11. In this figure, the flame front represented by a Propane production rate iso-surface is shown in light gray and combustor walls are illustrated with darker gray surfaces. To validate the results, the temperature and species mass fractions along the central vertical line (in the z -direction) are compared to a pseudo 1-D simulation in cylindrical coordinates obtained from REGATH in Fig. 6.12. Though the

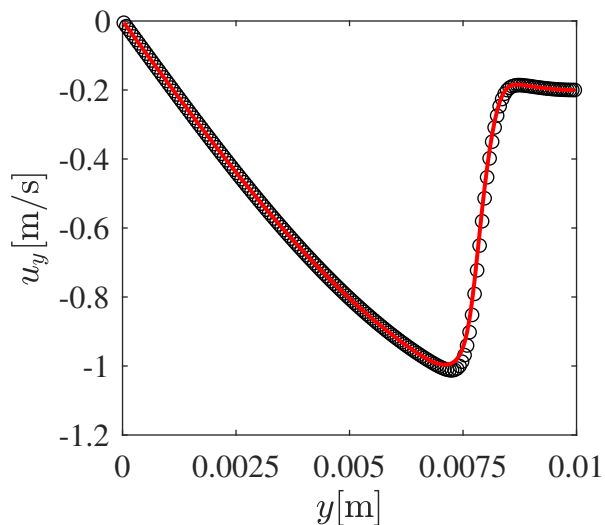


Figure 6.9: Profiles of y -component of velocity on the vertical centerline as obtained from (red plain line) Fluent and (black symbol) lattice Boltzmann simulations.

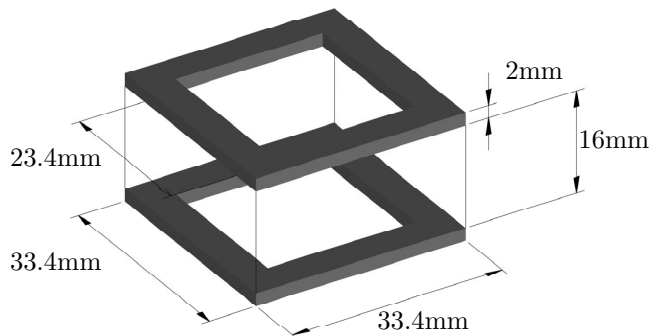


Figure 6.10: Geometrical configuration of the 3-D counter flow premixed Propane/Air flame.

LB simulation is 3-D while the solution from REGATH is 1D-axisymmetric, the distance from the vertical centerline to the domain boundaries is large enough so that boundary effects are negligible. As for all previous test-cases, the results obtained with the LB solver are in excellent agreement with their REGATH counterparts corresponding to a pure FD approximation.

6.2.2.3 Methane/air 2-D coflow diffusion flame with two-step chemistry

As a third configuration, to show that the proposed models are able to handle both premixed and diffusion flames, a 2-D coflow Methane/air diffusion flame is considered. The simulation uses the same thermo-chemical settings as those used in part 6.2.1.2, i.e. the BFER scheme along with detailed transport models. The geometrical configuration along with boundary conditions are given in Fig. 6.13 and Table 6.5. The fuel is injected at the center while a mixture of O_2/N_2 comes in from the sides. The time-step and grid-sizes were respectively

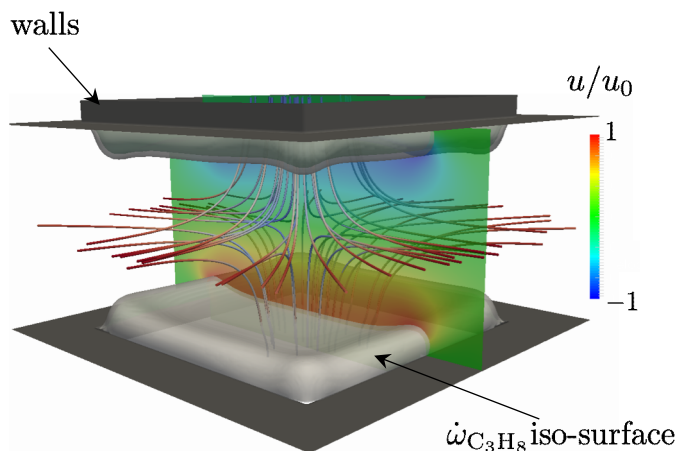


Figure 6.11: Flow field obtained at steady-state for the 3-D counterflow test-case. Shown in this figure: Iso-surface of Propane consumption rate $\dot{\omega}_{C_3H_8}$ in light gray; streamlines colored with normalized velocity magnitude (see color scale); cut showing the z -component of the velocity vector in the central plane (see color scale).

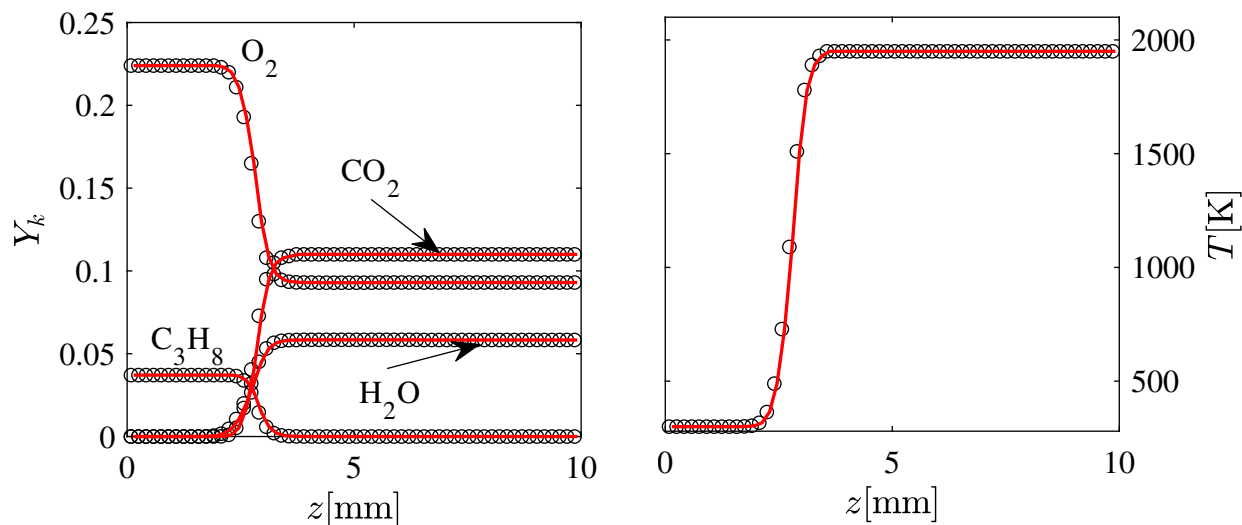


Figure 6.12: Profiles of (left) species mass fractions and (right) temperature along the centerline in the z -direction as obtained from (red plain lines) REGATH and (black symbols) LB simulation.

set to $\delta t = 9 \times 10^{-8}$ s and $\delta x = 3 \times 10^{-5}$ m. The choice of the time-step size was mainly dictated by the chemistry and not stability limits of solvers. The same configuration was ran on Fluent. The fluid velocity, temperature, CO, CO₂ and O₂ mass fraction fields at steady-state are shown in Fig. 6.14. The results obtained from this simulation are compared to their counterpart from Fluent in Fig. 6.15. As observed there, the species profiles are in excellent agreement with the reference solver. Small discrepancies are observed in the

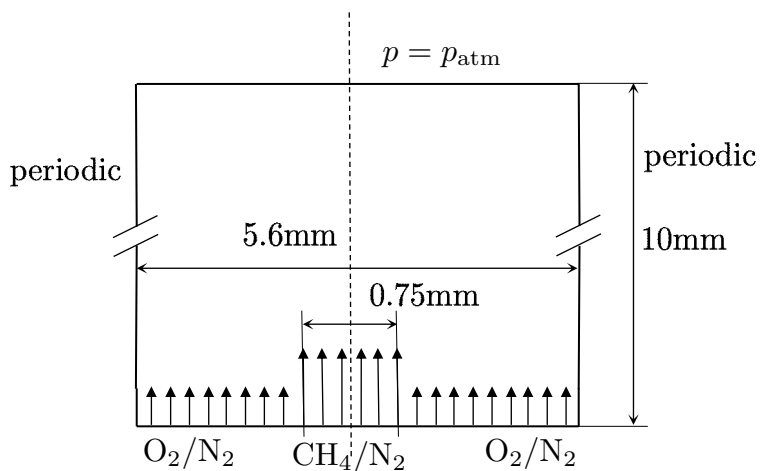


Figure 6.13: Geometrical configuration of the 2-D coflow Methane/air flame.

Parameter	central inlet	left/right inlets
T [K]	950	950
u_0 [m/s]	0.8	0.5
Y_{CH_4}	0.1	0
Y_{O_2}	0	0.224
$Y_{\text{H}_2\text{O}}$	0	0
Y_{CO_2}	0	0
Y_{CO}	0	0
Y_{N_2}	0.9	0.776

Table 6.5: 2-D Methane/air coflow burner boundary conditions data.

velocity profiles near the top outlet. These discrepancies can be attributed, at least partly, to the different treatment of outlet boundaries in the LB solver and Fluent simulations.

6.2.2.4 Flame/vortex interaction

The last case to be treated here illustrates the capability of the solver to model turbulent flows, by showing that it can reproduce different interaction regimes between a flame front and flow structures.

Looking into premixed flame interaction with turbulent flow structures, five distinct regimes have been identified [10], as illustrated through a diagram in Fig. 6.16 as a function of characteristic speeds and sizes of the flow structure and flame:

- *Laminar flame*: The flow remains laminar with minor wrinkling in the flame front,
- *Wrinkled flamelet*: The flow structure characteristic size is larger than the flame thickness and can not penetrate into the flame. However the turn-over velocity of the eddy

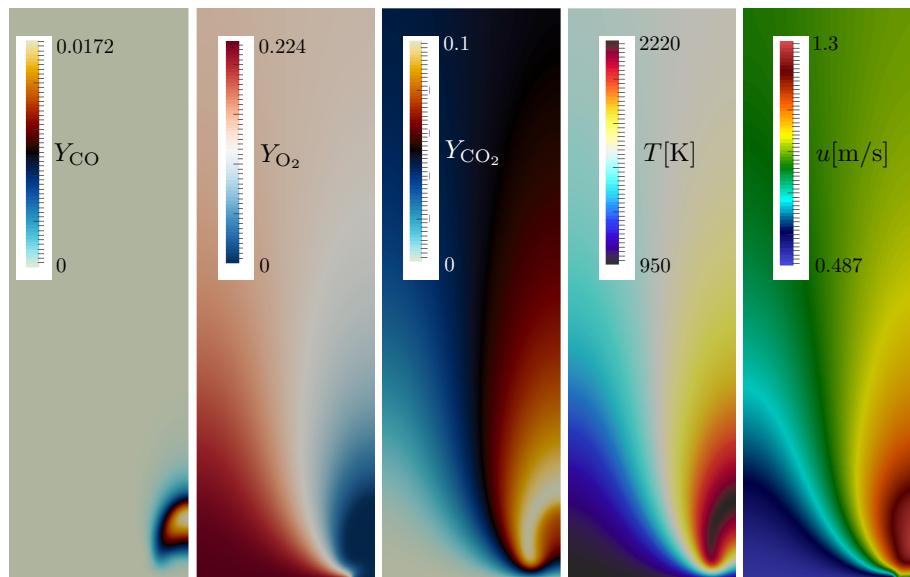


Figure 6.14: Steady-state species, velocity and temperature fields for the Methane/air coflow diffusion flame.

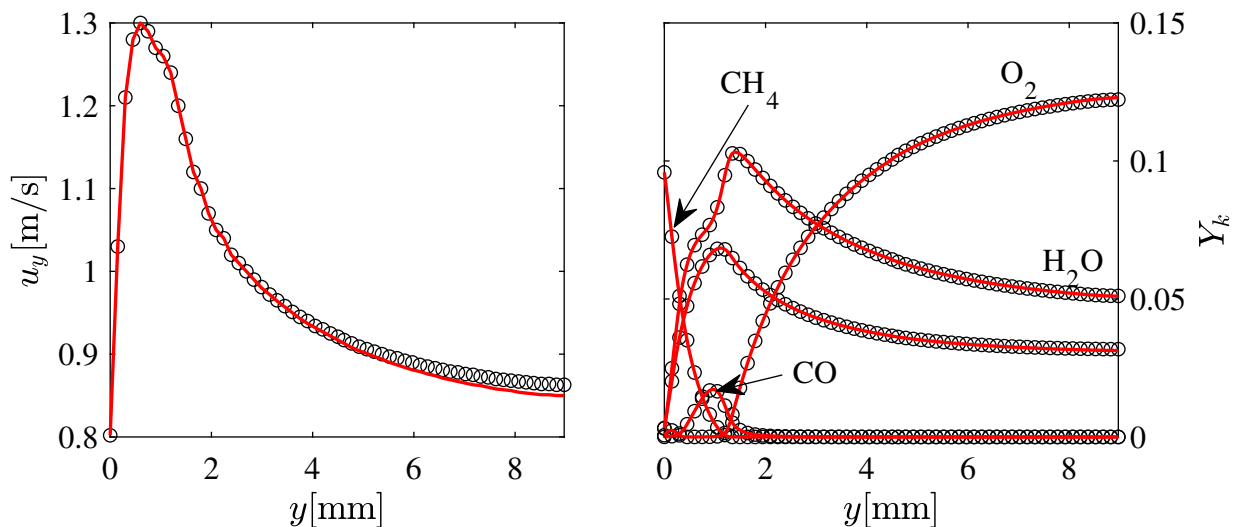


Figure 6.15: (left) velocity and (right) species mass fraction profiles along the vertical centerline as obtained from (red plain line) Fluent and (black symbols) the LB solver.

is smaller than the flame front speed, consuming the fresh gas before it can form a pocket,

- *Corrugated flamelet*: As for the previous regime, the flow structure is bigger than the flame thickness. Here the flow structure is able to stretch the flame front and eventually create small pockets with sizes comparable to that of the fluid structure,
- *Thin reaction zones*: The flow structure is smaller than or comparable to the flame

thickness, however it is still bigger than the thickness of the inner layer (typically one-tenth of the flame thickness). While not able to penetrate into the inner layer, the flow structure enhances energy and mass transfer in the pre-heat zone,

- *Broken reaction zone*: Mixing due to small turbulent structure becomes faster than the chemistry, and can lead to local extinction.

Indeed, it has been observed that flow structure size (as compared to the flame thickness) and energy (or velocity) are two parameters determining the effect of the flow structure on the flame front. To mimic flow/flame interactions, a number of studies have focused

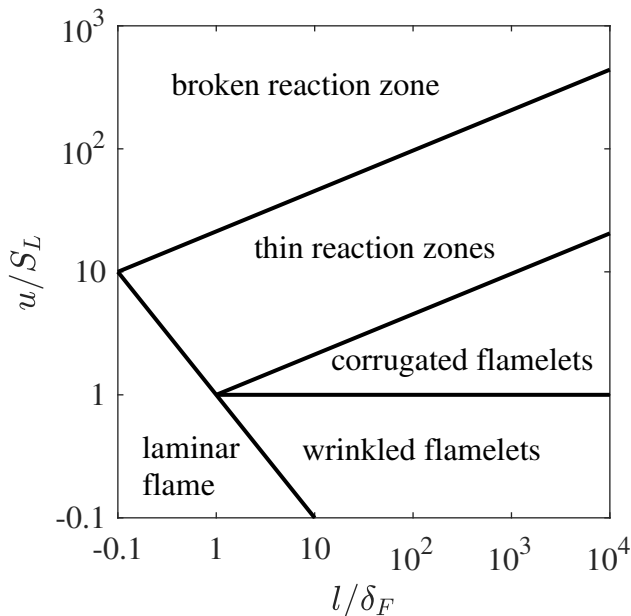


Figure 6.16: Regime diagram for premixed turbulent combustion [10].

on direct numerical simulations of the interaction between a pair of vortices and a flame front [219, 220]. As such, following those studies, the interaction of a Methane/air premixed flame front with two counter-rotating Lamb-Oseen vortices [221] is considered in a 2-D configuration. The overall configuration is illustrated in Fig. 6.17. Such a configuration, among other sources, was also studied with details in [222, 223, 2]. The simulations consist of a rectangular domain of size $L_x \times L_y$, with the flame front initially placed at $x = L_x/2$. A fresh gas mixture at equivalence ratio of 0.7 and temperature of 800K fills the left-hand side of the domain while the right-hand side is filled with burnt gas. Two counter-rotating Lamb-Oseen vortices of radius r_c are then placed at a horizontal distance d from the flame front. While top and bottom boundaries are periodic, at the inlet (on the left) constant temperature, composition and flow-rates are enforced. The outlet (on the right) is modeled using zero-gradient boundary conditions. The Lamb-Oseen vortices are initialized as:

$$u_\theta(r) = \frac{\Gamma}{2\pi r} \left[1 - \exp\left(-\frac{r^2}{r_c^2}\right) \right], \quad (6.2)$$

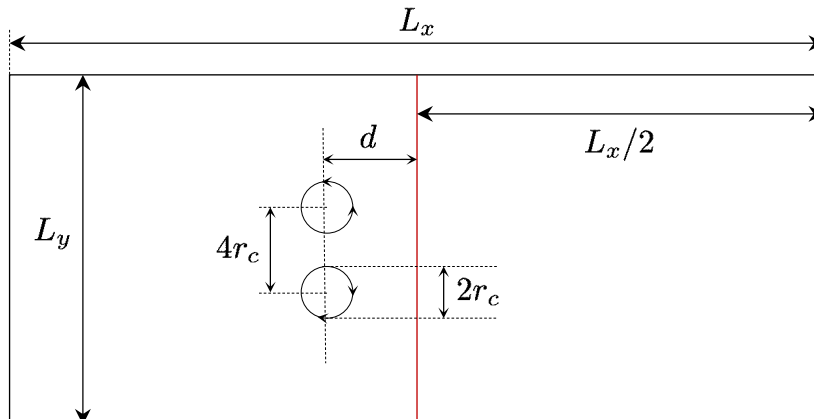


Figure 6.17: Overall configuration of the 2-D premixed flame/vortex interaction case.

where Γ is the vortex strength (also called vortex circulation) expressed in m^2/s and r the radial distance from the vortex center. For all cases studied here, the BFER chemical scheme is used to model the flame [218], δ_x is set to $4.26 \times 10^{-5}\text{m}$ and $\delta_t = 6 \times 10^{-8}\text{s}$. Furthermore, L_x is set to 42.6mm and L_y to 17.04mm. The species and temperature profiles are initialized using the solution of a 1-D freely-propagating flame at $\phi = 0.7$. The vortices are then initialized at a distance of $8r_c$ from the flame front.

Twelve different combinations of vortex strength and core radius are considered here. They are listed in Table 6.6. Before going into simulation of the different configurations and

case	$\Gamma[\text{m}^2/\text{s}]$	$r_c[\text{m}]$	$u_{\text{max}}[\text{m/s}]$
1	6.71×10^{-2}	3.43×10^{-4}	22.27
2	3.355×10^{-2}	3.43×10^{-4}	11.14
3	1.6775×10^{-2}	3.43×10^{-4}	5.57
4	8.3875×10^{-3}	3.43×10^{-4}	2.78
5	6.71×10^{-2}	1.715×10^{-4}	44.54
6	3.355×10^{-2}	1.715×10^{-4}	22.27
7	1.6775×10^{-2}	1.715×10^{-4}	11.14
8	8.3875×10^{-3}	1.715×10^{-4}	5.57
9	6.71×10^{-2}	8.575×10^{-5}	89.08
10	3.355×10^{-2}	8.575×10^{-5}	44.54
11	1.6775×10^{-2}	8.575×10^{-5}	22.27
12	8.3875×10^{-3}	8.575×10^{-5}	11.14

Table 6.6: Characteristics of considered configurations for the vortex/flame interaction study.

sets of parameters, a first simulation (corresponding to case number 1) was performed. The

resulting iso-temperature contours at different stages of the interaction were then extracted and compared to simulations reported in [2], performed with AVBP. Given that there were minor differences between the present study and that reported in [2], such as initial distance between the vortex pair and flame front, the comparison is only intended as a qualitative validation of the solver. Given that the study presented here does not make use of grid refinement, resolving the flame front and using the same domain size as that in [2] would have been time-consuming. Temperature fields at three stages of the pocket formation process as obtained from LB simulations and results from [2] are shown in Fig. 6.18. A good agreement, in terms of pocket size and shape, can be observed here. The different stages

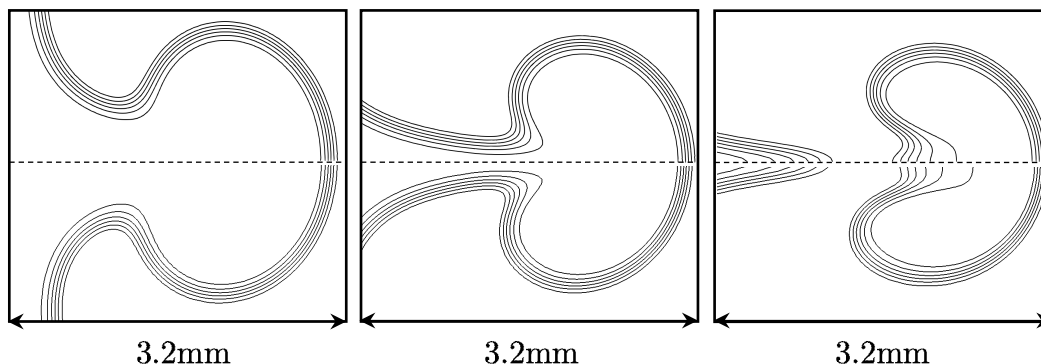


Figure 6.18: Snapshots of iso-temperature contours (from 1000 to 2000K with $\delta T = 200\text{K}$) at three stages of the pocket formation process as obtained (bottom halves) from LB simulations and (top halves) from [2] using AVBP.

of the pocket formation process are further illustrated in Fig. 6.19 via snapshots of the fuel mass fraction field at four different times. In the first three snapshots, the flame is stretched around the pair of vortices. Given that the rotation velocity of the vortices is larger than the flame speed they take a pocket of fresh gas into the burnt gas area. After entering the burnt gas area, as the vortices move, the pocket of fresh gas gets smaller due to consumption by the flame around the vortices. Finally, approximately 0.3ms after the initial interaction between the flame and the vortices, the pocket of fresh air disappears.

The simulations were then repeated for all sets of parameters in Table 6.6. The interactions between the vortices and flame front are illustrated in Fig. 6.20 through the temperature fields. Having in mind that at the fresh gas temperature and equivalence ratio considered here the flame front speed is $S_L = 1.79\text{m/s}$ while the thickness is $\delta_F = 3.43 \times 10^{-4}\text{m}$, it can be seen that for the largest vortices, at $u_{\text{max}} = 2.78\text{m/s}$, the flame propagation dominates over the convective flux induced by the vortex and the fresh gas pocket is not formed. Although the initial maximal velocity in the vortex is larger than the flame front speed, one must also take into account dissipative losses before the vortex pair gets to the flame front. At higher velocities, it can be observed that the vortex pair is able to form a pocket of fresh gas in the burnt gas region. Looking at simulations with smaller vortices, it can also be seen that the size of the pocket, as expected, is proportional to the size of the vortices. Furthermore, as the size of the perturbation gets smaller, and closer to the flame thickness, $\delta_F = 3.43 \times 10^{-4}\text{m}$, the vortices are unable to form pockets and only induce wrinkling in the flame front.

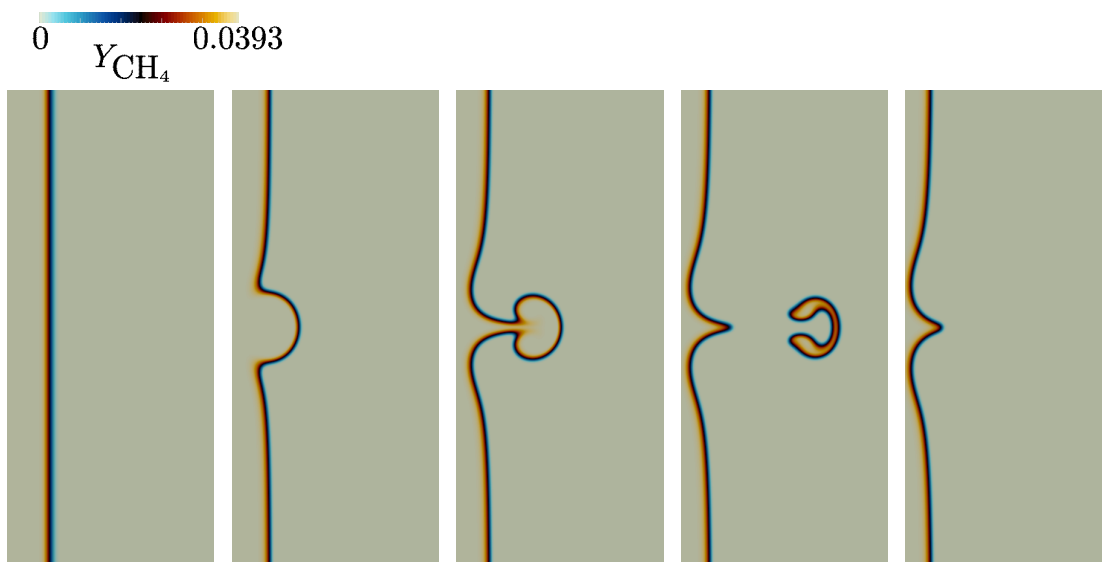


Figure 6.19: Fuel mass fraction fields at three different times, i.e. (from left to right): 0, 0.08, 0.16, 0.24 and 0.32ms for case 1.

Simulations performed in this section showed that the LB-based numerical schemes considered in the present manuscript can be used to model low Mach number combustion in multi-dimensional configurations, for both premixed and diffusion flames, and can correctly capture flame/flow interaction.

6.3 Concluding remarks

Out of the three different approaches considered in this chapter it was observed that the compressible solver based on thermal Hermite expansion had a more limited stability domain (at least based on first-neighbor stencils and using collision models considered in this manuscript). The low Mach formulation on the other hand, although not completely eliminating acoustic effects, allowed for larger time-steps. Furthermore, for the compressible formulation to be usable for complex flows, more advanced collision models along with at least a third-order EDF must be employed. These additional components surely affect the performances of the solver. To better illustrate their effect, the computational performances of different collision models in terms of million lattice updates per second (MLUPS) on a D3Q27 stencil and a $128 \times 128 \times 128$ domain and using a single processing unit were measured. The results are shown in Fig. 6.21. It must be noted that these performances only account for a single-species isothermal flow. Furthermore, the code not having been optimized, and written to be modular more than efficient, these results do not reflect best possible performances. As shown there, on a D3Q27 stencil, the addition of third-order terms has a non-negligible impact on the performances of the solver. Taking into account the full Hermite expansion in the EDF (order six) introduces a factor of nine in the computation

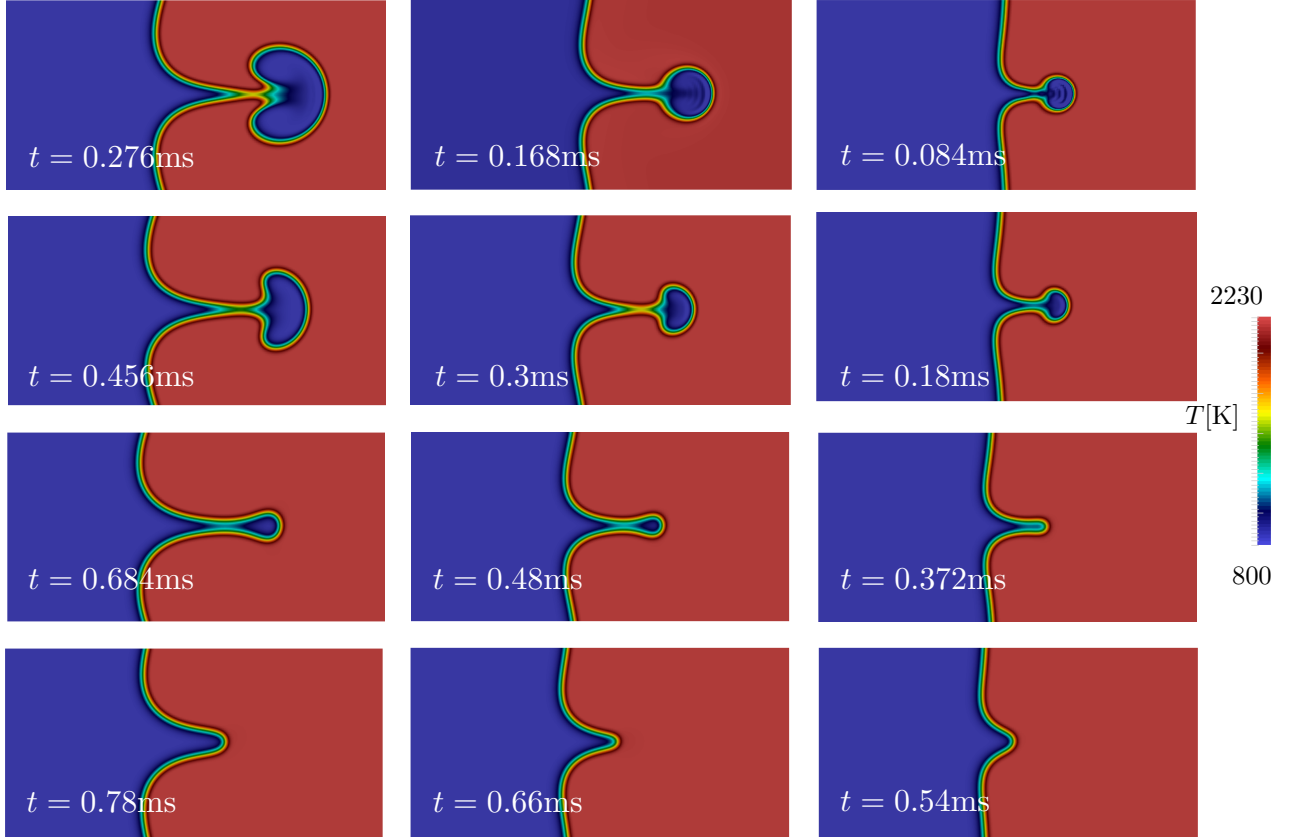


Figure 6.20: Instantaneous snapshots of temperature field as obtained for different sets of parameters: (from left to right) vortex core radii 3.43×10^{-4} , 1.715×10^{-4} and 8.575×10^{-5} m; and (from top to bottom) vortex strengths 6.71×10^{-2} , 3.355×10^{-2} , 1.6775×10^{-2} and $8.3875 \times 10^{-3} \text{m}^2/\text{s}$.

time of the scheme. Based on these results, the temperature-scaled central moments MRT collision operator is the most efficient way to take into account the full Hermite expansion in EDF and extend the stability domain of the collision operator as it only introduces a factor of 2.5 in the computation time. The low Mach formulation on the other hand, not needing the third-order components of the EDF and relying on a SRT collision operator is observed to match the performances of the bare second-order SRT solver and outperform the compressible solver by a factor of 2.7. Throughout the different simulations, it was also observed that using finite differences to solve additional fields in 3-D, i.e. energy and species mass balance, would result in a performance of 5.59 MLUPS per field while the corresponding LB solver would peak at 5.1 MLUPS for the smallest possible stencil, i.e. D3Q7. It must be noted that time spent on evaluating thermo-physical parameters and source terms is not taken into account here. The coupling to REGATH and computation of thermo-physical parameters and source terms, assuming a flow with three species and a single reaction accounts for approximately 60 percent of the computation time. The large amount of resources spent

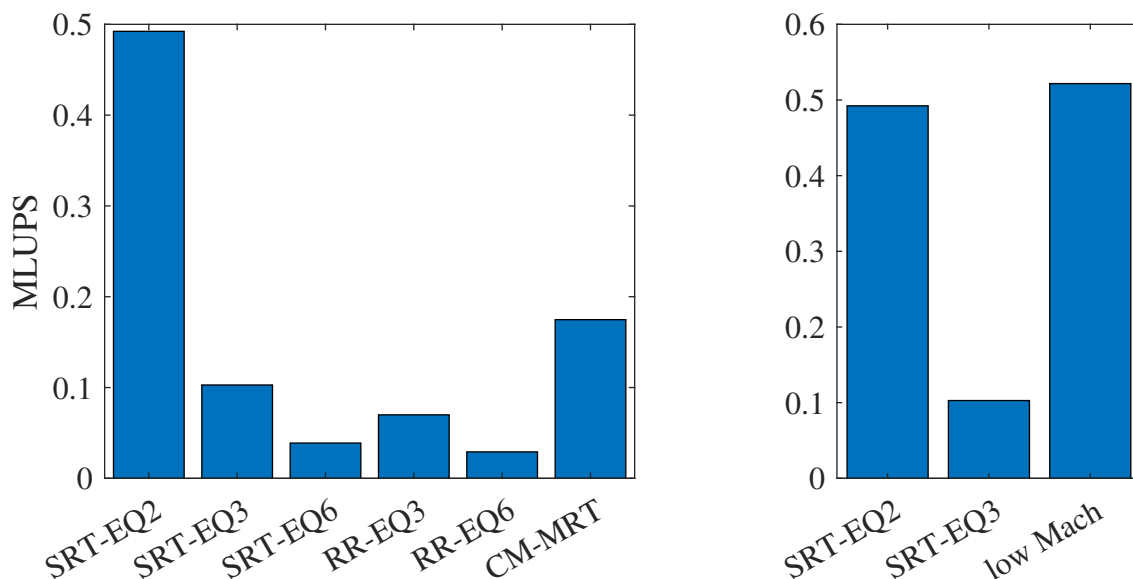


Figure 6.21: Performances of (left) the different collision models for the compressible formulation and (right) comparison of compressible solver to low Mach formulation. EQ N designates the order of the EDF, CM-MRT refers to the MRT collision operator in temperature-scaled central moment space, RR to the recursive regularized collision operator and low Mach to the low Mach dilatible solver with a second-order EDF, in terms of MLUPS, short for Million Lattice Updates Per Second.

on the evaluation of these parameters using REGATH might be explained, at least in part, by the fact that ALBORZ is a C++ code while REGATH is written in Fortran. Given the different approaches to memory allocation for multi-dimensional arrays in each one of these programming languages, non-negligible resources and time are spent on converting data arrays between them. As such, elaboration of a more efficient communication scheme between the two solvers is expected to have non-negligible impact on the performances of the overall code.

In conclusion, while all three approaches considered in this section are able to model low Mach number combustion, the low Mach formulation of section 5.1 coupled to FD solvers (approach I) for the additional fields allows both for larger time-steps and better performances. Furthermore, the use of FD solvers for energy and species balance equations allows for more flexibility in terms of the order of discretization in both space and time. It must also be noted that while FD solvers based on a first-order time-discretization were slightly faster than their LB counterparts, the latter were second-order accurate under both acoustic and diffusive scaling. To achieve a similar order of accuracy (for example using a second-order RK scheme) the cost would nearly double. The compressible solver on the other hand is a promising formulation for fully compressible flows, and can be further improved through concepts such as flow state-adaptive discretization of the distribution function. Some of these concepts and possible directions are reviewed and studied in the next chapter.

Chapter 7

Shifted stencils: A promising approach to extend the stability domain of the lattice Boltzmann method

Contents

7.1	Adaptive phase-space discretization of distribution function: brief overview	153
7.2	Galilean invariance of Gauss-Hermite quadratures	154
7.3	Shifted stencils with on-lattice streaming	155
7.4	Final remarks	162

Disclaimer

Part of this chapter has been published in:

[1] S.A. Hosseini, C. Coreixas, N. Darabiha and D. Thévenin. Extensive analysis of the lattice Boltzmann method on shifted stencils. *Physical Review E*, 100(6), p.063301, 2019

7.1 Adaptive phase-space discretization of distribution function: brief overview

Throughout the different sections of the present thesis, it was shown and observed through both theoretical analysis (asymptotic and spectral) and numerical applications that the non-dimensionalization strategy and parameters, also known as reference state, have a huge impact on the performances of the LB-based solver. They impact both stability and accuracy of the scheme. The error terms appearing at higher-order levels of the CE expansion, of no physical interest, usually tied to higher-order (not supported by the stencil) moments of the EDF are controlled by the scaling of the conserved variables. In chapters 2 and 5 it was clearly shown that deviations of the local flow state from reference temperature $\theta = 1$ tied to δ_x^2/δ_t^2 and velocity $\mathbf{u} = 0$ resulted in reduced stability domains and larger errors coming from higher-order moments. The same behavior was also observed for advection-diffusion based solvers in chapter 4. While one would expect the use of higher-order quadratures to help broaden the stability domain and reduce errors, their effect remains limited. Furthermore, these quadratures come at much larger computational costs (especially in terms of memory consumption and memory access bandwidth). A new concept, first introduced in [224, 225, 226] and later improved in [95], extended the applicability domain of the LBM by using adaptive discrete velocity stencils. While new in the LBM community, it is interesting to note that this approach to extending discrete Boltzmann solvers to high Mach number applications had already been proposed in [11, 12, 13] in the context of kinetic solvers with Eulerian discretization of physical space. In the model proposed in [11, 12, 13] the origin of the discrete velocity set was determined by the local fluid velocity while its unit was tied to the local internal energy (tied to local temperature). This approach is illustrated in Fig. 7.1. In this figure, the blue dashed vectors represent the discrete velocities used for phase-space discretization. These discrete velocities are composed of the local fluid velocity (red vector) and *peculiar velocity* components (black vectors), as appearing in the Maxwell-Boltzmann EDF. The peculiar components, are scaled with the local internal energy. The final discrete velocities are therefore direct results of the local fluid state. Another interesting point noted in [12] is that for a stencil based on first neighbors, in the limit of vanishing viscosities, this approach leads to the Euler equations. The benefits of such an adaptive construction of the discrete velocities are limited in the context of an Eulerian discretization of space, as the solver would still be limited by the CFL condition. The LB formulation however, based on an exact integration of the convection term in the Boltzmann equation could benefit much more from an adaptive reconstruction of the discrete populations, as it would guarantee that numerical scheme characteristics embed the analytical (from the continuous PDE) domain of dependence. That is why Sun et al. were able to model high Mach number flows using this approach and the LBM formalism in [224, 225, 226]. Adaptive discrete velocities were recently updated (with a predictor-corrector formulation) and reformulated in a more consistent theoretical framework in [95] as the PonD (Particles on Demand) formulation. In the PonD method, the populations are not guaranteed to fall on a discrete grid-point after the streaming step, as the discrete velocities have a continuous component stemming from the local fluid speed. As such, the collision and streaming steps are supplemented with a

reconstruction step (of populations on the discrete grid-points) using Lagrange polynomials. An on-grid version of the method (minus the adaptive nature of the velocity shift) was also used in [94]. To clarify the effect of adaptive stencils and their potential in modeling flows

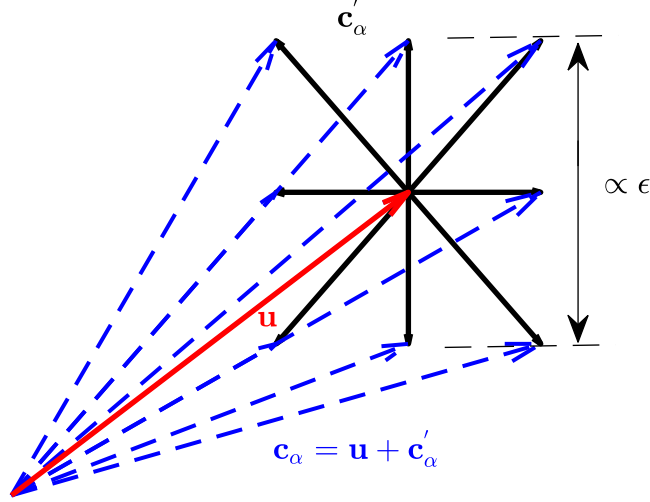


Figure 7.1: The concept of adaptive stencils as proposed in [11, 12, 13].

involving large temperature variations and Mach number, as a proof of concept, we will present a brief numerical and theoretical analysis of the LBM on shifted stencils.

7.2 Galilean invariance of Gauss-Hermite quadratures

To demonstrate the Galilean invariance of the Gauss-Hermite quadrature, one can start with the Maxwell-Boltzmann EDF and write it in a non-dimensional form as:

$$f^{(eq)}(\boldsymbol{\xi}^*, \mathbf{u}^*, \theta) = \rho (2\pi\theta)^{-D/2} \exp\left(-\frac{(\boldsymbol{\xi}^* - \mathbf{u}^*)^2}{2\theta^*}\right), \quad (7.1)$$

where D is the physical dimension of the system, $\theta^* = \frac{k_B T/m}{c_s}$ while $\boldsymbol{\xi}^* = \frac{\boldsymbol{\xi} - \mathbf{U}}{c_s}$ and $\mathbf{u}^* = \frac{\mathbf{u} - \mathbf{U}}{c_s}$. With this change of variable the reference velocity changes from zero to \mathbf{U} , while the reference sound speed is set to c_s . Proceeding as for the classical stencils to expand the EDF in terms of Hermite polynomials [90, 227, 88]:

$$f^{(eq)}(\boldsymbol{\xi}^*, \mathbf{u}^*, \theta^*) = w(\boldsymbol{\xi}^*) \sum_{n=0}^{\infty} \frac{1}{n!} \mathbf{a}_n^{(eq)}(\mathbf{u}^*, \theta^*) : \mathcal{H}_n(\boldsymbol{\xi}^*), \quad (7.2)$$

where the weight function $w(\boldsymbol{\xi}^*)$ is defined as:

$$w(\boldsymbol{\xi}^*) = (2\pi)^{-D/2} \exp\left(-\frac{\boldsymbol{\xi}^{*2}}{2}\right), \quad (7.3)$$

one obtains the first few Hermite polynomials as a function of the re-defined velocities:

$$\mathcal{H}_0 = 1, \quad (7.4a)$$

$$\mathcal{H}_{1,i_1} = \xi_{i_1}^*, \quad (7.4b)$$

$$\mathcal{H}_{2,i_1 i_2} = \xi_{i_1}^* \xi_{i_2}^* - \delta_{i_1 i_2}, \quad (7.4c)$$

$$\mathcal{H}_{3,i_1 i_2 i_3} = \xi_{i_1}^* \xi_{i_2}^* \xi_{i_3}^* - [\xi_{i_1}^* \delta_{i_2 i_3}]_{\text{cyc}}, \quad (7.4d)$$

$$\mathcal{H}_{4,i_1 i_2 i_3 i_4} = \xi_{i_1}^* \xi_{i_2}^* \xi_{i_3}^* \xi_{i_4}^* + [\delta_{i_1 i_2} \delta_{i_3 i_4}]_{\text{cyc}} - [\xi_{i_1}^* \xi_{i_2}^* \delta_{i_3 i_4}]_{\text{cyc}} \quad (7.4e)$$

It is interesting to note that the forms and expression of the polynomials are exactly similar to those in Eq. 2.44. Using these polynomials and the EDF, the corresponding coefficients can be computed:

$$a_0^{(eq)} = \rho, \quad (7.5a)$$

$$a_{i_1}^{(eq)} = \rho u_{i_1}^*, \quad (7.5b)$$

$$a_{i_1 i_2}^{(eq)} = \rho u_{i_1}^* u_{i_2}^* + \rho (\theta^* - 1) \delta_{i_1 i_2}, \quad (7.5c)$$

$$a_{i_1 i_2 i_3}^{(eq)} = \rho u_{i_1}^* u_{i_2}^* u_{i_3}^* + \rho (\theta^* - 1) [u_{i_1} \delta_{i_2 i_3}]_{\text{cyc}}, \quad (7.5d)$$

$$a_{i_1 i_2 i_3 i_4}^{(eq)} = \rho u_{i_1}^* u_{i_2}^* u_{i_3}^* u_{i_4}^* + \rho (\theta^* - 1)^2 [\delta_{i_1 i_2} \delta_{i_3 i_4}]_{\text{cyc}} + \rho (\theta^* - 1) [u_{i_1}^* u_{i_2}^* \delta_{i_3 i_4}]_{\text{cyc}}. \quad (7.5e)$$

As for the Hermite polynomials it is readily observed that, setting $U = 0$ and c_s to $\sqrt{k_B T_0 / m_0}$, one would recover the classical LBM formulation Hermite coefficients. Discretizing phase-space using the Gauss-Hermite quadrature [227, 88], at order three for example, one obtains exactly the same non-dimensional abscissae \mathbf{c}_α^* with (in the case of the D2Q9 stencil) $c_{\alpha,i}^* \in \{-\sqrt{3}, 0, \sqrt{3}\}$, and corresponding weights, i.e. $w_\alpha = \Pi_{i=x,y} w_{\alpha,i}$. This clearly establishes the Galilean invariance of the phase-space discretization procedure. To better convey the possibilities of such an approach let us first write down the resulting discrete EDF (expanded up to order two for simplicity) in terms of flow field variables:

$$f_\alpha^{(eq,2)} = w_\alpha \rho \left[1 + \frac{(\mathbf{c}_\alpha - \mathbf{U}) \cdot (\mathbf{u} - \mathbf{U})}{c_s^2} + \frac{[(\mathbf{c}_\alpha - \mathbf{U}) \cdot (\mathbf{u} - \mathbf{U})]^2}{2c_s^4} - \frac{(\mathbf{u} - \mathbf{U})^2}{2c_s^2} + \frac{[(\mathbf{c}_\alpha - \mathbf{U})^2 - D] (\theta^* - 1)}{2c_s^4} \right]. \quad (7.6)$$

Setting $\mathbf{U} = 0$ and $c_s = \frac{\delta_x}{\delta_t \sqrt{3}}$ one recovers the classical LBM formulation.

7.3 Shifted stencils with on-lattice streaming

In Eq. 7.6, setting $c_s = \frac{\delta_x}{\delta_t \sqrt{3}}$ and $\mathbf{U} = \mathcal{N}_x \frac{\delta_x}{\delta_t} \mathbf{e}_x + \mathcal{N}_y \frac{\delta_x}{\delta_t} \mathbf{e}_y$, where \mathbf{e}_x and \mathbf{e}_y are the unit vectors in the x - and y -directions and \mathcal{N}_x and \mathcal{N}_y integer constants, one can obtain *shifted* stencils with on-lattice propagation. Four sample D2Q9 shifted stencils are shown in Fig. 7.2.

Shifted stencils are very interesting as they retain all the main advantages of the LBM

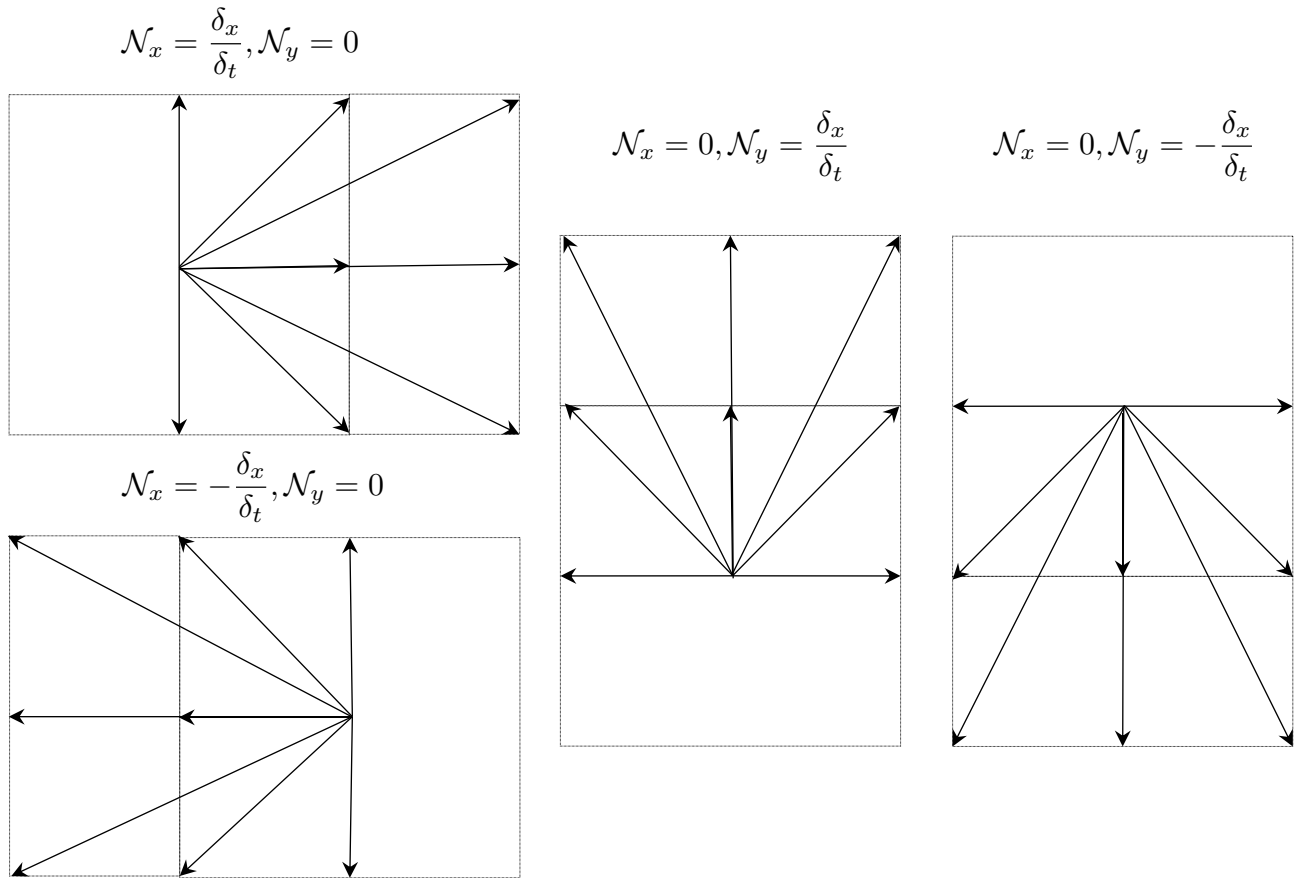


Figure 7.2: Shifted stencils as obtained through introducing unit shift velocities in the x - and y -directions.

formulation, namely exact advection step and linear collision operator. Furthermore, there is no computational overhead going from classical stencils to shifted ones. The shift in the stencil allows one to access much higher CFL (or Mach) numbers. This can be readily verified by looking at the higher-order error curves for different values of the shift velocity. The normalized errors for the diagonal and off-diagonal components of the third-order moments tensor, using a second-order EDF, are displayed in Fig. 7.3. Three different shifts in the x -direction are considered: $\mathcal{N}_x = 0$, $\mathcal{N}_x = \frac{\delta_x}{\delta_t}$ and $\mathcal{N}_x = 2\frac{\delta_x}{\delta_t}$. The span-wise Mach number is set to 0.2. While the non-shifted stencil admits very large errors at high Mach numbers, it can be seen that for the shifted stencils, the errors vanish at Mach numbers of $\sqrt{3}$ and $2\sqrt{3}$, which are the Mach numbers corresponding to the imposed shifts on the stencils. To further theoretically confirm that shifted stencils can extend the usability domain of the LBM in terms of Mach number, following the formalism introduced in subsection 3.2.1, linear stability domains of the shifted stencils have been computed.

In order to show that the shift in the stencil conserves all the properties of the different collision operators, these analyses have been performed with three different EDFs and an two

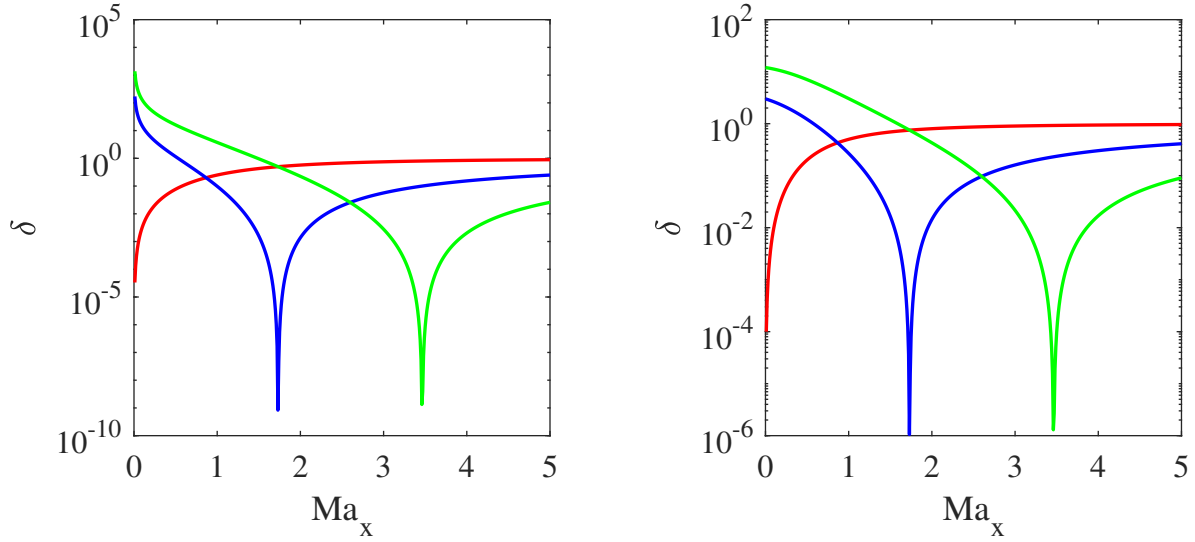


Figure 7.3: Normalized error of moments (left) Π_{x^3} and (right) Π_{x^2y} with (in red) $\mathcal{N}_x = 0$, (in blue) $\mathcal{N}_x = \frac{\delta_x}{\delta_t}$ and (in green) $\mathcal{N}_x = 2\frac{\delta_x}{\delta_t}$. The span-wise Mach number is set to 0.2 and a second-order expansion is used for the EDF.

collision operators. These include Hermite expanded EDFs of orders two and four and the entropic EDF, all with the SRT collision operator and the fourth-order LKS and recursive regularized collision operators. The obtained stability domains with a shift of $U_x = \frac{\delta_x}{\delta_t}$ are illustrated in Fig. 7.4. The stability domains are computed for different values of the non-dimensional viscosity and over the entire Mach number vector space (taking into account both the magnitude of the velocity vector and its orientation in 2-D space). As such the angle appearing in this figure represents the angle between the velocity vector and the x -axis. To get a clearer image of the effect of the velocity shift, the linear stability domains of these EDFs and collision operators on non-shifted stencils are also shown in Fig. 7.5. As observed by comparing the linear stability domains of Figs. 7.4 and 7.5, the shift in the stencil induces the same shift in the linear stability domain, making high Mach number flow simulations possible.

As a proof of concept, and to corroborate spectral analysis results, the case of the isothermal convected vortex is considered. This test-case consists of a vortex convected by a uniform background velocity field. The vortex is initialized as:

$$u_x = u_0 - \beta_0 u_0 \frac{y - y_c}{r_0} \exp - \frac{\mathbf{r}^2}{2r_0^2}, \quad (7.7a)$$

$$u_y = \beta_0 u_0 \frac{x - x_c}{r_0} \exp - \frac{\mathbf{r}^2}{2r_0^2}, \quad (7.7b)$$

$$\rho = 1 - \frac{\beta_0^2 u_0^2}{2c_s^2} \exp - \frac{\mathbf{r}^2}{r_0^2}, \quad (7.7c)$$

where u_0 is the background convection velocity, $\beta_0 u_0$ is the vortex strength, r_0 the vortex radius, x_c and y_c the coordinates of the vortex center. This configuration corresponds to

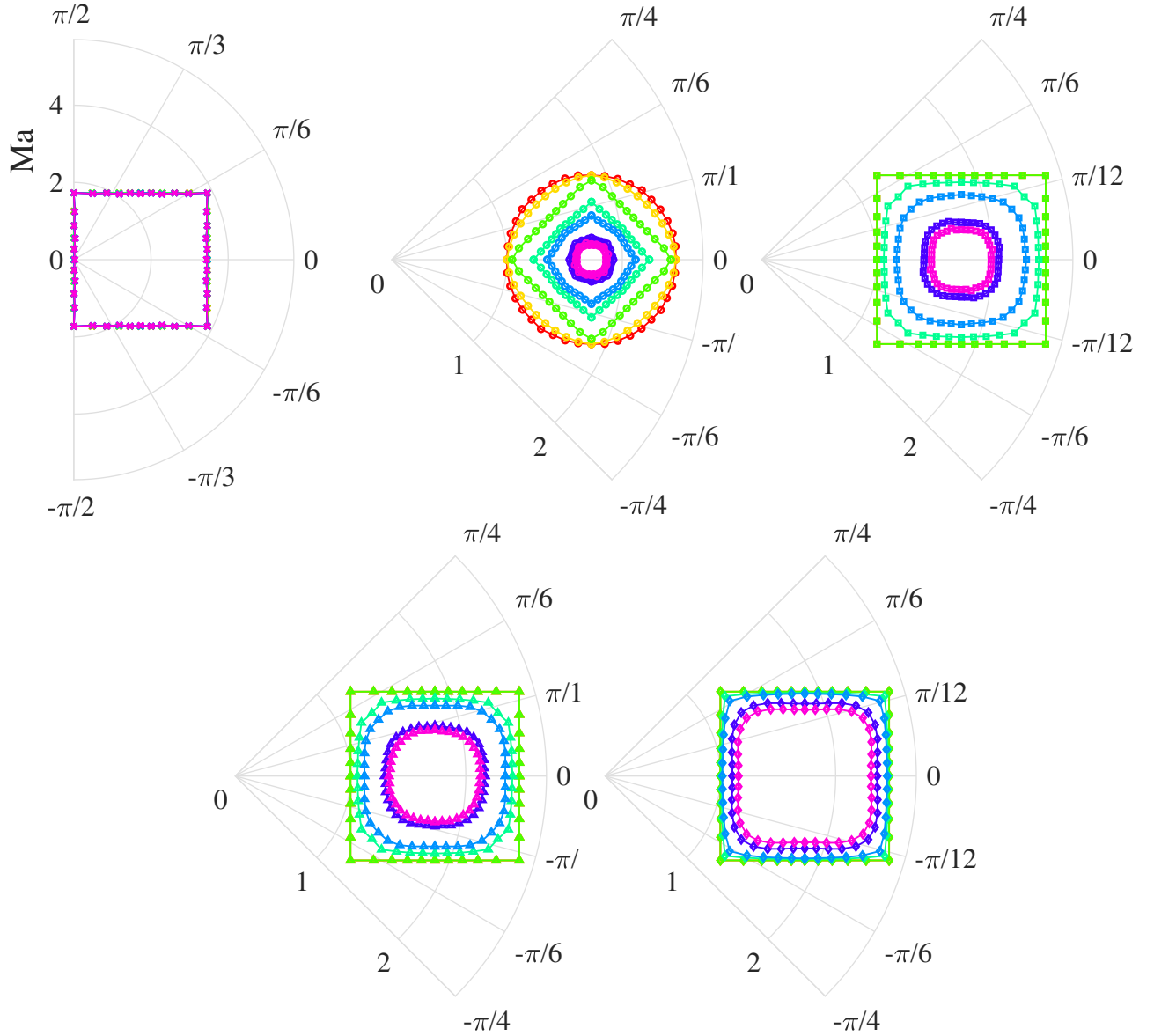


Figure 7.4: Linear stability domains of the shifted stencil ($U_x = \delta_x/\delta_t$) for (top row) different EDFs: (from left to right) entropic, second- and fourth-order, and (bottom row) different collision models (with the fourth-order EDF), i.e. (from left to right) LKS and recursive regularized, for different values of the non-dimensional viscosity: (—)0.5, (—)0.1, (—)0.05, (—)0.01, (—) 5×10^{-3} , (—) 1×10^{-3} , (—) 5×10^{-4} . The angles designate the orientation of the velocity (Mach number) vector. The Ma number axis scale is different for the entropic EDF as the domain is considerably larger.

the isothermal configuration of the isentropic vortex convection of [228]. To further amplify instabilities, for all simulation results presented in this section, the vortex strength is set to:

$$\beta_0 u_0 = \frac{|u_0 - U|}{5}, \quad (7.8)$$

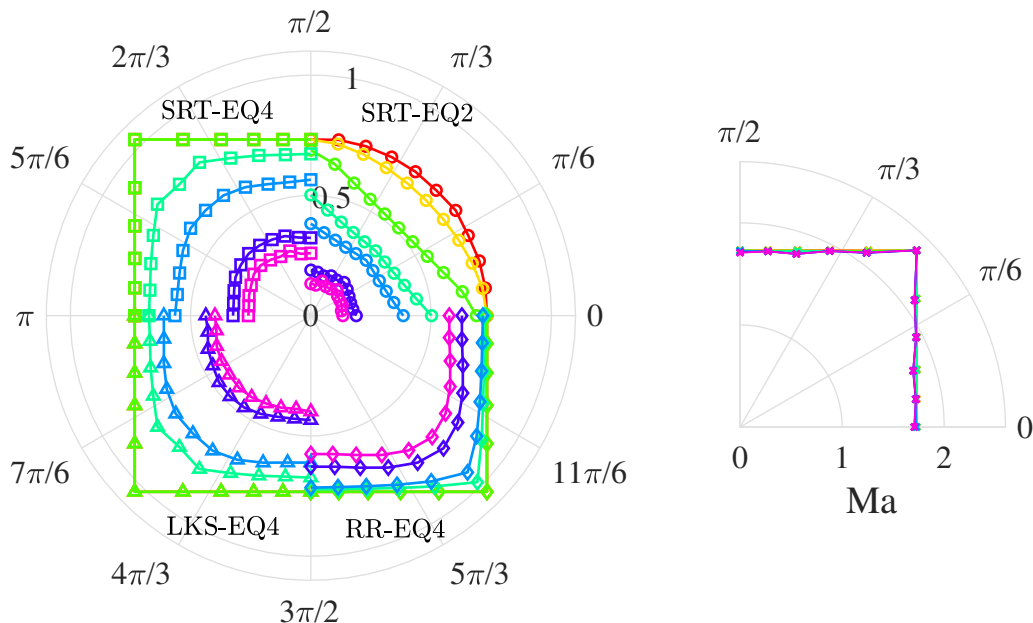


Figure 7.5: Linear stability domains of the non-shifted stencil for (left) second- and fourth-order SRT, LKS and recursive regularized (shown as RR) with fourth-order EDFs and (right) the entropic EDF, for different values of the non-dimensional viscosity: (—)0.5, (—)0.1, (—)0.05, (—)0.01, (—) 5×10^{-3} , (—) 1×10^{-3} , (—) 5×10^{-4} . While stability limits for each model are shown only in one quadrant, it should be noted that they are the same in the other quadrants. The Ma number axis scale used for the entropic EDF is different from the other schemes as the corresponding linear stability region is considerably larger.

and the vortex radius to 1/20 of the domain size. The simulation domain is bound by periodic boundary conditions all around. Furthermore, populations are initialized using the corresponding equilibrium function.

To confirm the effect of the velocity shift on stability when the shift coincides with the flow speed, inviscid cases are first considered. The resolution is fixed at 256×256 . For the inviscid configurations, simulations are performed over 20 convective cycles. The initial and final pressures, as obtained using the SRT collision operator with a second-order EDF for different velocities and corresponding shifts are shown in Fig. 7.6. Results shown in Fig. 7.6 correspond to $Ma = 1.73, 3.46$ and 5.19 , which would have been impossible to carry out on normal stencils. To further demonstrate the effect of the velocity shift on the behavior of the solver the isothermal convected vortex case was ran for different Mach numbers and non-dimensional viscosities, over 70 convective cycles. The overall kinetic energy of the domain was monitored to detect the onset of instability. The obtained results were then used to establish a stability domain for each one of the EDFs and collision operators. The results are displayed in Fig. 7.7. The entropic EDF was not considered in this study, as purely considering linear stability would not have been a good measure of its applicability domain. As mentioned previously and illustrated in Fig. 7.5, the entropic EDF is unconditionally stable for all velocities within the bounds set by the stencil. While linearly stable, the entropic

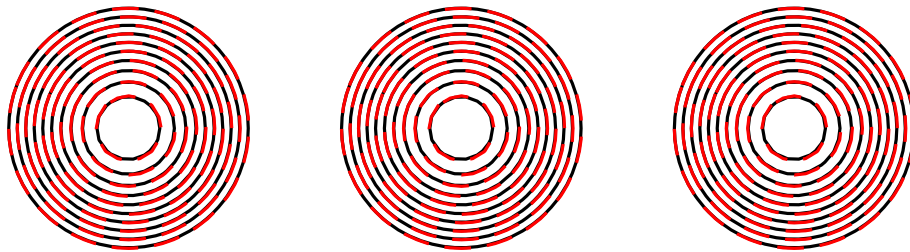


Figure 7.6: Comparison of pressure contours for an inviscid vortex at (dotted red lines) $t/t_c = 0$ and (plain black lines) $t/t_c = 20$ with $t_c = L/u_0$ being the convective characteristic time and L the simulation domain size. Vortices are convected at (from left to right) $u_0 = \delta_x/\delta_t$, $u_0 = 2\delta_x/\delta_t$ and $u_0 = 3\delta_x/\delta_t$ using SRT collision operator with the second-order polynomial EDF. The lattice shifts are set to the background velocity.

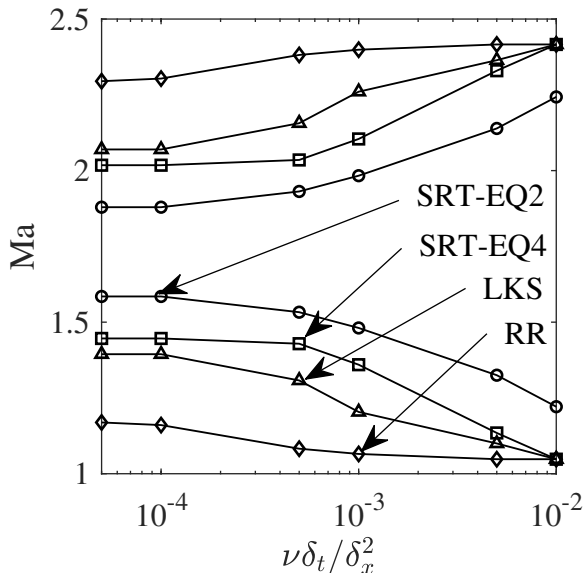


Figure 7.7: Stability domains of different EDFs and collision models as obtained from the isothermal vortex test-case on a shifted stencil with a shift of $U_x = \delta_x/\delta_t$. As shown in the plot, the SRT collision operator along with two different EDFs, i.e. second- (SRT-EQ2) and fourth-order (SRT-EQ4), are considered. Furthermore, the LKS and recursive regularized (RR) collision operators with fourth-order EDFs are also studied. Upper and lower lines represent the upper and lower stability limits.

EDF exhibits large errors (both dispersive and dissipative) as the local speed deviates from the reference state of the stencil. These errors are illustrated in Fig. 7.8 where the pressure contours after one convective cycle are compared to the initial ones for a simulation on a shifted stencil with $U_x = \frac{\delta_x}{\delta_t}$ and vortex convection velocities of $u_0 = 0.8\frac{\delta_x}{\delta_t}$ and $u_0 = 1.2\frac{\delta_x}{\delta_t}$. These errors can be further quantified by measuring the L_2 norm of the velocity field errors. Figure 7.9 compares the L_2 norm of the error in the velocity fields as obtained with the entropic and fourth-order Hermite expanded EDF for different values of the Mach number on a stencil with a shift of $U_x = \frac{\delta_x}{\delta_t}$. As expected, as the vortex convection velocity gets away

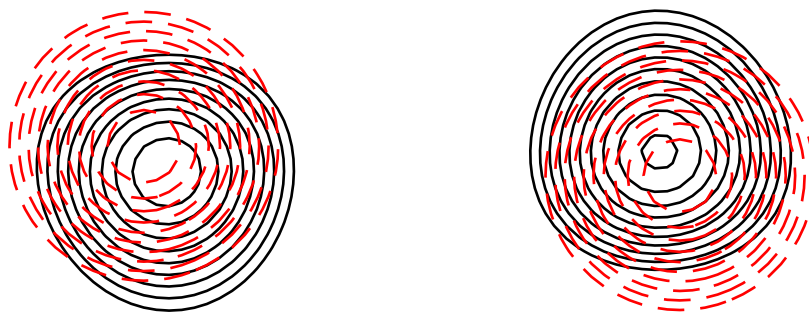


Figure 7.8: Comparison of pressure contours for an inviscid vortex at (red dashed lines) $t/t_c = 0$ and (black plain lines) $t/t_c = 1$ with $t_c = L/u_0$ being the convective characteristic time. Vortices are convected at (left) $u_0 = 0.8\delta_x/\delta_t$ and (right) $u_0 = 1.2\delta_x/\delta_t$, using the entropic EDF. The lattice shifts are set to $U_x = \delta_x/\delta_t$.

from the reference stencil velocity (or Mach number), the errors grow. However, comparing the errors of the fourth-order and entropic EDF, it can be observed that these errors are more pronounced for the latter. This in turn is in agreement with results shown in Fig. 7.8 and the higher-order error analysis presented earlier in this section.

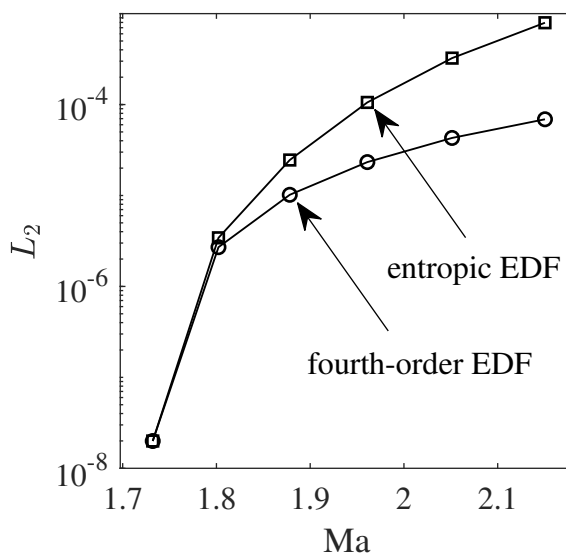


Figure 7.9: L_2 norm of error for the entropic and fourth-order EDFs at $t/t_c = 1$ on a shifted stencil with a shift of $U_x = \delta_x/\delta_t$.

All of the simulation and analyses provided in this part confirm that shifted stencils are potentially viable solutions towards simulation of high Mach number flows using the LBM. While the present analysis was limited to shifted-stencils with on-lattice propagation, one can readily refer to [95] for local flow state-adaptive stencils, supplemented with a predictor-corrector algorithm (to allow for better stability and smaller errors) and population reconstruction via higher-order interpolation through Lagrange polynomials. An adaptive scheme based solely on on-lattice shifts can not be achieved on first-neighbor stencils, as

there is no overlap of the stability domains to allow for stable transition from one stencil to another. However, going one order higher in quadratures, such an overlap can be achieved, and can potentially allow for adaptive shifted stencils with on-grid streaming.

7.4 Final remarks

The study detailed in this chapter clearly shows that the performances of the lattice Boltzmann solver are closely tied to the deviation of the local fluid state from the stencil reference state. It was also shown, through both theoretical and numerical analyses that adapting the stencil reference state to the local fluid state (through shifted stencils among many other possible approaches) is a very inexpensive and efficient way to improve the numerical properties of the solver and extend its usability domain to larger Mach numbers and inviscid flows. This approach will be further studied and possibly extended to multi-species kinetic models in the future.

Chapter 8

Conclusions and perspectives

Contents

8.1	Conclusions	164
8.2	Perspectives	165

8.1 Conclusions

The present thesis focused on the development and validation of numerical schemes based on the LBM formalism for reacting flows. Given that the aim was to develop a numerical solver for large-scale simulations and, possibly, detailed chemistry, from the very start of the work only decoupled approaches for the thermal multi-species flows were considered. The reason behind this choice was to minimize memory consumption and computational load, as fully multi-component formulations would have led to large stencils, for each one of the species. For example, for an isothermal multi-species flow with N_{sp} species, one would need a minimum of 19 discrete populations per grid-point per species, i.e. $19N_{sp}$ discrete populations. However, in the decoupled mixture-averaged formulation, the number of discrete populations to be stored in memory at each grid-point reduces to $7N_{sp} + 19$ (using a D3Q7 stencil for the species). To develop such decoupled models in the context of the LBM the following challenges and solutions were respectively identified and proposed:

- Stability issues of the SRT collision operator: To understand the stability of the SRT collision operator at vanishing viscosities and check the performance of more advanced collision operators found in the literature, their stability domains and spectral properties were systematically analyzed using the von Neumann formalism. It was shown that the MRT collision operator in central moments space had the widest stability domain, along with the recursive regularized model of the same order. While a systematic VN analysis of the free parameter (ghost moments relaxation coefficient) in the MRT collision operator showed that setting higher-order moments to their equilibrium counterparts would result in the widest linear stability domain, it must be noted that the search-space was limited by relaxing all higher-order moments at the same rate. Furthermore, it was also observed that using the regularization argument as closure for the relaxation of these moments would introduce pronounced grid-dependent hyper-viscosity.
- Minimalist LB-based solvers for energy and species mass balance equations: The classical passive scalar LB models, developed for classical advection-diffusion PDEs were extended to recover the correct forms of the energy and species mass balance equations. In addition, as an alternative to these solvers, finite-difference solvers were also considered and coupled to the LB code. These minimalist models were shown to correctly capture the target dynamics through a number of different test-cases.
- Introduction of dilatation effects in the LB flow solver: Two different approaches to introduce dilatation effects into the LB flow solver were studied. One is similar to the low Mach formulation used in classical combustion codes, relying on decoupling thermodynamic pressure and velocity field. The second approach relies on a thermal Hermite expansion recovering, with the appropriate correction term, the fully compressible NS equations. While both are able to capture dilatation effects, a systematic VN analysis showed that the latter is subject to accuracy and stability issues. To account for the issue with Galilean invariance of the shear mode dissipation rate it was

shown that a third-order (or higher) Hermite expansion is necessary. For the acoustic modes however, this artifact is tied to the order of the Gauss-Hermite quadrature and can only be accounted for through a correction term. The linear stability domain was also extended using an MRT collision operator in a temperature-scaled central moments space.

While all proposed schemes were shown to correctly model combustion, the low Mach formulation coupled to FD solvers for the energy and species mass balance equations was observed to yield the best performances. While the decoupling of acoustics from the flow field allowed for larger time-step sizes, the use of FD solvers with first-order Euler time-discretization slightly outperformed the full LB solver. This last assertion must be nuanced by the fact that while the FD solvers were first-order accurate under acoustic scaling, their LB counterparts showed second-order convergence under both diffusive and acoustic scaling. Furthermore, the use of FD solvers for the species mass and energy balance equations allows for more flexibility in terms of the discretization strategy (in both space and time). As such, for the applications targeted here, the hybrid LB-FD approach appears to be the most promising for future developments.

8.2 Perspectives

The von Neumann analysis along with numerical application of the first-neighbor stencil to thermal flows showed that it had a rather limited stability area and therefore applicability domain. To alleviate this issue, at least partly, a temperature-scaled collision operator was proposed. The von Neumann analysis showed that this modified collision operator extended the stability domain (while setting relaxation coefficient of all ghost modes to 1). It is clear that the additional degrees of freedom provided by the MRT nature of the collision operator provide a large search-space to ensure linear stability. Apart from the linear stability domain, it was also observed that the regularization path leads to pronounced over-dissipation of mid-range structures (in terms of the wave number). The entropic MRT, also referred to as KBC, can be a good alternative to provide closure for this collision operator while taking advantage of the full parameter space tied to the relaxation of ghost moments. As such, one interesting future work is to apply this closure to the relaxation coefficients of the temperature-scaled collision operator for the simulation of thermal flows.

Another aspect not treated in the present manuscript is the issue of efficient and accurate treatments of boundaries in the context of the presented formulations. The half-way bounce-back family of boundary conditions is one of the attractive features of the LB formulation, as they are both simple and efficient to implement, second-order accurate and allow to model walls without being confronted to the issue of providing closure for the pressure at the boundary. In practice, this is one of the most pressing issues when using incompressible solvers for flows in complex geometries. Given the complexity of specifying boundary conditions for the Poisson equation, complex geometries are usually handled with Immersed

Boundaries. Such an approach, while allowing for flow simulations in complex geometries [229] has serious effects on the performances (both in terms of accuracy and efficiency) of the solvers. Efficiency is affected by the fact that the NS equations have to be solved in the solid areas, introducing non-negligible overhead especially for flows in porous media. Furthermore, devising a high-order accurate Immersed Boundary treatment has proven to be a rather difficult task [230, 231, 232]. Bounce-back conditions are especially useful for the low Mach LB formulation used in the present work, as one does not need to explicitly enforce boundary conditions on the hydrodynamic pressure at the walls. While used for the present simulations, the boundary conditions still need improvements such as curved-boundary treatment (readily treated in the literature, e.g. [233, 234, 235]) and addition of non-reflective features, especially useful for the compressible solver.

During the course of the present thesis, and through the different numerical and theoretical analyses, it was observed that the stencil reference state controls the numerical behavior of the LB solver. This fact is readily confirmed by the fact that at this specific state, the discrete populations correctly match all the moments of their continuous counterpart, and exactly satisfy the H-theorem. It was also shown that using shifted stencils can open the door for high Mach number simulations. As such, the concept of adaptive phase-space discretization is a promising direction to enhance numerical properties of LB solvers and extend their application domain to higher Mach numbers and temperatures, and even efficient kinetic models for multi-species flows. Therefore, another possible feature work would focus on developing numerical solvers for appropriate multi-species kinetic models relying on state-adaptive phase-space discretization.

Bibliography

- [1] T. Ombrello, S.H. Won, Y. Ju, and S. Williams. Flame propagation enhancement by plasma excitation of oxygen. part I: Effects of O_3 . *Combustion and Flame*, 157(10):1906–1915, 2010. (page x, 99, 203)
- [2] B. Franzelli. *Impact of the chemical description on direct numerical simulations and large eddy simulations of turbulent combustion in industrial aero-engines*. PhD thesis, INP Toulouse, 2011. (page x, xvii, 145, 147, 204, 205)
- [3] A. Korichi and L. Oufer. Numerical heat transfer in a rectangular channel with mounted obstacles on upper and lower walls. *International Journal of Thermal Sciences*, 44(7):644–655, 2005. (page xiv, 80, 81, 82, 83)
- [4] B. Ničeno, A.D.T. Dronkers, and K. Hanjalić. Turbulent heat transfer from a multi-layered wall-mounted cube matrix: A large eddy simulation. *International Journal of Heat and Fluid Flow*, 23(2):173–185, 2002. (page xiv, 85, 86, 87, 89, 90)
- [5] E.R. Meinders and K. Hanjalić. Vortex structure and heat transfer in turbulent flow over a wall-mounted matrix of cubes. *International Journal of Heat and Fluid Flow*, 20(3):255–267, 1999. (page xiv, 85, 87, 89, 90)
- [6] G. Pareschi, N. Frapolli, S.S. Chikatamarla, and I.V. Karlin. Conjugate heat transfer with the entropic lattice Boltzmann method. *Physical Review E*, 94(1):013305, 2016. (page xiv, 87, 90)
- [7] K. Yamamoto, X. He, and G.D. Doolen. Simulation of combustion field with lattice Boltzmann method. *Journal of Statistical Physics*, 107(1-2):367–383, 2002. (page xiv, 2, 95, 96, 97, 98, 135, 139)
- [8] J. Vierendeels, B. Merci, and E. Dick. Benchmark solutions for the natural convective heat transfer problem in a square cavity with large horizontal temperature differences. *International Journal of Numerical Methods for Heat & Fluid Flow*, 13(8):1057–1078, 2003. (page xv, 110, 111)
- [9] M.H. Saadat, F. Bösch, and I.V. Karlin. Lattice Boltzmann model for compressible flows on standard lattices: Variable Prandtl number and adiabatic exponent. *Physical Review E*, 99(1):013306, 2019. (page xvi, 19, 37, 80, 116, 119, 120, 121, 122)

- [10] N.N. Peters. *Turbulent Combustion*. Cambridge University Press, 2000. (page xvii, 143, 145)
- [11] B.T. Nadiga and D.I. Pullin. A method for near-equilibrium discrete-velocity gas flows. *Journal of Computational Physics*, 112(1):162–172, 1994. (page xvii, 153, 154)
- [12] B.T. Nadiga. An Euler solver based on locally adaptive discrete velocities. *Journal of Statistical Physics*, 81(1-2):129–146, 1995. (page xvii, 153, 154)
- [13] J. Huang, F. Xu, M. Vallières, D.H. Feng, Y. Qian, B. Fryxell, and M.R. Strayer. A thermal LBGK model for large density and temperature differences. *International Journal of Modern Physics C*, 8(04):827–841, 1997. (page xvii, 153, 154)
- [14] G.R. McNamara and G. Zanetti. Use of the Boltzmann equation to simulate lattice-gas automata. *Physical Review Letters*, 61(20):2332, 1988. (page 2)
- [15] S. Succi. *The lattice Boltzmann equation for fluid dynamics and beyond*. Oxford university press, 2001. (page 2)
- [16] D. d’Humières, P. Lallemand, and U. Frisch. Lattice gas models for 3D hydrodynamics. *EPL (Europhysics Letters)*, 2(4):291, 1986. (page 2)
- [17] U. Frisch, B. Hasslacher, and Y. Pomeau. Lattice-gas automata for the Navier-Stokes equation. *Physical Review Letters*, 56(14):1505, 1986. (page 2)
- [18] B.G.M. Van Wachem, A.F. Bakker, J.C. Schouten, M.W. Heemels, and S.W. De Leeuw. Simulation of fluidized beds with lattice gas cellular automata. *Journal of Computational Physics*, 135(1):1–7, 1997. (page 2)
- [19] B.G.M. Van Wachem. *Derivation, implementation, and validation of computer simulation models for gas-solid fluidized beds*. PhD thesis, TU Delft, 2000. (page 2)
- [20] F.J. Higuera, S. Succi, and R. Benzi. Lattice gas dynamics with enhanced collisions. *EPL (Europhysics Letters)*, 9(4):345, 1989. (page 2)
- [21] S. Succi. Lattice Boltzmann 2038. *EPL (Europhysics Letters)*, 109(5):50001, 2015. (page 2)
- [22] R. Benzi, S. Succi, and M. Vergassola. The lattice Boltzmann equation: Theory and applications. *Physics Reports*, 222(3):145–197, 1992. (page 2)
- [23] S. Succi, R. Benzi, and F. Higuera. The lattice Boltzmann equation: A new tool for computational fluid-dynamics. *Physica D: Nonlinear Phenomena*, 47(1-2):219–230, 1991. (page 2)
- [24] X. Shan and H. Chen. Lattice Boltzmann model for simulating flows with multiple phases and components. *Physical Review E*, 47(3):1815, 1993. (page 2, 5)

- [25] S.S. Chikatamarla and I.V. Karlin. Entropic lattice Boltzmann method for multiphase flows. *Physical Review Letters*, 114(17):174502, 2015. (page 2)
- [26] A. Mazloomi Moqaddam, S.S. Chikatamarla, and I.V. Karlin. Simulation of binary droplet collisions with the entropic lattice Boltzmann method. *Physics of Fluids*, 28(2):022106, 2016. (page 2)
- [27] M. Wöhrwag, C. Semperebon, A. Mazloomi Moqaddam, I.V. Karlin, and H. Kusumaatmaja. Ternary free-energy entropic lattice Boltzmann model with a high density ratio. *Physical Review Letters*, 120(23):234501, 2018. (page 2)
- [28] A. Fakhari and M.H. Rahimian. Phase-field modeling by the method of lattice Boltzmann equations. *Physical Review E*, 81(3):036707, 2010. (page 2)
- [29] H. Safari, M.H. Rahimian, and M. Krafczyk. Consistent simulation of droplet evaporation based on the phase-field multiphase lattice Boltzmann method. *Physical Review E*, 90(3):033305, 2014. (page 2)
- [30] C. Pan, L.S. Luo, and C.T. Miller. An evaluation of lattice Boltzmann schemes for porous medium flow simulation. *Computers & Fluids*, 35(8-9):898–909, 2006. (page 2, 26)
- [31] Z. Guo and T.S. Zhao. Lattice Boltzmann model for incompressible flows through porous media. *Physical Review E*, 66(3):036304, 2002. (page 2)
- [32] L.S. Luo and S.S. Girimaji. Theory of the lattice Boltzmann method: Two-fluid model for binary mixtures. *Physical Review E*, 67(3):036302, 2003. (page 2, 90)
- [33] P. Asinari. Semi-implicit-linearized multiple-relaxation-time formulation of lattice Boltzmann schemes for mixture modeling. *Physical Review E*, 73(5):056705, 2006. (page 2)
- [34] S. Arcidiacono, I.V. Karlin, J. Mantzaras, and C.E. Frouzakis. Lattice Boltzmann model for the simulation of multicomponent mixtures. *Physical Review E*, 76(4):046703, 2007. (page 2, 90)
- [35] S. Arcidiacono, J. Mantzaras, and I.V. Karlin. Lattice Boltzmann simulation of catalytic reactions. *Physical Review E*, 78(4):046711, 2008. (page 2)
- [36] J. Kang, N.I. Prasianakis, and J. Mantzaras. Thermal multicomponent lattice Boltzmann model for catalytic reactive flows. *Physical Review E*, 89(6):063310, 2014. (page 2, 90)
- [37] S. Chen, Z. Liu, C. Zhang, Z. He, Z. Tian, B. Shi, and C. Zheng. A novel coupled lattice Boltzmann model for low Mach number combustion simulation. *Applied Mathematics and Computation*, 193(1):266–284, 2007. (page 2, 106)

- [38] S. Chen, Z. Liu, Z. Tian, B. Shi, and C. Zheng. A simple lattice Boltzmann scheme for combustion simulation. *Computers & Mathematics with Applications*, 55(7):1424–1432, 2008. (page 2, 106)
- [39] S. Succi, G. Bella, and F. Papetti. Lattice kinetic theory for numerical combustion. *Journal of Scientific Computing*, 12(4):395–408, 1997. (page 2)
- [40] E. Chiavazzo, I.V. Karlin, A.N. Gorban, and K. Boulouchos. Combustion simulation via lattice Boltzmann and reduced chemical kinetics. *Journal of Statistical Mechanics: Theory and Experiment*, 2009(06):P06013, 2009. (page 2)
- [41] E. Chiavazzo, I.V. Karlin, A.N. Gorban, and K. Boulouchos. Coupling of the model reduction technique with the lattice Boltzmann method for combustion simulations. *Combustion and Flame*, 157(10):1833–1849, 2010. (page 2)
- [42] E. Chiavazzo, I.V. Karlin, A.N. Gorban, and K. Boulouchos. Efficient simulations of detailed combustion fields via the lattice Boltzmann method. *International Journal of Numerical Methods for Heat & Fluid Flow*, 21(5):494–517, 2011. (page 2)
- [43] O. Filippova and D. Hänel. A novel lattice BGK approach for low Mach number combustion. *Journal of Computational Physics*, 158(2):139–160, 2000. (page 2, 106)
- [44] T. Lee, C.L. Lin, and L.D. Chen. A lattice Boltzmann algorithm for calculation of the laminar jet diffusion flame. *Journal of Computational Physics*, 215(1):133–152, 2006. (page 2, 106)
- [45] A. Eshghinejadfard. *Lattice Boltzmann simulation of laminar and turbulent two-phase flows*. PhD thesis, OvGU Magdeburg, 2017. (page 4)
- [46] S. Ansumali and I.V. Karlin. Single relaxation time model for entropic lattice Boltzmann methods. *Physical Review E*, 65(5):056312, 2002. (page 5, 29)
- [47] S.A. Hosseini, H. Safari, N. Darabiha, D. Thévenin, and M. Krafczyk. Hybrid lattice Boltzmann-finite difference model for low Mach number combustion simulation. *Combustion and Flame*, 209:394–404, 2019. (page 5, 135)
- [48] H. Safari, M. Krafczyk, and M. Geier. A lattice Boltzmann model for thermal compressible flows at low Mach numbers beyond the Boussinesq approximation. *Computers & Fluids*, 2018. (page 5, 106, 109, 110)
- [49] Z. Guo, C. Zheng, and B. Shi. Discrete lattice effects on the forcing term in the lattice Boltzmann method. *Physical Review E*, 65(4):046308, 2002. (page 5, 118)
- [50] A.L. Kupershtokh. New method of incorporating a body force term into the lattice Boltzmann equation. In *Proc. 5th International EHD Workshop, University of Poitiers, Poitiers, France*, pages 241–246, 2004. (page 5)

- [51] I. Ginzburg. Lattice Boltzmann modeling with discontinuous collision components: Hydrodynamic and advection-diffusion equations. *Journal of Statistical Physics*, 126(1):157–206, 2007. (page 5, 26)
- [52] T. Inamuro. A lattice kinetic scheme for incompressible viscous flows with heat transfer. *Philosophical Transactions of the Royal Society of London. Series A*, 360(1792):477–484, 2002. (page 5, 27)
- [53] S.A. Hosseini, N. Darabiha, and D. Thévenin. Theoretical and numerical analysis of the lattice kinetic scheme for complex-flow simulations. *Physical Review E*, 99(2):023305, 2019. (page 5, 27, 52)
- [54] S.A. Hosseini, C. Coreixas, N. Darabiha, and D. Thévenin. Stability of the lattice kinetic scheme and choice of the free relaxation parameter. *Physical Review E*, 99(6):063305, 2019. (page 5, 27, 42, 201)
- [55] D. d’Humières. Multiple-relaxation-time lattice Boltzmann models in three dimensions. *Philosophical Transactions of the Royal Society of London. Series A*, 360(1792):437–451, 2002. (page 5, 25, 26)
- [56] A. De Rosis, R. Huang, and C. Coreixas. Universal formulation of central-moments-based lattice Boltzmann method with external forcing for the simulation of multi-physics phenomena. *Physics of Fluids*, 31(11):117102, 2019. (page 5, 52)
- [57] J. Latt and B. Chopard. Lattice Boltzmann method with regularized pre-collision distribution functions. *Mathematics and Computers in Simulation*, 72(2-6):165–168, 2006. (page 5, 28, 29)
- [58] O. Malaspinas. Increasing stability and accuracy of the lattice Boltzmann scheme: Recursivity and regularization. *arXiv preprint arXiv:1505.06900*, 2015. (page 5, 29)
- [59] A.J.C. Ladd and R. Verberg. Lattice Boltzmann simulations of particle-fluid suspensions. *Journal of Statistical Physics*, 104(5-6):1191–1251, 2001. (page 5)
- [60] Z. Guo, C.G. Zheng, and B. Shi. Non-equilibrium extrapolation method for velocity and pressure boundary conditions in the lattice Boltzmann method. *Chinese Physics*, 11(4):366, 2002. (page 5)
- [61] S.A. Hosseini, N. Darabiha, and D. Thévenin. Lattice Boltzmann advection-diffusion model for conjugate heat transfer in heterogeneous media. *International Journal of Heat and Mass Transfer*, 132:906–919, 2019. (page 5)
- [62] R. Kamakoti and C. Pantano. High-order narrow stencil finite-difference approximations of second-order derivatives involving variable coefficients. *SIAM Journal on Scientific Computing*, 31(6):4222–4243, 2010. (page 5)

- [63] S.A. Hosseini, N. Darabiha, and D. Thévenin. Mass-conserving advection–diffusion lattice Boltzmann model for multi-species reacting flows. *Physica A: Statistical Mechanics and its Applications*, 499:40–57, 2018. (page 5, 92)
- [64] J. Liouville. A general kinetic theory of liquids I. the molecular distribution functions. *Journal de Mathématiques Pures et Appliquées*, 1(3):342–349, 1838. (page 8, 10)
- [65] J. Yvon. *La théorie statistique des fluides et l'équation d'état*, volume 203. Hermann & Cie, 1935. (page 8, 10)
- [66] J.G. Kirkwood. The statistical mechanical theory of transport processes I. general theory. *The Journal of Chemical Physics*, 14(3):180–201, 1946. (page 8, 10)
- [67] J.G. Kirkwood. The statistical mechanical theory of transport processes II. transport in gases. *The Journal of Chemical Physics*, 15(1):72–76, 1947. (page 8, 10)
- [68] M. Born and H.S. Green. A general kinetic theory of liquids I. the molecular distribution functions. *Proceedings of the Royal Society of London. Series A. Mathematical and Physical Sciences*, 188(1012):10–18, 1946. (page 8, 10)
- [69] G.M. Kremer. *An introduction to the Boltzmann equation and transport processes in gases*. Springer Science & Business Media, 2010. (page 12, 15)
- [70] P.L. Bhatnagar, E.P. Gross, and M. Krook. A model for collision processes in gases. I. small amplitude processes in charged and neutral one-component systems. *Physical Review*, 94:511–525, May 1954. (page 13)
- [71] Y. Zheng and H. Struchtrup. Ellipsoidal statistical Bhatnagar–Gross–Krook model with velocity-dependent collision frequency. *Physics of Fluids*, 17(12):127103, 2005. (page 13)
- [72] J. Meng, Y. Zhang, N.G. Hadjiconstantinou, G.A. Radtke, and X. Shan. Lattice ellipsoidal statistical BGK model for thermal non-equilibrium flows. *Journal of Fluid Mechanics*, 718:347–370, 2013. (page 14)
- [73] E.M. Shakhov. Generalization of the Krook kinetic relaxation equation. *Fluid Dynamics*, 3(5):95–96, 1968. (page 14)
- [74] E.M. Shakhov. Approximate kinetic equations in rarefied gas theory. *Fluid Dynamics*, 3(1):112–115, 1968. (page 14)
- [75] I.V. Karlin. Derivation of regularized Grad's moment system from kinetic equations: Modes, ghosts and non-Markov fluxes. *Philosophical Transactions of the Royal Society A: Mathematical, Physical and Engineering Sciences*, 376(2118):20170230, 2018. (page 15)
- [76] H. Struchtrup and M. Torrilhon. Regularization of Grad's 13 moment equations: Derivation and linear analysis. *Physics of Fluids*, 15(9):2668–2680, 2003. (page 15)

- [77] D. Enskog. The numerical calculation of phenomena in fairly dense gases. *Arkiv Mat. Astr. Fys*, 16(1):1–60, 1921. (page 16)
- [78] H. Struchtrup. *Macroscopic Transport Equations for Rarefied Gas Flows*. Springer, 2005. (page 16)
- [79] S. Chapman. On the kinetic theory of a gas. part II.A composite monatomic gas: Diffusion, viscosity, and thermal conduction. *Philosophical Transactions of the Royal Society of London. Series A*, 217(549-560):115–197, 1918. (page 16)
- [80] S. Chapman. VI. On the law of distribution of molecular velocities, and on the theory of viscosity and thermal conduction, in a non-uniform simple monatomic gas. *Philosophical Transactions of the Royal Society of London. Series A*, 216(538-548):279–348, 1916. (page 16)
- [81] V. Garzó and A. Santos. *Kinetic theory of gases in shear flows: Nonlinear transport*, volume 131. Springer Science & Business Media, 2013. (page 16)
- [82] C. Lin, K. Hong Luo, L. Fei, and S. Succi. A multi-component discrete Boltzmann model for nonequilibrium reactive flows. *Scientific reports*, 7(1):14580, 2017. (page 17, 22, 90)
- [83] C. Lin, A. Xu, G. Zhang, K.H. Luo, and Y. Li. Discrete Boltzmann modeling of Rayleigh-Taylor instability in two-component compressible flows. *Physical Review E*, 96(5):053305, 2017. (page 17, 22)
- [84] C. Lin and K.H. Luo. Discrete Boltzmann modeling of unsteady reactive flows with non-equilibrium effects. *Physical Review E*, 99(1):012142, 2019. (page 17, 22)
- [85] Y. Gan, A. Xu, G. Zhang, and H. Lai. Three-dimensional discrete Boltzmann models for compressible flows in and out of equilibrium. *Proceedings of the Institution of Mechanical Engineers, Part C: Journal of Mechanical Engineering Science*, 232(3):477–490, 2018. (page 17)
- [86] Y. Gan, A. Xu, G. Zhang, and Y. Yang. Lattice BGK kinetic model for high-speed compressible flows: Hydrodynamic and nonequilibrium behaviors. *EPL (Europhysics Letters)*, 103(2):24003, 2013. (page 17)
- [87] Y. Gan, A. Xu, G. Zhang, Y. Zhang, and S. Succi. Discrete Boltzmann trans-scale modeling of high-speed compressible flows. *Physical Review E*, 97(5):053312, 2018. (page 18)
- [88] X. Shan, X.F. Yuan, and H. Chen. Kinetic theory representation of hydrodynamics: A way beyond the Navier–Stokes equation. *Journal of Fluid Mechanics*, 550:413–441, 2006. (page 18, 154, 155)
- [89] H. Grad. Note on N-dimensional Hermite polynomials. *Communications on Pure and Applied Mathematics*, 2(4):325–330, 1949. (page 18)

- [90] H. Grad. On the kinetic theory of rarefied gases. *Communications on Pure and Applied Mathematics*, 2(4):331–407, 1949. (page 18, 154)
- [91] C. Sun and A.T. Hsu. Three-dimensional lattice Boltzmann model for compressible flows. *Physical Review E*, 68:016303, Jul 2003. (page 19)
- [92] C. Sun. Adaptive lattice Boltzmann model for compressible flows: Viscous and conductive properties. *Physical Review E*, 61:2645–2653, Mar 2000. (page 19)
- [93] C. Sun. Lattice Boltzmann models for high speed flows. *Physical Review E*, 58:7283–7287, Dec 1998. (page 19)
- [94] N. Frapolli, S.S. Chikatamarla, and I.V. Karlin. Lattice kinetic theory in a comoving Galilean reference frame. *Physical Review Letters*, 117(1):010604, 2016. (page 19, 21, 154)
- [95] B. Dorschner, F. Bösch, and I.V. Karlin. Particles on demand for kinetic theory. *Physical Review Letters*, 121(13):130602, 2018. (page 19, 153, 161)
- [96] S. Ansumali, I.V. Karlin, and H. Christian Öttinger. Minimal entropic kinetic models for hydrodynamics. *EPL (Europhysics Letters)*, 63(6):798, 2003. (page 21)
- [97] R.M. Beam and R.F. Warming. An implicit finite-difference algorithm for hyperbolic systems in conservation-law form. *Journal of Computational Physics*, 22(1):87–110, 1976. (page 22)
- [98] G. Jiang and C. Shu. Efficient implementation of weighted ENO schemes. *Journal of Computational Physics*, 126(1):202–228, 1996. (page 22)
- [99] C. Shu and S. Osher. Efficient implementation of Essentially Non-Oscillatory shock-capturing schemes. *Journal of Computational Physics*, 77(2):439–471, 1988. (page 22)
- [100] C. Shu. Essentially Non-Oscillatory and Weighted Essentially Non-Oscillatory schemes for hyperbolic conservation laws. In *Advanced Numerical Approximation of Nonlinear Hyperbolic Equations*, pages 325–432. Springer, 1998. (page 22, 128)
- [101] J. Shi, Y. Zhang, and C. Shu. Resolution of high order WENO schemes for complicated flow structures. *Journal of Computational Physics*, 186(2):690–696, 2003. (page 23)
- [102] D. Wilde, A. Krämer, D. Reith, and H. Foysi. Semi-Lagrangian lattice Boltzmann method for compressible flows. *arXiv preprint arXiv:1910.13918*, 2019. (page 24)
- [103] A. Krämer, K. Küllmer, D. Reith, W. Joppich, and H. Foysi. Semi-Lagrangian off-lattice Boltzmann method for weakly compressible flows. *Physical Review E*, 95(2):023305, 2017. (page 24)
- [104] G. Di Ilio, B. Dorschner, G. Bella, S. Succi, and I.V. Karlin. Simulation of turbulent flows with the entropic multirelaxation time lattice Boltzmann method on body-fitted meshes. *Journal of Fluid Mechanics*, 849:35–56, 2018. (page 24)

- [105] D. d’Humières. Generalized lattice-Boltzmann equations. *Prog. Astronaut. Aeronaut.*, 159:450–458, 1992. (page 25)
- [106] D. d’Humières. Multiple-relaxation-time lattice Boltzmann models in three dimensions. *Philosophical Transactions of the Royal Society of London. Series A*, 360(1792):437–451, 2002. (page 25)
- [107] P. Lallemand and L.S. Luo. Theory of the lattice Boltzmann method: Acoustic and thermal properties in two and three dimensions. *Physical Review E*, 68:036706, Sep 2003. (page 25)
- [108] P.J. Dellar. Bulk and shear viscosities in lattice Boltzmann equations. *Physical Review E*, 64(3):031203, 2001. (page 25, 49, 120)
- [109] M. Chávez-Modena, E. Ferrer, and G. Rubio. Improving the stability of multiple-relaxation lattice Boltzmann methods with central moments. *Computers & Fluids*, 172:397–409, 2018. (page 26, 42)
- [110] B. Dorschner, F. Bösch, S.S. Chikatamarla, K. Boulouchos, and I.V. Karlin. Entropic multi-relaxation time lattice Boltzmann model for complex flows. *Journal of Fluid Mechanics*, 801:623–651, 2016. (page 26)
- [111] I.V. Karlin, F. Bösch, and S.S. Chikatamarla. Gibbs’ principle for the lattice-kinetic theory of fluid dynamics. *Physical Review E*, 90(3):031302, 2014. (page 26, 31)
- [112] I. Ginzburg. Equilibrium-type and link-type lattice Boltzmann models for generic advection and anisotropic-dispersion equation. *Advances in Water resources*, 28(11):1171–1195, 2005. (page 26)
- [113] I. Ginzburg. Generic boundary conditions for lattice Boltzmann models and their application to advection and anisotropic dispersion equations. *Advances in Water Resources*, 28(11):1196–1216, 2005. (page 26)
- [114] D. d’Humières and I. Ginzburg. Viscosity independent numerical errors for lattice Boltzmann models: From recurrence equations to “magic” collision numbers. *Computers & Mathematics with Applications*, 58(5):823–840, 2009. (page 27)
- [115] I. Ginzburg, F. Verhaeghe, and D. d’Humières. Two-relaxation-time lattice Boltzmann scheme: About parametrization, velocity, pressure and mixed boundary conditions. *Communications in Computational Physics*, 3(2):427–478, 2008. (page 27)
- [116] I. Ginzburg. Consistent lattice Boltzmann schemes for the Brinkman model of porous flow and infinite Chapman-Enskog expansion. *Physical Review E*, 77(6):066704, 2008. (page 27)
- [117] I. Ginzburg. *Magic recipes for Lattice Boltzmann modeling of micro and macro flow*. PhD thesis, Habilitation Thesis, University Paris VI, 2009. (page 27)

- [118] A. Kuzmin, I. Ginzburg, and A.A. Mohamad. The role of the kinetic parameter in the stability of two-relaxation-time advection–diffusion lattice Boltzmann schemes. *Computers & Mathematics with Applications*, 61(12):3417–3442, 2011. (page 27)
- [119] L. Wang, J. Mi, X. Meng, and Z. Guo. A localized mass-conserving lattice Boltzmann approach for non-Newtonian fluid flows. *Communications in Computational Physics*, 17(4):908–924, 2015. (page 27)
- [120] Y. Kataoka and T. Inamuro. Numerical simulations of the behaviour of a drop in a square pipe flow using the two-phase lattice Boltzmann method. *Philosophical Transactions of the Royal Society A: Mathematical, Physical and Engineering Sciences*, 369(1945):2528–2536, 2011. (page 27)
- [121] M. Yoshino, Y. Hotta, T. Hirozane, and M. Endo. A numerical method for incompressible non-Newtonian fluid flows based on the lattice Boltzmann method. *Journal of non-Newtonian Fluid Mechanics*, 147(1-2):69–78, 2007. (page 27)
- [122] X. Meng and Z. Guo. Localized lattice Boltzmann equation model for simulating miscible viscous displacement in porous media. *International Journal of Heat and Mass Transfer*, 100:767–778, 2016. (page 27)
- [123] J. Perko and R.A. Patel. Single-relaxation-time lattice Boltzmann scheme for advection-diffusion problems with large diffusion-coefficient heterogeneities and high-advection transport. *Physical Review E*, 89(5):053309, 2014. (page 27)
- [124] M. Geier, A. Greiner, and J.G. Korvink. Cascaded digital lattice Boltzmann automata for high Reynolds number flow. *Physical Review E*, 73(6):066705, 2006. (page 27)
- [125] M. Geier. De-aliasing and stabilization formalism of the cascaded lattice Boltzmann automaton for under-resolved high Reynolds number flow. *International Journal for Numerical Methods in Fluids*, 56(8):1249–1254, 2008. (page 27)
- [126] P. Asinari. Generalized local equilibrium in the cascaded lattice Boltzmann method. *Physical Review E*, 78(1):016701, 2008. (page 27)
- [127] A. De Rosis and K.H. Luo. Role of higher-order Hermite polynomials in the central-moments-based lattice Boltzmann framework. *Physical Review E*, 99(1):013301, 2019. (page 28, 52)
- [128] J. Latt. *Hydrodynamic limit of lattice Boltzmann equations*. PhD thesis, University of Geneva, 2007. (page 28)
- [129] J. Jacob, O. Malaspinas, and P. Sagaut. A new hybrid recursive regularised Bhatnagar–Gross–Krook collision model for lattice Boltzmann method-based large eddy simulation. *Journal of Turbulence*, 19(11-12):1051–1076, 2018. (page 29)

- [130] Y.L. Feng, P. Boivin, J. Jacob, and P. Sagaut. Hybrid recursive regularized thermal lattice Boltzmann model for high subsonic compressible flows. *Journal of Computational Physics*, 394:82–99, 2019. (page 29, 116, 117)
- [131] I.V. Karlin, A. Ferrante, and H.C. Öttinger. Perfect entropy functions of the lattice Boltzmann method. *EPL (Europhysics Letters)*, 47(2):182, 1999. (page 29)
- [132] I.V. Karlin, A.N. Gorban, S. Succi, and V. Boffi. Maximum entropy principle for lattice kinetic equations. *Physical Review Letters*, 81(1):6, 1998. (page 29)
- [133] S.S. Chikatamarla, S. Ansumali, and I.V. Karlin. Entropic lattice Boltzmann models for hydrodynamics in three dimensions. *Physical Review Letters*, 97(1):010201, 2006. (page 29, 30, 31)
- [134] S. Ansumali, S.S. Chikatamarla, C.E. Frouzakis, and K. Boulouchos. Entropic lattice Boltzmann simulation of the flow past square cylinder. *International Journal of Modern Physics C*, 15(03):435–445, 2004. (page 29, 30)
- [135] N. Frapolli, S.S. Chikatamarla, and I.V. Karlin. Multispeed entropic lattice Boltzmann model for thermal flows. *Physical Review E*, 90(4):043306, 2014. (page 29)
- [136] B.M. Boghosian, P.J. Love, P.V. Coveney, I.V. Karlin, S. Succi, and J. Yepez. Galilean-invariant lattice-Boltzmann models with H-theorem. *Physical Review E*, 68(2):025103, 2003. (page 29)
- [137] A. Mazloomi, S.S. Chikatamarla, and I.V. Karlin. Entropic lattice Boltzmann method for multiphase flows. *Physical Review Letters*, 114(17):174502, 2015. (page 30)
- [138] M. Atif, P.K. Kolluru, C. Thantapanally, and S. Ansumali. Essentially entropic lattice Boltzmann model. *Physical Review Letters*, 119(24):240602, 2017. (page 30, 31)
- [139] B. Dorschner, S.S. Chikatamarla, and I.V. Karlin. Transitional flows with the entropic lattice Boltzmann method. *Journal of Fluid Mechanics*, 824:388–412, 2017. (page 31)
- [140] B. Dorschner, S.S. Chikatamarla, and I.V. Karlin. Fluid-structure interaction with the entropic lattice Boltzmann method. *Physical Review E*, 97(2):023305, 2018. (page 31)
- [141] N. Frapolli, S.S. Chikatamarla, and I.V. Karlin. Entropic lattice Boltzmann simulation of thermal convective turbulence. *Computers & Fluids*, 175:2–19, 2018. (page 31)
- [142] M. Geier, M. Schönherr, A. Pasquali, and M. Krafczyk. The cumulant lattice Boltzmann equation in three dimensions: Theory and validation. *Computers & Mathematics with Applications*, 70(4):507–547, 2015. (page 31)
- [143] M. Geier, A. Pasquali, and M. Schönherr. Parametrization of the cumulant lattice Boltzmann method for fourth order accurate diffusion part II: Application to flow around a sphere at drag crisis. *Journal of Computational Physics*, 348:889–898, 2017. (page 31)

- [144] N.I. Prasianakis and I.V. Karlin. Lattice Boltzmann method for simulation of compressible flows on standard lattices. *Physical Review E*, 78(1):016704, 2008. (page 37, 116)
- [145] Y.L. Feng, P. Sagaut, and W. Tao. A compressible lattice Boltzmann finite volume model for high subsonic and transonic flows on regular lattices. *Computers & Fluids*, 131:45–55, 2016. (page 37, 116, 117)
- [146] Y.L. Feng, P. Sagaut, and W. Tao. A three dimensional lattice model for thermal compressible flow on standard lattices. *Journal of Computational Physics*, 303:514–529, 2015. (page 37, 110, 116, 117)
- [147] J.D. Sterling and S. Chen. Stability analysis of lattice Boltzmann methods. *Journal of Computational Physics*, 123(1):196–206, 1996. (page 42)
- [148] R.A. Worthing, J. Mozer, and G. Seeley. Stability of lattice Boltzmann methods in hydrodynamic regimes. *Physical Review E*, 56(2):2243, 1997. (page 42)
- [149] P. Lallemand and L.S. Luo. Theory of the lattice Boltzmann method: Dispersion, dissipation, isotropy, Galilean invariance, and stability. *Physical Review E*, 61(6):6546, 2000. (page 42)
- [150] S.A. Hosseini, N. Darabiha, D. Thévenin, and A. Eshghinejadfard. Stability limits of the single relaxation-time advection–diffusion lattice Boltzmann scheme. *International Journal of Modern Physics C*, 28(12):1750141, 2017. (page 42, 74, 201)
- [151] G. Wissocq, P. Sagaut, and J.F. Boussuge. An extended spectral analysis of the lattice Boltzmann method: Modal interactions and stability issues. *Journal of Computational Physics*, 380:311–333, 2019. (page 42, 48)
- [152] S.A. Hosseini, C. Coreixas, N. Darabiha, and D. Thévenin. Extensive analysis of the lattice Boltzmann method on shifted stencils. *Physical Review E*, 100(10):063301, 2019. (page 45, 201)
- [153] X. Shan. Central-moment-based Galilean-invariant multiple-relaxation-time collision model. *Physical Review E*, 100(4):043308, 2019. (page 52)
- [154] C. Coreixas, B. Chopard, and J. Latt. Comprehensive comparison of collision models in the lattice Boltzmann framework: Theoretical investigations. *Physical Review E*, 100(3):033305, 2019. (page 52, 53, 125)
- [155] D.L. Brown. Performance of under-resolved two-dimensional incompressible flow simulations. *Journal of Computational Physics*, 122(1):165–183, 1995. (page 54)
- [156] M.L. Minion and D.L. Brown. Performance of under-resolved two-dimensional incompressible flow simulations, II. *Journal of Computational Physics*, 138(2):734–765, 1997. (page 54)

- [157] D. Ricot, S. Marié, P. Sagaut, and C. Bailly. Lattice Boltzmann method with selective viscosity filter. *J. Comput. Phys.*, 228(12):4478–4490, 2009. (page 54)
- [158] KK Kuo. *Principles of combustion*. Wiley, 1986. (page 66)
- [159] A. Ern and V. Giovangigli. Structure of transport linear systems in dilute isotropic gas mixtures. *Physical Review E*, 53(1):485, 1996. (page 67)
- [160] V. Giovangigli. *Multicomponent flow modeling*. Birkhäuser, 1999. (page 67, 71)
- [161] V. Giovangigli. Convergent iterative methods for multicomponent diffusion. *Impact of Computing in Science and Engineering*, 3(3):244–276, 1991. (page 67)
- [162] T. Poinso and D. Veynante. *Theoretical and numerical combustion*. RT Edwards, Inc., 2005. (page 68, 69)
- [163] B.J. McBride, M.J. Zehe, and S. Gordon. NASA Glenn coefficients for calculating thermodynamic properties of individual species. 2002. (page 70)
- [164] C.R. Wilke. A viscosity equation for gas mixtures. *The Journal of Chemical Physics*, 18(4):517–519, 1950. (page 71)
- [165] R.B. Bird. Transport phenomena. *Appl. Mech. Rev.*, 55(1):R1–R4, 2002. (page 71)
- [166] S. Mathur, P.K. Tondon, and S.C. Saxena. Thermal conductivity of binary, ternary and quaternary mixtures of rare gases. *Molecular Physics*, 12(6):569–579, 1967. (page 71)
- [167] J.H. Burgoyne and F. Weinberg. A method of analysis of a plane combustion wave. In *Symposium (International) on Combustion*, volume 4, pages 294–302. Elsevier, 1953. (page 71)
- [168] S.A. Hosseini, A. Eshghinejadfard, N. Darabiha, and D. Thévenin. Weakly compressible lattice Boltzmann simulations of reacting flows with detailed thermo-chemical models. *Computers & Mathematics with Applications*, 79(1):141–158, 2020. (page 71, 99)
- [169] N. Frapolli. *Entropic lattice Boltzmann models for thermal and compressible flows*. PhD thesis, ETH Zürich, 2017. (page 71)
- [170] C. Coreixas. *High-order extension of the recursive regularized lattice Boltzmann method*. PhD thesis, INP Toulouse, 2018. (page 71, 124)
- [171] X. Li, Y. Shi, and X. Shan. Temperature-scaled collision process for the high-order lattice Boltzmann model. *Physical Review E*, 100(1):013301, 2019. (page 71, 117)
- [172] X. Shan. Simulation of Rayleigh-Bénard convection using a lattice Boltzmann method. *Physical Review E*, 55(3):2780, 1997. (page 72)

- [173] X. He, S. Chen, and G.D. Doolen. A novel thermal model for the lattice Boltzmann method in incompressible limit. *Journal of Computational Physics*, 146(1):282–300, 1998. (page 72)
- [174] Y. Peng, C. Shu, and Y.T. Chew. Simplified thermal lattice Boltzmann model for incompressible thermal flows. *Physical Review E*, 68(2):026701, 2003. (page 72)
- [175] Y. Shi, T.S. Zhao, and Z.L. Guo. Thermal lattice Bhatnagar-Gross-Krook model for flows with viscous heat dissipation in the incompressible limit. *Physical Review E*, 70(6):066310, 2004. (page 72)
- [176] Q. Li, Y.L. He, Y. Wang, and W.Q. Tao. Coupled double-distribution-function lattice Boltzmann method for the compressible Navier-Stokes equations. *Physical Review E*, 76(5):056705, 2007. (page 72, 74)
- [177] Q. Li, K.H. Luo, Y.L. He, Y.J. Gao, and W.Q. Tao. Coupling lattice Boltzmann model for simulation of thermal flows on standard lattices. *Physical Review E*, 85(1):016710, 2012. (page 72, 74, 110, 116)
- [178] Z. Guo, C. Zheng, B. Shi, and T.S. Zhao. Thermal lattice Boltzmann equation for low Mach number flows: Decoupling model. *Physical Review E*, 75(3):036704, 2007. (page 72, 74)
- [179] L. Fei, K.H. Luo, C. Lin, and Q. Li. Modeling incompressible thermal flows using a central-moments-based lattice Boltzmann method. *International Journal of Heat and Mass Transfer*, 120:624–634, 2018. (page 72)
- [180] E. Fattahi, M. Farhadi, K. Sedighi, and H. Nemati. Lattice Boltzmann simulation of natural convection heat transfer in nanofluids. *International Journal of Thermal Sciences*, 52:137–144, 2012. (page 72)
- [181] Z. Guo and T.S. Zhao. A lattice Boltzmann model for convection heat transfer in porous media. *Numerical Heat Transfer, Part B*, 47(2):157–177, 2005. (page 72)
- [182] B. Chopard, J.L. Falcone, and J. Latt. The lattice Boltzmann advection-diffusion model revisited. *The European Physical Journal Special Topics*, 171(1):245–249, 2009. (page 76)
- [183] Y. Sun and Indrek S. W. On transient heat conduction in a one-dimensional composite slab. *International Journal of Heat and Mass Transfer*, 47(6-7):1555–1559, 2004. (page 79)
- [184] H. Mai, K. Lin, C. Yang, and C. Lin. A thermal lattice Boltzmann model for flows with viscous heat dissipation. *Computer Modeling in Engineering & Sciences*, 61(1):45–62, 2010. (page 80)

- [185] F.M. Elseid, S.W.J. Welch, and K.N. Premnath. A cascaded lattice Boltzmann model for thermal convective flows with local heat sources. *International Journal of Heat and Fluid Flow*, 70:279–298, 2018. (page 80)
- [186] A. Korichi and L. Oufer. Unsteady heat transfer and pressure drop in channels with obstacles mounted on the upper and lower walls. *Numerical Heat Transfer, Part A: Applications*, 48(7):711–729, 2005. (page 80, 81, 82)
- [187] T. Zhang, B. Shi, Z. Guo, Z. Chai, and J. Lu. General bounce-back scheme for concentration boundary condition in the lattice-Boltzmann method. *Physical Review E*, 85(1):016701, 2012. (page 81)
- [188] G. Silva and V. Semiao. Truncation errors and the rotational invariance of three-dimensional lattice models in the lattice Boltzmann method. *Journal of Computational Physics*, 269:259–279, 2014. (page 87)
- [189] M. Bauer, G. Silva, and U. Rude. Truncation errors of the D3Q19 lattice model for the lattice Boltzmann method. *Journal of Computational Physics*, 405:109111, 2020. (page 87)
- [190] E.P. Gross and M. Krook. Model for collision processes in gases: Small amplitude oscillations of charged two-component systems. *Physical Review*, 102(3):593, 1956. (page 90)
- [191] B.B. Hamel. Kinetic model for binary gas mixtures. *Physics of Fluids*, 8(3):418–425, 1965. (page 90)
- [192] S. Brull, V. Pavan, and J. Schneider. Derivation of a BGK model for mixtures. *European Journal of Mechanics-B/Fluids*, 33:74–86, 2012. (page 90)
- [193] P. Andries, K. Aoki, and B. Perthame. A consistent BGK-type model for gas mixtures. *Journal of Statistical Physics*, 106(5-6):993–1018, 2002. (page 90)
- [194] L.S. Luo and S.S. Girimaji. Lattice Boltzmann model for binary mixtures. *Physical Review E*, 66(3):035301, 2002. (page 90)
- [195] H. Yu, L.S. Luo, and S.S. Girimaji. Scalar mixing and chemical reaction simulations using lattice Boltzmann method. *International Journal of Computational Engineering Science*, 3(01):73–87, 2002. (page 90)
- [196] M.E. McCracken and J. Abraham. Lattice Boltzmann methods for binary mixtures with different molecular weights. *Physical Review E*, 71(4):046704, 2005. (page 90)
- [197] J. Zudrop, K. Masilamani, S. Roller, and P. Asinari. A robust lattice Boltzmann method for parallel simulations of multicomponent flows in complex geometries. *Computers & Fluids*, 153:20–33, 2017. (page 90)

- [198] R.C. Reid, J.M. Prausnitz, and B.E. Poling. The properties of gases and liquids. 1987. (page 94)
- [199] P.D. Neufeld, A.R. Janzen, and R.A. Aziz. Empirical equations to calculate 16 of the transport collision integrals $\omega(1, s)^*$ for the Lennard-Jones (12-6) potential. *The Journal of Chemical Physics*, 57(3):1100–1102, 1972. (page 94)
- [200] M.B. Schlaffer. *Non-reflecting boundary conditions for the lattice Boltzmann method*. PhD thesis, Technische Universität München, 2013. (page 96)
- [201] N. Darabiha and S. Candel. The influence of the temperature on extinction and ignition limits of strained hydrogen-air diffusion flames. *Combustion Science and Technology*, 86(1-6):67–85, 1992. (page 99, 100)
- [202] A. Majda and J. Sethian. The derivation and numerical solution of the equations for zero Mach number combustion. *Combustion Science and Technology*, 42(3-4):185–205, 1985. (page 105)
- [203] X. He, S. Chen, and R. Zhang. A lattice Boltzmann scheme for incompressible multiphase flow and its application in simulation of Rayleigh–Taylor instability. *Journal of Computational Physics*, 152(2):642–663, 1999. (page 106)
- [204] X. He, X. Shan, and G.D. Doolen. Discrete Boltzmann equation model for nonideal gases. *Physical Review E*, 57(1):R13, 1998. (page 106, 107)
- [205] M. Ashna, M.H. Rahimian, and A. Fakhari. Extended lattice Boltzmann scheme for droplet combustion. *Physical Review E*, 95(5):053301, 2017. (page 106, 109)
- [206] K. Sun, S. Yang, and C.K. Law. A diffuse interface method for simulating the dynamics of premixed flames. *Combustion and Flame*, 163:508–516, 2016. (page 106)
- [207] L. Fei and K.H. Luo. Cascaded lattice Boltzmann method for thermal flows on standard lattices. *International Journal of Thermal Sciences*, 132:368–377, 2018. (page 110, 116, 121, 122)
- [208] D. Thévenin. Using the Taylor-Green vortex as a benchmark for combustion DNS. In *17th International Conference on Numerical Combustion*, page 33, 2019. (page 111)
- [209] A. Abdelsamie. Taylor-Green vortex as a benchmark of DNS combustion codes: Results and comparisons for the reacting cases. In *17th International Conference on Numerical Combustion*, page 34, 2019. (page 111)
- [210] A Abdelsamie, G Fru, T Oster, F Dietzsch, Gábor Janiga, and D Thévenin. Towards direct numerical simulations of low-Mach number turbulent reacting and two-phase flows using immersed boundaries. *Computers & Fluids*, 131:123–141, 2016. (page 113)
- [211] N.I. Prasianakis and I.V. Karlin. Lattice Boltzmann method for thermal flow simulation on standard lattices. *Physical Review E*, 76(1):016702, 2007. (page 116)

- [212] Y.L. Feng, S.L. Guo, W. Tao, and P. Sagaut. Regularized thermal lattice Boltzmann method for natural convection with large temperature differences. *International Journal of Heat and Mass Transfer*, 125:1379–1391, 2018. (page 116, 117)
- [213] A.L. Kupershtokh. Incorporating a body force term into the lattice Boltzmann equation. *Vestnik NGU (Quarterly Journal of Novosibirsk State Univ.), Series: Math., Mech. and Informatics*, 4(2):75–96, 2004. (page 118)
- [214] A.L. Kupershtokh, D.A. Medvedev, and D.I. Karpov. On equations of state in a lattice Boltzmann method. *Computers & Mathematics with Applications*, 58(5):965–974, 2009. (page 118)
- [215] X. Liu, S. Osher, and T. Chan. Weighted essentially non-oscillatory schemes. *Journal of Computational Physics*, 115(1):200–212, 1994. (page 128)
- [216] Y.L. Feng, M. Tayyab, and P. Boivin. A lattice-Boltzmann model for low-Mach reactive flows. *Combustion and Flame*, 196:249–254, 2018. (page 135)
- [217] D.G. Goodwin, R.L. Speth, H.K. Moffat, and B.W. Weber. Cantera: An Object-oriented Software Toolkit for Chemical Kinetics, Thermodynamics, and Transport Processes. <https://www.cantera.org>, 2018. Version 2.4.0. (page 136)
- [218] B. Franzelli, E. Riber, L.Y.M. Gicquel, and T. Poinso. Large eddy simulation of combustion instabilities in a lean partially premixed swirled flame. *Combustion and Flame*, 159(2):621–637, 2012. (page 136, 146)
- [219] T. Poinso, D. Veynante, and S. Candel. Diagrams of premixed turbulent combustion based on direct simulation. In *Symposium (International) on Combustion*, volume 23, pages 613–619. Elsevier, 1991. (page 145)
- [220] T. Poinso, D. Veynante, and S. Candel. Quenching processes and premixed turbulent combustion diagrams. *Journal of Fluid Mechanics*, 228:561–606, 1991. (page 145)
- [221] C.W. Oseen. Über die wirbelbewegung in einer reibenden Flüssigkeit. *Ark. Mat. Astro. Fys.*, 7, 1912. (page 145)
- [222] J.M. Samaniego and T. Mantel. Fundamental mechanisms in premixed turbulent flame propagation via flame–vortex interactions: Part I: Experiment. *Combustion and Flame*, 118(4):537–556, 1999. (page 145)
- [223] T.J.M.S. Mantel and J.M. Samaniego. Fundamental mechanisms in premixed turbulent flame propagation via vortex–flame interactions part II: Numerical simulation. *Combustion and Flame*, 118(4):557–582, 1999. (page 145)
- [224] C. Sun. Lattice-Boltzmann models for high speed flows. *Physical Review E*, 58(6):7283, 1998. (page 153)

- [225] C. Sun. Adaptive lattice Boltzmann model for compressible flows: Viscous and conductive properties. *Physical Review E*, 61(3):2645, 2000. (page 153)
- [226] C. Sun and A.T. Hsu. Three-dimensional lattice Boltzmann model for compressible flows. *Physical Review E*, 68(1):016303, 2003. (page 153)
- [227] X. Shan and X. He. Discretization of the velocity space in the solution of the Boltzmann equation. *Physical Review Letters*, 80(1):65, 1998. (page 154, 155)
- [228] Z.J. Wang, K. Fidkowski, R. Abgrall, F. Bassi, D. Caraeni, A. Cary, H. Deconinck, R. Hartmann, K. Hillewaert, H.T. Huynh, N. Kroll, G. May, P. Persson, B. van Leer, and M. Visbal. High-order CFD methods: Current status and perspective. *Int. J. Numer. Meth. Fluids*, 72(8):811–845, 2013. (page 158)
- [229] C. Chi, A. Abdelsamie, and D. Thévenin. A directional ghost-cell immersed boundary method for incompressible flows. *Journal of Computational Physics*, 404:109122, 2020. (page 166)
- [230] W. Kim and H. Choi. Immersed boundary methods for fluid-structure interaction: A review. *International Journal of Heat and Fluid Flow*, 2019. (page 166)
- [231] R. Mittal and G. Iaccarino. Immersed boundary methods. *Annu. Rev. Fluid Mech.*, 37:239–261, 2005. (page 166)
- [232] G. Hou, J. Wang, and A. Layton. Numerical methods for fluid-structure interaction: A review. *Communications in Computational Physics*, 12(2):337–377, 2012. (page 166)
- [233] R. Mei, L.S. Luo, and W. Shyy. An accurate curved boundary treatment in the lattice Boltzmann method. In *14th Computational Fluid Dynamics Conference*, page 3353, 2000. (page 166)
- [234] S.S Chikatamarla and I.V. Karlin. Entropic lattice Boltzmann method for turbulent flow simulations: Boundary conditions. *Physica A: Statistical Mechanics and its Applications*, 392(9):1925–1930, 2013. (page 166)
- [235] S.S. Chikatamarla, S. Ansumali, and I.V. Karlin. Grad’s approximation for missing data in lattice Boltzmann simulations. *EPL (Europhysics Letters)*, 74(2):215, 2006. (page 166)
- [236] S.A. Hosseini, N. Darabiha, and D. Thévenin. Boltzmann on standard stencils : Effects of deviation from reference temperature. *Philosophical Transactions of the Royal Society of London. Series A*, 2020(submitted). (page 201)

Appendix A

Journal publications of the candidate

2020

[1] **S.A. Hosseini**, N. Darabiha, and D. Thévenin. Compressibility in lattice Boltzmann on standard stencils : Effects of deviation from reference temperature. *Phil. Trans. A*, 2020 (submitted).

2019

[2] **S.A. Hosseini**, N. Darabiha, and D. Thévenin. Theoretical and numerical analysis of the lattice kinetic scheme for complex-flow simulations. *Physical Review E*, 99(2), p.023305, 2019.

[3] **S.A. Hosseini**, C. Coreixas, N. Darabiha, and D Thévenin. Stability of the lattice kinetic scheme and choice of the free relaxation parameter. *Physical Review E*, 99(6), p.063305, 2019.

[4] **S.A. Hosseini**, H. Safari, N. Darabiha, D Thévenin, and M. Krafczyk. Hybrid Lattice Boltzmann-finite difference model for low mach number combustion simulation. *Combustion and Flame*, 209, pp.394-404, 2019.

[5] **S.A. Hosseini**, N. Darabiha, and D. Thévenin. Lattice Boltzmann advection-diffusion model for conjugate heat transfer in heterogeneous media. *International Journal of Heat and Mass Transfer*, 132, pp.906-919, 2019.

[6] **S.A. Hosseini**, C. Coreixas, N. Darabiha, and D Thévenin. Extensive analysis of the lattice Boltzmann method on shifted stencils. *Physical Review E*, 100(6), p.063301, 2019.

[7] A. Eshghinejadfard, **S.A. Hosseini** and D. Thévenin. Effect of particle density in turbulent channel flows with resolved oblate spheroids. *Computers & Fluids*, 184, pp.29-39, 2019.

2018

[8] **S.A. Hosseini**, N. Darabiha, and D. Thévenin. Mass-conserving advection-diffusion Lattice Boltzmann model for multi-species reacting flows. *Physica A: Statistical Mechanics and its Applications*, 499, pp.40-57, 2018.

2017

[9] A. Eshghinejadfard, **S.A. Hosseini**, and D. Thévenin. Fully-resolved prolate spheroids in turbulent channel flows: a lattice Boltzmann study. *AIP Advances*, 7(9), 095007, 2017

[10] A. Eshghinejadfard, A. Abdelsamie, **S.A. Hosseini** and D. Thévenin. Immersed boundary lattice Boltzmann simulation of turbulent channel flows in the presence of spherical particles. *International Journal of Multiphase Flow*, 96, pp.161-172, 2017.

[11] **S.A. Hosseini**, N. Darabiha, D. Thévenin, and A. Eshghinejadfard. Stability limits of the single relaxation-time advection-diffusion lattice Boltzmann scheme. *International Journal of Modern Physics C*, 28(12), p.1750141, 2017.

[12] **S.A. Hosseini**, A. Eshghinejadfard, N. Darabiha, and D. Thévenin. Weakly compressible Lattice Boltzmann simulations of reacting flows with detailed thermo-chemical models. *Computers & Mathematics with Applications*, 79(1), pp.141-158, 2020.

Appendix B

Hermite expansion

B.1 Single variable Hermite polynomials

The single variable Hermite polynomial \mathcal{H}_n of order n of a variable x is defined as:

$$\mathcal{H}_n(x) = \frac{(-1)^n}{w(x)} \frac{d^n}{dx^n} w(x), \quad (\text{B.1})$$

where the normalized function $w(x)$ is defined as:

$$w(x) = \frac{1}{\sqrt{2\pi}} e^{-\frac{x^2}{2}}. \quad (\text{B.2})$$

Based on this definition, the first few polynomials can be computed as:

$$\mathcal{H}_0 = 1, \quad (\text{B.3a})$$

$$\mathcal{H}_1 = x, \quad (\text{B.3b})$$

$$\mathcal{H}_2 = x^2 - 1, \quad (\text{B.3c})$$

$$\mathcal{H}_3 = x^3 - 3x, \quad (\text{B.3d})$$

$$\mathcal{H}_4 = x^4 - 6x^2 + 3, \quad (\text{B.3e})$$

$$\mathcal{H}_5 = x^5 - 10x^3 + 15x, \quad (\text{B.3f})$$

$$\mathcal{H}_6 = x^6 - 15x^4 + 45x^2 - 15. \quad (\text{B.3g})$$

These polynomials are mutually orthogonal with respect to the weight function, $w(x)$, i.e.:

$$\int_{-\infty}^{+\infty} \mathcal{H}_m(x) w(x) \mathcal{H}_n(x) dx = n! \delta_{mn}, \quad (\text{B.4})$$

where δ_{mn} is the Kronecker delta function. Furthermore, they form a complete orthogonal basis of the Hilbert space of functions $f(x)$ satisfying:

$$\int_{-\infty}^{+\infty} |f(x)|^2 w(x) dx < \infty. \quad (\text{B.5})$$

As such, one can express the function $f(x)$ as:

$$f(x) = \sum_{n=0}^{\infty} \mathbf{a}_n \mathcal{H}_n(x), \quad (\text{B.6})$$

where \mathbf{a}_n is the order n Hermite coefficient. Multiplying both sides by $\mathcal{H}_m(x)w(x)$ and integrating over x :

$$\int_{-\infty}^{+\infty} \mathcal{H}_m(x) w(x) f(x) dx = \sum_{n=0}^{\infty} \mathbf{a}_n \int_{-\infty}^{+\infty} \mathcal{H}_m(x) w(x) \mathcal{H}_n(x) dx, \quad (\text{B.7})$$

B.1. Single variable Hermite polynomials

and using the mutual orthogonality of Hermite polynomials, we get an expression for the Hermite coefficients as:

$$\mathbf{a}_m = \frac{1}{m!} \int_{-\infty}^{+\infty} \mathcal{H}_m(x) w(x) f(x) dx. \quad (\text{B.8})$$

Alternatively, one can also expand the function $f(x)$ as:

$$f(x) = w(x) \sum_{n=0}^{\infty} \frac{1}{n!} \mathbf{a}_n \mathcal{H}_n(x), \quad (\text{B.9})$$

resulting in the following expression for the coefficient $\mathbf{a}^{(m)}$:

$$\mathbf{a}_m = \int_{-\infty}^{+\infty} \mathcal{H}_m(x) f(x) dx. \quad (\text{B.10})$$

To better illustrate this, let us consider the example of the following function:

$$f(x) = \rho \frac{1}{\sqrt{2\pi\theta}} e^{-\frac{(x-u)^2}{2\theta}}. \quad (\text{B.11})$$

This function can be shown to be square-integrable with respect to the previously-defined weight function. As such the corresponding Hermite coefficients can be computed through Eq. B.10:

$$\mathbf{a}_m = \frac{1}{\sqrt{2\pi\theta}} \int_{-\infty}^{+\infty} \mathcal{H}_m(x) e^{-\frac{(x-u)^2}{2\theta}} dx, \quad (\text{B.12})$$

which using the change of variable $\eta = (x - u)/\sqrt{\theta}$ can be re-written as:

$$\mathbf{a}_m = \frac{1}{\sqrt{2\pi}} \int_{-\infty}^{+\infty} \mathcal{H}_m(\sqrt{\theta}\eta + u) e^{-\frac{\eta^2}{2}} d\eta. \quad (\text{B.13})$$

The different order coefficients can be easily evaluated using the following integral:

$$\int_{-\infty}^{+\infty} x^k e^{-ax^2} dx = \begin{cases} 0 & k = 2k' + 1 \\ \frac{(2k'-1)!}{(2a)^{k'}} \sqrt{\frac{\pi}{a}} & k = 2k' \end{cases}, \quad (\text{B.14})$$

leading to the following expansion:

$$f(x) = \sum_{n=0}^{\infty} \frac{\rho w(x)}{n!} \mathbf{a}_n \mathcal{H}_n(x). \quad (\text{B.15})$$

The first few terms are given in Table B.1.

B.2. Multivariate Hermite polynomials

n	\mathbf{a}_n	$\mathcal{H}_n(x)$
0	1	1
1	u	x
2	$u^2 + (\theta - 1)$	$x^2 - 1$
3	$u^3 + 3u(\theta - 1)$	$x^3 - 3x$
4	$u^4 + 6u^2(\theta - 1) + 3(\theta - 1)^2$	$x^4 - 6x^2 + 3$
5	$u^5 + 10u^3(\theta - 1) + 15u(\theta - 1)^2$	$x^5 - 10x^3 + 15x$
6	$u^6 + 15u^4(\theta - 1) + 45u^2(\theta - 1)^2 + 15(\theta - 1)^3$	$x^6 - 15x^4 + 45x^2 - 15$
7	$u^7 + 21u^5(\theta - 1) + 105u^3(\theta - 1)^2 + 105u(\theta - 1)^3$	$x^7 - 21x^5 + 105x^3 - 105x$
8	$u^8 + 28u^6(\theta - 1) + 210u^4(\theta - 1)^2 + 420u^2(\theta - 1)^3 + 105(\theta - 1)^4$	$x^8 - 28x^6 + 210x^4 - 420x^2 + 105$
9	$u^9 + 36u^7(\theta - 1) + 378u^5(\theta - 1)^2 + 1260u^3(\theta - 1)^3 + 945u(\theta - 1)^4$	$x^9 - 36x^7 + 378x^5 - 1260x^3 + 945x$

Table B.1: Hermite polynomials and coefficients for the Gaussian distribution function

B.2 Multivariate Hermite polynomials

In a D -dimensional space the Hermite polynomial of order n is defined as:

$$\mathcal{H}_n(\mathbf{x}) = \frac{(-1)^n}{w(\mathbf{x})} \nabla^n w(\mathbf{x}), \quad (\text{B.16})$$

where ∇^n is the n^{th} order derivative resulting in a tensor of rank n and $w(\mathbf{x})$ is the weight function defined as:

$$w(\mathbf{x}) = \frac{1}{2\pi^{D/2}} e^{-\frac{\mathbf{x}^2}{2}}. \quad (\text{B.17})$$

Orthogonality of the multivariate Hermite polynomials results in:

$$\int_{-\infty}^{+\infty} w(\mathbf{x}) \mathcal{H}_i(\mathbf{x}) : \mathcal{H}_j(\mathbf{x}) d\mathbf{x} = \begin{cases} 0 & m \neq n \\ n! \delta_{\mathbf{i}, \mathbf{j}} & m = n \end{cases}, \quad (\text{B.18})$$

where \mathbf{i} and \mathbf{j} are abbreviations for the set of indices $\{i_1, i_2, \dots, i_n\}$ and $\{j_1, j_2, \dots, j_n\}$ respectively, and $\delta_{\mathbf{i}, \mathbf{j}}$ is equal to unity if \mathbf{i} is a permutation of \mathbf{j} and zero otherwise. In a 3-D

B.2. Multivariate Hermite polynomials

space the first few Hermite polynomials are computed as:

$$\mathcal{H}_0 = 1, \quad (\text{B.19a})$$

$$\mathcal{H}_i = x_i, \quad (\text{B.19b})$$

$$\mathcal{H}_{ij} = x_i x_j - \delta_{ij}, \quad (\text{B.19c})$$

$$\mathcal{H}_{ijk} = x_i x_j x_k - (\delta_{ij} x_k + \delta_{ik} x_j + \delta_{jk} x_i), \quad (\text{B.19d})$$

$$\begin{aligned} \mathcal{H}_{ijkl} = & x_i x_j x_k x_l - (\delta_{ij} x_k x_l + \delta_{ik} x_j x_l + \delta_{il} x_j x_k + \delta_{jk} x_i x_l + \delta_{jl} x_i x_k + \delta_{kl} x_i x_j) \\ & + (\delta_{ij} \delta_{kl} + \delta_{ik} \delta_{jl} + \delta_{il} \delta_{jk}), \end{aligned} \quad (\text{B.19e})$$

$$\begin{aligned} \mathcal{H}_{ijklm} = & x_i x_j x_k x_l x_m - (\delta_{lm} x_i x_j x_k + \delta_{km} x_i x_j x_l + \delta_{kl} x_i x_j x_m + \delta_{jm} x_i x_k x_l \\ & + \delta_{jl} x_i x_k x_m + \delta_{kl} x_i x_l x_m + \delta_{im} x_j x_k x_l + \delta_{il} x_j x_k x_m + \delta_{ik} x_j x_l x_m + \delta_{ij} x_k x_l x_m) \\ & + x_m (\delta_{ij} \delta_{kl} + \delta_{ik} \delta_{jl} + \delta_{il} \delta_{jk}) + x_l (\delta_{ij} \delta_{km} + \delta_{ik} \delta_{jm} + \delta_{im} \delta_{jk}) \\ & + x_k (\delta_{ij} \delta_{lm} + \delta_{il} \delta_{jm} + \delta_{im} \delta_{jl}) + x_j (\delta_{ik} \delta_{lm} + \delta_{il} \delta_{km} + \delta_{im} \delta_{kl}) \\ & + x_i (\delta_{jk} \delta_{lm} + \delta_{jl} \delta_{km} + \delta_{jm} \delta_{kl}), \end{aligned} \quad (\text{B.19f})$$

$$\begin{aligned} \mathcal{H}_{ijklmnn} = & x_i x_j x_k x_l x_m x_n - (x_i x_j x_k x_l \delta_{mn} + x_i x_j x_k x_m \delta_{ln} + x_i x_j x_k x_n \delta_{lm} \\ & + x_i x_j x_l x_m \delta_{kn} + x_i x_j x_l x_n \delta_{km} + x_i x_j x_m x_n \delta_{lk} + x_i x_k x_l x_m \delta_{jn} \\ & x_i x_k x_l x_n \delta_{jm} + x_i x_k x_m x_n \delta_{jl} + x_i x_l x_m x_n \delta_{jk} + x_j x_k x_l x_m \delta_{in} \\ & + x_j x_k x_l x_n \delta_{im} + x_j x_l x_m x_n \delta_{ik} + x_j x_k x_l x_n \delta_{im} + x_j x_k x_m x_n \delta_{il} + x_k x_l x_m x_n \delta_{ij}) \\ & + x_i x_j (\delta_{kl} \delta_{mn} + \delta_{km} \delta_{ln} + \delta_{kn} \delta_{lm}) + x_i x_k (\delta_{jl} \delta_{mn} + \delta_{jm} \delta_{ln} + \delta_{jn} \delta_{ml}) \\ & + x_i x_l (\delta_{jk} \delta_{mn} + \delta_{jm} \delta_{kn} + \delta_{jn} \delta_{mk}) + x_i x_m (\delta_{jk} \delta_{ln} + \delta_{jl} \delta_{kn} + \delta_{jn} \delta_{lk}) \\ & + x_i x_n (\delta_{jk} \delta_{lm} + \delta_{jl} \delta_{km} + \delta_{jm} \delta_{lk}) + x_j x_k (\delta_{in} \delta_{lm} + \delta_{il} \delta_{nm} + \delta_{im} \delta_{ln}) \\ & + x_j x_l (\delta_{in} \delta_{km} + \delta_{ik} \delta_{nm} + \delta_{im} \delta_{kn}) + x_j x_m (\delta_{in} \delta_{kl} + \delta_{ik} \delta_{nl} + \delta_{il} \delta_{kn}) \\ & + x_j x_n (\delta_{il} \delta_{km} + \delta_{ik} \delta_{lm} + \delta_{im} \delta_{kl}) + x_k x_l (\delta_{mn} \delta_{ij} + \delta_{mi} \delta_{nj} + \delta_{mj} \delta_{in}) \\ & + x_k x_m (\delta_{ij} \delta_{ln} + \delta_{il} \delta_{jn} + \delta_{in} \delta_{lj}) + x_k x_n (\delta_{ml} \delta_{ij} + \delta_{mi} \delta_{lj} + \delta_{mj} \delta_{il}) \\ & + x_l x_m (\delta_{ij} \delta_{kn} + \delta_{ik} \delta_{jn} + \delta_{in} \delta_{kj}) + x_l x_n (\delta_{mk} \delta_{ij} + \delta_{mi} \delta_{kj} + \delta_{mj} \delta_{ik}) \\ & + x_n x_m (\delta_{ij} \delta_{kl} + \delta_{ik} \delta_{jl} + \delta_{il} \delta_{kj}) + \delta_{ij} (\delta_{kl} \delta_{mn} + \delta_{km} \delta_{ln} + \delta_{kn} \delta_{ml}) \\ & + \delta_{ik} (\delta_{jl} \delta_{mn} + \delta_{jm} \delta_{ln} + \delta_{jn} \delta_{ml}) + \delta_{il} (\delta_{kj} \delta_{mn} + \delta_{km} \delta_{jn} + \delta_{kn} \delta_{mj}) \\ & + \delta_{im} (\delta_{jl} \delta_{ln} + \delta_{jk} \delta_{ln} + \delta_{jn} \delta_{kl}) + \delta_{in} (\delta_{kj} \delta_{ml} + \delta_{km} \delta_{jl} + \delta_{kl} \delta_{mj}). \end{aligned} \quad (\text{B.19g})$$

As for the single variable case, for a square-integrable function $f(\mathbf{x})$, it can be expressed as:

$$f(\mathbf{x}) = w(\mathbf{x}) \sum_{n=0}^{\infty} \mathbf{a}_n : \mathcal{H}_n(\mathbf{x}), \quad (\text{B.20})$$

where the Hermite coefficients $\mathbf{a}^{(n)}$ are defined as:

$$\mathbf{a}_n = \frac{1}{n!} \int_{-\infty}^{+\infty} f(\mathbf{x}) \mathcal{H}_n(\mathbf{x}) d\mathbf{x}, \quad (\text{B.21})$$

resulting in the following coefficients for the Maxwell-Boltzmann distribution function:

$$\mathbf{a}_0 = \rho, \quad (\text{B.22a})$$

$$\mathbf{a}_i = \rho u_i, \quad (\text{B.22b})$$

$$\mathbf{a}_{ij} = \rho u_i u_j + \rho(\theta - 1) \delta_{ij}, \quad (\text{B.22c})$$

$$\mathbf{a}_{ijk} = \rho u_i u_j u_k + \rho(\theta - 1) (\delta_{ij} u_k + \delta_{ik} u_j + \delta_{jk} u_i), \quad (\text{B.22d})$$

$$\begin{aligned} \mathbf{a}_{ijkl} &= \rho u_i u_j u_k u_l + \rho(\theta - 1) (\delta_{ij} u_k u_l + \delta_{ik} u_j u_l + \delta_{il} u_j u_k + \delta_{jk} u_i u_l + \delta_{jl} u_i u_k + \delta_{kl} u_i u_j) \\ &\quad + \rho(\theta - 1)^2 (\delta_{ij} \delta_{kl} + \delta_{ik} \delta_{jl} + \delta_{il} \delta_{jk}), \end{aligned} \quad (\text{B.22e})$$

$$\begin{aligned} \mathbf{a}_{ijklm} &= \rho u_i u_j u_k u_l u_m + \rho(\theta - 1) (\delta_{lm} u_i u_j u_k + \delta_{km} u_i u_j u_l + \delta_{kl} u_i u_j u_m + \delta_{jm} u_i u_k u_l \\ &\quad + \delta_{jl} u_i u_k u_m + \delta_{kl} u_i u_l u_m + \delta_{im} u_j u_k u_l + \delta_{il} u_j u_k u_m + \delta_{ik} u_j u_l u_m + \delta_{ij} u_k u_l u_m) \\ &\quad + \rho(\theta - 1)^2 [u_m (\delta_{ij} \delta_{kl} + \delta_{ik} \delta_{jl} + \delta_{il} \delta_{jk}) + u_l (\delta_{ij} \delta_{km} + \delta_{ik} \delta_{jm} + \delta_{im} \delta_{jk}) \\ &\quad + u_k (\delta_{ij} \delta_{lm} + \delta_{il} \delta_{jm} + \delta_{im} \delta_{jl}) + u_j (\delta_{ik} \delta_{lm} + \delta_{il} \delta_{km} + \delta_{im} \delta_{kl}) \\ &\quad + u_i (\delta_{jk} \delta_{lm} + \delta_{jl} \delta_{km} + \delta_{jm} \delta_{kl})], \end{aligned} \quad (\text{B.22f})$$

$$\begin{aligned} \mathbf{a}_{ijklmn} &= \rho u_i u_j u_k u_l u_m u_n + \rho(\theta - 1) (u_i u_j u_k u_l \delta_{mn} + u_i u_j u_k u_m \delta_{ln} + u_i u_j u_k u_n \delta_{lm} \\ &\quad + u_i u_j u_l u_m \delta_{kn} + u_i u_j u_l u_n \delta_{km} + u_i u_j u_m u_n \delta_{lk} + u_i u_k u_l u_m \delta_{jn} \\ &\quad + u_i u_k u_l u_n \delta_{jm} + u_i u_k u_m u_n \delta_{jl} + u_i u_l u_m u_n \delta_{jk} + u_j u_k u_l u_m \delta_{in} \\ &\quad + u_j u_k u_l u_n \delta_{im} + u_j u_l u_m u_n \delta_{ik} + u_j u_k u_l u_n \delta_{im} + u_j u_k u_m u_n \delta_{il} + u_k u_l u_m u_n \delta_{ij}) \\ &\quad + \rho(\theta - 1)^2 [u_i u_j (\delta_{kl} \delta_{mn} + \delta_{km} \delta_{ln} + \delta_{kn} \delta_{lm}) + u_i u_k (\delta_{jl} \delta_{mn} + \delta_{jm} \delta_{ln} + \delta_{jn} \delta_{ml}) \\ &\quad + u_i u_l (\delta_{jk} \delta_{mn} + \delta_{jm} \delta_{kn} + \delta_{jn} \delta_{mk}) + u_i u_m (\delta_{jk} \delta_{ln} + \delta_{jl} \delta_{kn} + \delta_{jn} \delta_{lk}) \\ &\quad + u_i u_n (\delta_{jk} \delta_{lm} + \delta_{jl} \delta_{km} + \delta_{jm} \delta_{lk}) + u_j u_k (\delta_{in} \delta_{lm} + \delta_{il} \delta_{nm} + \delta_{im} \delta_{ln}) \\ &\quad + u_j u_l (\delta_{in} \delta_{km} + \delta_{ik} \delta_{nm} + \delta_{im} \delta_{kn}) + u_j u_m (\delta_{in} \delta_{kl} + \delta_{ik} \delta_{nl} + \delta_{il} \delta_{kn}) \\ &\quad + u_j u_n (\delta_{il} \delta_{km} + \delta_{ik} \delta_{lm} + \delta_{im} \delta_{kl}) + u_k u_l (\delta_{mn} \delta_{ij} + \delta_{mi} \delta_{nj} + \delta_{mj} \delta_{in}) \\ &\quad + u_k u_m (\delta_{ij} \delta_{ln} + \delta_{il} \delta_{jn} + \delta_{in} \delta_{lj}) + u_k u_n (\delta_{ml} \delta_{ij} + \delta_{mi} \delta_{lj} + \delta_{mj} \delta_{il}) \\ &\quad + u_l u_m (\delta_{ij} \delta_{kn} + \delta_{ik} \delta_{jn} + \delta_{in} \delta_{kj}) + u_l u_n (\delta_{mk} \delta_{ij} + \delta_{mi} \delta_{kj} + \delta_{mj} \delta_{ik}) \\ &\quad + u_n u_m (\delta_{ij} \delta_{kl} + \delta_{ik} \delta_{jl} + \delta_{il} \delta_{kj})] + \rho(\theta - 1)^3 [\delta_{ij} (\delta_{kl} \delta_{mn} + \delta_{km} \delta_{ln} + \delta_{kn} \delta_{ml}) \\ &\quad + \delta_{ik} (\delta_{jl} \delta_{mn} + \delta_{jm} \delta_{ln} + \delta_{jn} \delta_{ml}) + \delta_{il} (\delta_{kj} \delta_{mn} + \delta_{km} \delta_{jn} + \delta_{kn} \delta_{mj}) \\ &\quad + \delta_{im} (\delta_{jl} \delta_{ln} + \delta_{jk} \delta_{ln} + \delta_{jn} \delta_{kl}) + \delta_{in} (\delta_{kj} \delta_{ml} + \delta_{km} \delta_{jl} + \delta_{kl} \delta_{mj})]. \end{aligned} \quad (\text{B.22g})$$

Appendix C

First-neighbor stencils

C.1 2-Dimensional stencils

In the context of this manuscript, two sets of discrete velocities are employed: (a) D2Q5 and D2Q9. Both of these stencils are shown in Fig. C.1.

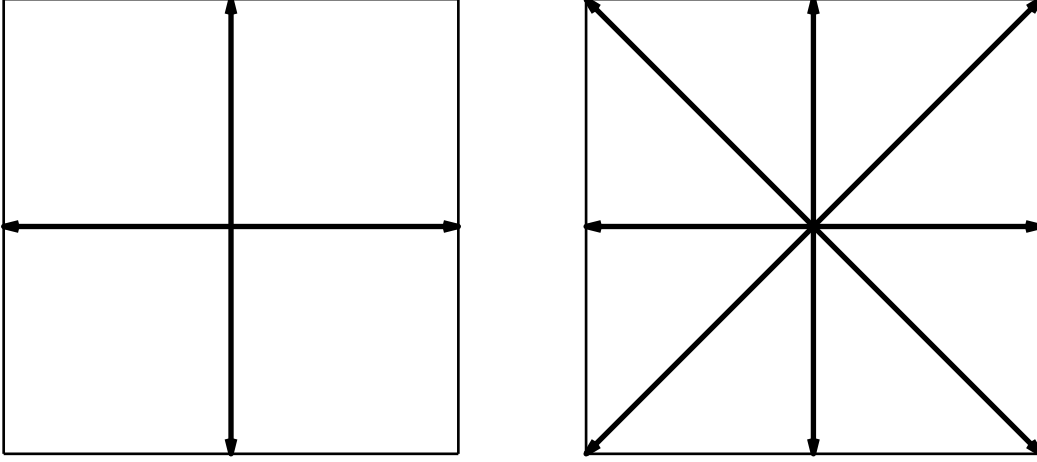


Figure C.1: 2-D stencils used in this manuscript: (left) D2Q5 and (right) D2Q9.

- The D2Q5 stencil consists of the following velocity vectors:

$$\mathbf{c}_\alpha = \begin{pmatrix} 0 & 1 & 0 & -1 & 0 \\ 0 & 0 & 1 & 0 & -1 \end{pmatrix}, \quad (\text{C.1})$$

associated to the following discrete weights:

$$w_\alpha = \left(\frac{1}{3} \quad \frac{1}{6} \quad \frac{1}{6} \quad \frac{1}{6} \quad \frac{1}{6} \right). \quad (\text{C.2})$$

Given the number of degrees in the quadrature leading to the stencil, it can only correctly recover moments associated to the following Hermite polynomials: $\mathcal{H} = \{\mathcal{H}_0, \mathcal{H}_x, \mathcal{H}_y, \mathcal{H}_{x^2}, \mathcal{H}_{y^2}\}$. As such it can not be used for the flow field, as it is unable to recover moments appearing in the stress tensor.

- The D2Q9 stencil on the other hand has the following vectors:

$$\mathbf{c}_\alpha = \begin{pmatrix} 0 & 1 & 0 & -1 & 0 & 1 & -1 & -1 & 1 \\ 0 & 0 & 1 & 0 & -1 & 1 & 1 & -1 & -1 \end{pmatrix}, \quad (\text{C.3})$$

associated to the following discrete weights:

$$w_\alpha = \left(\frac{4}{9} \quad \frac{1}{9} \quad \frac{1}{9} \quad \frac{1}{9} \quad \frac{1}{9} \quad \frac{1}{36} \quad \frac{1}{36} \quad \frac{1}{36} \quad \frac{1}{36} \right). \quad (\text{C.4})$$

This stencil can correctly recover moments associated to the following Hermite polynomials: $\mathcal{H} = \{\mathcal{H}_0, \mathcal{H}_x, \mathcal{H}_y, \mathcal{H}_{x^2}, \mathcal{H}_{y^2}, \mathcal{H}_{xy}, \mathcal{H}_{x^2y}, \mathcal{H}_{xy^2}, \mathcal{H}_{x^2y^2}\}$. It can therefore be used for

the momentum conservation equation with an error in NS level stress tensor associated to the diagonal components of the third-order moments tensor.

C.2 3-Dimensional stencils

Of all possible first-neighbour 3-D stencils, four are used within the context of this work. All of them all shown in Fig. C.2. Starting with the largest one:

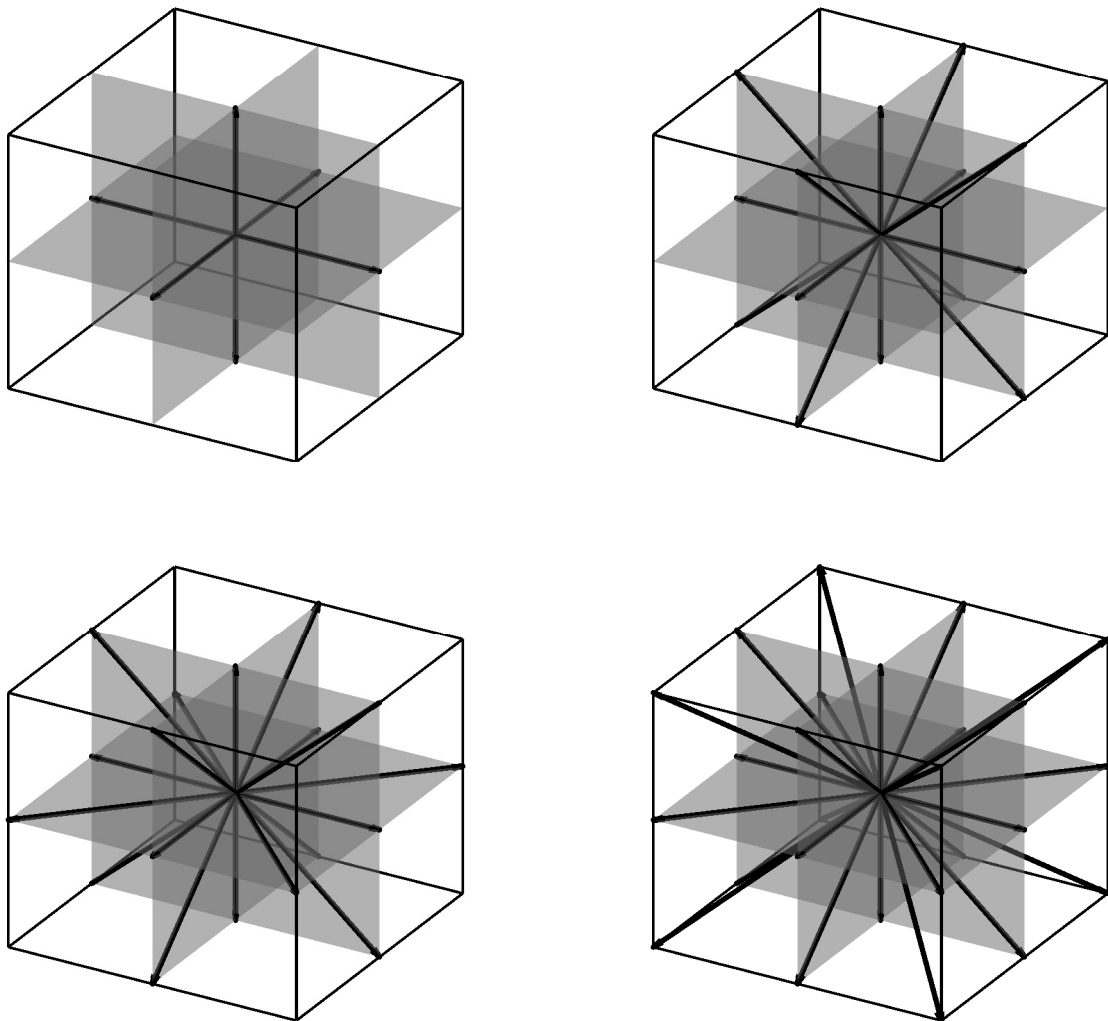


Figure C.2: 3-D stencils used in this manuscript: (top left) D3Q7, (top right) D3Q15, (bottom left) D3Q19 and (bottom right) D3Q27.

- D3Q27, it is made up of the following discrete velocities:

$$\mathbf{c}_\alpha = \begin{pmatrix} 0 & 1 & -1 & 0 & 0 & 0 & 0 & 1 & -1 & 1 & -1 & 1 & -1 & 1 & -1 & 0 & 0 & 0 & 0 & 1 & -1 & 1 & -1 & 1 & -1 & 1 & -1 \\ 0 & 0 & 0 & 1 & -1 & 0 & 0 & 1 & 1 & -1 & -1 & 0 & 0 & 0 & 0 & 1 & -1 & 1 & -1 & 1 & 1 & -1 & -1 & 1 & 1 & -1 & -1 \\ 0 & 0 & 0 & 1 & -1 & 0 & 0 & 1 & 1 & -1 & -1 & 0 & 0 & 0 & 0 & 1 & -1 & 1 & -1 & 1 & 1 & -1 & -1 & 1 & 1 & -1 & -1 \end{pmatrix}, \quad (\text{C.5})$$

associated to these weights:

$$w_\alpha = \left(\frac{8}{27} \frac{2}{27} \frac{2}{27} \frac{2}{27} \frac{2}{27} \frac{2}{27} \frac{2}{27} \frac{1}{54} \frac{1}{54} \frac{1}{54} \frac{1}{54} \frac{1}{54} \frac{1}{54} \frac{1}{54} \frac{1}{54} \frac{1}{54} \frac{1}{54} \frac{1}{54} \frac{1}{54} \frac{1}{216} \frac{1}{216} \frac{1}{216} \frac{1}{216} \frac{1}{216} \frac{1}{216} \frac{1}{216} \frac{1}{216} \frac{1}{216} \right). \quad (\text{C.6})$$

This stencil can support the following set of independent Hermite polynomials:

$$\mathcal{H} = \{ \mathcal{H}_0, \mathcal{H}_x, \mathcal{H}_y, \mathcal{H}_z, \mathcal{H}_{xy}, \mathcal{H}_{xz}, \mathcal{H}_{yz}, \mathcal{H}_{x^2}, \mathcal{H}_{y^2}, \mathcal{H}_{z^2}, \mathcal{H}_{x^2y}, \mathcal{H}_{xy^2}, \mathcal{H}_{x^2z}, \mathcal{H}_{xy^2z}, \mathcal{H}_{yz^2}, \mathcal{H}_{xyz}, \mathcal{H}_{x^2y^2}, \mathcal{H}_{x^2z^2}, \mathcal{H}_{y^2z^2}, \mathcal{H}_{xy^2z^2}, \mathcal{H}_{x^2yz^2}, \mathcal{H}_{x^2y^2z}, \mathcal{H}_{x^2yz^2}, \mathcal{H}_{xy^2z^2}, \mathcal{H}_{x^2y^2z^2} \}. \quad (\text{C.7})$$

- The D3Q19 stencil can also be used for both the flow field and advection-diffusion equations. It consists of the following discrete velocities:

$$\mathbf{c}_\alpha = \begin{pmatrix} 0 & 1 & -1 & 0 & 0 & 0 & 0 & 1 & -1 & 1 & -1 & 1 & -1 & 1 & -1 & 0 & 0 & 0 & 0 \\ 0 & 0 & 0 & 1 & -1 & 0 & 0 & 1 & 1 & -1 & -1 & 0 & 0 & 0 & 0 & 1 & -1 & 1 & -1 \\ 0 & 0 & 0 & 1 & -1 & 0 & 0 & 1 & 1 & -1 & -1 & 0 & 0 & 0 & 0 & 1 & -1 & 1 & -1 \end{pmatrix}, \quad (\text{C.8})$$

and weights:

$$w_\alpha = \left(\frac{1}{3} \frac{1}{18} \frac{1}{18} \frac{1}{18} \frac{1}{18} \frac{1}{18} \frac{1}{18} \frac{1}{18} \frac{1}{36} \frac{1}{36} \frac{1}{36} \frac{1}{36} \frac{1}{36} \frac{1}{36} \frac{1}{36} \frac{1}{36} \frac{1}{36} \frac{1}{36} \frac{1}{36} \frac{1}{36} \frac{1}{36} \frac{1}{36} \frac{1}{36} \frac{1}{36} \frac{1}{36} \frac{1}{36} \right). \quad (\text{C.9})$$

- The D3Q15 is made up of the following discrete velocities:

$$\mathbf{c}_\alpha = \begin{pmatrix} 0 & 1 & -1 & 0 & 0 & 0 & 0 & 1 & -1 & 1 & -1 & 1 & -1 & 1 & -1 \\ 0 & 0 & 0 & 1 & -1 & 0 & 0 & 1 & 1 & -1 & -1 & 0 & 0 & 0 & 0 \\ 0 & 0 & 0 & 1 & -1 & 0 & 0 & 1 & 1 & -1 & -1 & 0 & 0 & 0 & 0 \end{pmatrix}, \quad (\text{C.10})$$

with their associated weights:

$$w_\alpha = \left(\frac{2}{9} \frac{1}{9} \frac{1}{9} \frac{1}{9} \frac{1}{9} \frac{1}{9} \frac{1}{9} \frac{1}{9} \frac{1}{72} \frac{1}{72} \frac{1}{72} \frac{1}{72} \frac{1}{72} \frac{1}{72} \frac{1}{36} \frac{1}{36} \frac{1}{36} \right). \quad (\text{C.11})$$

- The smallest stencil used in this study, only applicable to advection-diffusion equations is the D3Q7:

$$\mathbf{c}_\alpha = \begin{pmatrix} 0 & 1 & -1 & 0 & 0 & 0 & 0 \\ 0 & 0 & 0 & 1 & -1 & 0 & 0 \\ 0 & 0 & 0 & 1 & -1 & 0 & 0 \end{pmatrix}, \quad (\text{C.12})$$

with weights:

$$w_\alpha = \left(\frac{1}{4} \frac{1}{8} \frac{1}{8} \frac{1}{8} \frac{1}{8} \frac{1}{8} \frac{1}{8} \right). \quad (\text{C.13})$$

Appendix D

Raw moments-based MRT solvers

D.1 Transformation matrices

Given that larger stencils such as D3Q19 or D3Q27 would result in rather large transform matrices, only transforms for smaller stencils are explicitly given here. Transforms for higher-order stencils and central moments and scaled-central moments space can be readily computed using the discrete velocity vectors and definitions of chosen sets of moments.

D.1.1 D2Q5 stencil

For the D2Q5 stencil the first five 2-D Hermite polynomials are used as the moments basis, i.e. $\Pi \in \{\mathcal{H}_0, \mathcal{H}_x, \mathcal{H}_y, \mathcal{H}_{x^2}, \mathcal{H}_{y^2}\}$. The moments transformation matrix and its inverse are given as:

$$\mathbf{M} = \begin{pmatrix} 1 & 1 & 1 & 1 & 1 \\ 0 & 1 & 0 & -1 & 0 \\ 0 & 0 & 1 & 0 & -1 \\ -c_s^2 & 1 - c_s^2 & -c_s^2 & 1 - c_s^2 & -c_s^2 \\ -c_s^2 & -c_s^2 & 1 - c_s^2 & -c_s^2 & 1 - c_s^2 \end{pmatrix} \quad (\text{D.1})$$

$$\mathbf{M}^{-1} = \begin{pmatrix} 1 - 2c_s^2 & 0 & 0 & -1 & -1 \\ \frac{c_s^2}{2} & \frac{1}{2} & 0 & \frac{1}{2} & 0 \\ \frac{c_s^2}{2} & 0 & \frac{1}{2} & 0 & \frac{1}{2} \\ \frac{c_s^2}{2} & -\frac{1}{2} & 0 & \frac{1}{2} & 0 \\ \frac{c_s^2}{2} & 0 & -\frac{1}{2} & 0 & \frac{1}{2} \end{pmatrix} \quad (\text{D.2})$$

D.1.2 D2Q9 stencil

For the D2Q9 stencil the first nine 2-D Hermite polynomials are used as the moments basis, i.e. $\Pi \in \{\mathcal{H}_0, \mathcal{H}_x, \mathcal{H}_y, \mathcal{H}_{xy}, \mathcal{H}_{x^2}, \mathcal{H}_{y^2}, \mathcal{H}_{x^2y}, \mathcal{H}_{xy^2}, \mathcal{H}_{x^2y^2}\}$, resulting in the following transformation matrices:

$$\mathbf{M} = \begin{pmatrix} 1 & 1 & 1 & 1 & 1 & 1 & 1 & 1 & 1 \\ 0 & 1 & 0 & -1 & 0 & 1 & -1 & -1 & 1 \\ 0 & 0 & 1 & 0 & -1 & 1 & 1 & -1 & -1 \\ 0 & 0 & 0 & 0 & 0 & 1 & -1 & 1 & -1 \\ -c_s^2 & 1 - c_s^2 & -c_s^2 & 1 - c_s^2 & -c_s^2 & 1 - c_s^2 & 1 - c_s^2 & 1 - c_s^2 & 1 - c_s^2 \\ -c_s^2 & -c_s^2 & 1 - c_s^2 & -c_s^2 & 1 - c_s^2 & 1 - c_s^2 & 1 - c_s^2 & 1 - c_s^2 & 1 - c_s^2 \\ 0 & 0 & -c_s^2 & 0 & c_s^2 & 1 - c_s^2 & 1 - c_s^2 & c_s^2 - 1 & c_s^2 - 1 \\ 0 & -c_s^2 & 0 & c_s^2 & 0 & 1 - c_s^2 & c_s^2 - 1 & c_s^2 - 1 & 1 - c_s^2 \\ c_s^4 & c_s^2 (c_s^2 - 1) & c_s^2 (c_s^2 - 1) & c_s^2 (c_s^2 - 1) & c_s^2 (c_s^2 - 1) & (c_s^2 - 1)^2 & (c_s^2 - 1)^2 & (c_s^2 - 1)^2 & (c_s^2 - 1)^2 \end{pmatrix} \quad (\text{D.3})$$

$$\mathbf{M}^{-1} = \begin{pmatrix}
(c_s^2 - 1)^2 & 0 & 0 & 0 & c_s^2 - 1 & c_s^2 - 1 & 0 & 0 & 1 \\
-\frac{c_s^2(c_s^2 - 1)}{2} & \frac{1}{2} - \frac{c_s^2}{2} & 0 & 0 & \frac{1}{2} - \frac{c_s^2}{2} & -\frac{c_s^2}{2} & 0 & -\frac{1}{2} & -\frac{1}{2} \\
-\frac{c_s^2(c_s^2 - 1)}{2} & 0 & \frac{1}{2} - \frac{c_s^2}{2} & 0 & -\frac{c_s^2}{2} & \frac{1}{2} - \frac{c_s^2}{2} & -\frac{1}{2} & 0 & -\frac{1}{2} \\
-\frac{c_s^2(c_s^2 - 1)}{2} & \frac{c_s^2}{2} - \frac{1}{2} & 0 & 0 & \frac{1}{2} - \frac{c_s^2}{2} & -\frac{c_s^2}{2} & 0 & \frac{1}{2} & -\frac{1}{2} \\
-\frac{c_s^2(c_s^2 - 1)}{2} & 0 & \frac{c_s^2}{2} - \frac{1}{2} & 0 & -\frac{c_s^2}{2} & \frac{1}{2} - \frac{c_s^2}{2} & \frac{1}{2} & 0 & -\frac{1}{2} \\
\frac{c_s^4}{4} & \frac{c_s^2}{4} & \frac{c_s^2}{4} & \frac{1}{4} & \frac{c_s^2}{4} & \frac{c_s^2}{4} & \frac{1}{4} & \frac{1}{4} & \frac{1}{4} \\
\frac{c_s^4}{4} & -\frac{c_s^2}{4} & \frac{c_s^2}{4} & -\frac{1}{4} & \frac{c_s^2}{4} & \frac{c_s^2}{4} & \frac{1}{4} & -\frac{1}{4} & \frac{1}{4} \\
\frac{c_s^4}{4} & -\frac{c_s^2}{4} & \frac{c_s^2}{4} & -\frac{1}{4} & \frac{c_s^2}{4} & \frac{c_s^2}{4} & \frac{1}{4} & -\frac{1}{4} & \frac{1}{4} \\
\frac{c_s^4}{4} & -\frac{c_s^2}{4} & -\frac{c_s^2}{4} & \frac{1}{4} & \frac{c_s^2}{4} & \frac{c_s^2}{4} & -\frac{1}{4} & -\frac{1}{4} & \frac{1}{4} \\
\frac{c_s^4}{4} & \frac{c_s^2}{4} & -\frac{c_s^2}{4} & -\frac{1}{4} & \frac{c_s^2}{4} & \frac{c_s^2}{4} & -\frac{1}{4} & \frac{1}{4} & \frac{1}{4}
\end{pmatrix} \quad (\text{D.4})$$

D.1.3 D3Q7 stencil

For the D3Q7 stencil the first seven 3-D Hermite polynomials are used as the moments basis, i.e. $\Pi \in \{\mathcal{H}_0, \mathcal{H}_x, \mathcal{H}_y, \mathcal{H}_z, \mathcal{H}_{x^2}, \mathcal{H}_{y^2}, \mathcal{H}_{z^2}\}$. The populations are transformed into moments and back through the following matrices:

$$\mathbf{M} = \begin{pmatrix}
1 & 1 & 1 & 1 & 1 & 1 & 1 \\
0 & 1 & -1 & 0 & 0 & 0 & 0 \\
0 & 0 & 0 & 1 & -1 & 0 & 0 \\
0 & 0 & 0 & 0 & 0 & 1 & -1 \\
-c_s^2 & 1 - c_s^2 & 1 - c_s^2 & -c_s^2 & -c_s^2 & -c_s^2 & -c_s^2 \\
-c_s^2 & -c_s^2 & -c_s^2 & 1 - c_s^2 & 1 - c_s^2 & -c_s^2 & -c_s^2 \\
-c_s^2 & -c_s^2 & -c_s^2 & -c_s^2 & -c_s^2 & 1 - c_s^2 & 1 - c_s^2
\end{pmatrix} \quad (\text{D.5})$$

$$\mathbf{M}^{-1} = \begin{pmatrix}
1 - 3c_s^2 & 0 & 0 & 0 & -1 & -1 & -1 \\
\frac{c_s^2}{2} & \frac{1}{2} & 0 & 0 & \frac{1}{2} & 0 & 0 \\
\frac{c_s^2}{2} & -\frac{1}{2} & 0 & 0 & \frac{1}{2} & 0 & 0 \\
\frac{c_s^2}{2} & 0 & \frac{1}{2} & 0 & 0 & \frac{1}{2} & 0 \\
\frac{c_s^2}{2} & 0 & -\frac{1}{2} & 0 & 0 & \frac{1}{2} & 0 \\
\frac{c_s^2}{2} & 0 & 0 & \frac{1}{2} & 0 & 0 & \frac{1}{2} \\
\frac{c_s^2}{2} & 0 & 0 & -\frac{1}{2} & 0 & 0 & \frac{1}{2}
\end{pmatrix} \quad (\text{D.6})$$

Appendix E

Jacobians of different collision operators

For the expressions presented here to be valid for both shifted and regular stencils, the derivations are made using the non-dimensional variables \mathbf{u}^* and \mathbf{c}_α^* introduced in chapter 7. A more detailed derivation of the Jacobians can be found in [150, 54, 152, 236].

E.1 SRT collision model

E.1.1 Hermite-expansion based EDF

For the D2Q9 stencil, the fourth-order EDF can be explicitly written as:

$$f_\alpha^{(eq,4)} = w_\alpha \rho \left[\underbrace{1 + \mathbf{c}_\alpha^* \cdot \mathbf{u}^* + \frac{1}{2} \mathcal{H}_{\alpha,2} : \mathbf{a}_2^{(eq)}}_{f_\alpha^{(eq,2)}} + \frac{1}{2} \left(\mathcal{H}_{\alpha,x^2y} a_{x^2y}^{(eq)} + \mathcal{H}_{\alpha,xy^2} a_{xy^2}^{(eq)} \right) + \frac{1}{4} \mathcal{H}_{\alpha,x^2y^2} a_{x^2y^2}^{(eq)} \right]. \quad (\text{E.1})$$

To compute the Jacobian of the EDF at different orders, the following equations can be used:

$$\frac{\partial \rho a_{3,x^2y}^{(eq)}}{\partial f_\beta} = 2c_{\beta,x}^* u_x^* u_y^* + c_{\beta,y}^* u_x^{*2} - 2u_y^* u_x^{*2}, \quad (\text{E.2a})$$

$$\frac{\partial \rho a_{3,xy^2}^{(eq)}}{\partial f_\beta} = 2c_{\beta,y}^* u_y^* u_x^* + c_{\beta,x}^* u_y^{*2} - 2u_x^* u_y^{*2}, \quad (\text{E.2b})$$

$$\frac{\partial \rho a_{4,x^2y^2}^{(eq)}}{\partial f_\beta} = 2c_{\beta,x}^* u_y^{*2} u_x^* + c_{\beta,x}^* u_y^* u_x^{*2} - 3u_x^{*2} u_y^{*2}, \quad (\text{E.2c})$$

E.1.2 Exact entropic EDF

For the entropic EDF, re-writing it as:

$$f_\alpha^{(eq)} = w_\alpha \rho \prod_{i=x,y} \Lambda_i \Gamma_{\alpha,i}, \quad (\text{E.3})$$

the Jacobian can be expressed as:

$$\frac{\partial f_\alpha^{(eq)}}{\partial f_\beta} = w_\alpha \left[\prod_{i=x,y} \Lambda_i \Gamma_{\alpha,i} + \sum_{i=x,y} \rho \left(\Gamma_{\alpha,i} \frac{\partial \Lambda_i}{\partial f_\beta} + \Lambda_i \frac{\partial \Gamma_{\alpha,i}}{\partial f_\beta} \right) \prod_{j \neq i} \Lambda_j \Gamma_{\alpha,j} \right], \quad (\text{E.4})$$

where:

$$\Lambda_i = 2 - \frac{S_i}{\rho}, \quad (\text{E.5a})$$

$$\Gamma_{\alpha,i} = \left(\frac{2u_i^* + \frac{S_i}{\rho}}{1 - u_i^*} \right)^{c_{\alpha,i}^*}, \quad (\text{E.5b})$$

$$S_i = \rho \sqrt{3u_i^{*2} + 1}, \quad (\text{E.5c})$$

and :

$$\frac{\partial \Lambda_i}{\partial f_\beta} = \frac{S_i}{\rho^2} - \frac{1}{\rho} \frac{\partial S_i}{\partial f_\beta}, \quad (\text{E.6a})$$

$$\frac{\partial \Gamma_{\alpha,i}}{\partial f_\beta} = c_{\alpha,i}^* \left[\frac{2c_{\beta,i}^* + \frac{\partial S_i}{\partial f_\beta}}{\rho(1 - u_i^*)} - \frac{(2\rho u_i^* + S_i)(1 - c_{\beta,i}^*)}{\rho^2(1 - u_i^*)^2} \right] \left(\frac{2u_i^* + \frac{S_i}{\rho}}{1 - u_i^*} \right)^{c_{\alpha,i}^* - 1}, \quad (\text{E.6b})$$

$$\frac{\partial S_i}{\partial f_\beta} = \frac{\rho(3c_{\beta,i}^* u_i^* + 1)}{S_i}. \quad (\text{E.6c})$$

E.2 RLBM collision model

For the fourth-order recursive regularized collision operator, one must compute the Jacobian of the reconstructed non-equilibrium part of the distribution function:

$$\begin{aligned} \frac{\partial f_\alpha^{(neq,4)}}{\partial f_\beta} = w_\alpha \left[\frac{1}{2} \mathcal{H}_{2,\alpha} : \left(\sum_\beta \mathcal{H}_{2,\beta} f_\beta - \mathbf{a}_2^{(eq)} \right) \right. \\ \left. + \frac{1}{2} \left(\mathcal{H}_{\alpha,x^2y} \frac{\partial a_{x^2y}^{(1)}}{\partial f_\beta} + \mathcal{H}_{\alpha,xy^2} \frac{\partial a_{xy^2}^{(1)}}{\partial f_\beta} \right) + \frac{1}{4} \mathcal{H}_{\alpha,x^2y^2} \frac{\partial a_{x^2y^2}^{(1)}}{\partial f_\beta} \right] \quad (\text{E.7}) \end{aligned}$$

where:

$$\frac{\partial a_{x^2y}^{(1)}}{\partial f_\beta} = \frac{\partial \left(\frac{a_y^{(eq)} a_{x^2}^{(1)}}{a_0^{(eq)}} + 2 \frac{a_x^{(eq)} a_{xy}^{(1)}}{a_0^{(eq)}} \right)}{\partial f_\beta} = u_y^* \frac{\partial a_{x^2}^{(1)}}{\partial f_\beta} + 2u_x^* \frac{\partial a_{xy}^{(1)}}{\partial f_\beta}, \quad (\text{E.8a})$$

$$\frac{\partial a_{xy^2}^{(1)}}{\partial f_\beta} = \frac{\partial \left(\frac{a_x^{(eq)} a_{y^2}^{(1)}}{a_0^{(eq)}} + 2 \frac{a_y^{(eq)} a_{xy}^{(1)}}{a_0^{(eq)}} \right)}{\partial f_\beta} = u_x^* \frac{\partial a_{y^2}^{(1)}}{\partial f_\beta} + 2u_y^* \frac{\partial a_{xy}^{(1)}}{\partial f_\beta}, \quad (\text{E.8b})$$

$$\frac{\partial a_{x^2y^2}^{(1)}}{\partial f_\beta} = \frac{\partial \left(\frac{a_y^{(eq)} a_{x^2y}^{(1)}}{a_0^{(eq)}} + \frac{a_x^{(eq)2} a_{y^2}^{(1)}}{a_0^{(eq)2}} + \frac{a_x^{(eq)} a_y^{(eq)} a_{xy}^{(1)}}{a_0^{(eq)2}} \right)}{\partial f_\beta} = u_y^* \frac{\partial a_{x^2y}^{(1)}}{\partial f_\beta} + u_x^{*2} \frac{\partial a_{y^2}^{(1)}}{\partial f_\beta} + u_x^* u_y^* \frac{\partial a_{xy}^{(1)}}{\partial f_\beta}. \quad (\text{E.8c})$$

Appendix F

Detailed chemical schemes

F.1 Detailed kinetic scheme for an Ozone/air reacting flow (from [1])

	$k = AT^\beta e^{-\frac{E}{RT}}$ for reaction:	A	β	E
1	$2O + M \leftrightarrow O_2 + M$	1.200000E+17	-1.000000E+00	0.000000E+00
2	$O_3 + O_2 \rightarrow O_2 + O + O_2$	1.540000E+14	0.000000E+00	2.305850E+04
3	$O_3 + O \rightarrow O_2 + O + O$	2.480000E+15	0.000000E+00	2.272160E+04
4	$O_3 + O_3 \rightarrow O_2 + O + O_3$	4.400000E+14	0.000000E+00	2.305850E+04
5	$O_3 + N_2 \rightarrow O_2 + O + N_2$	4.000000E+14	0.000000E+00	2.266190E+04
6	$O_2 + O + O_2 \rightarrow O_3 + O_2$	3.260000E+19	-2.100000E+00	0.000000E+00
7	$O_2 + O + N_2 \rightarrow O_3 + N_2$	1.600000E+14	-4.000000E-01	-1.390700E+03
8	$O_2 + O + O \rightarrow O_3 + O$	2.280000E+15	-5.000000E-01	-1.390700E+03
9	$O_2 + O + O_3 \rightarrow O_3 + O_3$	1.670000E+15	-5.000000E-01	-1.390700E+03
10	$O_2 + O_2 \rightarrow O + O + O_2$	9.800000E+24	-2.500000E+00	1.180382E+05
11	$O_2 + O \rightarrow O + O + O$	3.500000E+25	-2.500000E+00	1.180382E+05
12	$O_2 + O_3 \rightarrow O + O + O_3$	1.200000E+19	-1.000000E+00	1.180382E+05
13	$O + O + O_2 \rightarrow O_2 + O_2$	1.500000E+16	-4.000000E-01	0.000000E+00
14	$O + O + N_2 \rightarrow O_2 + N_2$	6.000000E+13	0.000000E+00	-1.789700E+03
15	$O + O + O \rightarrow O_2 + O$	5.340000E+16	-4.000000E-01	0.000000E+00
16	$O + O + O_3 \rightarrow O_2 + O_3$	1.300000E+14	0.000000E+00	-1.789700E+03
17	$O_2 + O_2 \rightarrow O_3 + O$	1.200000E+13	0.000000E+00	1.003871E+05
18	$O_3 + O \rightarrow O_2 + O_2$	4.820000E+12	0.000000E+00	4.095600E+03

F.2 Two-step BFER scheme for Methane/air flame [2])

	$k = A[\text{CH}_4]^{\nu_{\text{CH}_4}}[\text{O}_2]^{\nu_{\text{O}_2}}T^\beta e^{-\frac{E}{RT}}$ for reaction:	A	β	E	ν_{CH_4}	ν_{O_2}
1	$\text{CH}_4 + \frac{3}{2}\text{O}_2 \rightarrow \text{CO} + 2\text{H}_2\text{O}$	4.900000E+9	0.000000E+00	3.550000E+04	0.5	0.65
2	$\text{CO} + \frac{1}{2}\text{O}_2 \leftrightarrow +\text{CO}_2$	2.000000E+8	0.700000E+00	1.200000E+04	0	0

The units of A , β and T are all based on moles, calories and seconds. M is used to represent an arbitrary third-body for the reaction.

